



**HAL**  
open science

# Synthesis and Characterization of Hybrid Metal-Metallic Oxide Composite Nanofibers by Electrospinning and Their Applications

Xiaojiao Yang

► **To cite this version:**

Xiaojiao Yang. Synthesis and Characterization of Hybrid Metal-Metallic Oxide Composite Nanofibers by Electrospinning and Their Applications. Materials and structures in mechanics [physics.class-ph]. Université de Lyon, 2016. English. NNT : 2016LYSE1022 . tel-01435191

**HAL Id: tel-01435191**

**<https://theses.hal.science/tel-01435191>**

Submitted on 13 Jan 2017

**HAL** is a multi-disciplinary open access archive for the deposit and dissemination of scientific research documents, whether they are published or not. The documents may come from teaching and research institutions in France or abroad, or from public or private research centers.

L'archive ouverte pluridisciplinaire **HAL**, est destinée au dépôt et à la diffusion de documents scientifiques de niveau recherche, publiés ou non, émanant des établissements d'enseignement et de recherche français ou étrangers, des laboratoires publics ou privés.

THESE DE L'UNIVERSITE DE LYON  
Délivrée par  
L'UNIVERSITE CLAUDE BERNARD LYON 1  
ECOLE DE CHIMIE

DIPLOME DE DOCTORAT  
(arrêté du 7 août 2006)

Soutenance prévue le 27 Janvier 2016  
par

**YANG Xiaojiao**

---

**Synthesis and Characterization of Hybrid Metal-Metallic Oxide  
Composite Nanofibers by Electrospinning and Their Applications**

---

Directeur de thèse : **Pr. Arnaud BRIOUDE**

Encadrant : **Dr. Vincent SALLES**

**COMPOSITION DU JURY :**

**Rapporteurs :**

Pr. Guy SCHLATTER  
Dr. Jean-Pierre SIMONATO

ICPEES, UMR 7515 CNRS, Université de Strasbourg  
LITEN / DTNM / SEN / LSIN, CEA-Grenoble

**Examineurs :**

Dr. Christophe GEANTET  
Dr. Sara CAVALIERE  
Pr. Sylvie FOUCAUD  
Pr. Arnaud BRIOUDE  
Dr. Vincent SALLES  
Dr. Mathieu MAILLARD

IRCELYON, UMR 5256 CNRS, Université Lyon 1  
ICGM, UMR5253, Université de Montpellier 2  
SPCTS, Centre Européen de la Céramique, Limoges  
LMI, UMR 5615 CNRS, Université Lyon 1  
LMI, UMR 5615 CNRS, Université Lyon 1  
LMI, UMR 5615 CNRS, Université Lyon 1



# UNIVERSITE CLAUDE BERNARD - LYON 1

**Président de l'Université**

**M. François-Noël GILLY**

Vice-président du Conseil d'Administration

M. le Professeur Hamda BEN HADID

Vice-président du Conseil des Etudes et de la Vie  
Universitaire

M. le Professeur Philippe LALLE

Vice-président du Conseil Scientifique

M. le Professeur Germain GILLET

Directeur Général des Services

M. Alain HELLEU

## ***COMPOSANTES SANTE***

Faculté de Médecine Lyon Est – Claude Bernard

Directeur : M. le Professeur J. ETIENNE

Faculté de Médecine et de Maïeutique Lyon Sud – Charles  
Mérieux

Directeur : Mme la Professeure C. BURILLON

Faculté d'Odontologie

Directeur : M. le Professeur D. BOURGEOIS

Institut des Sciences Pharmaceutiques et Biologiques

Directeur : Mme la Professeure C. VINCIGUERRA

Institut des Sciences et Techniques de la Réadaptation

Directeur : M. le Professeur Y. MATILLON

Département de formation et Centre de Recherche en Biologie  
Humaine

Directeur : Mme. la Professeure A-M. SCHOTT

## ***COMPOSANTES ET DEPARTEMENTS DE SCIENCES ET TECHNOLOGIE***

Faculté des Sciences et Technologies

Directeur : M. F. DE MARCHI

Département Biologie

Directeur : M. le Professeur F. FLEURY

Département Chimie Biochimie

Directeur : Mme Caroline FELIX

Département GEP

Directeur : M. Hassan HAMMOURI

Département Informatique

Directeur : M. le Professeur S. AKKOUICHE

Département Mathématiques

Directeur : M. le Professeur Georges TOMANOV

Département Mécanique

Directeur : M. le Professeur H. BEN HADID

Département Physique

Directeur : M. Jean-Claude PLENET

UFR Sciences et Techniques des Activités Physiques et  
Sportives

Directeur : M. Y. VANPOULLE

Observatoire des Sciences de l'Univers de Lyon

Directeur : M. B. GUIDERDONI

Polytech Lyon

Directeur : M. P. FOURNIER

Ecole Supérieure de Chimie Physique Electronique

Directeur : M. G. PIGNAULT

Institut Universitaire de Technologie de Lyon 1

Directeur : M. le Professeur C. VITON

Ecole Supérieure du Professorat et de l'Education

Directeur : M. le Professeur A. MOUGNIOTTE

Institut de Science Financière et d'Assurances

Directeur : M. N. LEBOISNE



## ACKNOWLEDGEMENTS

### **ONLY LYON, ONLY YOU!**

I want to start the acknowledgements with this simple memorable phase.

**ONLY LYON:** It is a kind of destiny for me to study at **LYON**, not to choose other cities. Lyon, it's one of the most beautiful and significance cities in my mind. It has the most well-known festival of "Fête des Lumières" on 8<sup>th</sup> December, what a coincidence, it is the same day of my solar calendar birthday. Meanwhile, It is the hometown of Antoine Saint-Exupéry, the writer of my favorite book "Le Petit Prince", the "Rose" in the book also has reality story at Lyon that the world-class biggest Rose Festival has been taken at the "parc de la Tête d'Or". I have been there with "le petit prince" and tried to find prince's "Rose".

**ONLY YOU:** Lyon also has many beautiful views and delicious food. BUT the most important for me is the lovely people I met there. **My supervisor, co-supervisors, colleagues, neighbors, friends, travel companions** and so on, all of them are the special one for me, which is the expression of ONLY YOU. It is the worthwhile experience. So I want to deliver my sincere thanks to them here, without their help, this thesis would not have been possible.

Many thanks must firstly be delivered to my supervisor **Arnaud BRIOUDE**, the professor of "**Université Claude Bernard Lyon 1**" (UCBL). I have been very fortunate to be advised by him. During these 40 months studying in France, Arnaud has provided me with numerous important suggestions, remarks for guiding this thesis, and helped me directly when I had problems or troubles with the administrative procedures. He always encouraged me and pointed out directions of my research during the monthly progress report. He is intelligent and always has the best solutions. He also has done great contributions to the team work of our lab, which makes a very comfortable, motivated, and united group. Thanks Arnaud.

Thanks should go to Dr. **Vincent SALLES**, my co-supervisor, on his tutorial on Electrospinning, making presentation and writing reports, my communication and writing skills are made huge progress. Vincent has the good sense of humor, so working with him is very relax and happy. I enjoyed all the meetings with him and Arnaud. He is smart and creative, that he has lots of good ideas to overcome the problems during the research. Sometimes I was not confident, but he has his own way to encourage me. I still remember all the moved tears streaming in front of him including the last time at the end of my defense.

I also want to express my thanks to Dr. **Mathieu MAILLARD**. Mathieu helped me a lot during my research, not only for the photocatalysis experiments in the lab, but also for teaching me the calculations, characterizations, and discussions during my important report meetings. He also has great efforts of giving many recommendations and comments for this thesis, and revising the manuscript for me with Arnaud and Vincent. Mathieu is wisdom and good-natured, and is enthusiasm to help others in the team. We all like him very much.

Special thanks should go to **Xuchuan JIANG**, the professor of University of New South Wales, Australia. Now he is working at the University of Melbourne, Australia. I appreciate his efforts in organizing my visit to Australia. In my second year, I have been very fortunate to have a whole month academic visit to Australia with an international project between France and Australia. In composing this thesis, he has taught me lots of new knowledge of photocatalysis and gas sensor with great patience. He has contributed many important thoughts to the achievement of this thesis. Meanwhile, thanks **Yusuf Valentino Kanet**, the post-doc of Xuchuan's group, for helping me on the analysis in Australia.

Whom I wish to thank: **Catherine JOURNET, Rodica CHIRIAC, Françoise TOCHE**,

**Bruno GARDIOLA**, and **Laurence BOIS**. Thanks Catherine for her help on TEM. She is so kind and I really enjoyed the pleasant chatting with her all the time. Thanks Rodica and Françoise for their help on TGA and BET. Rodica's beautiful flowers in her office were impressive. The green plants she gave to me as gift were always on my desk and brought me good mood every day. Thanks Bruno for his help on XRD and the guide for using the software of Brass. Thanks Laurence for her help on literature research and encouragement for the final defense. Thanks all the permanent staffs in our group of "*Laboratoire des multimatériaux et interfaces*" (LMI), they are **Fernand CHASSAGNEUX**, **Cedric DESROCHES**, **Bérangère TOURY**, **Catherine MARICHY**, **Yannick TAURAN**. I also want to thank the secretaries of our lab: **Patricia**, **Fabienne**, and **Nicolas**.

Although in LMI, we are in two buildings (Berthollet and Chevrel), the different location can't separate us. LMI likes a warm family. What most impressed me is the lunch time at Domus, all the group members have lunch together on working days. A good cohesion unites everyone during the lunch time by chatting. I have had many lovely colleagues that I missed them too much and want to send my thanks and best wishes to them. They are **Bastien BESSAIRE**, **Niall O'TOOLE**, **Wenjun HAO**, **Tony GERGES**, **Franck HALLY**, **Meriem**, **Mélanie**, **Nicolas**, **Victor**, **Françoise**, **Brice**, **Sébastien LINAS**, **Nelly COUZON**, **Gwenaël BONFANTE**, **Adrien**, **Julien**, **Laurence OURRY**, **Yangdi LI**, and **Shiqi ZHANG**. I can't forget the help from Meriem and Franck from the daily life to the French learning at the beginning. The memories of swimming, climbing, and all the other activities that we did together, were meaningful for me. Tony, who also worked on electrospinning like me with Vincent, we should still talk on the reason of "Chinese boy" and "Lebanese girl". Bastien and Niall, we spent the longest and happiest time in the office. There were many laughs with you. Wenjun, we are like sisters, the emotions between us can't be written by the words.

I don't know how to send my thanks to **Sheng YUAN** and **Dawei WANG**. Sheng is always on my side since the first day he picked me up at the airport. He provides the greatest help to me with his wife **Ying ZHU**. Dawei was accompany and encouraged me at the last high pressure and dark period. I appreciate for your participation in a part of my life. I also want to thank all my neighbors and friends: **Min YAO**, **Xi YU**, **Wenjing WANG**, **Liping ZHANG**, **Rui XU**, **Xi JIANG**, and **Xun SUN**, we lived together in our "*Castle of Sky*". Min is my best Chinese friends in Lyon. We are the "Kappa Combination". No words can describe our friendship. Xi is the head of us. He always organized the activities in the castle. Delicious food that we cooked together would memorize our happy time together. We always learned from each other by organizing unofficial seminar to exchange ideas, useful techniques in our own research area. Thanks for the travel companions. We had good moments during skydiving, rock climbing, skiing and visiting beautiful cities in Europe. I also thank my friends in Lyon: **Hui REN**, **Huijing SUN**, **Dajun WU**, **Bin BAO**, **Jingping LI**, **Quanyi YIN**, **Hu XIONG**, **Sasa GAO**, **Xichen YUAN**, **Qing LIU**, **Jing XIE**, **Zemeng SU**, **Yanjun CAI**, **Mingchao JI**, and **Zheng SONG**. The friendship will never fade as the time flies.

I also wish to sincerely thank the juries for evaluating my PhD thesis: **Guy SCHLATTER**, **Jean-Pierre SIMONATO**, **Christophe GEANTET**, **Sara CAVALIERE**, and **Sylvie FOUCAUD**. The financial support of this thesis was provided by the **China Scholarship Council (CSC)**.

In the end, I wish to thank my parents. Thanks for their support and encouragement. Their trust encourages me to continue my study and to live my dream. When it comes to the word of dream, **Xiaojiao**, do you know what you want?

**Dream it possible!**

## RÉSUMÉ

Nous présentons dans ce manuscrit l'élaboration par électrofilage (ES) de nanofibres hybrides métal/oxyde métallique (HMMOC) et leurs caractérisations physico-chimiques. Leurs utilisations dans le cadre d'applications de type « énergie » et « environnement » ont été évaluées. En particulier, la photocatalyse de nanofibres TiO<sub>2</sub>-Au pour la dégradation en solution aqueuse du bleu de méthylène et l'utilisation de nanofibres WO<sub>3</sub>-Au comme capteurs de gaz (VOCs) ont été examinées.

En lien étroit avec les résultats obtenus sur l'évaluation des performances comme photocatalyseurs ou capteurs à gaz de ces nouvelles structures HMMOC, l'influence de nombreux paramètres a été étudiée : la concentration en ions aurique, la méthode utilisée pour introduire ces derniers à l'intérieur ou les déposer à la surface des nanofibres d'oxydes et finalement le traitement thermique. En effet, on peut soit mélanger directement, avant la procédure d'électrofilage, la solution contenant les ions aurique à la solution polymérique (composée de PVP, PAN, ou PVA contenant le précurseur d'oxyde métallique), soit déposer sous forme de goutte cette solution d'ions Au à la surface des nanofibres d'oxyde métallique une fois la procédure d'électrofilage effectuée. Quant au traitement thermique, il joue un rôle multiple puisqu'il permet à la fois, d'éliminer les composés organiques des solutions polymériques, participant ainsi à la structuration de la partie oxyde du HMMOC, mais aussi de réduire les ions Au sous forme de nanoparticules.

Des résultats prometteurs en photocatalyse ont été obtenus sur des fibres optimisées de TiO<sub>2</sub> contenant des nanoparticules d'au de 10 nm (concentration en Au : 4 wt%). En effet, pour cet échantillon, on montre une dégradation 3 fois plus rapide du bleu de méthylène en solution aqueuse que celle obtenue sur les nanofibres de TiO<sub>2</sub> de références et sur le catalyseur commercial P25. De la même manière, des nanofibres de WO<sub>3</sub> décorées de nanoparticules d'au de 10 nm, utilisées comme capteurs de gaz, permettent d'obtenir une réponse 60 fois plus importante que dans le cas de nanofibres de WO<sub>3</sub> pure et en améliorant grandement la sélectivité par rapport au *n*-butanol.

### Mots clés:

or; dioxyde de titane; trioxyde de tungstène; polymère; nanofibres; électrofilage; photocatalyse; capteur de gaz



## ABSTRACT

We present in this manuscript the elaboration by Electrospinning (ES) process of hybrid metal-metallic oxide composite (HMMOC) nanofibers (NFs), and their physical-chemical characterizations. Their applications, especially the photocatalysis of TiO<sub>2</sub>-Au composite NFs for photocatalytic degradation for methylene blue (MB) in an aqueous solution and WO<sub>3</sub>-Au composite NFs for gas sensing of the volatile organic compounds (VOCs) have been investigated.

According to the performance evaluation results as photocatalysts or gas sensors, the influence of many parameters have been studied: gold ions concentration, the way to introduce them into or at the NFs surface, typically by mixing them into the polymeric solution (composed of PVP, PAN, or PVA with the metallic oxide precursor) before the ES process or by simple droplet deposition onto the NFs after ES process, and finally the annealing treatment. This latter plays an important role since it both removes the organic components of the polymeric solution, thus forming the metallic oxide and in-situ participates to the Au reduction.

Concerning the photocatalytic properties, an optimized HMMOC material based on TiO<sub>2</sub> NFs including 10 nm Au nanoparticles (NPs) has been obtained and shows 3 times significantly improvement of MB degradation compared to pure TiO<sub>2</sub> NFs and the commercial catalyst P25. For gas sensing elaboration, we have shown that a HMMOC material based on WO<sub>3</sub> NFs decorated at their surface with 10 nm Au NPs can exhibit 60 times higher response and significantly improved selectivity toward *n*-butanol compared with pure WO<sub>3</sub> NFs.

### **Keywords:**

gold; titanium oxide; tungsten oxide; polymer; nanofibers; electrospinning; photocatalysis; gas sensor



## ABBREVIATIONS

Abbreviation	Meaning
<b>1D</b>	one dimension
<b>A/R</b>	anatase : rutile
<b>AMT</b>	ammonium metatungstate hydrate
<b>CB</b>	conduction band
<b>DMF</b>	N,N-dimethyl-formamide
<b>DMFCs</b>	direct methanol fuel cells
<b>DSSC</b>	dye sensitized solar cells
<b>ES</b>	electrospinning
<b>HMMOC</b>	hybrid metal @ metallic oxide composites
<b>LSPR</b>	localized surface plasmon resonance
<b>MB</b>	methyl blue
<b>NHE</b>	normal hydrogen electrode
<b>NPs</b>	nanoparticles
<b>NRs</b>	nanorods
<b>NTs</b>	nanotubes
<b>NWs</b>	nanowires
<b>PAN</b>	polyacrylonitrile
<b>PPX</b>	polymer poly(p-xylylene)
<b>PVA</b>	polyvinyl alcohol
<b>PVDF</b>	polyvinylidene fluoride
<b>PVP</b>	poly(vinyl pyrrolidone)
<b>R<sub>air</sub></b>	sensor resistance in ambient air
<b>R<sub>gas</sub></b>	sensor resistance in the target gas
<b>S</b>	sensitivity
<b>SC</b>	semiconductor
<b>SERS</b>	surface enhanced raman spectroscopy or surface enhanced raman scattering
<b>SPRE</b>	surface plasmon resonance effect
<b>TTIP</b>	titanium isopropoxide
<b>UV</b>	ultraviolet
<b>VB</b>	valence band
<b>VOCs</b>	volatile organic compounds
<b>T<sub>rec</sub></b>	recovery time
<b>T<sub>res</sub></b>	response time



---

## CONTENTS

<b>ACKNOWLEDGEMENTS .....</b>	<b>5</b>
<b>RÉSUMÉ .....</b>	<b>7</b>
<b>ABSTRACT .....</b>	<b>9</b>
<b>ABBREVIATIONS.....</b>	<b>11</b>
<b>CONTENTS .....</b>	<b>13</b>
<b>GENERAL INTRODUCTION .....</b>	<b>21</b>
<b>CHAPTER I BIBLIOGRAPHIC STUDY .....</b>	<b>25</b>
<b>1 Hybrid Metal @ Metallic Oxide Composites (HMMOC) .....</b>	<b>25</b>
1.1 State of the art .....	25
1.1.1 Introduction of HMMOC semiconducting part.....	26
1.1.2 Structures and properties of titanium oxide (TiO <sub>2</sub> ).....	28
1.1.3 Structures and properties of tungsten oxide (WO <sub>3</sub> ).....	30
1.1.4 Introduction of HMMOC metallic part .....	31
1.1.5 Specific electronic properties of noble metal: Surface Plasmon Resonance .....	32
1.2 Influence of size for applications of HMMOC materials .....	35
1.3 Influence of shape for applications of HMMOC materials.....	35
1.4 Conclusions .....	37
<b>2 The particular case of 1D HMMOC materials .....</b>	<b>38</b>
2.1 General point of view .....	38
2.2 Synthesis of HMMOC nanofibers – electrospinning and related techniques .....	38
2.2.1 Direct-dispersed electrospinning.....	39
2.2.2 Sol-gel method.....	39
2.2.3 <i>In situ</i> photoreduction .....	40

2.2.4 Gas-solid reaction .....	41
2.3 Conclusions .....	41
<b>3 Electrospinning .....</b>	<b>42</b>
3.1 State of the art .....	42
3.1.1 Historical background .....	42
3.1.2 Basic principles of electrospinning .....	42
3.1.3 Electrospinning process .....	43
3.2 Influential parameters of the electrospinning process.....	44
3.2.1 Solution properties .....	44
3.2.2 Spinning parameters.....	45
3.3 Applications.....	46
3.3.1 Templates.....	46
3.3.2 Superhydrophobic surfaces .....	47
3.3.3 Electronic and optical nanodevices .....	47
3.3.4 Biomedical applications .....	48
3.3.5 Environmental applications .....	48
3.3.6 Energy applications.....	48
3.3.7 Catalysis applications.....	49
3.3.8 Chemical and biological sensors.....	50
<b>4 Applications of HMMOC nanofibers .....</b>	<b>50</b>
4.1 State of the art .....	50
4.2 Applications in energy.....	50
4.3 Applications in nanoelectronic devices.....	51
4.4 Applications in catalytic field .....	52
4.4.1 Historical background .....	52
4.4.2 Photocatalysis mechanism .....	54
4.4.3 Photocatalysis applications.....	56
4.5 Applications in sensor field .....	56
4.5.1 Historical background .....	56
4.5.2 Gas-sensing mechanism .....	57
4.5.3 Gas-sensing applications .....	58

---

<b>5 Conclusions .....</b>	<b>59</b>
5.1 Main challenges and opportunities for photocatalysis .....	59
5.2 Main challenges and opportunities for gas sensor .....	60
<b>CHAPTER II EXPERIMENTAL METHODS AND CHARACTERIZATIONS .....</b>	<b>63</b>
<b>1 Materials and Instruments .....</b>	<b>64</b>
1.1 Materials .....	64
1.1.1 Precursors .....	64
1.1.2 Solubility of precursors and spinnable polymers .....	64
<b>2 Synthesis routes and processes .....</b>	<b>65</b>
2.1 General information on equipment .....	66
2.1.1 Electrospinning setup .....	66
2.1.2 Thermal treatments .....	67
2.2 Description of the different Au addition routes .....	67
2.2.1 Synthesis processes and different Au addition routes .....	67
2.2.2 Thermal treatment processes .....	68
2.3 Preparation of pure polymer nanofibers .....	69
2.4 Synthesis of polymer–Au composite nanofibers .....	70
2.4.1 PVP–Au nanofibers .....	70
2.4.2 PVA–Au nanofibers .....	71
2.4.3 PAN–Au nanofibers .....	71
2.5 Synthesis of metallic oxide nanofibers .....	72
2.5.1 TiO <sub>2</sub> nanofibers .....	72
2.5.2 WO <sub>3</sub> nanofibers .....	73
2.6 Synthesis of HMMOC nanofibers .....	73
2.6.1 TiO <sub>2</sub> –Au composite nanofibers .....	73
2.6.2 WO <sub>3</sub> –Au composite nanofibers .....	74
2.7 Summary of Au addition routes .....	75
<b>3 Composite nanofibers characterizations .....</b>	<b>76</b>
3.1 Morphological characterizations .....	76

3.1.1 Scanning Electron Microscopy (SEM) .....	76
3.1.2 High Resolution Transmission Electron Microscopy (HR-TEM).....	77
3.2 Physico-chemical characterizations.....	78
3.2.1 Thermogravimetric Analysis (TGA) .....	78
3.2.2 Fourier Transform – Infrared Spectroscopy (FT-IR).....	79
3.2.3 X-ray Powder Diffraction (XRD).....	79
3.2.4 Nitrogen adsorption-desorption isotherms (BET) .....	80
3.2.5 Inductively Coupled Plasma – Optical Emission Spectroscopy (ICP-OES).....	81
<b>4 Performance measurement systems.....</b>	<b>81</b>
4.1 Photocatalysis performance measurement system.....	82
4.1.1 Photocatalytic measurement system .....	82
4.1.2 Ultraviolet – Visible Spectroscopy (UV-Vis).....	82
4.2 Gas-sensing performance measurement system .....	83
4.2.1 Gas-sensing measurement system .....	83
4.2.2 Gas-sensing performance characteristics.....	84
<b>CHAPTER III STUDY AND OPTIMIZATION OF THE FABRICATING CONDITIONS OF GOLD-CONTAINING NANOFIBERS .....</b>	<b>87</b>
<b>1 Introduction .....</b>	<b>87</b>
<b>2 Volume inclusion .....</b>	<b>87</b>
2.1 Study of different starting polymers .....	87
2.1.1 Basic information for electrospinning conditions.....	88
2.1.2 The influence of different polymer.....	89
2.2 Thermal behaviour of PVP-Au nanofibers.....	90
2.3 Morphology and composition of PVP-Au nanofibers .....	93
2.4 Gold nanoparticles formation with temperature .....	99
<b>3 Surface deposition .....</b>	<b>100</b>
3.1 Stability of different polymer nanofibers.....	101
3.2 Thermal behaviour of PAN-Au.....	101
3.2.1 Stabilization temperatures .....	102

---

3.2.2 Au deposition on PAN nanofibers.....	103
3.3 Optimization of the surface deposition method.....	105
3.3.1 Au amount .....	105
3.3.2 Reducing method.....	107
3.4 Morphology and composition of PAN-Au composite nanofibers .....	108
<b>4 Conclusions .....</b>	<b>110</b>
<b>CHAPTER IV CHARACTERIZATION AND PHOTOCATALYTIC ACTIVITY OF TiO<sub>2</sub>-Au COMPOSITE NANOFIBERS .....</b>	<b>111</b>
<b>1 Introduction .....</b>	<b>111</b>
<b>2 Influence experimental parameters for TiO<sub>2</sub> nanofibers .....</b>	<b>113</b>
2.1 Concentration of titanium precursor .....	113
2.2 Thermal temperatures .....	114
2.3 Morphologies and composition of TiO <sub>2</sub> nanofibers.....	115
2.4 Conclusions .....	117
<b>3 Influence experimental parameters for TiO<sub>2</sub>-Au composite nanofibers .....</b>	<b>118</b>
3.1 Gold salt concentrations .....	118
3.2 Annealing temperature .....	122
3.3 Versatile experimental routes .....	123
3.4 Conclusions .....	129
<b>4 Photocatalytic performances .....</b>	<b>130</b>
4.1 Influence of concentration of titanium precursor .....	130
4.2 Influence of anatase and rutile phase.....	132
4.3 Influence of Au nanoparticles .....	134
4.4 Influence of experimental routes.....	135
4.5 Comparison with P25 .....	136
4.6 Photocatalysis under different wavelength irradiations .....	139
4.7 Photocatalytic mechanisms .....	140
<b>5 Conclusions .....</b>	<b>143</b>

<b>CHAPTER V CHARATERIZATION AND GAS SENSING ACTIVITY OF WO<sub>3</sub>-Au COMPOSITE NANOFIBERS .....</b>	<b>145</b>
<b>1 Introduction .....</b>	<b>145</b>
<b>2 Influence experimental parameters for WO<sub>3</sub> nanofibers .....</b>	<b>146</b>
2.1 Influence of starting polymers .....	146
2.2 Influence of calcination process.....	148
2.2.1 Atmosphere .....	148
2.2.2 Calcination temperatures .....	149
2.3 Conclusions .....	149
<b>3 Morphology and composition of WO<sub>3</sub> nanofibers.....</b>	<b>150</b>
<b>4 Influence experimental parameters for WO<sub>3</sub>-Au composite nanofibers.....</b>	<b>152</b>
4.1 Influence parameter of different starting polymers .....	152
4.2 Influence parameters during calcination process .....	153
4.2.1 Atmosphere .....	153
4.2.2 Stabilization temperatures .....	154
4.3 Influence parameters of Au addition .....	155
4.3.1 Au addition routes .....	156
4.3.2 Au concentrations.....	157
4.4 Conclusions .....	158
<b>5 Morphologies and composition of WO<sub>3</sub>-Au composite nanofibers .....</b>	<b>159</b>
<b>6 Gas-sensing performances .....</b>	<b>162</b>
6.1 Operating temperature .....	162
6.2 Response of the sensors.....	164
6.2.1 Selectivity --- response towards different gases.....	164
6.2.2 Properties of different gases.....	165
6.2.3 Sensitivity with gas concentrations .....	167
6.3 Response ( $T_{res}$ ) and Recovery ( $T_{rec}$ ) times.....	168
6.4 Stability.....	170
6.5 Sensing Mechanism .....	171

---

<b>7 Conclusions .....</b>	<b>173</b>
<b>GENERAL CONCLUSION .....</b>	<b>175</b>
<b>LIST OF FIGURES .....</b>	<b>179</b>
<b>LIST OF TABLES.....</b>	<b>187</b>
<b>REFERENCES .....</b>	<b>189</b>
<b>APPENDICES .....</b>	<b>201</b>



## GENERAL INTRODUCTION

Hybrid metal-metallic oxide composites (HMMOC) materials have attracted much attention due to their specific properties and intriguing applications. It is a promising material to solve serious problems linked to environmental pollution, energy storage, self-cleaning of air or water, deodorization, detection of harmful gases, gas alarms. The fact that those materials often combine a noble metal, and a metallic oxide with particular properties depending on the targeted applications, which confers to HMMOC materials important versatility to be efficient in many domains like photocatalysis and gas sensing.

Concerning the metallic oxide part, titanium oxide ( $\text{TiO}_2$ ) and tungsten oxide ( $\text{WO}_3$ ) are the commonly used semiconductors (SC) due to their unique electronic/optical properties, long-term stability, strong oxidizing ability, and inexpensive properties. However, there are still some research gaps limiting their further advancement for typical catalysis or sensors. Indeed, for example, due to its wide band gap,  $\text{TiO}_2$  exhibits a low solar light harvesting and a high rate of recombination of photoexcited electron-hole ( $e^-/h^+$ ) pairs, which considerably limits its photocatalytic activity. In the same way,  $\text{WO}_3$  based gas sensor materials still have a big challenge to achieve ultrahigh sensitivity, reversibility, reproducibility, and stability especially for detecting the volatile organic compounds (VOCs), which is dangerous to human health or cause harm to the environment.

Gold is mainly chosen due to its chemical stability among all the noble metals. At the nanoscale, noble metal, when it is excited with visible light, exhibits a strong surface plasmon resonance effect (SPRE), which can enhance the photocatalysis or gas sensing efficiencies of  $\text{TiO}_2$  and  $\text{WO}_3$ , respectively. This enhancement is related to the shape and the size of the noble metal nanoparticles (NPs).

Various advanced techniques have been developed to fabricate HMMOC with well-controlled morphology and chemical composition. Electrospinning (ES) is a simple and cost-effective technology to fabricate various materials of one-dimensional (1D) nanofibers (NFs). This method allows to perform large-scale and self-supporting productions with high specific surface areas. The surface morphologies and the nanostructures dimensions are controllable depending on the processing route employed, which make the final products flexible for

photocatalyst or sensor devices integration.

In this thesis, different kinds of polymers (PVP, PVA and PAN) were introduced to fabricate polymer-Au, metallic oxide NFs ( $\text{TiO}_2$  or  $\text{WO}_3$ ), and HMMOC ( $\text{TiO}_2$ -Au or  $\text{WO}_3$ -Au) composite NFs by combining the ES technique with subsequent calcination. The experimental factors that can influence the morphology and composition of the final products have been investigated, including the starting polymers, precursors concentration, thermal process factors (temperature and atmosphere), and Au addition routes (Au contents and reducing method). A particular attention has been done concerning three different Au addition routes designed as below:

**Volume inclusion (i)**: addition Au ions into ES solution directly before ES process;

**Surface deposition (ii)**: addition Au ions on the surface of as-spun NFs after ES;

**Surface deposition (iii)**: addition Au ions on the surface of oxide NFs after calcination.

The optimized samples of  $\text{TiO}_2$ -Au and  $\text{WO}_3$ -Au composite NFs were investigated for photocatalytic degradation of methyl blue (MB) aqueous solution and gas sensing performance of VOCs, respectively. Meanwhile, the photocatalytic and gas sensing mechanisms were discussed.

This thesis has five chapters:

The first introduces the basic physico-chemical properties of HMMOC materials. It is followed with a brief explanation on NFs obtained by ES technique. The applications of HMMOC NFs and their limitations with the research background have been mentioned. The main challenges and opportunities of HMMOC for photocatalysis and gas sensor are proposed.

In chapter 2, the basic information of the raw materials and instruments are listed. The three designed Au addition routes are defined. The synthesis routes and experimental parameters and conditions are described for polymer-Au (PVP-Au, PVA-Au, and PAN-Au), metallic oxide ( $\text{TiO}_2$  and  $\text{WO}_3$ ) and HMMOC ( $\text{TiO}_2$ -Au and  $\text{WO}_3$ -Au) composite NFs. Then, the methods used for the chemical and structural characterizations of the NFs composite are explained in details. The performance systems used for photocatalysis and gas sensor are introduced at the end of this chapter.

Chapter 3 is focusing on the results of feasibility of obtaining polymer-Au composite NFs and their optimization. The influence parameters of polymer-Au composite NFs including the starting polymers, calcination process conditions and Au addition routes are discussed. Then, the morphologies, composition and thermal behavior of polymer-Au composite NFs are studied. Fabrication conditions of Au containing NFs are also investigated and optimized.

For Chapter 4, we present results on the TiO<sub>2</sub>-Au composite NFs fabricated by ES with the three different routes of addition Au ions and combined with calcination. The contents, size, location and the interface of TiO<sub>2</sub> and Au NPs are investigated. The influence experimental parameters for TiO<sub>2</sub> and TiO<sub>2</sub>-Au composite NFs have been studied including the concentration of titanium isopropoxide (TTIP), the thermal temperatures of the calcination process, Au addition routes and Au concentrations. The morphologies and composition of TiO<sub>2</sub> and TiO<sub>2</sub>-Au NFs are described. Then the photocatalytic performances of the samples, which can be varied with irradiation light, concentration of TTIP, the ratio of anatase and rutile phases in TiO<sub>2</sub>, Au addition routes, and Au contents are presented. The photocatalytic mechanism implied for those samples has been also discussed.

In Chapter 5, the main research objective is to discuss on the WO<sub>3</sub>-Au composite NFs fabrication with ES. The influence experimental parameters of WO<sub>3</sub> and WO<sub>3</sub>-Au NFs, including the different starting polymers, calcination atmosphere and temperatures, Au addition routes and Au concentration are investigated. The morphologies and compositions of related WO<sub>3</sub> and WO<sub>3</sub>-Au composite NFs were described. The gas-sensing performance of Au-functionalized WO<sub>3</sub> composite NFs toward different gases (methanol, ethanol, acetone and *n*-butanol) has been studied in details. In particular, we focused on *n*-butanol due to its excellent sensitivity compared to other gases, such as lower operating temperatures, shorter response ( $T_{res}$ ) and recovery ( $T_{rec}$ ) times, and longer stability. Meanwhile, the mechanism of gas sensing has been discussed.

Finally, a general conclusion highlights the most significant achievements of this work. Possible and interesting outlook is proposed for the further work in the last part.



## CHAPTER I BIBLIOGRAPHIC STUDY

### 1 Hybrid Metal @ Metallic Oxide Composites (HMMOC)

#### 1.1 State of the art

Environmental pollution and energy storage are serious problems that humanity is facing, and that need to be solved in the 21<sup>st</sup> century. For the sustainable development of human society, an urgent task is to develop both pollution-free technologies for environmental remediation and alternative clean energy supplies. Compared with single component materials, hybrid metal @ metallic oxide composite (HMMOC) nanostructure materials exhibit specific properties with new functionalities that have attracted much attention in the past few years, due to their related intriguing applications in many areas and their promises to meet the requirement and solve the problems mentioned above [1].

HMMOC materials have two main components: a semiconducting part and a metallic part described as follows:

(1) For the first part, polymers, metallic oxides or their blends can be used. Semiconductor (SC) materials can be introduced in two types: single element, like germanium or silicon for example or elements combinations belonging to different groups of the periodic table. Compound materials are particularly issued from elements of the Groups *III* (Ga and In) and *V* (P, As and Sb) such as GaAs, GaP and InP; Groups *II* and *VI* or Groups *IV* and *VI* to form binary compounds  $A^{II}B^{VI}$  (ZnTe, ZnO and CdTe) or  $A^{IV}B^{VI}$  (PbS, PbTe and SnTe); Groups *VI* with abundant or rare elements to form compounds like WS<sub>2</sub>, NiS, MoSe, TiO<sub>2</sub> and WO<sub>3</sub>. Indeed, SC materials have the ability to vary their electrical properties so as to revolutionize the design and capabilities of modern electronics in order to make devices smaller and faster.

(2) For the second part, noble metals, like gold (Au), silver (Ag), platinum (Pt), and palladium (Pd) have far-reaching potential applications in electronics due to their stable electrical properties, excellent catalytic activities and environmental stability. They can also be used as additions for SC and can be elaborated in various different nanostructures such as nanoparticles (NPs), nanorods (NRs), nanowires (NWs) and nanotubes (NTs).

### 1.1.1 Introduction of HMMOC semiconducting part

#### Elementary processes in a semiconductor (SC)

Taking into account that SC should influence drastically the resulting HMMOC material, the understanding of their natural properties is of main importance. In particular, the typical electrical conductivity, which is based on the movement of electrons and holes generated inside their crystal lattice, is tunable from that of a pure conductor and an insulator. This is the foundation of modern electronic and optoelectronic devices that we do not mention in details in this manuscript.

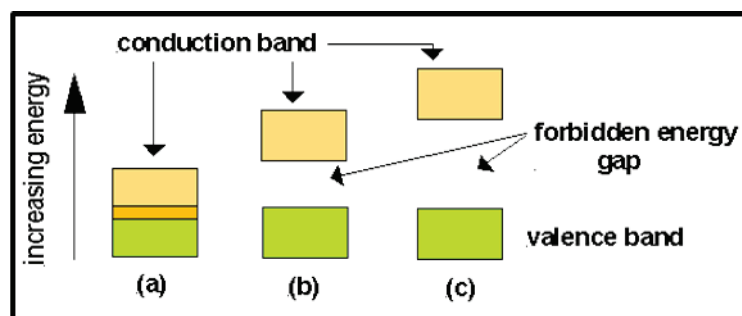


Figure 1.1 Energy bands in (a) conductors, (b) SC, and (c) insulators [2].

In a few words, the main characteristics of a SC are given by the conduction band (CB), valence band (VB), band gap, traps sites and Fermi level (as shown in Figure 1.1). The highest range of electron energies in which electrons are normally present at absolute zero temperature is called VB while the next available lowest empty energy level is called the CB, which quantifies the range of energy to free an electron from its bond to an atom. The bands between CB and VB are the allowed energy state that an electron can occupy in a material, which are differentiated in a SC and in a metal. The band gap generally refers to the energy difference (in electron volts) between the top of VB and the bottom of CB in SC. At a certain temperature, the statistical distribution of the electron on each quantum state is completely determined. The Fermi level can be considered as a hypothetical energy level of an electron, such that at thermodynamic equilibrium this energy level would have a 50% probability to be occupied at any given time, if it does not lie in the forbidden gap.

SC is poor conductor in its natural state due to the filled VB. Several strategies such as doping and gating are used to overcome this problem and to make SC behave like conducting materials. They result in an excess or a shortage of electrons, which leads to *n*-type and *p*-type SC, respectively. The consequence is an unbalanced number of electrons which causes the current in the material. In the case of doping, the conductivity is improved by adding impurity atoms to SC material, thus increasing the number of charge carriers. By playing a role as

electron donors or acceptors, the suitable dopants produce the desired controlled charges depending on the atomic properties. For example, the most common dopants from Group III and Group V in the periodic table can modify silicon to form SC material of  $n$ -type or  $p$ -type (as shown in Figure 1.2).

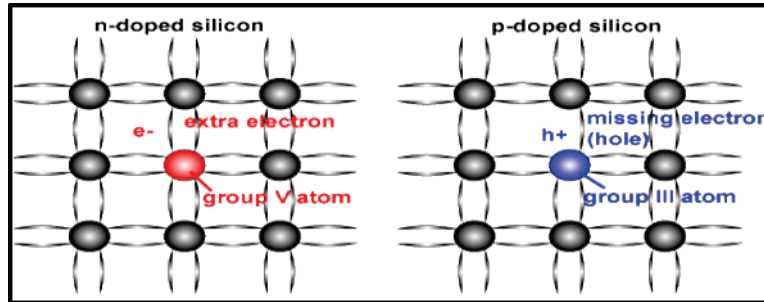


Figure 1.2 Schematic of a silicon crystal lattice doped with impurities for  $n$ -type and  $p$ -type SC material[3].

As a consequence, different properties can be achieved with tunable SC materials. For example, heterojunctions are generated when two different doped semiconducting materials of  $n$ -type and  $p$ -type are joined together. An exchange of electrons and holes takes place between the differently doped semiconducting materials. Before equilibrium, the electrons of the  $n$ -type enter the holes of the  $p$ -type: this leads to a process called recombination and results in an electric field.

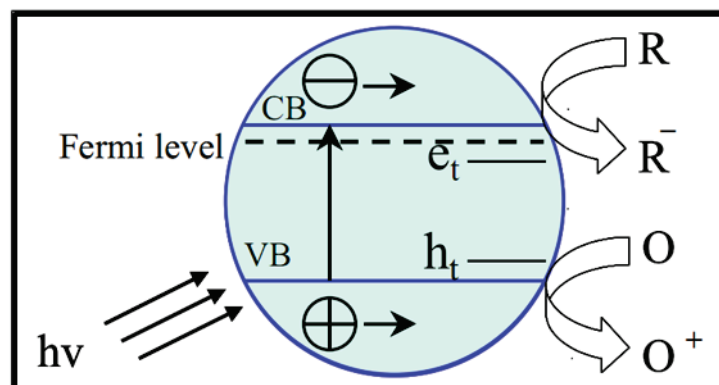


Figure 1.3 Electron-hole pair generation in a photo illuminated  $n$ -type SC nanoparticle.

The thermal equilibrium in a SC can also be disturbed by modifying the amount of electrons and holes. Such disruptions can occur as a result of a temperature difference or the presence of photons. For example, a photon that penetrates in the SC can create a pair

(electrons  $e^-$ , holes  $h^+$ ) that can relax by emitting light. Processes of creating and annihilating the pair ( $e^-$ ,  $h^+$ ) are called generation and recombination. In certain SC, as the most favorable relaxation phenomenon is to emit light instead of heat, they are used to design light emitting diodes and fluorescent quantum dots. One challenging situation is to limit this recombination process in order to let the generated electrons and holes participating to others reactions like reduction or oxidation in photocatalysis experiments (as shown in Figure 1.3).

### **Metallic oxide SC: related properties and applications**

Based on those particular properties, SC have potential applications in various fields such as fuels, energy, optoelectronic, photovoltaics, light harvesting, selectivity, sensors, and pollution control. Photocatalysis implying SC is one of the most important promising technologies among a variety of green earth and renewable energy projects underway. This is due to the fact that natural sunlight or artificial indoor illumination, used as resource energy is abundantly available everywhere in the world. To date, it has undoubtedly been proven that among all the SC studied,  $TiO_2$  is the best photocatalyst for water splitting and oxidative decomposition of many organic compounds [4].  $WO_3$  is also an important SC and has been investigated in many application areas including sensing, electrochromism and for its enhanced catalytic behavior [5]. In particular, due to the promising applications in the field of gas sensing,  $WO_3$  has been widely used to detect toxic gases and volatile organic compounds (VOCs) [6]. Based on all these reasons, the present manuscript dedicated to HMMOC materials will focus on  $TiO_2$  and  $WO_3$ . The sections 1.1.2 and 1.1.3 will describe the structures and properties of these two  $n$ -type SC materials.

#### ***1.1.2 Structures and properties of titanium oxide ( $TiO_2$ )***

$TiO_2$  is a polymorph compound and a common  $n$ -type SC. It occurs in nature as well-known minerals like Anatase, Rutile or Brookite with different crystal structures (shown in Figure 1.4). Anatase and Brookite are unstable phases with bandgap energy of 3.3 eV and 3.5 eV, respectively. Rutile is the most stable phase with bandgap energy of 3.06 eV (shown in Table 1.1 with other crystalline structures of  $TiO_2$ ).

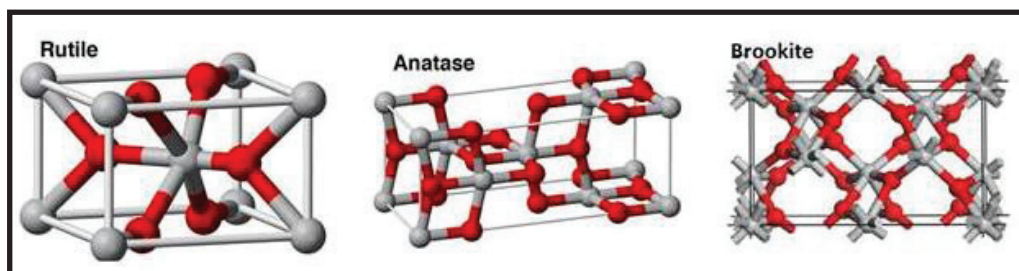


Figure 1.4 Crystal structures of TiO<sub>2</sub> a) Rutile b) Anatase c) Brookite [7].

The first property related to the photocatalytic activity of a SC is its energy band configuration. This latter determines the absorption of incident photons, the photoexcitation of electron-hole pairs, the migration of carriers, and the redox capabilities of excited-state electrons and holes [8]. Indeed, TiO<sub>2</sub> photocatalysts are indirect band gap SC, but it exhibits an abrupt onset of absorption like direct band gap SC.

Table 1.1 XRD data of different TiO<sub>2</sub> crystalline structures.

TiO <sub>2</sub> Structures	Crystal System	Space Group	Lattice parameters / nm			Band gap (eV)	JCPDS Card No.
			a	b	c		
Anatase	tetragonal	I41/amd	0.378	0.378	0.951	3.3	00-021-1272
Rutile	tetragonal	P42/mnm	0.459	0.459	0.296	3.06	00-021-1276
Brookite	orthorhombic	Pcab	0.545	0.918	0.514	3.5	00-015-0875

In order to modulate the band gap and band edge positions in a precise manner, two different approaches of doping with different elements and solid-solution strategies have been investigated and applied. For example, intensive studies have been carried out to improve the visible light sensitivity of Ti oxide-based catalysts [9]–[11]. One of the strategies for inducing visible light response in TiO<sub>2</sub> was the chemical doping of TiO<sub>2</sub> with metal ions with partially filled d-orbitals (V, Cr, Fe, Co, Ni, ...) [12], [13]. The metal ions may be incorporated into the TiO<sub>2</sub> by chemical (like impregnation or precipitation) and physical methods. Although TiO<sub>2</sub> chemically doped with metal ions could induce a visible light response, these catalysts show the limitations in reactivity for practical applications, because dopants in the photocatalyst act not only as visible light adsorption centers but also as recombination sites between photogenerated electrons and holes [14]. This is the key point we would like to discuss in this manuscript. Meanwhile, it is also the fundamental reason of working with another component to form a hybrid material.

### 1.1.3 Structures and properties of tungsten oxide ( $WO_3$ )

The crystal structure of  $WO_3$  is temperature dependent. It has four different crystal structures including tetragonal, orthorhombic, monoclinic, and triclinic. It is tetragonal at temperature above  $740^\circ\text{C}$ , orthorhombic from 330 to  $740^\circ\text{C}$ , monoclinic from 17 to  $330^\circ\text{C}$ , and triclinic from  $-50$  to  $17^\circ\text{C}$  (as shown in Table 1.2). These phases are not stable at room temperature contrary to the monoclinic structure with space group  $P2_1/n$  [15]. Electronic properties including the band gap are variable in function of the different structures.  $WO_3$ , which possesses a small band gap between 2.4 and 2.8 eV, has many advantages for visible-light-driven photocatalysis including a deeper valence band (+3.1 eV), strong absorption within the solar spectrum, stable physico-chemical properties.

**Table 1.2 XRD data of different  $WO_3$  crystalline structures.**

Crystal System	Space Group	Temperature $^\circ\text{C}$	Lattice parameters / nm			JCPDS Card No.
			a	b	c	
Triclinic		$-50 \sim 17$				
Monoclinic	$P2_1/c$	$17 \sim 330$	0.728	0.751	0.383	00-005-0363
Orthorhombic	$Pcnb$	$330 \sim 740$	0.738	0.751	0.384	00-020-1324
Tetragonal	$P4/nmm$	$>740$	0.525	0.525	0.391	00-005-0388

In gas detection,  $WO_3$  is an extensively studied SC material for its high response speed, good stability and low cost. It has been widely used to detect many gases like  $H_2$ , EtOH,  $H_2S$ ,  $NO_x$ ,  $CO_x$ ,  $NH_3$ , and VOCs [16],[17]. There are various structures of  $WO_3$  such as powder, thin films, NRs, NTs, NPs, NFs, nanoneedles and nanoplates that are fabricated with different methods including vapor or gas deposition, sputtering, spin-coating, sol-gel, hydrothermal synthesis, templates and electrospinning (ES). However, the electron transfer is greatly limited during the sensing reactions because of the large grain boundary barriers. Meanwhile, in order to obtain the good sensing properties, a certain operating temperature is required, which can cause the particles aggregation. In this case, the surface area will be reduced and the gas has less chance to be adsorbed on the sample surface [18]. Several effective steps are investigated, such as doping, dimension control, and phase structure design. The response of Cu-doped  $WO_3$  hollow fibers exhibits high response and good selectivity to acetone [19]. Jun Seop Lee and his colleagues showed that the minimum detectable amount of  $NO_2$  gas can be lowered down to 1 ppm at room temperature with  $WO_3$  nanonodule-decorated carbon NFs [20]. Pd catalysts functionalized  $WO_3$  NFs have remarkably improved toluene response and superior cross-sensitivity against  $H_2S$  molecules [6]. One important issue for improving gas

sensing performance of  $\text{WO}_3$  is to decrease the grain size and increase the surface-to-volume ratio. Moreover it is possible to modify the material properties by combining this oxide to another kind of material.

#### 1.1.4 Introduction of HMMOC metallic part

The second component of HMMOC materials is the metallic part, and noble metals (as shown in Table 1.3) are commonly used. In chemistry, noble metals are metals that are resistant to corrosion and oxidation in moist air (unlike most base metals). The short list of chemically noble metals thus comprises Au, Pt, Pd, Ag, and Cu. In physics, the definition of a noble metal is most strict. It requires that the d-bands of the electronic structure are filled. From this perspective, only Cu, Ag and Au are noble metals, as all d-like bands are filled and do not cross the Fermi level. However, d-hybridized bands do cross the Fermi level to a minimal extent. For Pt, two d-bands cross the Fermi level, changing its chemical behavior such that it can function as a catalyst. In ultra-high vacuum, surfaces of pure Au are easy to clean and usually remain clean for a longer time than those made of Pt or Pd, which are quickly covered by carbon monoxide.

**Table 1.3 Information about several noble metals.**

Element	Atomic number	Group	Period	Reaction	Potential / eV
gold (Au)	79	11	6	$\text{Au}^{3+} + 3\text{e}^- \rightarrow \text{Au}$	1.56
Platinum (Pt)	78	10	6	$\text{Pt}^{2+} + 2\text{e}^- \rightarrow \text{Pt}$	1.18
Palladium (Pd)	46	10	5	$\text{Pd}^{2+} + 2\text{e}^- \rightarrow \text{Pd}$	0.987
Silver (Ag)	47	11	5	$\text{Ag}^+ + \text{e}^- \rightarrow \text{Ag}$	0.7996
Copper (Cu)	29	11	4	$\text{Cu}^{2+} + 2\text{e}^- \rightarrow \text{Cu}$	0.337

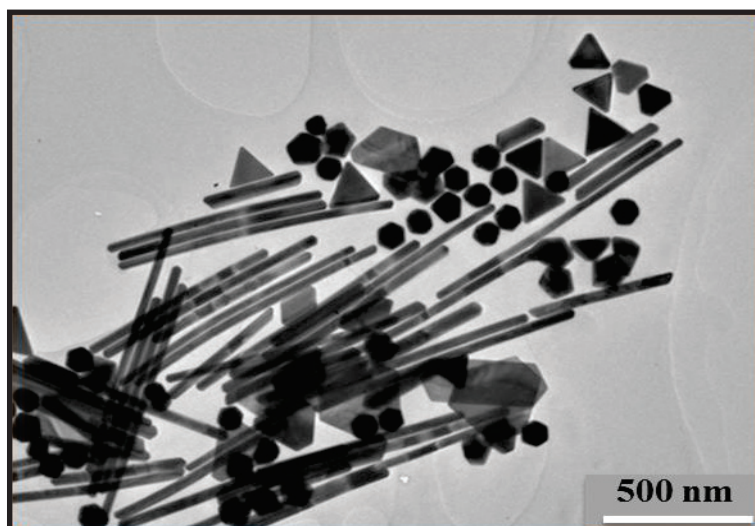


Figure 1.5 TEM image of gold nano-objects.

The metallic NPs with nanoscale size have unique electrical, optical, magnetic, and chemical properties, and their applications as catalysts in the fields of photocatalysis and sensors have been widely explored [21]. For instance, Au NPs have size-dependent surface plasmon resonance (SPR) property and generally exhibit visible SPR absorption, which can extend the absorption range from UV light to visible light for photocatalysis [22]. By functionalizing polyaniline NFs with Pt/Pd NPs, the electrochemical properties of devices composed of those NFs can be enhanced. Metallic NPs can effectively catalyze the redox processes of some molecules and improve obviously the analytical performances with lower detection limit and shorter deposition time for sensor applications [23]. In our study, it was more convenient to work with gold because of its chemical stability and its particular electronic properties in nanoscale. Moreover, our research group has already synthesized many gold nano-objects of different shapes and sizes giving a large panel of materials solutions to the present work (as shown in Figure 1.5).

#### ***1.1.5 Specific electronic properties of noble metal: Surface Plasmon Resonance***

From a theoretical point of view, when a small noble metallic particle in nanoscale, is irradiated by light, an oscillating electric field causes the conduction electrons to oscillate coherently. This is schematically pictured in Figure 1.6. When the electron cloud is displaced relative to the nuclei, a restoring force arises from Coulomb attraction between electrons and nuclei that results in oscillation of the electron cloud relative to the nuclear framework. The

oscillation frequency is determined by four factors: the density of electrons, the effective electron mass, and the shape and size of the NP. This collective oscillation of the electrons is called the dipole plasmon resonance of the particle. Higher modes of plasmon excitation can occur, such as the quadrupole mode where half of the electron cloud moves parallel to the applied field and half moves antiparallel [24], [25].

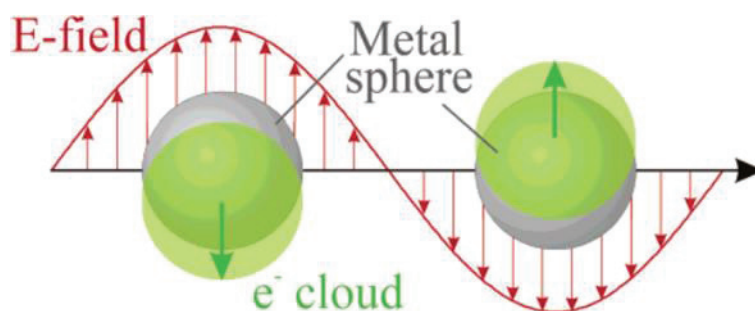


Figure 1.6 Schematic of plasmon oscillation for a sphere, showing the displacement of the conduction electron charge cloud relative to the nuclei [25].

The incident light polarization is also an important point since asymmetric NPs (ellipsoid, rod, ...) exhibiting two main resonances (longitudinal and transversal modes) can be selectively excited by polarized light fixed along their main axis or diameter. In other words, the localized surface plasmon resonance (LSPR) endows metal nanocrystals with very large absorption and scattering cross-sections at the LSPR wavelength. For plasmonic metal nanocrystals, both absorption and scattering cross-sections are important and can be synthetically tailored [26]. Electric field localization is another prominent property of plasmonic metal nanocrystals. Typically, absorption spectra depend on the shape and the size of gold nano-objects in the visible range [27]. As shown in Figure 1.7, in order to evolve from a prolate ellipsoid (I) to a quasicylinder (IV), keeping the same aspect ratio that the extinction cross-section is normalized to the nanorods volume to show only its shape dependence. The red-shift and peak amplitude increase of the longitudinal SPR when flattening the NRs caps [28].

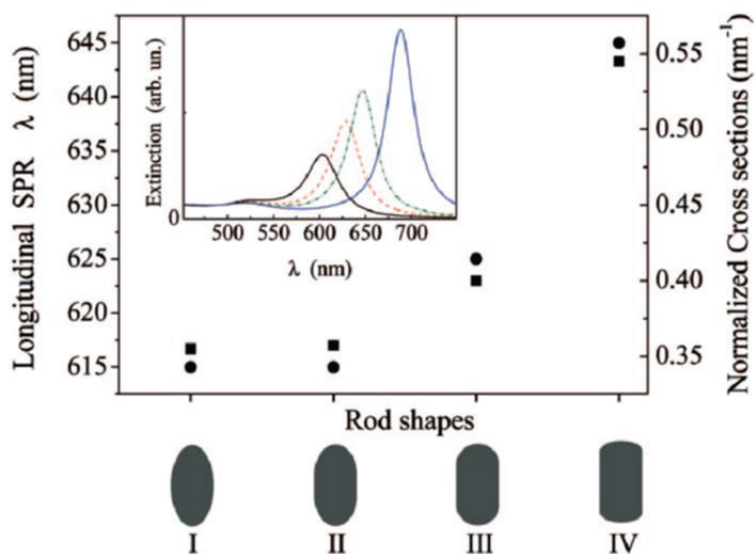


Figure 1.7 Longitudinal Surface Plasmon Resonance mode and Normalized Cross sections in function of the Au nanorods shape. In insert Extinction spectra in function of the nanorods aspect ratio [28].

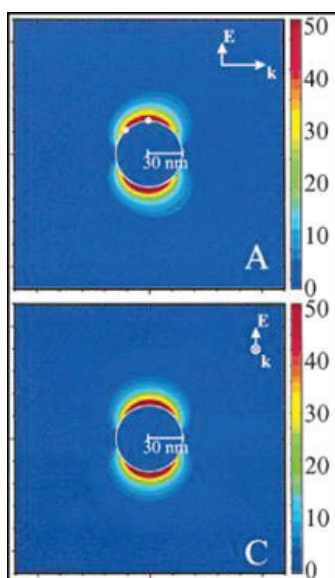


Figure 1.8 Electric field contours for radius 30 nm Ag spheres in vacuum [29].

Another specific property related to SPR based on the enhancement of Raman scattering by molecules adsorbed on rough noble metal surface is used in many optical characterization techniques like Surface Enhanced Raman Spectroscopy or Surface Enhanced Raman Scattering, often abbreviated SERS. When the incident light in the experiment strikes the surface, localized surface plasmon is excited. The field enhancement (as shown in Figure 1.8) is greatest when the plasmon frequency is in resonance with the radiation. In our case, the role of “adsorbates” is played by the SC in the HMMOC material. The idea beyond this last point

is that the effect of this enhanced electrical field is to increase greatly the lifetime of the charge carriers in the SC and to offer opportunities for them to participate in other types of interactions (oxidation/reduction process) implied in photocatalysis or sensing processes. It is well known that the size and shape of NPs are the key factors for determining, revealing and enhancing the functions of HMMOC based materials. The next two sections will discuss the influence of size and shape for applications of HMMOC materials.

### **1.2 Influence of size for applications of HMMOC materials**

Nanomaterials have unique physical and chemical properties including mechanical, thermal, optical, electrical and magnetic properties for widely technological applications, which are different from those of the corresponding bulk materials or constituting atoms. Decreasing the material size down to the nanoscale results in different properties, caused by a large surface-to volume ratio and/or the quantum confinement effect [1]. These two factors play an important role for related applications. Various nanostructures of HMMOC materials have been prepared, composed by metal and SC nanocrystals. Controlling the size to nanoscale allows increasing the surface-to-volume ratio and reducing the scale of transport lengths for both mass and charge carriers. As surface area increasing, more amount of the material can come into contact with surrounding materials, and then affecting reactivity during the photocatalysis or gas sensing processes. Meanwhile, when the size of HMMOC materials reduces to nanoscale, intriguing plasmonic properties in the visible-to-near-infrared regions can be observed. The absorption wavelength can be varied with the size of nanocrystals in a certain range. Consequently, controlling the size of nanocrystals precisely allows tuning the absorption wavelength to satisfy targeted application requirements. For example, the LSPR wavelengths of Au, Ag, Pt, and Pd nanocrystals can be synthetically tuned from the visible to near-infrared region by controlling the size and morphology of nanocrystals, to finally achieve high catalytic activities [30]–[32].

### **1.3 Influence of shape for applications of HMMOC materials**

Low-dimensional systems are usually classified according to the number of reduced dimensions: zero-dimension (0D), one-dimension (1D), and two-dimension (2D). These nanomaterials have many beneficial properties for applications related to photocatalysis and sensors, such as large surface areas, abundant surface states, easy device modeling and

diverse morphologies with good chemical and thermal stabilities under different operating conditions. In recent years, the development of novel HMMOC nanomaterials has made significant progress conducting to nanostructures with variable shapes: NPs, NRs, NTs, NFs, nanobelts, nanoribbons, nanowhiskers, nanopushins, fiber-mats, urchins, lamellar, hierarchical dendrites and core-shell systems have been fabricated by different methods, combining processing route and treatments such as ES, hydrothermal, ultrasonic irradiation, electrochemical anodization, sol-gel, thermal evaporation, vapor-phase transport, sputtering, chemical vapor deposition, UV lithography and dry plasma etching [33].

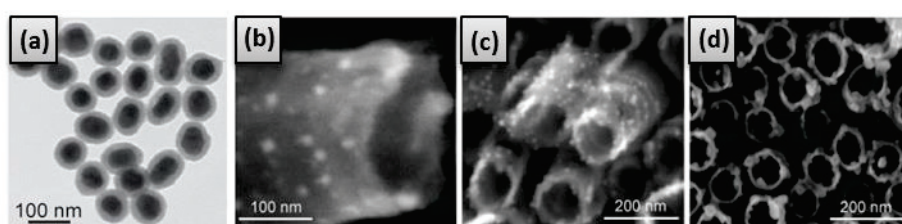


**Figure 1.9** SEM and TEM images of metal/TiO<sub>2</sub> nanostructures: (a)(Au core)/(TiO<sub>2</sub> shell) ; (b) (Cu NPs)/(TiO<sub>2</sub> NTs); (c) (Ag NPs)/(TiO<sub>2</sub> NTs); (d) (Au NPs)/(TiO<sub>2</sub> NTs) [1].

For HMMOC based on metal/TiO<sub>2</sub> nanostructures, many studies start with TiO<sub>2</sub> nanotube arrays fabricated by electrochemical anodization of highly pure Ti foils [34]. The metallic part is obtained by photochemical reduction on the TiO<sub>2</sub> NTs arrays. Figure 1.9 shows the scanning electron microscopy (SEM) images of typical TiO<sub>2</sub> NTs arrays decorated with Ag and Au NPs, respectively [35]. (Au,Ag core)@(TiO<sub>2</sub> shell) nanostructures in different morphologies have also been prepared by hydrothermal process [36] and sol-gel approach [37]. The thickness of the TiO<sub>2</sub> shell can be tuned by changing the reaction time and the concentration of TiO<sub>2</sub> precursor.

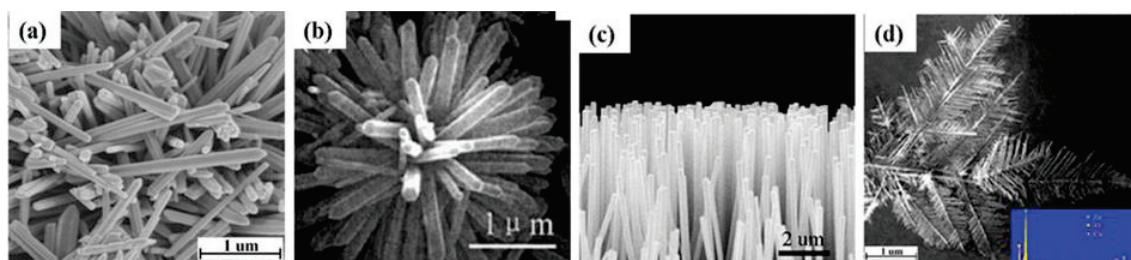


**Figure 1.10** SEM images of different WO<sub>3</sub> nanostructures [38].

For HMMOC based on metal/WO<sub>3</sub> nanostructures, it is important to notice that gas sensing

efficiency drastically depends on material shapes. As a consequence, recent attention has been focused to establish numerous strategies to obtain several shapes for the same materials (as shown in Figure 1.10) and compared them both together with their capacity as sensor. For example, as shown in Table 1.4, different WO<sub>3</sub> nanostructures (including thin films, NRs, NNs, NPs, and nanoplates) functionalized with noble metal NPs (like Au, Pt, Pd, and Ag) present different sensitivities towards targeted gases such as ethanol, methane, NO<sub>x</sub>, CO, and H<sub>2</sub>S. The experimental methods to obtain such nanostructures can be summarized by vapor deposition, sol-gel, sputtering, hydrothermal, chemical vapor deposition, ES and chemical reducing.

**Table 1.4 Sensitivity of different nanostructured materials based on WO<sub>3</sub>.**

Materials	Structures	Method	HT/ °C	Analyte	Sensitivity	Reference
WO <sub>3</sub> -Au	0.5 nm thin films	Vapor deposited	450	2% Ethanol	177	[39]
WO <sub>3</sub> -Au	300 nm Thin films	Reactive sputtering	400	400 ppm NO	78	[40]
WO <sub>3</sub> -Au	NRs	hydrothermal	180	50 ppm H <sub>2</sub>	6.6	[41]
WO <sub>3</sub> -Au	NNs	Chemical Vapour Deposition	-	1.5 ppm Ethanol	12	[42]
WO <sub>3</sub> -Ag	Powder	doping	600	40 ppm NO <sub>x</sub>	38.3	[43]
WO <sub>3</sub> -Ag	nanoplates	Photoinduced reducing method	500	1 ppm NO	55	[44]
WO <sub>3</sub> -Pt	Films	Spin-coating	180	2000 ppm CO	469	[45]
WO <sub>3</sub> -Au	NPs	Screen-printed	600	2 ppm H <sub>2</sub> S	12.4	[16]
WO <sub>3</sub> -Pd	Porous NFs	electrospinning	700	1 ppm H <sub>2</sub> S	5.5	[7]
WO <sub>3</sub> -Au	Nanoplates	Chemically reducing	400	NO	200	[46]

## 1.4 Conclusions

Various advanced techniques have been developed to fabricate HMMOC with well-controlled morphologies and chemical compositions. The surface morphologies and dimension of nanostructures are controllable depending on the processing route employed, which make the products flexible and tunable for desired devices. However, there are still some research gaps limiting the further advancement for HMMOC materials. For example, a few studies have been reported on the mechanism behind the formation of structures and the interface effects between the SC and metallic part of HMMOC are not well understood. It is still a big challenge to fabricate gas sensors and photocatalysts with ultrahigh sensitivity, very short response and recovery time, and good reversibility, reproducibility, and stability.

## **2 The particular case of 1D HMMOC materials**

### **2.1 General point of view**

In recent years, various materials of 1D nanostructure in form of fibers, wires, rods, belts, and tubes, whose lateral dimensions fall anywhere in the range of 1-100 nm, have attracted considerable attention due to their unique electronic, optical and chemical properties and intriguing applications in many areas. Compared with other nanostructures, NFs have variety significant advantages for added applications such as medical, battery separators, filtration, energy storage, fuel cells, and information technology [47]. As an important 1D nanostructure material, NFs connect the nano- and micro-world because of their specific morphologies with diameters in the nanoscale and lengths ranging from a few hundreds of nanometers (nm) to several meters.

More precisely, NFs are defined as fibers with diameters less than 100 nm. In the textile industry, the definition of NFs is often extended to include fibers with diameter of 1000 nm or less [48]. It exhibits special properties mainly due to its extremely high surface-to-volume ratio. It also has low density, and in some cases, small pore size and high porosity. Moreover, their mechanical properties are also compatible with a dedicated use in textile industry. This advantage makes also the NFs based materials to be free standing, flexible and easy to recycle. These exceptional functional properties promote the opportunities for versatile applications in different electrochemical energy conversion systems and electronic devices, such as photocatalysis, solar cells, rechargeable batteries, and gas sensors.

### **2.2 Synthesis of HMMOC nanofibers – electrospinning and related techniques**

There are many methods to synthesize HMMOC NFs, including melting process, template synthesis, wet chemical method and ES. A traditional melting process needs to reach high temperature to get the melting point, and usually forms particles with a size about the micrometer scale. Scaffold replication is a good way to design the structure by choosing suitable hard or soft templates with desired structures, and combined with electrochemical deposition to fabricate the NFs. However, the length of NFs is limited by the template so it is hard to get long and continuous NFs with this route. Wet chemical is another way that attracted much attention to obtain NFs. Normally, this method needs to fabricate quantum dots firstly as the seed for NFs growth. Meanwhile it always needs reactants to modify the growth process, and the aspect ratio is limited. Among these methods, ES is one of the simplest most

versatile to lead to a wide range of suitable materials, with high production efficiency. Since the beginning, ES has been mainly focused on fabricating polymer NFs. Up to now, more than hundred types of natural and synthetic polymer have been electrospun into NFs, including poly(vinyl pyrrolidone) (PVP), polyvinyl alcohol (PVA), polyacrylonitrile (PAN) and others [49] not mentioned in this manuscript. More recently, the fabrication of electrospun ceramic or other inorganic NFs has been reported [50]–[52]. The most straightforward strategy to insert an inorganic nanocomponent into a polymer fiber is to disperse the inorganic nanocomponent into the polymer solution prior to spinning. Combining ES with sol-gel method, many kinds of composite NFs can be synthesized including metal/polymer, metallic oxide/polymer [53], [54]. Then, these composite NFs can be calcined to remove the polymer part and convert them into ceramic or HMMOC NFs [55]–[57]. Varied strategies have been investigated to spin HMMOC materials by several innovative ES methods including direct-dispersed ES, coaxial ES, *in situ* photoreduction, gas-solid reaction, co-evaporation method. These different fabrication routes will be described in the next part.

### ***2.2.1 Direct-dispersed electrospinning***

Direct-dispersed ES is the simplest method to fabricate HMMOC materials [58]. The most important strategy of this method is to disperse the inorganic nanocomponent in a polymer solution for ES. These inorganic nanocomponent including metal/metallic oxide NPs, NRs, carbon nanotubes are good candidates for incorporation into the electrospun NFs due to their potential ability to improve the polymer NFs properties such as mechanical strength, thermal conductivity and electronic conductivity. However, they can easily aggregate and be difficult to disperse in the raw solution with the small size of the inorganic fillers, hence inside the polymer fibers. Surfactants are usually used to solve this problem. By adding a certain surfactant into the ES solution, the surface tension and viscosity of the polymer solution are modified to suit the best conditions of ES.

### ***2.2.2 Sol-gel method***

Various of hybrid composite NFs can be synthesized by sol-gel method combined with ES, including metal/polymer, metallic oxide/polymer, and sulfide/polymer. With a subsequent treatment, the metallic oxide/polymer composite NFs can be converted into HMMOC NFs by calcination. In the early days, Ag/polymer composites attracted researchers' interests for their

applications in the fields of catalysis and biomedical. J.H. Youk with his co-workers prepared Ag/polymer (such as PVP, PAN, PVA) composites by this method using DMF as the reducing agent to reduce the silver ions into  $\text{Ag}^0$ . Small Ag NPs were well dispersed homogeneously in the solid polymer NFs and the size of Ag NPs was influenced by the type of polymer: 5.8 nm with PAN, 3.4-3.5 nm with PVP and 6.0 nm with PVA/PVP [59]. For the work of R. Ostermann and his co-workers,  $\text{V}_2\text{O}_5/\text{TiO}_2$  composite NFs were fabricated by ES with the hydrolysis of titanium tetraisopropoxide followed by calcination in air. The  $\text{V}_2\text{O}_5$  grew as single-crystal NRs on the surface of  $\text{TiO}_2$  NFs [60].

### 2.2.3 *In situ* photoreduction

Photochemical reduction (like UV irradiation) is a facile and versatile method to obtain the metal colloids. Based on this idea, polymer/metal composite NFs can be synthesized by ES with this technique. C. Wang's group reported the elaboration of PAN/Ag composite nanofibers using this method [61]. The diameter of Ag nanoparticles (NPs) can be tuned by varying the molar ratio of  $\text{Ag}^+$  : PAN. Au NPs have the different formation from Ag NPs. The Au NPs can only be reduced to form Au colloids very slowly under UV irradiation in the presence of some organic stabilizers such as PVP, PVA, and PEG.

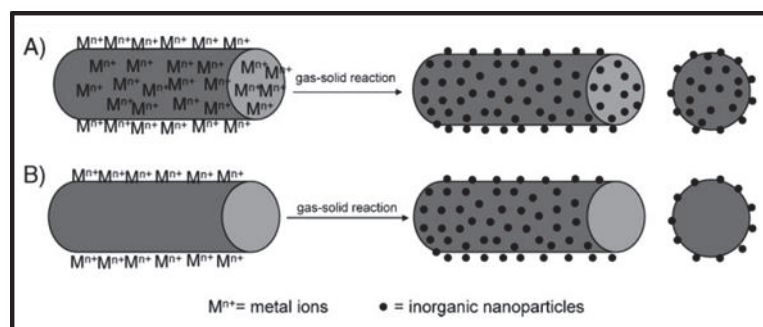


Figure 1.11 Schematic of two different ways for *in situ* photoreduction of NPs with polymer [49].

Base on this fact, Xia's group demonstrated that  $\text{TiO}_2/\text{Au}$  composite NFs could be fabricated in the presence of  $\text{TiO}_2$  NFs and organic stabilizers [62].  $\text{TiO}_2$  can make the reaction much faster. The shapes of Au NPs (e.g. NPs, fractal nanosheets, or nanowires) depend on the type and concentration of organic stabilizers. Compared to the direct-dispersion method, the gas solid reaction affords a simple way to disperse inorganic semiconducting NPs into polymer NFs. The location of the metal NPs (only on the surface or in the volume of

polymer NFs) can be controlled by two different ways as shown in Figure 1.11 [49].

#### **2.2.4 Gas-solid reaction**

Compared with direct-dispersion methods, gas-solid reaction is a simple way to disperse inorganic NPs into polymer NFs. The synthetic strategy of gas-solid reaction combined with ES to incorporate metallic oxide nanostructures into polymer NFs can be involved in three steps: (a) a homogeneous ES solution of co-dissolved metal salt with polymer into one solvent; (b) ES process to fabricate NFs; (c) formation of metal sulfide NPs *in situ* in polymer NFs by exposition of the electrospun polymer/metal salt composite NFs to H<sub>2</sub>S gas at room temperature. Different interactions between the polymer molecules and different metal ions have been researched by X.F.Lu and his co-workers [63]. The results showed that the metallic oxide NPs using this method were inside as well as outside the polymer NFs. This can be tuned by functionalizing the surface of polymer NFs with some anionic groups to control the metal ions location on the surface of the polymer NFs, before their *in situ* reduction as metallic oxide nanostructures.

### **2.3 Conclusions**

The most simplest and efficient technique to fabricate HMMOC NFs is ES. For a variety of electrospun materials, the final composition and morphology of the composite are facile to control by combining ES and complementary methods. In order to obtain the targeted HMMOC NFs for defined applications (photocatalysis and sensing), it is necessary to understand the basic principle, process and controllable aspect of NFs prepared by ES. The next section will focus on ES technique and their potentialities.

## **3 Electrospinning**

### **3.1 State of the art**

#### ***3.1.1 Historical background***

ES, also known as electrostatic spinning, is a spinning method which has been gradually described through old studies. In 1745, G.M. Bose described aerosols generated by the application of high electric potentials to drops of fluids [64]. In 1882, the requirement of charges to overcome the surface tension of a drop has been investigated by Lord Rayleigh [65]. At the beginning of 1900s, Cooley and Morton have patented the first devices to spray liquids through the application of an electrical charge [66]. In 1929, K. Hagiwaba et al have fabricated the artificial silk by using the electrical charge [67]. In 1934, A. Formhals firstly demonstrated the description of an apparatus for ES through a patent [68]. Despite these early discoveries, the procedure was not utilized commercially. In 1970s, Simm et al have reported with several patents, fibers with diameters of less than 1  $\mu\text{m}$  [69]. It did not receive much attention before the early 1990s. The first commercialized applications of electrospun fibers were used for filter as part of nonwovens industry in 1991 [70]. D.H. Reneker and his co-workers made a great contribution to this technique [71]. They studied the ES process for a series of different polymers and gave physical explanations about the polymer fiber formation.

#### ***3.1.2 Basic principles of electrospinning***

Figure 1.12 shows a schematic illustration of the basic setup and process for ES. It is composed by three major components: a high voltage power supply, a spinneret (a metallic needle), and a collector (a grounded conductor). The spinneret is connected to a syringe in which the ES solution is hosted. By using a syringe pump, the solution (molten polymer or solid polymer solubilized in a solvent) can be fed through the spinneret at a constant and controllable rate. During the ES process, the pendent drop of the solution at the nozzle of the spinneret will become highly electrified and induced charges are evenly distributed over the drop surface by adding a high voltage. There are two major types of electrostatic forces: the electrostatic repulsion between the surface charges, and the columbic force exerted by the external electric field. Increasing the value of voltage, once the electrostatic forces can overcome the surface tension of the ES solution, the ejection of a liquid jet from the nozzle is possible. A Taylor cone is formed from the surface of the liquid drop under the action of the

electrostatic force (see the inset of Figure 1.12) [72]. Subjected to a stretching and whipping process, this electrified jet forms a long and thin thread. Its diameter can be reduced greatly from hundreds of micrometers to tens of nanometers due to the continuously elongation of the liquid jet and the evaporation of the solvent. Finally, the charged fiber is deposited with a random orientation on the grounded collector.

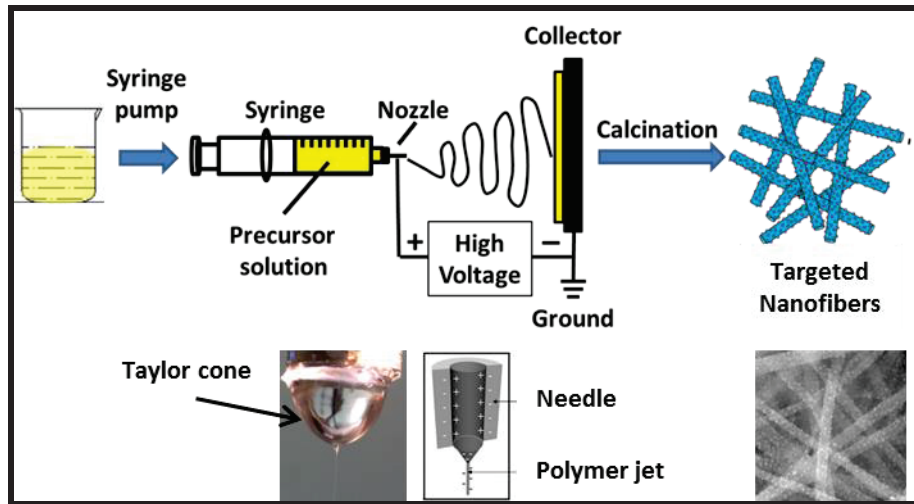


Figure 1.12 Schematic illustration of the basic setup and process for electrospinning.

### 3.1.3 Electrospinning process

In a typical experiment, metallic oxide NFs can be produced using the three main steps described as follows (Figure 1.13):

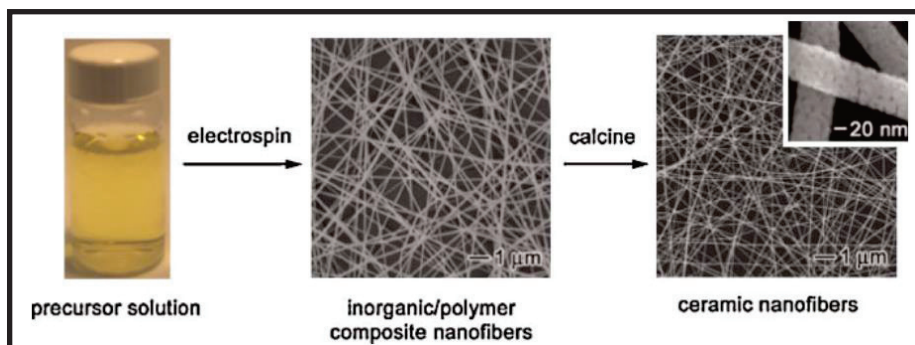


Figure 1.13 Three main steps of typical electrospinning process to produce metallic oxide nanofibers.

(a) Preparation of the ES solution: the most important factor of this part is to find the suitable solvent and polymer related to the certain precursor. Then the adjusted concentration

of the precursor is the key point to get the best viscoelasticity for ES.

(b) ES process: the basic ES setup includes the high voltage power supply, a pump to control the feeding rate, a syringe with a conductive needle and a collector. The working distance between the needle tip and the collector, the feeding rate, as well as the applied voltage has an impact on the final diameter and morphology of NFs.

(c) Subsequent calcination: This last step consists in removing the polymer part to form the metallic oxide NFs. The heating ambience and the procedure used during the thermal treatment have to be adapted according to the thermal decomposition behavior of the NFs to be calcined.

### **3.2 Influential parameters of the electrospinning process**

Various parameters influence the spinnability of polymer solutions. These parameters can be classified into two categories: solution properties and spinning parameters. In principle, nearly all polymers can be processed into fibers by ES if it is soluble or fusible. However, the actual situation is complex and critical. Even the environment conditions like atmospheric composition and humidity, can have a significant impact on the ES process [73]. Sometimes the ES solution requires high voltage to transform from solution to NFs. In this case, specific vacuum conditions are needed to avoid the danger of electric shock caused by such large electric fields. More and more new targeted adjustment of the chemical and physical properties of the electrospun materials are created by the variation possibilities of spinning parameters techniques.

#### ***3.2.1 Solution properties***

One of the most important consideration parameters are the choice of polymer and relevant solvent. Generally, the solution spinnability is affected by the polymer itself. Besides molecular weight, the most important parameter, all its natural properties could influence the ES process: solubility, glass-transition temperature, melting point and crystallization velocity [74]. The solvent vapor pressure and its volatility are very important for the spinning stability. By dissolving the polymer inside the solvent, the spinnability of the obtained solution mainly depends on the solution viscoelastic property (linked to the polymer concentration), and its electrical conductivity. There is a range of polymer concentrations that allows the solution to be electrospun. If the concentration is not high enough, the solution is just electrospayed, the

filament formation is not possible whatever the spinning conditions since the polymer chains entanglement is not sufficient. Above a threshold, the solution can be spun. Sometimes the presence of beaded filaments is observed. This phenomenon is a natural manifestation of the role played by surface tension, which tends to give a spherical shape to the liquid phase (contrary to the electric field). Above a threshold, it is not possible to spin the solution anymore either because of the high viscosity achieved preventing the solution to be extruded, or because of the stretching force which becomes too high for the fiber mechanical property.

### 3.2.2 Spinning parameters

The basic experimental factors are working voltage, working distance, feeding rate, and spinneret diameter. The voltage and distance determined a stable electric field between the needle tip and the collector. Meanwhile, the distance still influences the evaporation efficiency. During ES process, an increase in the applied voltage can alter the structure and morphology of the fibers by causing a change in the shape of the jet initiating point as shown in Figure 1.14. When the voltage is increased while the other parameters are kept constant, the fiber diameter decreases but if the applied electric field rises too much, the Taylor cone changes from one jet to several jets (multi-jets mode) and the resulting the decrease of fiber diameter.

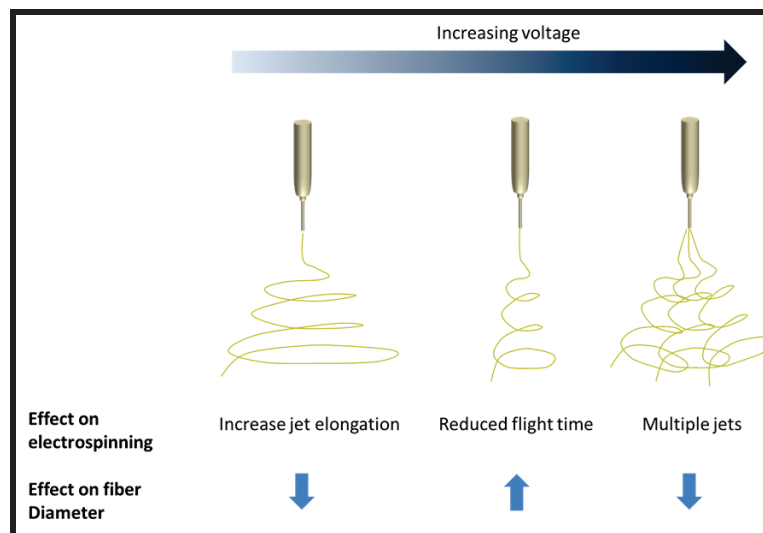
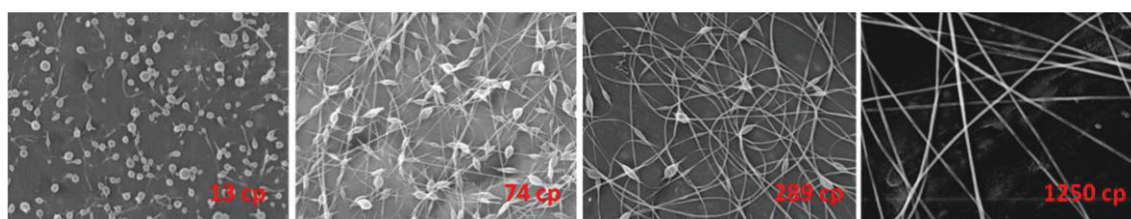


Figure 1.14 General effect of increasing voltage on electrospinning process and fiber diameter [75].

The feeding rate of the solution from the syringe is an important experimental process factor as it can influence the jet velocity. If the feeding rate is not suitable, electrospun fibers with spindle-like beads occur shown in Figure 1.15. As the viscosity of polymer ES solution increasing, the beads number with the fiber decreases. When the voltage, feeding rate and

viscosity are in a suitable condition, the as-spun fibers with uniform diameter and smooth surface are obtained. Different types of collectors have been utilized, such as foils, metals, rotating drums or pairs of electrodes. Aluminum foil is the most widely used due to its inexpensive price, availability and its ease of use. In order to provide a path for the current to travel, the foil should be connected to a grounded electrode. Rotating drums are used normally when there are some special requirements of NFs like uniform thickness and orientation of filaments.



**Figure 1.15** SEM images of poly (ethyleneoxide) fibers (each image shows a 20  $\mu\text{m}$  wide area), together with viscosity value (in red). Evolution of the morphology of polymer fibers upon increase of solution viscosity. Adapted from [76].

With a wet spinning, it is known that volatile solvents can cause problems for the spinning process due to a high rate of solvent evaporation. In this context, the relative humidity as well as the temperature are two very important environmental parameters and have to be controlled, and even monitored when necessary for the spinning procedure. The following part is dedicated to show the interest of electrospinning in different fields of applications.

### 3.3 Applications

ES is a remarkably simple and powerful technique for generating 1D composite multifunctional properties nanomaterials, and they are expected to be applied in many fields, such as templates, superhydrophobic surfaces, electronic and optical nanodevices, chemical and biological sensors, biomedical, environment, energy, and catalysis applications.

#### 3.3.1 Templates

Electrospun NFs can be used as sacrificial templates to prepare 1D nanostructure with hollow interiors. Coated electrospun polymer NFs with a particular material and followed by selective removal of the templates is the most popular method to fabricate nanotubes made of polymers, metals, or ceramics. Hollow fibers could also be obtained directly by coaxial ES.

Oils have been used as template liquids for hollow fibers of ceramics by I.G. Loscertales [77]. Compared to the conventionally fabricated structures with elliptical cross-sections and sharp corners, the electrospun NFs provide the uniform size and long axial length as a template, which have smooth liquid flow.

### ***3.3.2 Superhydrophobic surfaces***

ES can prepare hierarchical micro/nanostructures with low surface energy, which meets the requirement of contact angles larger than  $150^\circ$  of superhydrophobic surfaces for self-cleaning applications. Long alkyl chains are usually further modified on the surface of a hydrophobic substrate in order to obtain a superhydrophobic surface. M.Kanehata and his co-workers have prepared super hydrophobicity electrospun silica NFs with a contact angle larger than  $164^\circ$  by modifying the surface of silica NFs with fluoroalkylsilane [78]. The surface texturing of the material in the form of NFs is also highly influencing the contact angle between a liquid and the material surface. Electrospun smart materials can present a switch effect between super hydrophobicity and super hydrophilicity with some special stimuli-responsive NFs.

### ***3.3.3 Electronic and optical nanodevices***

NFs synthesized by ES have attracted much attention and have been studied as a model of electronic and electro-optical devices. In principle, electrospun NFs fabricated by ES could be used for nonvolatile memory elements and nanoswitches. A.G. MacDiarmid and his co-workers found that the conductivities of PANI/PEO blends were strongly dependent on their diameters [79]. When the diameter was below 15 nm, the material was electrically insulating. Based on the observation of Xia and his co-workers that the polarization direction of light can be tuned by the intensity of light scattered from NFs, the arrays of uniaxial aligned NFs can be used as inexpensive optical polarizers [80]. Another example from the literature, published by X.F.Lu and his co-workers and concerning a coating of electrospun  $\text{TiO}_2$  NFs with a layer of a conducting polymer showed a reversal of the surface photovoltage response [81]. These few examples are not exhaustive and give an idea of the possibilities offered by the ES technique for the electronic and optical nanodevices.

### ***3.3.4 Biomedical applications***

In the past few years, electrospun NFs have brought a lot applications in biomedical, such as in drug delivery, tissue engineering, and wound dressing, due to their interconnected, 3D porous structures and relatively large surface areas. For drug delivery [82], a release of water-soluble drug, polymer and solvent are the component of ES emulsion solution. Electrospun NFs have many advantages like easy implementation, little influence on the drug activity, well-controlled release rate. The hydrophilicity of the drugs influence the degradation and drug release rates of the composite NFs. For tissue engineering [83], electrospun NFs meet the requirement of man-made scaffolds, to bear similarity in terms of chemical composition, morphology, and surface functional groups, with all the natural human tissues and organs including bone, dentin, collagen, cartilage, and skin. For wound dressing [84], porous structure of electrospun NFs can protect the wound from bacterial penetration via the aerosol particle capturing mechanism, and can also present a good breathability for the transport of vapors.

### ***3.3.5 Environmental applications***

The electrospun NF mat is a potential candidate as an environment-cleaning material due to its large surface area, porous structure and cost-effective preparation, free standing and recycle properties. NFs have already been used in air filters to enhance the filter efficiencies. The size of the channels and pores (typically about a few  $\mu\text{m}$ ) in the NFs mat filter can increase significantly the filter efficiency by using chemically selective materials like “Smart Dust” reported by T.A.Schmedake et al [85]. They are also used as water cleaner because they can prevent the release of NPs into the environment and avoid or reduce the cost associated with separation of nanomaterials from treated water [86]. In addition, some electrospun NFs have the ability to adsorb the toxic heavy metals, poisonous gas, and VOCs [87].

### ***3.3.6 Energy applications***

Energy is one of the most serious problems that our society is facing in the 21<sup>st</sup> century, requiring developing technologies and devices for highly efficient and clean energy. This efficiency is usually connected with energy-conservation devices including solar cells, fuel cells, and energy storage devices like supercapacitors. Electrospun NFs offer a set of benefits like high efficiency and low production costs for solar cells applications by improving the

performance of dye sensitized solar cells (DSSC). Han and co-workers have synthesized Pt cluster supported carbon fibrous mats by ES for direct methanol fuel cells (DMFCs), they studied for their room temperature operation and potential high energy density [88]. The supporting carbon fibrous mats are good stable electron conductor and have a large surface area, which provides a great effect on the catalytic activity of Pt NPs. Li ion batteries are one of the most promising power sources for electric vehicles and power tools with the high capacity. L. Wang and co-workers have fabricated carbon/cobalt composite NFs by ES and a subsequent calcination. This kind of composite NFs has a good conductivity, a good cycling performance, and a large reversible capacity of more than  $800 \text{ mA}\cdot\text{h}\cdot\text{g}^{-1}$  [89]. Compared with lithium ion batteries and conventional capacitors, supercapacitors do not present only a high power density, but also a stable cycle life. Electrospun composite carbon NFs containing carbon NTs have been produced for supercapacitors in combination with ES and carbonization as well [90].

### ***3.3.7 Catalysis applications***

Electrospun NFs are investigated as photocatalysts with examples including metallic/polymer or metallic oxide NFs. Meanwhile some electrospun NF mats also play a role as catalytic supports due to their large surface area and a high porosity. It has solved the critical problem in catalysis to remove and recycle the catalyst after the reaction. The photocatalysis performance of SC through the LSPR of the metal NPs can be greatly improved by the corporation of metal NPs in SC NFs. These hybrid composite materials have been extensively employed in many different plasmon-enhanced catalytic reactions, such as photodegradation of organic pollutants, photosynthesis of organic molecules, photocatalytic production of hydrogen, and photocatalytic reduction of carbon dioxide [91]. The photocatalytic production of hydrogen from water splitting using SC, which has been researched as a potential clean process for converting solar energy into chemical fuels. Unlike photocatalytic water splitting, which does not need any additional compounds to act as reducing or oxidizing agents, the formation of photocatalytic carbon dioxide reduction (especially for  $\text{CH}_3\text{OH}$  and  $\text{CH}_4$ ) requires a reducing agent to act as the hydrogen source. Very recently, various  $\text{Ag}/\text{TiO}_2$  nanostructures have been investigated for photocatalytic  $\text{CO}_2$  reduction [92].

### **3.3.8 Chemical and biological sensors**

ES technique can afford a simple approach for the fabrication of 1D composite nanomaterial for chemical and biological sensing. A broad range of NFs materials including SC ( $\text{TiO}_2$ ,  $\text{WO}_3$ ,  $\text{SnO}_2$ , and  $\text{ZnO}$ ), organic/inorganic composites, conducting polymers and graphite, act as sensitive, fast, stable and reproducible gas, humidity, and optical sensors. H.Q. Liu and co-workers have fabricated gas sensors based on the PANI/PEO composite NFs by ES and found that the response times were related to the diameter of the composite NFs [93]. Composite NFs can act as a biosensor device by converting a biological signal into an electrical output with a biological recognition mechanism. K. Swicka and co-workers have fabricated urease-immobilized PVP NFs by ES a mixture of the corresponding compounds in ethanol for a use as urea biosensor [94]. The large surface area of PVP/urease composite NF mats offered an improved adsorption rate and reduced the response time.

As seen in this third part, a wide variety of applications are thus existing for electrospun objects and, in order to give more details about the inorganic NFs and the targeted fields, the following part concerns the HMMOC NFs.

## **4 Applications of HMMOC nanofibers**

### **4.1 State of the art**

HMMOC NFs, including the matrix of semiconducting metallic oxide such as  $\text{TiO}_2$ ,  $\text{WO}_3$ ,  $\text{SnO}_2$ ,  $\text{ZnO}$ ,  $\text{Fe}_2\text{O}_3$  and other wide band gap metallic oxides functionalized with different dopants, are well known for their ability in many application areas, like energy, nanoelectronic devices or catalytic and sensing materials [95]. In this section, we will introduce a brief induction for these applications with HMMOC NFs, especially for photocatalysis and gas sensor. More information is given hereafter about these two applications.

### **4.2 Applications in energy**

Taking into account the rapid speed of the global economic developments, the fossil fuels including coal, oil, and natural gas supply most of the energy we purchase. However, the fossil fuels are not renewable and they deplete while the energy demand continues to grow. Furthermore, pollutants emitted during the burning of fossil fuels degrade the environment

and greenhouse gases lead to the global-warming problems, which are deteriorating. Therefore, it is an urgent priority to find new alternative energy. How to enhance the efficiency, energy conversion and storage by using the solar light energy becomes an important issue of concern for the scientific researchers [95]. The HMMOC NFs are promising materials to meet these requirements in two directions of energy: (a) energy-conversion devices such as solar cells, fuel cells, and (b) energy-storage devices such as lithium ion battery, and super capacitor.

Long Q et al combined intermittent microwave radiation and ES methods to fabricate TiO<sub>2</sub>-Pt composite NFs with high electrochemical catalysis properties for Proton exchange membrane fuel cell [96]. For the dye-sensitized solar cells (DSSC), it is believed that metallic oxide nanostructures with 1D morphology have a better charge conduction for increasing energy conversion efficiency. The DSSC imitate the process of photosynthesis and use the nanoporous semiconducting thin film as the negative electrode. Electrospun TiO<sub>2</sub> NFs or nanorods (NRs) are most widely studied for DSSC for their high surface area and large pores for increased adsorption of dye sensitizers [97]. Fujihara K. et al have grinded the electrospun TiO<sub>2</sub> NFs to nanorods, and then deposited the TiO<sub>2</sub> NSs as a layer on the surface of DSSC to get 5.8% of efficiency [98]. Besides the materials related to carbon, the semiconducting metallic oxides also have potential applications in lithium ion battery due to their good electrochemical properties. Reddy M.V. [99] and Zhu P.N. [100] have fabricated TiO<sub>2</sub> NFs with high cycle stability by ES for lithium ion battery.

### 4.3 Applications in nanoelectronic devices

The technique of ES fabricates the continuous HMMOC NFs with long length and can lead to orderly arrangement of NFs. When the size of materials reaches a nanometric range, it is observed a quantization of the electronic energy levels, leading to new electrical properties. Thus the electrospun HMMOC NFs have broad application prospects in the field of electronic devices such as nanoconducting wires, field-effect transistor, and diode. In principle, the ES technique could directly fabricate metal NPs/polymer composite NFs, which could be used for nonvolatile memory elements and nanoswitches. Pol V. G. has synthesized Au NFs with diameter of 300 nm by ES with subsequent calcination [101]. After removing the polymer from the NFs, the final products were piled, which reduces the conductivity to  $1.2 \times 10^{-4}$  S/cm. Compared to the normal Au electrode plate, the current peak of Au NFs after calcination at 450°C and 600°C is enhanced of 20%. X. F. Lu's group has found that the

surface photovoltage response became reversal when the electrospun TiO<sub>2</sub> NFs were coated with a layer of conducting polymers [81].

#### **4.4 Applications in catalytic field**

ES affords an effective way to fabricate a HMMOC NF mat, which can be used as a photocatalyst. The electrospun HMMOC NFs is a good catalyst supporting materials due to their large specific surface area and high porosity. In principle, HMMOC composite catalysts based on the electrospun polymeric or ceramic NFs mats can be synthesized in two ways. The first way is to mix the polymer or ceramic precursors in the ES solution with the metal salt and then yield mats of composite fibers by ES process. Subsequently the reduction of metal salt can be achieved by heating at high temperature or in the presence of a reducing agent [102]. Another way is a post treatment of the electrospun NFs mats to deposit metal NPs on the surface of the NFs [103]. Formo E. [104] and Obuya E. A. [105] have modified the surface of TiO<sub>2</sub> NFs by Pt and Pd NPs, respectively. This material shows excellent catalytic activities in the hydrogenation reaction of methyl red and the coupling reaction of C-C. Xia and co-workers have reported the decoration of Pt NPs with different sizes on the surface of TiO<sub>2</sub> NFs by a polyol reduction method in the presence of PVP [106]. TiO<sub>2</sub> NFs, as one of the most attracted materials for photocatalysis, have the nanometric range and 1D structure with obviously surface effect and quantum size effect, which is widely used in various areas like wastewater treatment. Compared to the traditional catalysts, the TiO<sub>2</sub> electrospun NFs can react with the reactants due to their high specific surface area and enhance the catalytic efficiency, and also have advantages including chemical stability, low cost and ease recovered by filtration for recycle.

##### ***4.4.1 Historical background***

The development of photocatalysis has gradually formed two main research directions: photocatalytic solar energy conversion and environmental photocatalysis. The photocatalytic solar energy conversion focuses on new energy development (solar energy) and energy storage (water photolysis) by water splitting to produce hydrogen. The high calorific value, clean and renewable hydrogen energy can replace the dwindled, polluted and impossible renewable petroleum energy [107]. Meanwhile, for the environmental photocatalysis, there are three main directions: (a) photo-decomposition or photo-oxidization of harmful substances,

like decomposition of harmful organic compounds, deodorizing, anti-bacterial, anti-viral, fungicidal, air purification and water treatment; (b) photo-induced super hydrophilicity which has been used for various areas including anti-fog, self-cleaning, quick dry, cooling, water absorptive, enhancement in coating material performances; (c) artificial photosynthesis and photoelectron chemical conversion for solar cells and photofuel cells [108].

The particle size of photocatalyst normally is around 10 ~ 30 nm with the specific surface area of 100 ~ 300 m<sup>2</sup>/g. The granularity of catalyst influence the catalytic activity. As the particle size decreasing, the specific surface area increases which results in the higher activity. However, if the particle size is too small, they could have the secondary cohesion and make the practicability worse. The mechanism of TiO<sub>2</sub> in aqueous suspension is stuck in speculation and it is still lacking means of verification about the reaction mechanism. Due to the imprecision of the amount of species adsorbed in water like H<sub>2</sub>O, O<sub>2</sub>, it is hard to know the sites of activity on the surface and the role of H<sub>2</sub>O, OH<sup>-</sup>, and O<sub>2</sub>. During the photocatalytic process, the reaction products CO<sub>2</sub> and H<sub>2</sub>O can adsorb easily due to the super hydrophilic and basic center on the surface of TiO<sub>2</sub> catalyst, which reduces the reaction rate and selectivity of the photocatalyst.

The history of photocatalysis can be traced back to the 1960s. The photoinduced phenomena have been found by many researcher groups since 1960s and have been explained by the band theory of SC, which is now well understood [109]–[111]. In 1964, TiO<sub>2</sub> was reported as photocatalyst for the oxidation reaction of tetralin in the liquid phase under UV-illuminated by S. Kato and F. Masuo, which could be considered as the first paper to report a photocatalytic reaction on TiO<sub>2</sub> under UV irradiation [112]. Some molecules such as O<sub>2</sub> and H<sub>2</sub>O are adsorbed on or desorbed from the solid SC surfaces (like TiO<sub>2</sub> and ZnO) under UV light irradiation depending on the respective surface conditions. In 1972, the landmark event of photocatalytic methods was by A. Fujishima and K. Honda, which promoted the investigation of photonic energy conversion [113]. They discovered the photosensitization effect of a TiO<sub>2</sub> electrode for the electrolysis of water into H<sub>2</sub> and O<sub>2</sub> using a Pt metal electrode as cathode under UV light irradiation. Compared to normal electrolysis, the bias voltage of the electrolysis of water was much lower under UV light irradiation of the TiO<sub>2</sub> electrode. Since then, many researchers have reported various reactions in the gas phase employing UV-illuminated semiconducting TiO<sub>2</sub> as catalyst. Understanding the fundamental principles, enhancing the photocatalytic efficiency, and expanding the scope of applications are the key points have been focused on [114], [115].

#### 4.4.2 Photocatalysis mechanism

The role of photocatalysis is to initiate or accelerate specific reduction and oxidation (redox) reactions from the point of view of SC photochemistry. The input energy is used to overcome the activation barrier in order to accelerate the rate of photocatalysis under milder conditions. When the energy of the incident photons matches or exceeds the band gap, the SC absorbs the light and then the electron-hole pairs have photoexcitation consequently [116]. In SC, the CB electrons act as reductants with a chemical potential of +0.5 to -1.5V versus the normal hydrogen electrode (NHE). The VB holes exhibit a strong oxidative potential of +1.0 to +3.5 V versus NHE [114]. In general, a SC photocatalytic cycle comprises three steps: first, the vacant sites (holes) occur because the illumination induces a transition of electrons from the VB to the CB; second, the migration of the holes and excited electrons to the surface; third, the holes and excited electrons react with the adsorbed electron donors (D) and electron acceptors (A), respectively.

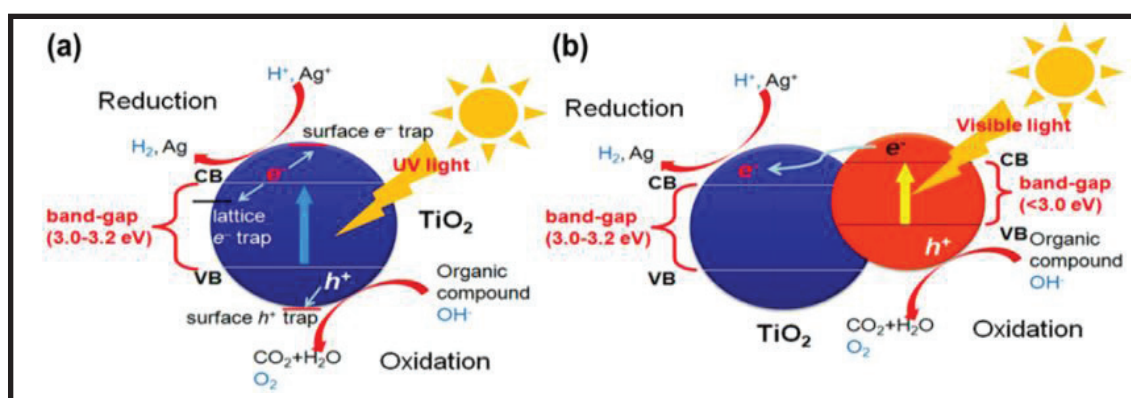


Figure 1.16 (a) General model of photocatalysis on TiO<sub>2</sub>. Reactions occur in three steps: (1) absorption of photons greater than the band gap energy to produce an electron-hole pair; (2) separation of charges and migration to the surface; (3) redox reactions with adsorbed reactants. (b) TiO<sub>2</sub> composite structure exhibiting a heterojunction and charge trapping on TiO<sub>2</sub> and the second component [117].

During the process of holes and electrons migration, a large proportion of electron-hole pairs recombine, and the input energy is dissipated in the form of heat or emitted light. In order to enhance the efficiency, the electron-hole pairs recombination should be prevented by different approaches. Loading Au, Pt, Pd, Ag and other co-catalysts on the surface of SC has generally been applied. The co-catalysts and the host SC form the heterojunctions to provide an internal electric field, which facilitates to separate the electron-hole pairs and induces faster carrier migration. Due to the better conductivity, lower over potential and higher

catalytic activity of the co-catalysts than the host SC, those co-catalysts often act as ideal active sites for photocatalytic reactions to proceed [117]. A general model of photocatalysis on  $\text{TiO}_2$ -Ag composite reactions with UV light and visible light is shown in Figure 1.16.

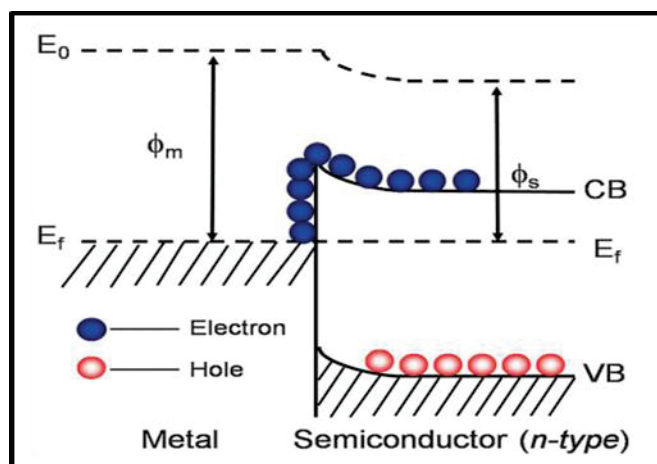


Figure 1.17 Schematic of the Schottky barrier [118].

According to the third law of thermodynamics, all the physical systems have different degrees of irregular distribution except at the absolute zero. The actual crystals are the approximation of the space lattice structure, and they always have one or more defects. When a slight amount of impurities dopes the crystals, it can replace some of the atoms and cause the defects. These defects play an important role for the activity of  $\text{TiO}_2$  catalyst. Introducing noble metal or other metallic oxide/ or sulfide, doping inorganic ions, photosensitization, surface reduction treatments and other methods can introduce impurities or defects, which is benefit to enhance the light absorption of  $\text{TiO}_2$  and increase the efficiency of photocatalysis. The electron distribution of the  $\text{TiO}_2$  catalyst can be modified by introducing noble metal. When these two materials combine together, electrons transfer from  $\text{TiO}_2$  to noble metal until the Fermi levels of them are the same. In space charge layer between  $\text{TiO}_2$ /noble metal, the extra negative charges on the surface of  $\text{TiO}_2$  transfer to the surface of metal and then improve the transportation rate of photogenerated electrons to adsorbed oxygen. Meanwhile, a Schottky energy barrier forms on the surface of  $\text{TiO}_2$  to capture trapped electrons, in this case the recombination of the electron-hole pairs could be inhibited (as shown in Figure 1.17) [118].

#### 4.4.3 Photocatalysis applications

The HMMOC composite NFs as photocatalyst can be used in many practical fields such as anti-soiling, anti-fogging, anti-bacterial sterilization, air cleaning and water cleaning as shown in Figure 1.18.

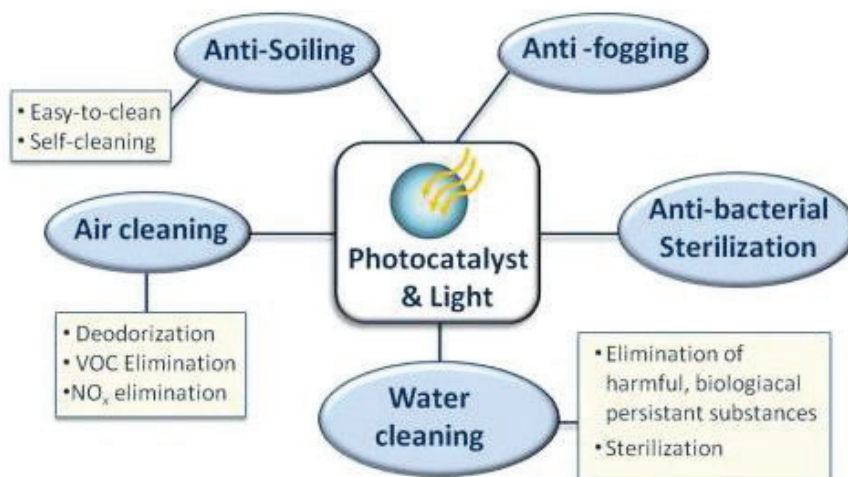


Figure 1.18 Application map of photocatalysts [119].

## 4.5 Applications in sensor field

### 4.5.1 Historical background

WO<sub>3</sub> is a chemical compound containing oxygen and the transition metal tungsten, which has been discovered in 18<sup>th</sup> century. It is obtained as an intermediate in the recovery of tungsten from its minerals. Peter Woulfe found a new element in the naturally occurring mineral wolframite firstly, and Carl Wilhelm Scheele also studied on the mineral scheelite [120]. In 1841, Robert Oxland reported the first procedures to prepare tungsten trioxide and sodium tungstate and granted patents, which is considered to be the founder of systematic tungsten chemistry [121]. In particular, WO<sub>3</sub>, an n-type SC with a wide band-gap of 3.7 eV, has recently attracted much interest in gas sensors. Currently, a low-cost approach to fabricate gas sensor materials with excellent sensitivity and selectivity is highly desired [122]. Several effective methods, including doping, dimension control and phase structure design, are increasingly being adopted by researchers to further improve the gas sensing performance [123]–[125]. Size reduction of the sensing material is a well-known method to increase the gas-sensing performance. This is mainly due to a large surface to volume ratio achieved in this case leading to more available surface reaction sites for the absorption of gas species.

### 4.5.2 Gas-sensing mechanism

The gas sensitivity is based on the diffusion-reaction mechanism that the analytic gas (like air, oxygen molecules) that diffuses and chemisorbs or interacts with pre-adsorbed species such as  $O_2^-$  ions formed on the surface of the metallic oxide particles by capturing an electron from the conduction band [126] (as illustrated in Figure 1.19). In order to achieve high sensitivity, the gas sensing materials should be porous and the particle size of the metallic oxide should be in nanometric range to maximize the surface to volume ratio, in order to ensure the gas penetration and exchange between the analytic gas and the sensor. Compared to other methods, ES enables to obtain highly porous layer with large and small pores and nanosized particles that optimally satisfy both these requirements [127].

Semiconducting metallic oxide materials generally have their own conductivity to their deviation from stoichiometry, and the conductivity can be influenced by the interstitial cation and anion vacancies during the gas sensing process [128]. When the gas adsorption on the surface of semiconducting metallic oxide sensor, the electrical resistance of the oxide changes and the change is tested by the measurement. The SC materials are divided into two groups for *n*-type (electrons are major carrier, e.g.  $TiO_2$ ,  $WO_3$ ,  $SnO_2$ ,  $ZnO$ ) and *p*-type (holes are major carrier, e.g.  $CuO$ ,  $NiO$ ,  $TeO_2$ ) based on the charge carrier. The extra electrons are provided to the material surface when a reducing gas is chemisorbed on the surface of an *n*-type semiconducting material, the as consequence result the resistivity of *n*-type material decreases. The *p*-type materials are observed on the opposite.

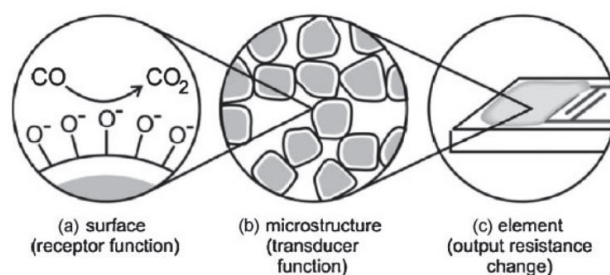


**Figure 1.19 Receptor transduce function of a semiconductor gas sensor: (a) surface, providing the receptor function, (b) microstructure of the sensing layer, providing the transducer function, and (c) element, enabling the detection of the change in output resistance of the sensing layer, here deposited on an interdigital microelectrode. Reprinted with permission from Reference [129].**

According to the published literatures, the main performance parameters of a sensor are including the sensitivity, response and recovery time, optimum working temperatures and low

detected limitations [130]. The sensor sensitivity ( $S$ ) is defined in several different forms like  $S = R_{\text{air}}/R_{\text{gas}}$ ,  $S = R_{\text{gas}}/R_{\text{air}}$ ,  $S = \Delta R/R_{\text{gas}}$  and  $S = \Delta R/R_{\text{air}}$ , where  $R_{\text{air}}$  is the sensor resistance in ambient air,  $R_{\text{gas}}$  is the sensor resistance in the target gas, and  $\Delta R = |R_{\text{air}} - R_{\text{gas}}|$ . The response time ( $\mathcal{T}_{\text{res}}$ ) is defined as the time required by the sensor to achieve 90% of its maximum response of the signal such as resistance upon exposure to the target gas. The recovery time ( $\mathcal{T}_{\text{rec}}$ ) is the time taken by the sensor to reach 10% of its initial resistance after removal the target gas.

The charge transfer dynamics between the target gas molecules and the oxide matrix strongly determines the sensitivity of the metallic oxide. Depositing metal NPs onto the surface of the metallic oxide surface is an effective approach to improve the sensitivity. Due to the presence of metal NPs, the “chemical sensitization” mechanism accelerates the spillover effect due to the large Helmholtz double-layer capacitance of the NPs, which act as electron sinks [131]. The deposition of metal NPs on the surface of semiconducting metallic oxide leads to a negative charge accumulation on the nanoparticle surface, by the partial charge transfer from the center of oxide metal to the NPs. In this case, the dissociative adsorption of oxygen can be facilitated on the particle surface to enhance the formation of the electron depleted layer. Meanwhile, the deposition of NPs on the surface of semiconducting metallic oxide may leads structural defects at the interface, which can serve as active surface sites to adsorb more oxygen and target gas molecules.

#### ***4.5.3 Gas-sensing applications***

The electrospun semiconducting metallic oxide NFs like  $\text{TiO}_2$ ,  $\text{WO}_3$ ,  $\text{ZnO}$ ,  $\text{SnO}_2$  have specific surfaces approximately one to two orders of the magnitude larger than flat films, which makes them to be excellent candidates for potential applications in sensors, HMMOC NFs materials based sensors are targeted to show many good properties such as corrosion resistance, good stability, low working temperature, rapid response and recovery time, and low detection limitation. The metallic oxide NFs have small size, large specific surface area, high sensitivity, good selectivity, and are used as the sensor material in different applications areas such as process control industries, environmental monitoring, boiler control, fire detection, alcohol breath tests, detection of harmful gases in mines, home safety, and grading of agro-products like coffee and spices. The potential applications in process control systems, medical diagnosis, security, and environmental monitoring are frequently employed in solid state gas sensor for various applications ranging from simple gas alarms to complicated electronic noses [132]. Due to the high sensitivity towards many targets gases, the

semiconducting metallic oxides as the promising candidates for gas sensing have many advantages, including simple fabricated, low cost and high compatibility with other parts and processes [133]. Ding Y. et al have reported that the TiO<sub>2</sub>-Pt hybrid NFs can greatly enhance the oxidation of hydrazine in neutral solution in the amperometric hydrazine sensor [134]. The synthesis and gas-sensing characteristics of WO<sub>3</sub> NFs via ES for gas sensors are with the fast response and recovery features [135]. The size of the nanograins influences the gas-sensing ability of metallic oxide NFs such as SnO<sub>2</sub>, In<sub>2</sub>O<sub>3</sub>, and WO<sub>3</sub> [135]–[137]. The size of the grain increases that the area of the grain boundary reduces. The grain boundary resistance as a function of metallic oxide grain size.

## 5 Conclusions

To date, various 1D HMMOC NFs materials have been succeed to be fabricated through different synthesis routes. The surface morphologies and dimension of nanostructures are controllable depending on the processing route employed, which make the products of photocatalyst or sensor devices flexible and tunable. However, there are still some research limitations of the further advancement for 1D structured HMMOC NFs catalysts or sensors. The main challenges and opportunities for photocatalysis and gas sensors will be described in section 5.1 and section 5.2, respectively.

### 5.1 Main challenges and opportunities for photocatalysis

The wide bandgap SC nanostructures have relatively small optical cross-sections in the visible region and therefore their interaction with visible light is very weak. In principle, TiO<sub>2</sub> is a wide bandgap (3-3.2 eV) *n*-type SC and the absorption wavelength is around 387.5 nm in the UV light region, which is less than 5% of the solar energy impinging on the surface of the earth, meanwhile the pure TiO<sub>2</sub> photocatalysts have a high recombination rate of photogenerated electron-hole pairs, the quantum efficiency of TiO<sub>2</sub> is no more than 20% [138]. So the utilization efficiency of the solar light is only around 1%, which is the important limitation of the photocatalytic activities of TiO<sub>2</sub> photocatalysts. This low quantum efficiency is the main problem of photocatalysis for practical application and industrialization.

A number of commercial photocatalytic products like air purifiers and self-cleaning windows are already on the market [139]. However, the other important applications including production of hydrogen and organic fuel or the fabrication of photoelectron

chemical solar cells still need more developments for possible commercialization. The efficiency, stability and cost of these nanomaterials should be carefully considered in order to meet engineering requirements. So it is a challenge of great importance to identify and design new SC materials that are efficient, stable and abundant.

## **5.2 Main challenges and opportunities for gas sensor**

Not all the studies have reported the low detected limitation for a given gas, the work about the optimum working temperature, the response and recovery time. In some cases, the mechanism behind the formation of structures and gas interactions are not well understood. It is still a big challenge to fabricate gas sensors with ultrahigh sensitivity, very short response and recovery time, and good reversibility, reproducibility, and stability based on various sensing techniques and principles.

The contamination of water by toxic heavy metals and air by poisonous gas and VOCs is a world-wide environmental problem. A gas sensor is a device which detects the presence of different gases in a given area for monitoring environmental pollution focusing frequently on those gases which might be harmful to humans or animals. Semiconducting metallic oxide are known for their ability of detecting the trace concentrations of various gases in air via the modification of the sensor's resistance by the charge transfer interactions between the sensor and chemisorbed species [140]. Many of previous studies on  $\text{WO}_3$ -based sensors were focused on the detection of  $\text{NO}$ ,  $\text{NO}_2$ ,  $\text{H}_2$ ,  $\text{H}_2\text{S}$  and  $\text{NH}_3$  [141]–[143], and only a few studies have investigated the gas-sensing performance toward VOCs, such as n-butanol, methanol, ethanol and acetone [144]. Therefore, it is necessary to fabricate sensitive and selective gas-sensing materials for the detection VOCs. Compared to the widely used approaches of vacuum deposition [145], spin-coating [146], sputtering [147], sol-gel synthesis [144] and thermal evaporation [148] for the synthesis  $\text{WO}_3$ -based materials, ES technique is a cost-effective and versatile method for large-scale production of 1D composite materials with high surface areas. Another advantage of this technique is that the self-supporting material is made of entangled fibers giving a huge accessible porosity which can be interesting for the above-mentioned targeted applications. Moreover, the generated foam-like morphology allows open pores and large voids to be generated by the consecutive heat treatment, resulting in enhanced sensing performances. Indeed, rapid response/recovery behaviors are facilitated by the good gas accessibility onto the surface for reaction [149]. In addition, the catalytic functionalization of noble metal nanoparticles onto oxide NFs has been introduced to promote gas sensing

reactions by reducing the activation energy, and thereby increasing the sensing response and selectivity while also decreasing the maximum working temperature of the sensors. Noble metals such as Pd, Pt and Au are known to be used as catalysts for gas activation [150]. Therefore, the WO<sub>3</sub> NFs functionalized by Au NPs is an effective method for enhancing the sensing response of WO<sub>3</sub> NFs and ES is a highly attractive method for the large scale synthesis of such composite NFs.

Therefore, the two above-mentioned materials, TiO<sub>2</sub> and WO<sub>3</sub>, will be studied in the following chapters for their photocatalytic and gas sensing properties, respectively. Their properties will be optimized and studied by combining these ceramic materials with gold nanoparticles. The work hereafter is firstly focused on the synthesis of the nanostructures, and then on of their physical properties.



## CHAPTER II EXPERIMENTAL METHODS AND CHARACTERIZATIONS

In this chapter, the experimental routes and processes followed with characterizations are described sequentially, and divided into four main sections: (1) materials and instruments introduction; (2) synthesis of polymer or oxide ( $\text{TiO}_2$  or  $\text{WO}_3$ ) filaments, and HMMOC composite NFs:  $\text{TiO}_2$ -Au or  $\text{WO}_3$ -Au, (3) characterization techniques used to analyze the synthesized samples, (4) the measurement system for photocatalysis and gas-sensing performance. The used materials including the precursors, polymers and solvents to synthesize the composite NFs are described in section 2.1. The polymer/Au, pure oxide NFs ( $\text{TiO}_2$  or  $\text{WO}_3$ ), and oxide-Au ( $\text{TiO}_2$ -Au or  $\text{WO}_3$ -Au) composite NFs were fabricated by combining the electrospinning technique with subsequent calcination. Detailed information about the experiment routes and processes are reported in section 2.2. Characterization methods of the synthesized material include: Thermogravimetric Analysis (TGA), Fourier Transform – Infrared Spectroscopy (FT-IR), Ultraviolet – Visible Spectroscopy (UV-Vis), X-ray Diffraction Studies (XRD), Scanning Electron Microscopy (SEM), High Resolution Transmission Electron Microscopy (HRTEM), Nitrogen Sorption Studies (BET), and Inductively Coupled Plasma – Optical Emission Spectroscopy (ICP). The detailed information on these characterization methods are described in section 2.3. The measurement systems for photocatalysis and gas-sensing performance are described in section 2.4 and 2.5, respectively.

## 1 Materials and Instruments

### 1.1 Materials

#### 1.1.1 Precursors

Hydrogen tetrachloroaurate (III) trihydrate ( $\text{HAuCl}_4 \cdot 3\text{H}_2\text{O}$ ,  $\geq 99.9\%$ , Sigma Aldrich), Titanium isopropoxide (TTIP,  $\text{C}_{12}\text{H}_{28}\text{O}_4\text{Ti}$ ,  $\geq 99.9\%$ , Sigma Aldrich) and Ammonium metatungstate hydrate (AMT,  $(\text{NH}_4)_6\text{H}_2\text{W}_{12}\text{O}_{40} \cdot n\text{H}_2\text{O}$ ,  $\geq 99.9\%$ , Sigma Aldrich) were used as gold, titanium and tungsten precursors, respectively. The structure formulas of each precursor are shown in Figure 2.1. They were chosen for their high solubility, their ease to use and their ability to lead to the targeted materials with the desired synthesis route of this work.

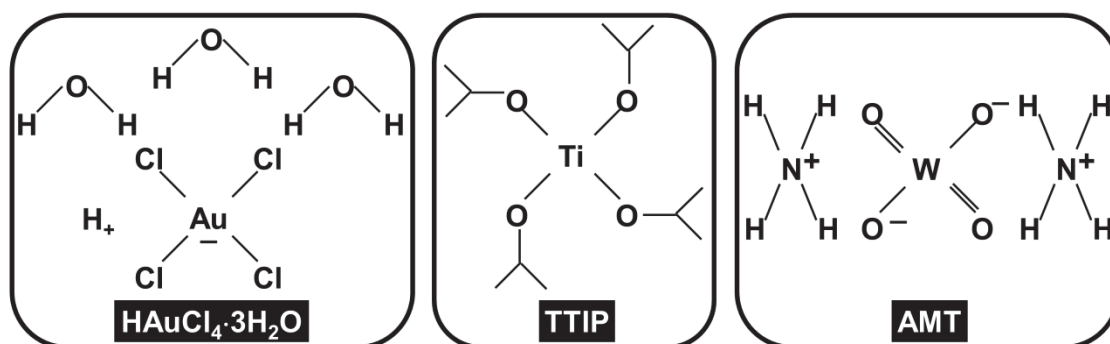


Figure 2.1 Chemical structures of the three different precursors of metallic oxides.

#### 1.1.2 Solubility of precursors and spinnable polymers

Taking into account the structure of each precursor, it is impossible to shape them as filaments by a direct electrospinning. The electrospaying of the solution is unavoidable in that case. Firstly,  $\text{HAuCl}_4 \cdot 3\text{H}_2\text{O}$  has good solubility with EtOH, DMF and  $\text{H}_2\text{O}$ . In order to fabricate polymer–Au NFs, suitable polymer is required for each solvent. For TTIP precursor of titanium, a well-known system of PVP–TTIP combined with a mount of acetic acid to fabricate  $\text{TiO}_2$  NFs was reported for the first time by Dan Li and Younan Xia in Nano Letters at 2003 [51]. Moreover, AMT has good solubility in all the above mentioned solvents. According to former results (from our lab and literature) [151]–[153], Polyvinyl pyrrolidone–EtOH, Polyacrylonitrile–DMF, and Polyvinyl alcohol– $\text{H}_2\text{O}$  are the best candidates since they lead to a stable and an easy spinning when the solution is prepared with suitable weight ratios: 7 wt%, 10 wt%, and 10 wt%, respectively.

In the present work, polyvinlyl pyrrolidone (PVP,  $[C_6H_9NO]_n$ , Aldrich,  $M_w \sim 1\,300\,000\text{ g}\cdot\text{mol}^{-1}$ ,  $\geq 99\%$ , Sigma Aldrich), Polyvinyl alcohol (PVA,  $[C_2H_4O]_n$ ,  $M_w \sim 72\,000\text{ g}\cdot\text{mol}^{-1}$ , Sigma Aldrich) and Polyacrylonitrile (PAN,  $(C_3H_3N)_n$ ,  $M_w \sim 150\,000\text{ g}\cdot\text{mol}^{-1}$ , Sigma Aldrich), were used as matrix polymers since they present excellent properties to get good NFs by electrospinning and they are soluble in different suitable solvents, which can co-dissolve the gold, titanium or tungsten precursors. The structure formula of these three polymers is shown in Figure 2.2.

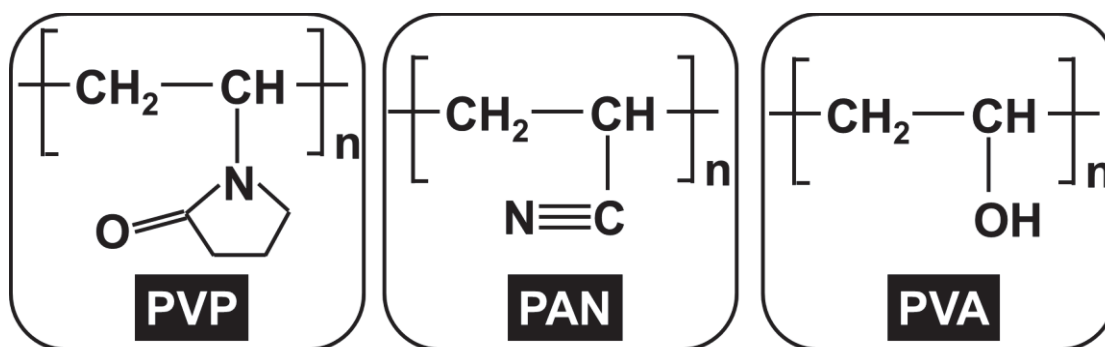


Figure 2.2 Chemical structures of three different polymers.

The solubilization of the corresponding polymers was selectively performed in the following solvent: N, N-dimethyl-formamide (DMF,  $C_3H_7NO$ , 99.8%), methanol ( $CH_4$ , 99.9%), absolute ethanol (EtOH,  $C_2H_6O$ , 99.9%), n-butanol ( $C_4H_{10}O$ , 99.9%), and acetone ( $C_3H_6O$ , 99.9%), used as received without further purification. Deionized water was used in all the synthesis processes.

## 2 Synthesis routes and processes

The typical synthesis routes and processes of HMMOC NFs by ES are including three main parts as shown in Figure 2.3: (1) Preparation of the ES solution precursors with polymers dissolved in suitable solvents. The stirring time, temperature, concentration and solvent volatility are the main parameters influencing the spinnability of the solution; (2) ES process to fabricate as-spun NFs by controlling the experiment factors including working voltage, distance, feeding rate, even the atmosphere, humidity and temperature; (3) Subsequent calcination to remove the polymer components and form the target products, in this part the heating temperature, heating rate and atmosphere would affect the final products.

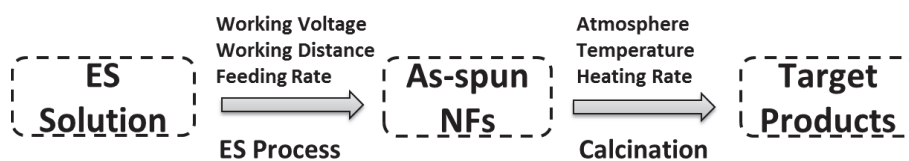


Figure 2.3 the typical synthesis routes and processes of electrospinning with experiment factors.

## 2.1 General information on equipment

### 2.1.1 Electrospinning setup

The basic setup for electrospinning in our experiments shown in Figure 2.4 including five parts as below: (a) high-voltage power supply (HV supply from Iseg Co., T1CP 300 304 p), which can offer a positive voltage varying from 0 ~ 30 kV with continuous current up to 0.3 mA; (b) a syringe pump (KDS-100, Bioseb Co.) to control a continuous feeding rate; (c) a plastic syringe with volume of 5 mL or 10 mL equipped with a conductive metal needle; (d) a 21 gauge stainless steel needle with the inner diameter of 0.51 mm; (e) a piece of grounded aluminum foil used as collector. By applying a voltage, feeding rate and working distance (the distance from the tip of the needle to the collector), there is a stable electric field between the needle and aluminum film, and the composite NFs are collected onto the aluminum film target.

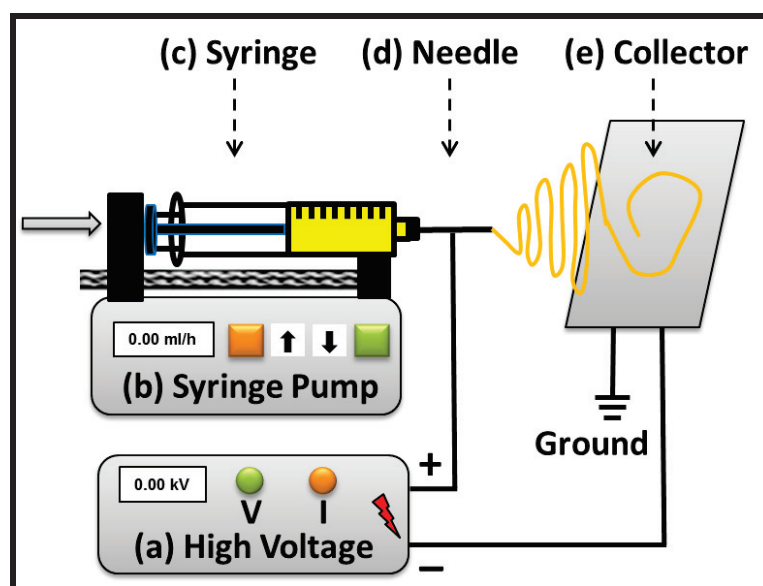


Figure 2.4 Electrospinning setup: (a) high voltage supply, (b) syringe pump, (c) plastic syringe, (d) needle, (e) collector.

### **Comment about the effect of relative humidity**

Relative humidity can strongly influence the spinning conditions according to the solvent used inside the polymer solution. In the present work, humidity was systematically measured, but not controlled, since all the ES experiments were performed in ambient air, under a hood. The corresponding values were typically ranged from 25 to 45%, which is sufficient for reproducible experiment in our case.

### **2.1.2 Thermal treatments**

All the thermal treatments were achieved in a Muffle furnace (Nabertherm LE6/11) with the temperature up to 1000°C in air. The heating rate is fixed at 1 °C·min<sup>-1</sup>, with such slow heating rate to remove the polymer components and form the inorganic crystals, by keeping the filament shape.

## **2.2 Description of the different Au addition routes**

### **2.2.1 Synthesis processes and different Au addition routes**

Based on the typical ES process to fabricate HMMOC NFs, the key point is to introduce the Au NPs. Considering our system and target properties of photocatalysis and gas sensing, the gold ions can be introduced in several different points from beginning to end of the experiment process.

Three ways have been studied to introduce Au NPs, with dispersion as homogeneous as possible (Figure 2.5). The first one, already investigated by previous works [154], consists in dissolving gold ions in the ES solution (route (i) Figure 2.5 and Figure 2.6). In that case, a good and homogeneous dispersion is expected, both at the surface and in the NFs volume.

The second method envisaged is the deposition of gold ions on the surface of the filaments, either before or after treatment. This route should allow having a higher amount of gold at the surface and maybe give different physical properties than those obtained with the first route. This method is divided in two distinct sub-routes, according to the time when gold ions are deposited on the surface of the filaments. It can be done either before or after calcination (routes (ii) and (iii) respectively, Figure 2.5 and Figure 2.6). Since the polymer stabilization at low temperature will be considered, gold deposition of route (ii) will be possible before or after this stabilization treatment (route (ii) detailed Figure 2.6).

To summarize, the three designed Au addition routes (shown in Figure 2.5) are as following:

**Volume inclusion (i)**: addition Au ions into ES solution directly before ES process;

**Surface deposition (ii)**: addition Au ions on the surface of as-spun NFs after ES;

**Surface deposition (iii)**: addition Au ions on the surface of oxide NFs after calcination.

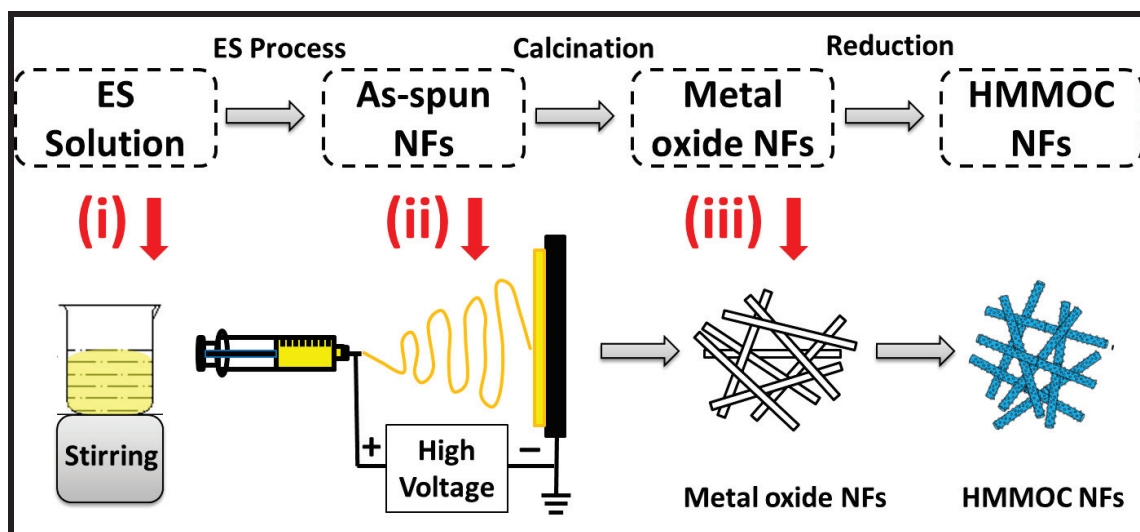
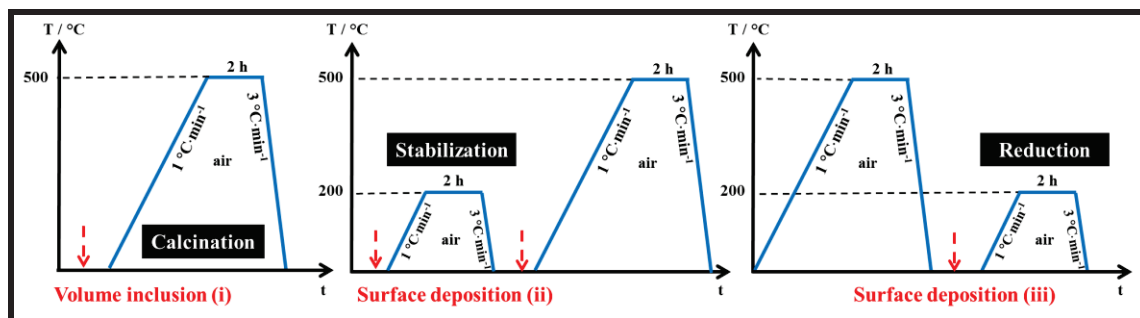


Figure 2.5 Synthesis processes and three different Au addition routes.

### 2.2.2 Thermal treatment processes

As shown in Figure 2.6, three different addition routes related to different thermal treatment processes. For volume inclusion (i) route, the as-spun NFs obtained from ES are calcined under air at 500°C directly for 2h to produce the final sample. For second route of surface deposition (ii), Au ions have been deposited on the surface of electrospun polymer composite NFs with or without stabilization at 200°C in air, and then after deposition the sample is heated at 500°C for 2h in air. For third route of surface deposition (iii), Au ions have been deposited on the surface of metallic oxide NFs obtained from thermal treatment at 500°C for 2h in air, and then followed with an Au reduction heating at 200°C for 2h in air. All the calcinations were taken place in air atmosphere for 2 h with the heating rate of 1 °C·min<sup>-1</sup> and cooling rate of 3 °C·min<sup>-1</sup>.



**Figure 2.6** Different thermal treatment processes for three different addition routes. Red arrows indicate when gold ions are introduced in the system: (i) with co-spinning of gold ions and polymer solution, (ii) with deposition either before or after stabilization of polymer filaments and (iii) with deposition after filament calcination.

In order to figure out the influence of each synthesis parameter, before fabricating oxide NFs containing gold (described in section 2.5), the shaping process was improved by spinning pure polymer solutions (section 2.3), and the ability to form gold nanoparticles inside (or/and) at the surface of polymer filaments was studied without any oxide precursor (section 2.4).

### 2.3 Preparation of pure polymer nanofibers

In order to investigate the ES and thermal behaviors of different polymers with Au precursor ( $\text{HAuCl}_4 \cdot 3\text{H}_2\text{O}$ ), three polymers (PVP, PVA, PAN) were chosen as the polymer matrix. To prepare the ES solution, PVP, PVA and PAN were dissolved in EtOH,  $\text{H}_2\text{O}$  and DMF, respectively, and stirred during several hours to lead to homogenous spinnable solutions with concentrations of 7 wt%, 10 wt%, 10 wt%, respectively, as shown in Table 2.1. PVP–EtOH was stirred at room temperature directly, while PVA– $\text{H}_2\text{O}$  and PAN–DMF needed to be heated in oil bath at the temperature ranging from 50 to 80 °C, depending on the stirring time (the lower the temperature, the longer the stirring time). With a typical ES process, pure as-spun PVP, PVA, and PAN polymer NFs can be obtained without any further treatment, which could be blank samples comparing with other samples.

**Table 2.1 Detailed information of polymer ES solution and ES conditions.**

Sample	Polymer	Solvent	Concentration wt%	Stirring T/°C	Voltage kV	Distance cm	Feeding Rate mL·h <sup>-1</sup>
PVP	PVP	EtOH	7	RT	10	10	1.0
PVA	PVA	H <sub>2</sub> O	10	75	10	10	0.6
PAN	PAN	DMF	10	80	12	15	2.0

## 2.4 Synthesis of polymer–Au composite nanofibers

Volume inclusion (i) was chosen as the main route for obtaining polymer–Au composite NFs. Generally, an amount of HAuCl<sub>4</sub>·3H<sub>2</sub>O was mixed in the ES solution of PVP–EtOH, PVA–H<sub>2</sub>O, PAN–DMF to add Au ions in the system. To ensure homogeneity, the mixed solutions were then stirred at room temperature for 12 h. Different ES factors were researched for different polymer–Au composites NFs. All the ES conditions were shown as Table 2.2.

**Table 2.2 Detailed information of polymer–Au ES solution and ES conditions.**

	Au contents polymer: Au	Voltage kV	Distance cm	Feeding Rate mL·h <sup>-1</sup>	Calcination temperature/°C	Atmosphere	Heating time / h
PVP–Au	3:1, 6:1, 9:1	6.5	10	0.6	200,300,400,500	air, Ar–H <sub>2</sub> , H <sub>2</sub>	2
PVA–Au	10:1	12	10	0.1	200,500	air	2
PAN–Au	10:1	8	10	0.6	200,500	air	2

### 2.4.1 PVP–Au nanofibers

For PVP–Au, the factors of Au contents, atmosphere, and heating temperatures were investigated. HAuCl<sub>4</sub>·3H<sub>2</sub>O was dissolved in the prepared spinning solution PVP–EtOH to make three different weight ratios of PVP: HAuCl<sub>4</sub>·3H<sub>2</sub>O were 3:1, 6:1, and 9:1. The working distance was about 10 cm from the needle tip to the collector and the working voltage was 6.5 kV. The feeding rate was 0.6 mL·h<sup>-1</sup>. Under these working conditions, an electric field of 0.65 kV·cm<sup>-1</sup> led to a stable jet. The as-spun PVP/HAuCl<sub>4</sub> composite NFs were collected on aluminum film, and then collected NFs were annealed at 500 °C for 2 h in ambient air with the heating rate of 1 °C·min<sup>-1</sup> and cooled in furnace to obtain the target NFs. The target samples with different Au contents were named as PVP–Au–3:1, PVP–Au–6:1, PVP–Au–9:1,

respectively. For the temperature and atmosphere factors influences, sample PVP–Au–6:1 was chosen and treated at different temperatures (including 200, 300, 400, 500°C) in different atmospheres (including air, H<sub>2</sub>, and Ar–H<sub>2</sub>) the related samples were numbered as PVP–Au–200, PVP–Au–300, PVP–Au–400, and PVP–Au–500, respectively.

#### **2.4.2 PVA–Au nanofibers**

An amount of H<sub>2</sub>AuCl<sub>4</sub>·3H<sub>2</sub>O was dissolved in the prepared spinning solution PVA–H<sub>2</sub>O to make the weight ratio of 10:1 for PVA: H<sub>2</sub>AuCl<sub>4</sub>·3H<sub>2</sub>O. To ensure homogeneity, the solution was then stirred at room temperature for 12 h. The working distance was 10 cm from the needle tip to the collector and the working voltage was 12 kV. The feeding rate was 0.1 mL·h<sup>-1</sup>. Under these working conditions, an electric field of 1.2 kV·cm<sup>-1</sup> led to a stable jet. The as-spun PVA/H<sub>2</sub>AuCl<sub>4</sub> composite NFs were collected on aluminum film, and then collected NFs were annealed at 200 and 500 °C for 2 h in ambient air with the heating rate of 1 °C·min<sup>-1</sup> and cooled in furnace to obtain the target NFs. The target sample was named as PVA–Au–200 and PVA–Au–500.

#### **2.4.3 PAN–Au nanofibers**

##### **Volume inclusion (i):**

An amount of H<sub>2</sub>AuCl<sub>4</sub>·3H<sub>2</sub>O was dissolved in the prepared spinning solution PAN–DMF to make the weight ratio of PAN: H<sub>2</sub>AuCl<sub>4</sub>·3H<sub>2</sub>O were 10:1. To ensure homogeneity, the solution was then stirred at room temperature for 12 h. The working distance was 10 cm from the needle tip to the collector and the working voltage was 8 kV. The feeding rate was 0.6 mL·h<sup>-1</sup>. Under these working conditions, an electric field of 0.8 kV·cm<sup>-1</sup> led to a stable jet. The as-spun PAN/H<sub>2</sub>AuCl<sub>4</sub> composite NFs were collected on aluminum film, and then collected NFs were annealed at 200 and 500°C for 2 h in ambient air with the heating rate of 1 °C·min<sup>-1</sup> and cooled in furnace to obtain the target NFs. The target sample was named as PAN–Au–200 and PAN–Au–500.

##### **Surface deposition(ii):**

By many times of testing, PAN–DMF composite NFs were more stable to keep the fiber morphology with the Au aqueous solution than PVP–EtOH and PVA–H<sub>2</sub>O. Thus, the second route of Au addition by deposition (ii) was focusing on PAN–Au NFs. In order to get the

optimization conditions, stabilization was introduced to the process. The stabilized temperature including room temperature, 200, 250, 280 °C were tested according to the thermal behavior of PAN [155]. The deposition with different concentration of Au aqueous solution (including 0.01M, 0.1M, and 1M) was also investigated. After deposition of Au ions on the surface of PAN–DMF composite NFs, reduction Au ions to Au NPs by different methods (including calcination at different temperatures (200, 300, 400, and 500 °C), using reducing agents like citrate acid and hydrazine) was also researched. All these experimental factors and varying conditions were listed in Table 2.3.

**Table 2.3 Details of PAN–Au prepared by second route of surface deposition (ii)**

Experimental Factors	Varying Conditions			
Stabilization Temperature / °C	RT	200	250	280
Calcination Temperature / °C	200	300	400	500
Au concentration	0.01 M	0.1 M	1 M	
Deposition times	1	3	5	
Reduction method	calcination	citrate acid	hydrazine	

## 2.5 Synthesis of metallic oxide nanofibers

The synthesis of metallic oxide (both TiO<sub>2</sub> and WO<sub>3</sub> NFs) is very similar to route (i) since the metal precursor was directly mixed with the polymer solution prior to ES. For TiO<sub>2</sub> NFs, the concentration of precursor TTIP–PVP–EtOH and calcination temperatures have been investigated and optimized. For WO<sub>3</sub> NFs, different types of polymer with related solvents (including PVP–EtOH, PVA–H<sub>2</sub>O and PAN–DMF) were considered.

### 2.5.1 TiO<sub>2</sub> nanofibers

To prepare TiO<sub>2</sub> NFs, in a typical procedure, an amount of TTIP was dissolved in a volume of acetic acid and EtOH, and then mixed with 6.43 g of the previous ES solution of 7 wt% PVP–EtOH, to get the weight ratio of PVP:TTIP to be 9:30, 9:10, 9:3 and 9:1, respectively. To ensure good mixture homogeneity, the resulting solution was then stirred at room temperature for 2 h. After a typical ES process, the as-spun PVP–TTIP composite NFs were obtained and treated at different temperatures in air for 2 h. The related final samples

heat treated at 500 °C with different concentration of TTIP were named as TiO<sub>2</sub>-9:3, TiO<sub>2</sub>-9:10, and TiO<sub>2</sub>-9:30, respectively. All the experimental details were shown in Table 2.4.

**Table 2.4 Experimental details of TiO<sub>2</sub> NFs by first route of volume inclusion (i).**

Sample TiO <sub>2</sub>	TTIP / g	PVP-EtOH 7 wt% / g	Acetic acid / mL	EtOH / mL	ES Conditions / kV, / cm, / mL·h <sup>-1</sup>	Calcination / °C
9:30	1.5	6.43	3	3	10, 10, 1.5	500, 600, 700, 800
9:10	0.5	6.43	3	3	10, 10, 1.5	500
9:3	0.15	6.43	3	3	10, 10, 1.5	500

## 2.5.2 WO<sub>3</sub> nanofibers

A amount of AMT was mixed with 10 mL of the three previous ES solutions (including 7 wt% PVP-EtOH, 10 wt% PVA-H<sub>2</sub>O, 10 wt% PAN-DMF) to get the weight ratio of Polymer:AMT 1:1, respectively. To ensure good mixture homogeneity, the resulting solution was then stirred at room temperature for 6 h. After a typical ES process, the as-spun PVP-AMT, PVA-AMT, PAN-AMT composite NFs were obtained and treated at 500 °C in air/H<sub>2</sub>/N<sub>2</sub> for 2 h. All the experimental details were shown in Table 2.5. The final samples of pure WO<sub>3</sub> NFs obtained from different starting polymers were named as PVP-WO<sub>3</sub>, PVA-WO<sub>3</sub>, and PAN-WO<sub>3</sub>, respectively.

**Table 2.5 Experimental details of WO<sub>3</sub> NFs by first route of volume inclusion (i).**

Sample WO <sub>3</sub>	AMT / g	ES solution wt% / g	Polymer:AMT Weight ratio	EtOH / mL	ES Conditions / kV, / cm, / mL·h <sup>-1</sup>	Calcination / 500 °C
PVP-AMT	0.7	7 / 10	1:1	3	10, 10, 0.2	air, H <sub>2</sub> , N <sub>2</sub>
PVA-AMT	1	10 / 10	1:1	3	10, 10, 0.2	air, H <sub>2</sub> , N <sub>2</sub>
PAN-AMT	1	10 / 10	1:1	3	6.5, 10, 0.2	air, H <sub>2</sub> , N <sub>2</sub>

## 2.6 Synthesis of HMMOC nanofibers

### 2.6.1 TiO<sub>2</sub>-Au composite nanofibers

The TiO<sub>2</sub>-Au composite NFs were achieved by three different Au addition routes.

**Volume inclusion (i):**

The first way was using a facile method by volume inclusion (i) combining a subsequent annealing treatment. An amount of Au precursor was dissolved in the PVP/TTIP solution (9:30) to make the contents of Au in the final TiO<sub>2</sub>-Au composites are 2wt%, 4wt%, 8wt%, respectively. Then a calcination step at 500 °C for 2 h is performed, not only to remove the polymer part, but also to reduce the gold salt and obtain Au NPs. The samples of pure TiO<sub>2</sub> NFs and TiO<sub>2</sub>-Au with different Au contents were named as TiO<sub>2</sub>-Au-0wt%, TiO<sub>2</sub>-Au-2wt%, TiO<sub>2</sub>-Au-4wt%, and TiO<sub>2</sub>-Au-8wt%, respectively. Meanwhile, the sample of TiO<sub>2</sub>-Au-4wt% also named as TiO<sub>2</sub>-Au-i in order to compare with other two Au addition routes.

**Surface deposition (ii):**

This route is to introduce the Au aqueous solution with the concentration of 0.1M on the surface of PVP/TTIP composite NFs (with or without stabilization). Stabilization is to pretreat the PVP/TTIP composite NFs at 200 °C for 2 h in ambient air, in order to keep the NFs morphology without dissolving by deposition of the gold aqueous solution. The final sample was named as TiO<sub>2</sub>-Au-ii.

**Surface deposition (iii):**

The third way is to add Au ions after the formation of TiO<sub>2</sub> NFs. The final sample was named as TiO<sub>2</sub>-Au-iii.

### ***2.6.2 WO<sub>3</sub>-Au composite nanofibers***

The WO<sub>3</sub>-Au composite NFs were achieved by three different Au addition routes. These are facile methods by electrospinning combining a two-step annealing treatment including the Au salt reduction. The influence of different starting polymers of PVP, PVA, and PAN and different atmospheres of air and N<sub>2</sub> were investigated.

**Volume inclusion (i):**

The first way was using a facile method by volume inclusion (i) combining a subsequent annealing treatment. An amount of Au precursor was dissolved in the PVP-AMT, PVA-AMT, and PAN-AMT solution, respectively. Then a calcination step at 500 °C for 2 h is performed, not only to remove the polymer part, but also to reduce the gold salt and obtain Au NPs.

**Surface deposition (ii):**

The as spun PVA-AMT composite NFs were stabilized with different temperatures (RT, 200 °C, 500 °C) for 2 h in ambient air firstly. Secondly, a known volume of Au ions solution is simply deposited on the NFs surface and absorbed due to capillarity action. The latter concentration is adjusted at two values 0.001M, 0.01M and 0.1M, respectively. Finally, a calcination step at 500 °C for 2 h is performed, not only to remove the polymer part, but also to reduce the gold salt and obtain Au NPs. The samples of pure WO<sub>3</sub> and WO<sub>3</sub>-Au with various Au contents were named as WO<sub>3</sub>, WO<sub>3</sub>-Au-0.001M, WO<sub>3</sub>-Au-0.01M and WO<sub>3</sub>-Au-0.1M, respectively.

**Surface deposition (iii):**

The third way is to add Au ions after the formation of WO<sub>3</sub> NFs.

**2.7 Summary of Au addition routes**

Table 2.6 shows the details information of the three different Au addition routes. The most important difference of the three routes is their starting materials, which are ES solution, as-spun NFs and metallic oxide NFs, respectively. For volume inclusion (i) route, PVP, PVA and PAN, three polymers were used firstly to fabricate polymer-Au (including PVP-Au, PVA-Au, PAN-Au) and metallic oxide NFs (like TiO<sub>2</sub> and WO<sub>3</sub>), then HMMOC NFs of TiO<sub>2</sub>-Au and WO<sub>3</sub>-Au were also obtained by this method. The type of polymer, heating temperature, Au contents, and atmosphere were the factors researched for the influence of final products morphology and properties. The second route of surface deposition (ii), Au ions was deposited onto the surface of as-spun polymer NFs. Due to the polymer natural properties, the morphologies PVP/EtOH and PVA/H<sub>2</sub>O as-spun NFs is easily to be destroyed by addition of Au ions aqueous solution on their surface because the PVP and PVA dissolve in water. In order to avoid this problem, a prior stabilization has been used to keep the fiber morphology before depositing Au aqueous solution. For the surface deposition (iii), Au ions are added onto the surface of metallic oxide NFs (TiO<sub>2</sub> and WO<sub>3</sub>), and then reduced to Au NPs. The different reduction ways like using citrate acid, hydrazine, and calcination were discussed. The concentration of Au aqueous solution was also varied.

**Table 2.6 Detailed information of the three different Au addition routes.**

	Volume inclusion (i)	Surface deposition (ii)	Surface deposition (iii)
Starting Materials	ES solution	as-spun NFs	metallic oxide NFs
Polymer	PVP, PVA, PAN	PAN	PVP, PVA, PAN
Precursor	TTIP, AMT , Au	TTIP, AMT , Au	TTIP, AMT , Au
Polymer–Au NFs	PVP–Au, PVA–Au, PAN–Au	PAN–Au	—
Metallic oxide NFs	TiO <sub>2</sub> , WO <sub>3</sub>	—	—
HMMOC NFs	TiO <sub>2</sub> –Au, WO <sub>3</sub> –Au	TiO <sub>2</sub> –Au, WO <sub>3</sub> –Au	TiO <sub>2</sub> –Au, WO <sub>3</sub> –Au

### 3 Composite nanofibers characterizations

This section contains two main parts for the composite NFs characterization: morphological characterizations and physico–chemical ones. Both of them give a brief introduction of principles of each characterization technique used and the preparation method of testing samples.

#### 3.1 Morphological characterizations

All the morphological characterizations, like Scanning Electron Microscopy (SEM) and High Resolution Transmission Electron Microscopy (HRTEM), were tested in the Center Technologies of Microstructures (CT $\mu$ ) of University of Claude Bernard Lyon 1 (UCBL).

##### 3.1.1 Scanning Electron Microscopy (SEM)

Scanning electron microscope (SEM) is used to produce images of a sample by scanning it with a focused beam of electrons. A very fine electron beam with energies up to tens keV is generally scanned in a raster scan pattern and the beam's position is combined with the detected signal to produce an image. The information about the sample's surface topography and composition can be obtained by detecting the various signals produced by the electrons interacting with atoms in the sample, for example, the intensity of emission of secondary and backscattered electrons is very sensitive to the angle at which the electron beam strikes the surface of the sample. The ratio between the dimension of the final image display and the field scanning on the specimen can influence the magnification. Usually, the magnification range produced by the SEM is between 10 to 222,000 times, and the resolution is better than few nanometers.

The conditions of SEM analysis can be in high vacuum, in low vacuum, in wet conditions (in environmental SEM), and at a wide range of cryogenic or elevated temperatures depending on different types of samples. The conductive or semiconductive materials  $\text{TiO}_2$  and  $\text{WO}_3$  can be imaged directly by SEM without a common preparation technique of coating to cover the sample with a several nanometer layer of conductive material (like gold or platinum) from a sputtering machine. It should also be mentioned that the sample of polymer–Au composite NFs might be damaged by the electron beam focusing for a long time on a small spot. The phases based on qualitative chemical analysis and/or crystalline structure and precise measurement of very small features and objects down to 50 nm in size can be identified by SEM. By using the backscattered electron detectors (BSED), the different phases of multiphase samples can be discriminated rapidly, such as distinguish the gold from the matrix of semiconductor or polymer. SEM measurements were conducted to determine the size and morphology of synthesized nanomaterials using FEI Quanta 250 Scanning Electron Microscope.

**Preparation of samples:**

All the samples tested by SEM were adhered on the surface of aluminum support with carbon tape without any other treatments.

**Method of measuring the diameter of NFs and size of NPs:**

The main diameter of NFs and average size of NPs for each samples were determined from measurements of SEM images performed on 100 filaments or particles using the software Nano Measurer.

### ***3.1.2 High Resolution Transmission Electron Microscopy (HR–TEM)***

High–resolution transmission electron microscopy (HR–TEM) is a powerful technique to study properties of materials on the atomic scale and allow for direct imaging of the atomic structure of the sample, such as semiconductors, metals, nanoparticles [154]. HR–TEM is often used to refer to high resolution scanning TEM, mostly in high angle annular dark field mode and also referred to as phase contrast TEM for disambiguation. The individual atoms of a crystal and its defects can be resolved with high resolution at small scales. The image formation relies on phase contrast, which is not necessarily intuitively interpretable, as the

image is influenced by aberrations of the imaging lenses in the microscope. The diffraction patterns of HR-TEM images are also very useful for studying the nanocrystalline phases and nanoceramics. The instrument used in the experiment is JEOL, 2100F with an accelerating voltage of 200 kV.

***Preparation of samples:***

Each sample with a small amount was dispersed in EtOH by using ultrasonic processor (hielscher, UP400S) to get a transparent homogenous solution and then deposited on the Cu grid drop by drop.

### **3.2 Physico-chemical characterizations**

All the physico-chemical characterizations were tested in Laboratory of Multimaterials and Interfaces (LMI) at University of Claude Bernard Lyon 1 (UCBL), including Thermogravimetric Analysis (TGA), Fourier Transform – Infrared Spectroscopy (FT-IR), Ultraviolet – Visible Spectroscopy (UV-Vis), X-ray Powder Diffraction (XRD), Nitrogen adsorption-desorption isotherms (BET), Inductively Coupled Plasma – Optical Emission Spectroscopy (ICP-OES).

#### ***3.2.1 Thermogravimetric Analysis (TGA)***

Thermogravimetric analysis (TGA) is a method of thermal analysis to measure the changes in physical and chemical properties of materials as a function of increasing temperature with constant heating rate, or as a function of time with constant temperature and/or constant mass loss. It is an especially useful technique for the study of various polymeric materials including thermoplastics, elastomers, composites, plastic films and fibers. TGA is commonly used to determine selected characteristics of materials that exhibit either mass loss or gain due to decomposition, oxidation, or loss of volatiles (such as moisture). The common applications of TGA including (a) materials characterization through analysis of characteristic decomposition patterns, (b) studies of degradation mechanisms and reaction kinetics, (c) determination of organic or inorganic content in a sample.

***Preparation of samples:***

TGA, in this work was performed with a Mettler Toledo Instruments TGA/SDTA 851<sup>e</sup> at

the platform of thermal analysis in LMI. Around 5 mg of samples (including as-spun NFs of PVP, PVA, PAN, PVP–Au–3:1, PVP–Au–6:1, and PVP–Ti–9:30) were heated at a heating rate of  $3^{\circ}\text{C}\cdot\text{min}^{-1}$  from 30 to  $800^{\circ}\text{C}$ , in a  $150\ \mu\text{L}$  alumina crucible, under air atmosphere ( $100\ \text{mL}\cdot\text{min}^{-1}$ ).

### 3.2.2 Fourier Transform – Infrared Spectroscopy (FT–IR)

Fourier transform infrared spectroscopy (FT–IR) is a powerful tool for *in situ* measurement of concentration, solubility, and super-saturation in crystallization processes for the chemical and pharmaceutical industries. This technique is obtained from performing a mathematical Fourier Transform on the interferogram. An FTIR spectrometer simultaneously collects high spectral resolution data over a wide spectral range to determine the molecular structure by analyzing the absorption frequency, at which chemical bonds vibrate in either a stretching or bending mode. This confers a significant advantage over a dispersive spectrometer which measures intensity over a narrow range of wavelengths at a time.

#### Preparation of samples:

Fourier transform infrared spectroscopy (FT–IR, SAFAS, IR 700) were recorded on a spectrometer by using the model of attenuated total reflection (ATR) with the mats of all the samples annealing at different temperatures (including as-spun PVP–EtOH, PVP–Au–200, PVP–Au–300, PVP–Au–400, and PVP–Au–500) directly from  $4000$  to  $600\ \text{cm}^{-1}$  at room temperature with a step of  $2\ \text{cm}^{-1}$ .

### 3.2.3 X-ray Powder Diffraction (XRD)

X-ray powder diffraction (XRD) is a rapid and common analytical technique primarily used for phase identification of a crystalline material. It is based on constructive interference of monochromatic X-rays and a crystalline sample, which can provide valuable information about the crystalline phase and average crystallite size. The analyzed material is finely ground, homogenized, and average bulk composition is determined. The X-rays diffraction of a crystal can be formulated by means of Bragg's law:

$$2d\sin\theta=n\lambda$$

where  $d$  is the  $d$ =spacing, perpendicular distance between pairs of adjacent planes in the

crystal,  $\theta$  is the incident angle,  $n$  is the layer of planes, and  $\lambda$  is the wavelength of the  $X$ -rays. This law relates the wavelength of electromagnetic radiation to the diffraction angle and the lattice spacing in a crystalline sample. These diffracted  $X$ -rays are then detected, processed and counted. By scanning the sample through a range of  $2\theta$  angles, all possible diffraction directions of the lattice should be attained due to the random orientation of the powdered material.

XRD was performed utilizing a Phillips PANalytical X'Pert PRO instrument with a PW 3040/60 type of generator and a X'celerator type of detector (employing Cu  $K\alpha$  1  $\lambda=1.54056$  Å radiation with a power of 45 kV–30 mA for the crystalline analysis). The broad-scan analysis was typically conducted within the  $2\theta$  range from  $10^\circ$  to  $120^\circ$ . The average size of the metallic oxide ( $TiO_2$ ,  $WO_3$ ) and gold nanocrystalline was determined by the strongest peak using Scherrer's equation, where  $D$  is the average nanocrystalline size (nm),  $\lambda$  is the  $X$ -rays wavelength (1.54056 Å),  $\beta$  is the full-width at half-maximum (FWHM) intensity (in radians), and  $\theta$  is the half of the diffraction peak angle [156].

$$D=0.9 \lambda / \beta \cos \theta$$

#### **Preparation of samples:**

For the samples, which can keep the physical morphology to be an entire piece, taking a piece (around  $1 \text{ cm}^2$ ) to adhere on the surface of monocrystalline silicon substrate by a double-sided adhesive, including the samples of as-spun polymer NFs, polymer–Au, PVP–TTIP, PVP–TTIP–Au, polymer–AMT, and polymer–AMT–Au. For the samples which are brittle that is hard to keep an entire piece, a monocrystalline silicon substrate with a shallow groove is used to contain the grinded sample, in order to have a flat and smooth face for testing.

#### **3.2.4 Nitrogen adsorption–desorption isotherms (BET)**

The surface area, pore volume and the pore size distribution of the as-prepared aerogels and oxides can be obtained by nitrogen ( $N_2$ ) adsorption–desorption isotherms. Adsorption on porous materials includes the monolayer adsorption followed by multilayer adsorption and capillary condensation [157]. Brunauer–Emmett–Teller (BET) theory refers to multilayer adsorption and aims to explain the physical adsorption of gas molecules on a solid surface and serves as the basis for an important analysis technique for the measurement of the specific surface area of a material. It usually adopts non-corrosive gases (like  $N_2$ , Ar,  $CO_2$  etc.) as

adsorbents to determine the surface area data. N<sub>2</sub> adsorption–desorption isotherms for semiconductor oxide NFs were determined using a sorptomatic system (Thermo Electron Corporation). The specific surface area of powdered samples was estimated by applying the BET equation in the  $0.05 \leq P/P_0 \leq 0.35$  intervals of relative pressure and using a value of  $16.2 \text{ \AA}^2$  for the cross–sectional area of molecular N<sub>2</sub>. A non–linear regression by the least–squares method was performed to fit the interval data (nads vs. P/P<sub>0</sub>) in the experimental isotherms. WO<sub>3</sub> NFs obtained from different polymers have been tested by N<sub>2</sub> adsorption–desorption isotherms and their surface areas have been estimated by BET equation.

### ***3.2.5 Inductively Coupled Plasma – Optical Emission Spectroscopy (ICP–OES)***

Inductively coupled plasma–optical emission spectrometry (ICP–OES) is a flame analytical technique with a flame temperature in a range from 6000 to 10000 K, which uses the inductively coupled plasma to produce excited atoms and ions that emit electromagnetic radiation at wavelengths characteristic of a particular element, so it is used for the detection of trace metals. The technique is also a solution technique, and is employed standard silicate dissolution methods [158]. The intensity of this emission is indicative of the concentration of the element within the sample. The Au contents of different TiO<sub>2</sub>–Au and WO<sub>3</sub>–Au samples were determined by inductively coupled plasma optical emission spectrometry (ICP–OES, Varian, Vista–MPX).

#### **Preparation of samples:**

Firstly, using several drop of the fresh aqua regia which is the mixture of nitric acid and hydrochloric acid with the ratio of 1:3 (HNO<sub>3</sub>+3HCl) to dissolve the Au in the samples, and then diluted with water for testing.

## **4 Performance measurement systems**

All the gas sensing performance and the most part of photocatalysis performance were tested in the Lab of Simulation and Modelling of Particulate Systems (Simpas) at University of New South Wales, Australia. A part of photocatalysis performance was tested in Laboratory of Multimaterials and Interfaces (LMI) at University of Claude Bernard Lyon 1 (UCBL).

## 4.1 Photocatalysis performance measurement system

### 4.1.1 Photocatalytic measurement system

The photocatalytic activities of the samples were determined by measuring the decolorization of methyl blue (MB) under UV irradiation in a batch reaction. In the lab of Simpas, the reactor volume is 500 mL. A 150 W UVA light was set in the center of the reactor; the luminance of the light source over the reactant solution was  $0.7 \text{ W}\cdot\text{cm}^{-2}$  and the total irradiation time was 1 h. A 100 mL solution of 30 ppm dyes was injected into the reaction system, while 20 mg of the photocatalyst was added with well dispersed by ultrasonic. In LMI, a rectangular quartz groove with the volume of 5 mL is used as the reactor. The lamps with different wavelength of 360 nm and 528 nm were used and set in front of the reactor. Each time 1 mL solution of 30 ppm dyes with the same concentration of photocatalyst was injected into the reaction system. After decolorization, the supernatant of the solution was obtained via centrifugation and then characterized by UV–vis spectroscopy.

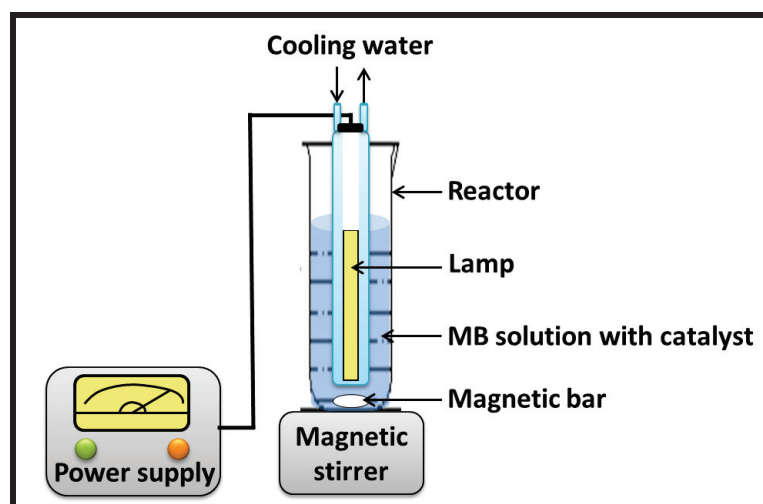


Figure 2.7 Schematic of Photocatalysis performance measurement system

### 4.1.2 Ultraviolet – Visible Spectroscopy (UV–Vis)

Ultraviolet–visible spectroscopy (UV–Vis) refers to absorption spectroscopy or reflectance spectroscopy in the ultraviolet–visible spectral region. It uses light in the visible and adjacent (near–UV and near–infrared) ranges and is relatively straightforward. The absorption or reflectance in the visible range directly affects the perceived color of the chemicals involved. In this region of the electromagnetic spectrum, molecules undergo electronic transitions. Absorption may be presented as transmittance ( $T = I / I_0$ ) or absorbance ( $A = \log I_0 / I$ ).  $I_0$  is the intensity of the reference beam, which should have suffered little or no

light absorption, and  $I$  is the intensity of the sample beam. Over a short period of time, the spectrometer automatically scans all the component wavelengths in the manner described. If no absorption has occurred,  $T = 1.0$  and  $A = 0$ . Most spectrometers display absorbance on the vertical axis, and the commonly observed range is from 0 (100% transmittance) to 2 (1% transmittance). The ultraviolet (UV) region scanned is normally from 200 to 400 nm, and the visible portion is from 400 to 800 nm. The Beer-Lambert law forms the mathematical physical basis for the light absorption measurements on gas and in solution. According to this law, Molar absorptivity ( $\epsilon$ ) is defined as:  $\epsilon = A / lc$ , where  $A$  is the absorbance,  $c$  the concentration of the absorbing substance, and  $l$  is the path length) [159].

### **Preparation of samples:**

The instrument used in the experiment is UV-Vis, SAFAS, Monaco, UV mc<sup>2</sup>, registered from 300 nm to 1000 nm with the spectrophotometer interval is 2 nm and integration time is 0.1s. For the powder samples (like TiO<sub>2</sub> NFs obtained with different concentration or temperatures and TiO<sub>2</sub>-Au NFs prepared from first route of volume inclusion (i)), we use ultrasonic processor (hielscher, UP400S) to disperse powder with the weight around 10 mg homogenous in 10 ml dioxide water and then for testing by suitable dilution times. For the solution samples, like the experimental solution of MB-catalysts after the photocatalytic process, using the centrifuge (Eppendorf, 5810) to separate the catalysts from the solution and then tested the supernatant by suitable dilution times.

## **4.2 Gas-sensing performance measurement system**

### ***4.2.1 Gas-sensing measurement system***

As shown in Figure 2.8, the preparation processes of gas sensors were as follows: (1) in Figure 2.8 a, the sample of composite NFs was mixed with the binder (polyvinylidene fluoride (PVDF)), and then be grinded homogenously in an agate mortar; (2) adding some drops of the solvent (1-methyl-2-pyrrolidone) to the agate mortar to form a slurry; (3) the slurry was subsequently coated on an alumina ceramic tube, the tube was with a pair of Au electrodes and four Pt wires for resistance measurements (as shown in Figure 2.8 b); (4) the alumina ceramic tube was annealed in air at 350 °C for 3 h to remove the organic binder and to improve the stability of the sensor; (5) Prior to the test, a Ni-Cr resistor was inserted into

the ceramic tube as a heater (Figure 2.8 c), which allows for the control of the working temperature by adjusting the heating voltage; (6) A reference resistor was placed in series with the sensor to form a complete measurement circuit (seen in Figure 2.8 d). (7) The test gas was injected into the testing chamber using a micro-syringe as shown in Figure 2.8 e. Figure 2.8 f was the gas-sensing measurement system connected to a computer for data collection. The schematic of sensor and gas-sensing measurements system was shown in Figure 2.9 in details.

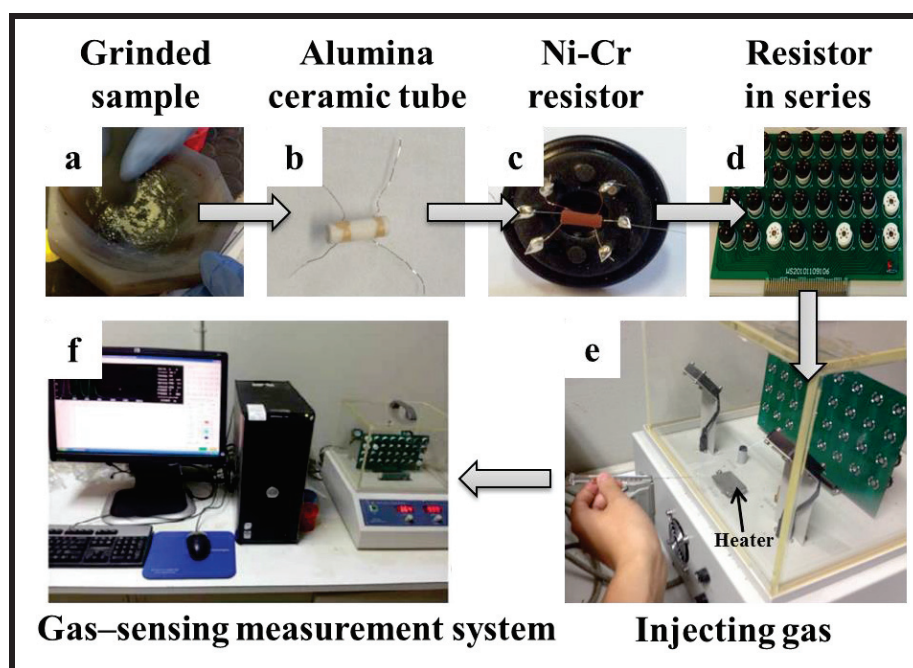


Figure 2.8 the sensor prepared process and gas-sensing measurement system.

#### 4.2.2 Gas-sensing performance characteristics

The response ( $S$ ) of the sensor is defined as  $S = R_{\text{air}} / R_{\text{gas}}$ , the ratio of the electrical resistances measured in air ( $R_{\text{air}}$ ) and in the tested gas atmosphere ( $R_{\text{gas}}$ ). The gas-sensing performance of  $\text{WO}_3$  and  $\text{WO}_3\text{-Au}$  composites NFs were tested using a commercial WS-30A gas-sensing measurement system (Zhengzhou Winsen Electronics Technology Co., Ltd., Zhengzhou, China), at a relative humidity of 50~65%. The response time ( $\tau_{\text{res}}$ ) is defined as the time required by the sensor to achieve 90% of its maximum response after the gas injection, whereas the recovery time ( $\tau_{\text{rec}}$ ) is the time taken by the sensor to reach 10% of its initial resistance after removal of the gas.

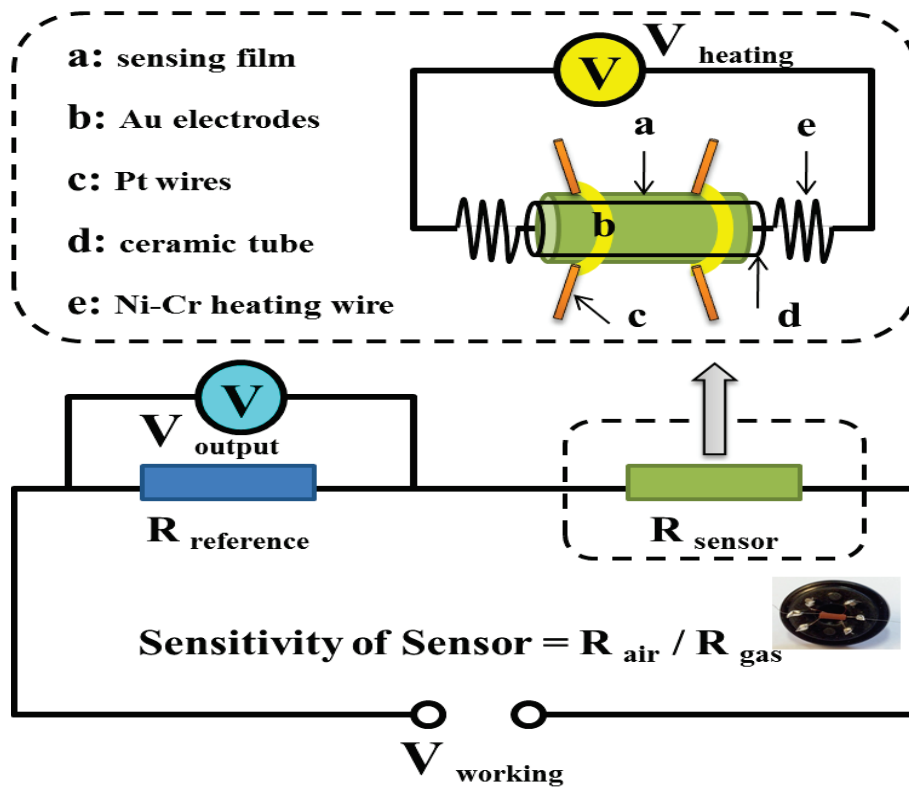


Figure 2.9 Schematic giving more details about the sensing part of the detector (part c of Figure 2.8)



## **CHAPTER III STUDY AND OPTIMIZATION OF THE FABRICATING CONDITIONS OF GOLD-CONTAINING NANOFIBERS**

### **1 Introduction**

In this chapter, the screening of the fabricating conditions for Au-containing NFs has been studied. It is important and necessary to understand the properties of polymer-Au composite NFs in order to fabricate HMMOC NFs. The polymer-Au composite NFs starting with Au ions have been fabricated by two Au-introduction routes: volume inclusion and surface deposition. These two routes are investigated in section 2 “volume inclusion” and section 3 “surface deposition”, respectively. The thermal behavior is a key point for polymer-Au composite NFs and has been investigated. The influences of experimental parameters have been studied, including the different starting polymers, calcination conditions, and Au introducing routes with different concentrations, deposition times, and reduction methods. Subsequent thermal treatments with different temperatures have been investigated to optimize this experimental procedure. The morphology and composition of polymer-Au composite NFs are also described. The thermal decompositions, morphologies and structures of  $\text{HAuCl}_4/\text{PVP}$  composite NFs and resulting Au NFs obtained from thermal treatment have been studied and discussed by electron microscopy, thermal analysis and spectroscopies.

### **2 Volume inclusion**

Volume inclusion (i) is the route to dissolve Au ions in the ES solution directly, followed with ES and thermal treatment to obtain the composite NFs. Since Au ions are mixed directly with the precursor solution, the final Au NPs are dispersed in the volume of the resulting filaments, thus defined as a volume inclusion. The first part will help to choose the suitable polymer and solvent to fabricate composite NFs which corresponding thermal behavior will be studied considering the influence of the furnace atmosphere.

#### **2.1 Study of different starting polymers**

### 2.1.1 Basic information for electrospinning conditions

A short screening was performed with three different polymers: PVP, PVA, and PAN by using volume inclusion by ES. Those polymers were chosen because they are easy to electrospin and soluble in the same solvent as Au ions. As the final target is to obtain hybrid oxide NFs, heat treatments were conducted under air.

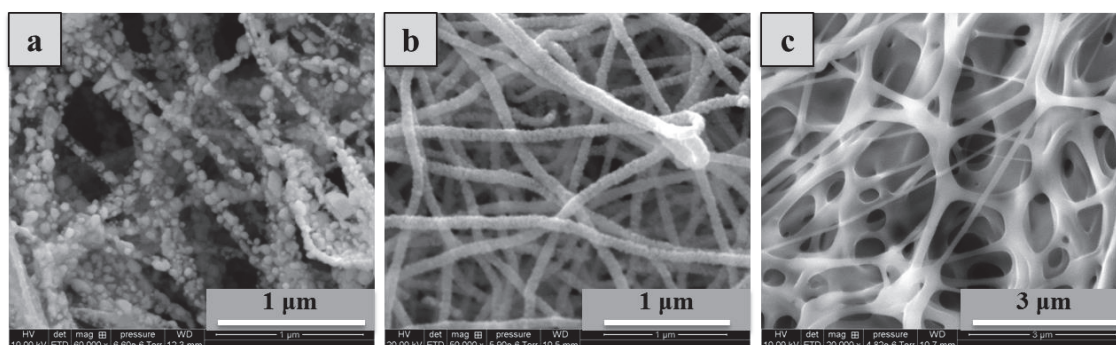


**Figure 3.1** SEM images of PVP-Au composite NFs fabricated with different Au contents by volume inclusion with ES and calcined at 500°C in air for 2h: (a) PVP-Au-3:1; (b) PVP-Au-6:1; (c) PVP-Au-9:1.

Adding Au precursor into the ES solution has several impact factors such as the dissolving contents of Au and the influence of solution spinnability. For different polymers, the maximum dissolving contents of Au precursor are different. If the Au content is too high, it is hard to get a homogenously and spinnable solution in order to obtain NFs by ES. If the Au content is too low, the final sample after calcination cannot keep the fiber morphology. As we tested the sample of PVP-Au-3:1, PVP-Au-6:1, and PVP-Au-9:1, the samples have different morphologies after calcination in air as shown in Figure 3.1. For sample PVP-Au-3:1, it contains the highest Au content which could dissolve in the PVP-EtOH ES solution, the final results after calcination contains large particles and blocks among the fibers as shown in Figure 3.1a. As reducing the Au content to PVP-Au-6:1, the sample keep the fiber morphology as shown in Figure 3.1b. Keep decreasing the Au content to PVP-Au-9:1 shown in Figure 3.1c, the sample changed so as to the fiber adhered to each other and form large holes. So for each polymer with several tested experiment, we found the suitable and fixed Au content for ES, the weight ratios between the polymer and Au precursor are 6:1, 10:1, and 10:1 for PVP, PVA, and PAN, respectively. The optimized ES conditions for these three different polymers containing Au ions are fixed as 6.5 kV, 10 cm, 0.6 mL·h<sup>-1</sup> for PVP-Au; 12 kV, 10 cm, 0.1 mL·h<sup>-1</sup> for PVA-Au; and 8 kV, 10 cm, 0.6 mL·h<sup>-1</sup> for PAN-Au, respectively.

### 2.1.2 The influence of different polymer

As shown in Figure 3.2, the polymer-Au composite NFs were calcined at 200°C, and this temperature was high enough to reduce Au ions and form Au NPs. All the polymer-Au composite NFs were obtained with reduced Au and present remaining fiber morphology. In Figure 3.2a, the sample of PVP-Au, we can see bright dots which should be related to Au NPs located homogeneously in polymer NFs with a uniform size around 10 nm by image analysis of several high magnification SEM images with software of Nano measurer. For starting polymer of PVA shown in Figure 3.2b, the polymer also contained some reduced Au nanostructures, not only Au NPs, but also some larger triangles with edges of 265 nm measured by the same way of image analysis. The dispersed Au NPs in PVA-Au were less homogenous than in PVP-Au. Figure 3.2c shows the sample of PAN-Au, the Au NPs were more inserted on the surface of polymer matrix. According to the results of different starting polymers, the Au NPs were formed by *in situ* reduction in air below 200°C. Based on these observations, PVP seems to be the most suitable polymer to obtain the polymer-Au composite NFs with uniform size of Au NPs around 10 nm.

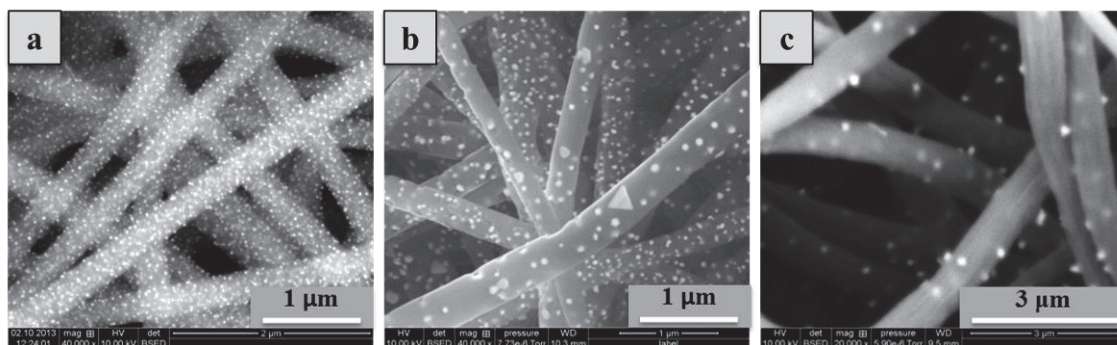
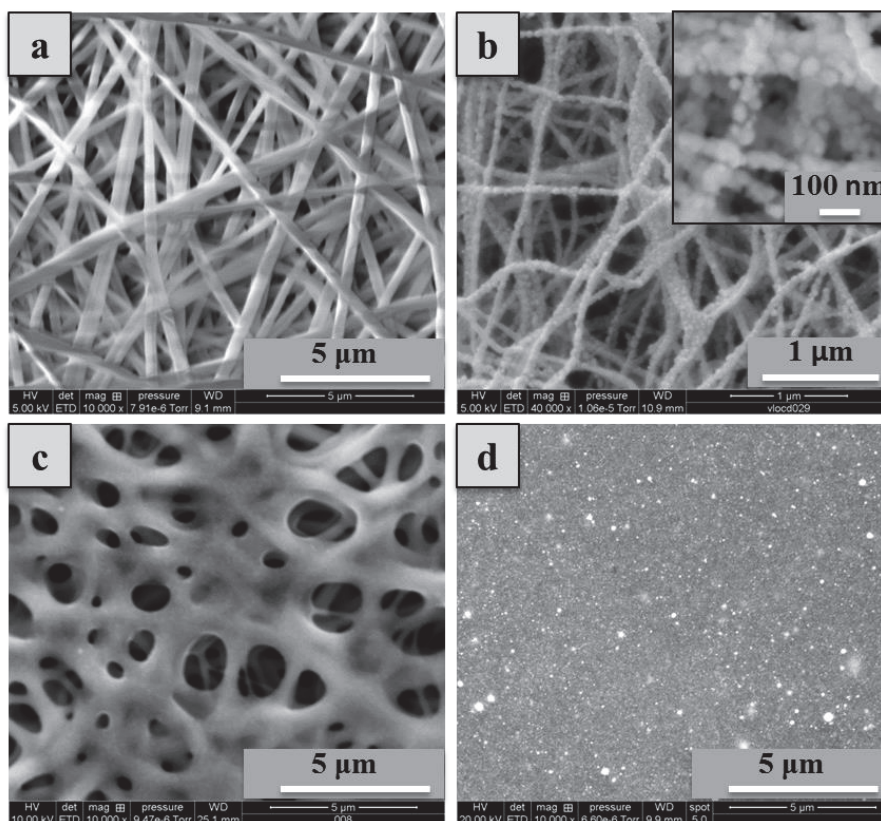


Figure 3.2 SEM images of polymer-Au composite NFs fabricated with different starting polymers by Direct ES and calcined at 200°C in air for 2h, respectively: (a) PVP-Au; (b) PVA-Au; (c) PAN-Au.

In the following parts, all the samples called PVP-Au are fixed with Au contents of 6:1, in order to keep the influence of polymer and Au concentration as a constant factor, and then to study the thermal behavior of PVP-Au composite NFs calcination in different atmospheres and temperatures, which will discuss in section 2.2.

## 2.2 Thermal behaviour of PVP-Au nanofibers

Compared to the previous part, three kinds of annealing atmosphere were studied to observe the influence of either oxidizing or reducing conditions on PVP-Au samples. Subsequent thermal treatment at 500°C for 2h in different atmospheres including air, Ar-H<sub>2</sub>, and H<sub>2</sub> are then performed. As shown in Figure 3.3a, the as-spun PVP-Au samples have fiber morphology with smooth surface. This sample (shown in Figure 3.3b) was heated in air. It still kept the fiber morphology with roughness surface, as shown in the insert of Figure 3.3b, composed of particles. When the calcination was performed under Ar-H<sub>2</sub>, the sample morphology changed from filaments to interconnected and flattened structures rendering the sample much less flexible than after treatment under air (Figure 3.3c). The Au ions were reduced by *in situ* reduction of the Au precursor and the reduction from H<sub>2</sub>. When the atmosphere changed into pure H<sub>2</sub>, as shown in Figure 3.3d, the fibers totally destroyed, leading to the formation of a containing Au NPs. A better understanding of these behaviors is possible with thermal analysis of the filaments under the corresponding atmospheres.



**Figure 3.3** SEM images of as spun PVP-Au composite NFs fabricated by volume inclusion and then heated in different atmospheres at 500°C for 2 h: (a) as-spun; (b) air (high resolution in insert); (c) Ar-H<sub>2</sub>; (d) H<sub>2</sub>.

In order to further understand the thermal behavior of our sample during the whole heat treatment, pure PVP NFs and PVP-Au NFs were analyzed by TGA and DTG (as shown in Figure 3.4). For both samples, four weight loss stages could be observed in the TG curves. For pure PVP NFs, a 10.92% weight loss is observed at the first stage below 190°C, which corresponds to the solvent and adsorbed water evaporation. From 190°C to 360°C, a second stage with a weight loss of 15.86% is attributed to the degradation of -CH<sub>3</sub> side chain in PVP. As the temperature continues increasing, the pyrrolidone rings begin to decompose. The third stage occurred below 450°C, corresponding to the major weight loss (42.11%), which was possibly caused by the decomposition of PVP squeueleton [160]. Finally, during the last part of the heat treatment, the fourth stage occurred with 29.85% weight loss. All the C-H, C-C, C=C, and C-N bonds were broken, and the pure PVP polymer degraded completely into carbon oxide and nitrogen oxide compounds [160]. At this stage, only 1.09% of carbon remains. Above 650°C, there was no further weight loss, indicating the complete decomposition of pure PVP NFs and the final decomposition products are CO<sub>2</sub>, H<sub>2</sub>O, NH<sub>3</sub> [160].

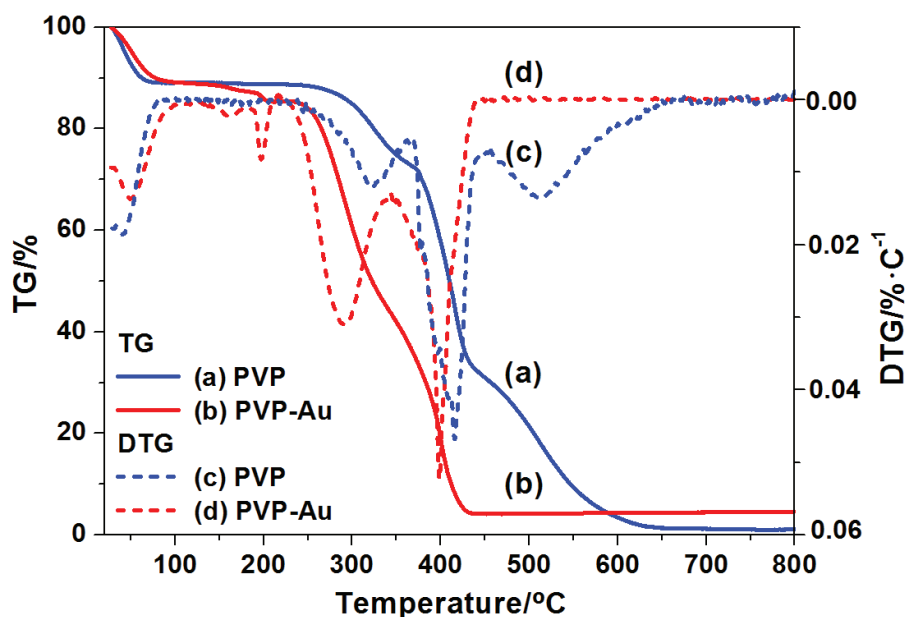


Figure 3.4 TGA of and DTG thermograms for pure PVP, PVP-Au precursor NFs.

The weight loss corresponding to the as-spun PVP-Au NFs seems to be similar to that of pure PVP but with a curve shifted to lower temperatures. The first weight loss of 12.62% appears below 180°C, which was almost the same as pure PVP NFs due to the evaporation of adsorbed moisture and solvent. A second stage, with a weight loss of 2.03% is assigned to the evolution of water initially contained in H<sub>2</sub>AuCl<sub>4</sub>·3H<sub>2</sub>O. As in case of pure PVP, the major

weight loss 41.69% is for the third stage, but appears at lower temperature (220-340°C) compared to pure PVP (360-450°C). The decomposition of PVP side chain increases the value of weight loss. The last stage occurs from 340-450°C with 36.56% of weight loss. The total decomposition finishes around 450°C, which is 200°C lower than for the pure PVP NFs (650°C). It indicates that the temperature that has to be reached to obtain the final product is decreased by adding  $\text{HAuCl}_4 \cdot 3\text{H}_2\text{O}$  to PVP polymer.

The thermal degradation data can be studied through the FT-IR absorption bands. Figure 3.5 shows the FT-IR spectra of PVP NFs, and PVP-Au as-spun NFs and heated at 200°C or 300°C under air. From spectra of PVP NFs (Figure 3.5a), the characteristic band at 1662  $\text{cm}^{-1}$  corresponds to the C=O stretching vibration of the pyrrolidone ring. Absorption peak located at 1288  $\text{cm}^{-1}$  is assigned as the stretching vibration of C-N. The band 1426  $\text{cm}^{-1}$  is attributed to C-H bending vibration. For the sample tested at 200°C, two small new peaks appear at 1772  $\text{cm}^{-1}$  and 696  $\text{cm}^{-1}$ , possibly due to the starting decomposition of PVP as discussed before with TGA.

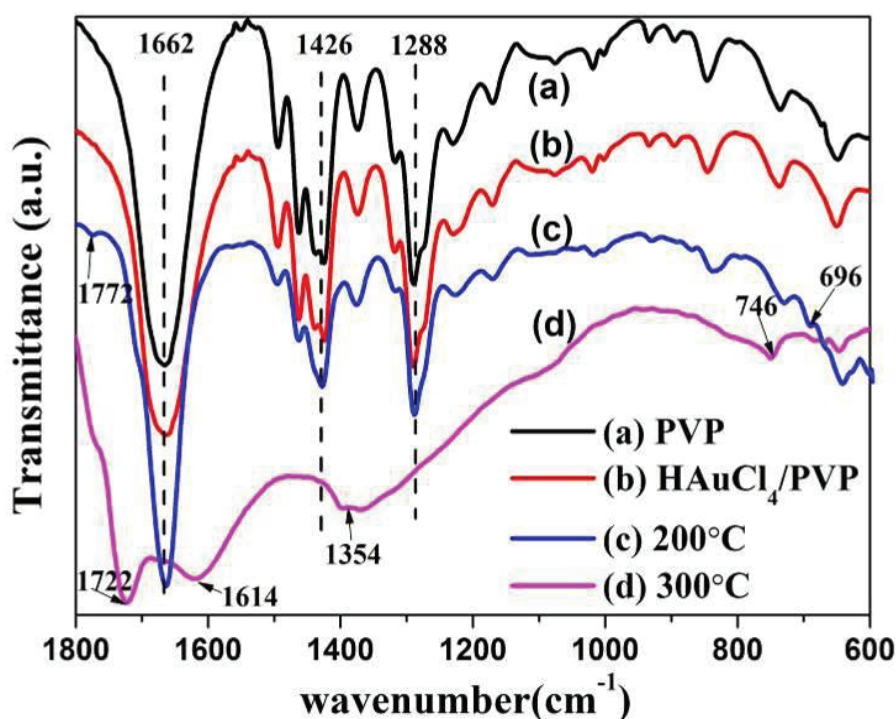


Figure 3.5 FT-IR spectra of (a) PVP NFs and (b) PVP-Au precursor NFs prepared at different calcination temperatures: (c) 200°C; (d) 300°C; Calcination was performed in air.

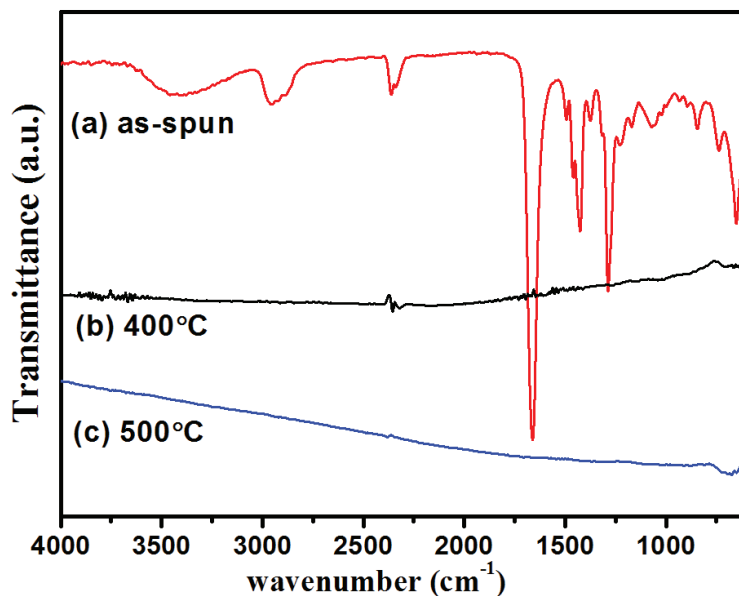


Figure 3.6 FT-IR spectra of PVP-Au precursor NFs prepared at different calcination temperatures: (a) as spun; (b) 400°C; (c) 500°C; Calcination was performed under air.

When the temperature rises to 300°C (Figure 3.5d), the characteristic peaks of PVP disappear to new peaks located at 1722  $\text{cm}^{-1}$ , 1614  $\text{cm}^{-1}$ , 746  $\text{cm}^{-1}$  and 1354  $\text{cm}^{-1}$  corresponding to substituted amide and -CH- rocking, these chemical groups being generated during PVP decomposition. The FT-IR spectra of samples with thermal treatment over 400°C and 500°C as shown in Figure 3.6 do not clearly reveal the presence of any remaining organic groups. This result is consistent with the TGA curves discussed previously since the final weight loss is around 400°C.

### 2.3 Morphology and composition of PVP-Au nanofibers

It is well known that calcination temperature and time govern the crystallization degree which plays also a role *in fine* on the morphology of NFs. In our case, the annealing time was fixed at 2 h. The morphologies of as spun PVP-Au composite NFs and samples obtained from volume inclusion and with subsequent annealing at different temperatures were investigated by SEM (as shown in

Figure 3.7). The surface of as spun  $\text{HAuCl}_4/\text{PVP}$  composite NFs is smooth and continuous as the pure polymer NFs. After calcination at 200°C in air for 2 h, the sample surface becomes a little rough presenting bright dots at the surface observed using a back-scattered electrons detector (BSED) of the SEM.

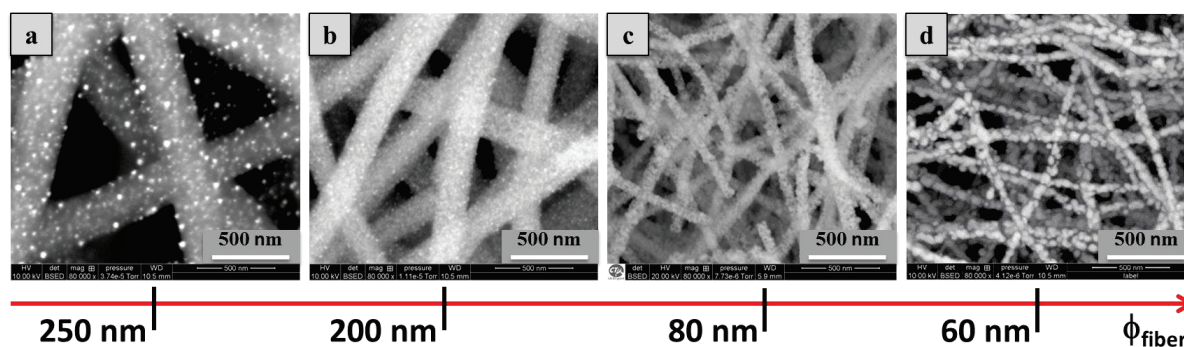


**Figure 3.7** SEM images of PVP-Au composite NFs fabricated by volume inclusion (i) and then heat treated in air at different temperatures for 2 h: (a) 200°C; (b) 300°C; (c) 400°C; (d) 500°C

When the temperature rises to 300°C (as shown in

Figure 3.7b), small bright dots seem to cover the whole NFs surface leading to the idea that a larger amount of Au is available at the surface than after treatment at 200°C. At this point, the PVP polymer has already started to decompose (see Figure 3.4). This is consistent with a diameter of the filaments diminishing by increasing the calcining temperature. This phenomenon continues after calcination at 400°C (

Figure 3.7c) since almost all the organic parts should be removed from the NFs at this temperature. The consequence is that the sample is composed of filaments much smaller (diameter 3 times smaller than after treatment at 300°C), and porous. In order to complete the polymer removal, the annealing temperature is finally fixed at 500°C. By comparing

Figure 3.7c and

Figure 3.7d, NPs drastically grow between 400°C and 500°C and are still supported by the filaments, similarly to a “chaplet” structure. As thermal annealing temperature increased from room temperature to 500°C, the diameter of NFs decreased from 250 nm to 60 nm and the grain size of NPs showed substantial increased from small bright dots (several nanometers) to 30 nm crystallized size calculated by XRD results with Scherrer’s Formula at 500°C. The final diameter of the NFs is related to the NPs size resulting of calcination.

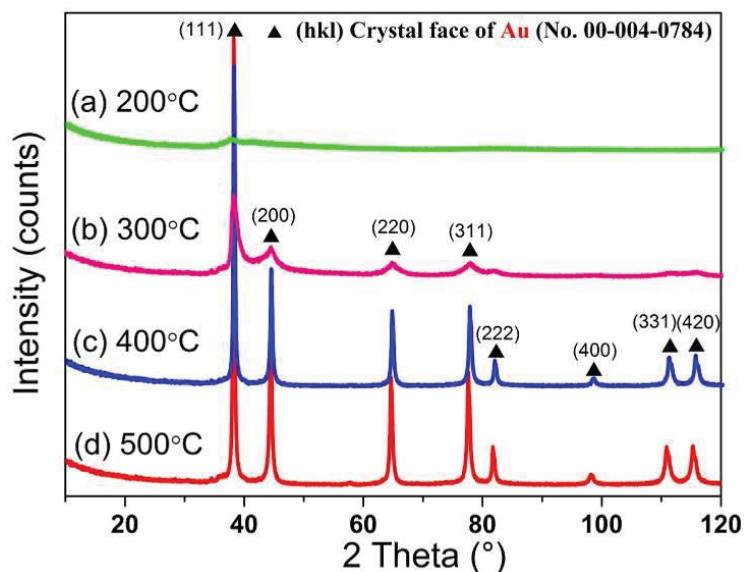
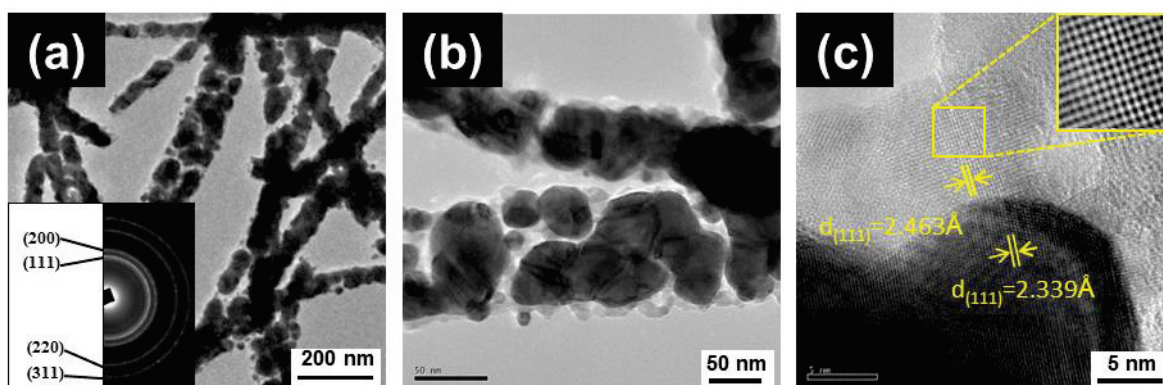


Figure 3.8 XRD patterns of as-spun PVP-Au composite NFs prepared at different calcination temperatures: (a) 200°C; (b) 300°C; (c) 400°C; (d) 500°C.

The crystal structures of as-spun PVP-Au composite NFs calcined at different temperatures were determined by XRD (Figure 3.8). All of the XRD patterns of PVP-Au precursor NFs after thermal treatment at different temperatures were investigated in  $10^{\circ}$ - $120^{\circ}$   $2\theta$  mode range. When the thermal treatment temperature was at 200°C (Figure 3.8a, there was no obviously diffraction peak, except a slight wide peak around  $38^{\circ}$ , which can be attributed to the reduction of Au ions to Au NPs in very small amount at low temperature (previously observed by SEM). At 300°C, four diffraction peaks at  $2\theta$  values of  $38.18^{\circ}$ ,  $44.39^{\circ}$ ,  $64.58^{\circ}$ ,  $81.72^{\circ}$  were observed, which correspond to (111), (200), (220), and (311) crystal planes of the face centered cubic (fcc) crystalline Au (JCPDS No. 00-004-0784), respectively. While increasing temperature to 400°C as shown in Figure 3.8c, the diffraction peaks become sharper and more intense, and four other peaks (indexed (222), (400), (311), and (420), respectively) appeared. The diffraction peak (111) is much stronger than the others, indicating that Au were mainly dominated by the crystal facet (111) and thus the growth direction was mostly oriented parallel to the [111] direction [161]. The average crystallite size ( $D$ ) of Au NPs is around 30 nm after heating at 500°C, which was estimated by full width half maximum (FWHM) of the main peak (111) from the Scherrer's Formula with XRD results [162].

To obtain a clear understanding of the crystallinity of Au NFs, high-resolution transmission electron microscopy (HR-TEM) and selected-area electron diffraction pattern (SAED) measurements of the Au NFs were carried out on few filaments of the sample at 500°C (Figure 3.9). The SAED pattern (inset of Figure 3.9a) shows very thin rings evidence a

polycrystalline orientation of NFs. Those rings are indexed according to the (111), (200), (220), and (311) reflections of face centered cubic (fcc) Au (JCPDS No. 00-004-0784). From the HR-TEM images, one can observe that Au NFs annealed at 500°C for 2 h in air consisted of nanocrystals with size distributions ranging from 5 to 30 nm as shown in Figure 3.9b. HR-TEM images show clearly that the NF is entirely poly-crystallized and the FFT (inset in Figure 3.9c) performed is a small area coniferous the classic plane of Au with the (111) planes. As a consequence, Au NFs with diameter around 60 nm and lengths of several hundred micrometers, composed of Au NPs, were obtained by annealing as-spun PVP-Au composite NFs at 500°C for 2 h in air.



**Figure 3.9** (a) HRTEM images of Au NFs prepared at 500°C in air for 2 h; (a-insert) SAED pattern of the Au NFs at 500°C; (b) HR-TEM image of Au NF at 500°C; (c) HR-TEM lattice images of Au NFs at 500°C.

For further understanding of the final Au NFs sample, semi-quantitative technique of EDS has been performed with SEM, and the results are shown in Figure 3.10. The main component of Au NFs is Au with 92.9%. There are some slight amounts of carbon (C) and oxygen (O) with 0.61% and 1.5% respectively, which might come from the carbon tape and absorption oxygen during the sample preparation for EDS. However, 4.99% of iron (Fe) is detected in the sample. Taking account of all the possible impurity source, the stainless needle used during the ES process is the most likely original source of Fe. Due to the corrosive property of gold chloride aqueous solution, the stainless steel needle is damaged, leading to introduction of iron impurities inside the as-spun PVP-Au composite NFs.

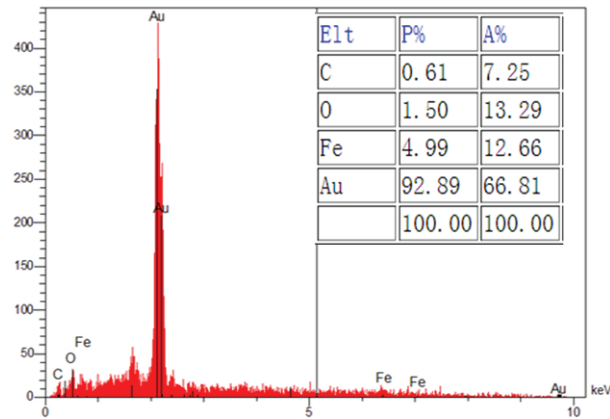


Figure 3.10 EDS spectrum of Au NFs obtained by calcined the volume inclusion (i) electrospun PVP-Au composite NFs in air at 500°C for 2 h and its elements compositions.

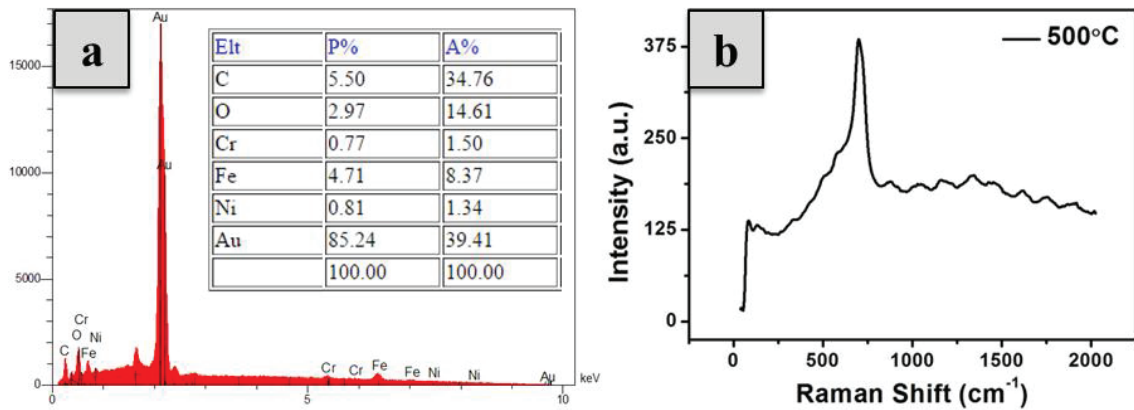


Figure 3.11 (a) EDS spectrum of sample obtained after 10 h electrospinning process and then calcined the as-spun PVP-Au composite NFs in air at 500°C for 2 h and its elements compositions; (b) Raman spectrum of Au NFs calcined at 500°C with stainless steel after ES process for 10 h.

In order to be sure about this point, a comparable experiment with stainless steel needle was performed with different continued ES time for 2h and 10h, respectively. Increasing the experiment time is considered to have sufficient reaction time for enlarging the influence of corrosion by gold chloride aqueous solution to the stainless steel needle. In this case, the final composition of the sample can be obviously identified.

In order to figure out this phenomenon, the sample with 10 h electrospun process has been prepared and followed with the exactly same procedure of calcination and checked by EDS. Increasing the time of ES process is to obtain the as-spun PVP-Au composite NFs that the ES solution of gold chloride aqueous solution reacted sufficiently with the stainless needle to increase the impurity amount. The result is shown in EDS spectrum of

Figure 3.11a, where the basic elements of stainless such as iron (Fe), nickel (Ni), and

chromium (Cr) have been found with 4.71%, 0.81%, and 0.77%, respectively. The Raman spectrum of the same sample is shown in

Figure 3.11 b. There is a sharp peak located at around  $700\text{ cm}^{-1}$ , which can be attributed to the oxide form of  $\text{Fe}_2\text{O}_3$ ,  $\text{NiO}$ ,  $\text{Cr}_2\text{O}_3$ , and  $\text{FeOOH}$  ( $\text{Fe}_x\text{Cr}_{1-x}$ ) $_2\text{O}_3$  impurities. To solve this problem of impurity, a designed spinning nozzle using an inert Pt wire inserted through a plastic tube was used to perform the new tests of spinning, instead of the stainless needle (Figure 3.12).

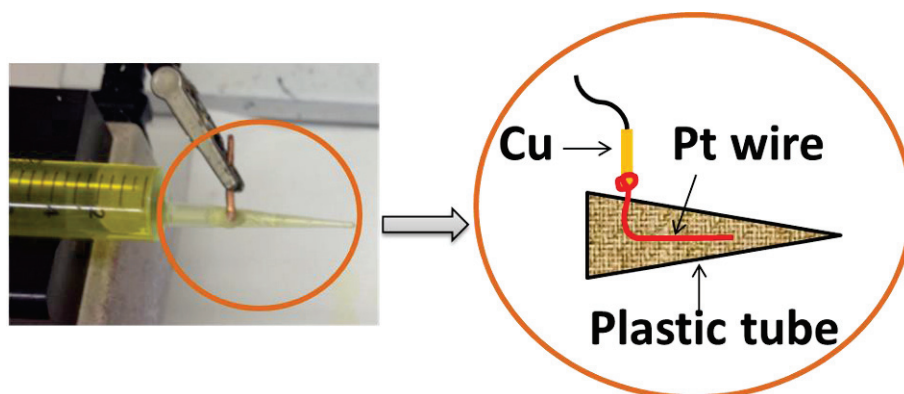


Figure 3.12 Schematic of the designed spinning nozzle using an inert Pt wire inserted through a plastic tube.

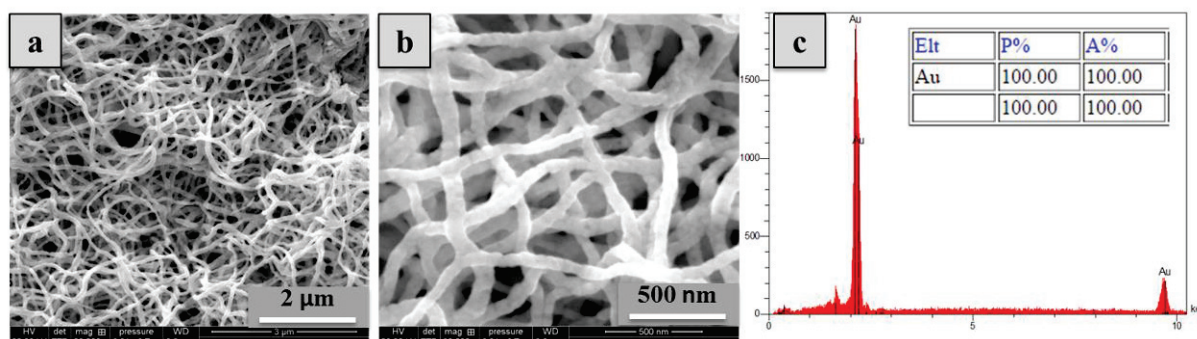


Figure 3.13 The SEM images and EDS spectrum of Au NFs fabricated with Pt wire calcined in air at  $500^\circ\text{C}$  for 2 h.

The final sample fabricated with Pt wire and followed with the same calcination process has been investigated by SEM and EDS (as shown in

Figure 3.13). Compared to the sample obtained with the stainless needle (discussed before in

Figure 3.7d), the Au NFs obtained with the new nozzle are more curved and seem to be attached to each other. According to the EDS result, there are no more impurities. This route leads to pure electrospun Au NFs.

## 2.4 Gold nanoparticles formation with temperature

By removing cationic impurities, the PVP-Au thermal decomposition is thus similar to that of pure PVP (as shown in Figure 3.14). By comparing the two SDTA curves, it seems that Au salt is responsible of the presence of three endothermal peaks, the first one being peaked at 75°C, a small one around 150°C and another one around 220°C. According to a study of the thermal behavior of  $\text{HAuCl}_4$  performed in 2014, Otto *et al.* have followed the thermal decomposition of  $\text{HAuCl}_4 \cdot 3\text{H}_2\text{O}$  and attributed the first peak to the salt melting, and the two last peaks to the first and the second decomposition steps of the Au salt [163].

The authors proposed the following reactions:

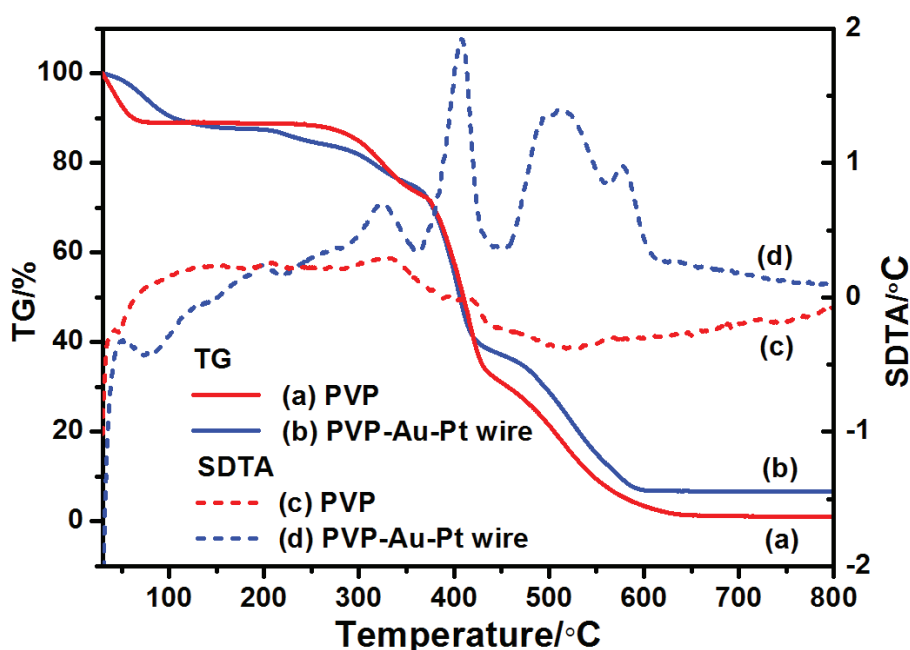
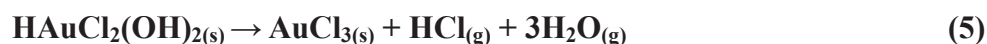
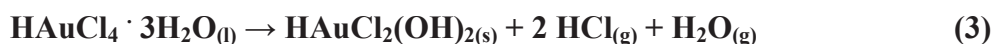


Figure 3.14 TGA and SDTA of pure PVP NFs and PVP-Au Pt-wire NFs.

The authors mentioned that the final decomposition lasts up to 320°C, but in the sample synthesized during our work, chlorine is not detected anymore by EDS after 2h of treatment at 200°C under air (as shown in Figure 3.15). Moreover, Au NPs are already formed at 200°C and seem to be present in a large part of the filament volume. The complete reduction of Au can be thus achieved at 200°C, we can wonder if this phenomenon is facilitated by a high mobility of the ions inside the PVP matrix (filament), and the presence of the exothermal phenomenon measured for PVP around 175°C that could produce a local heating enhancing Au reduction and lead to NPs [164]. It has been demonstrated here that it is possible to use the volume inclusion of Au as a reliable route to prepare Au NFs with the PVP polymer. This route will be useful for further studies using inorganic precursors soluble in the same solvents as PVP is, like ethanol for instance.

The following part is dealing with a “surface deposition” of Au. This route should be very interesting for precursors which are not soluble in alcohols, and to maximize the amount of Au available at the filament surface if the targeted applications are directly linked to the surface properties of the composite materials.

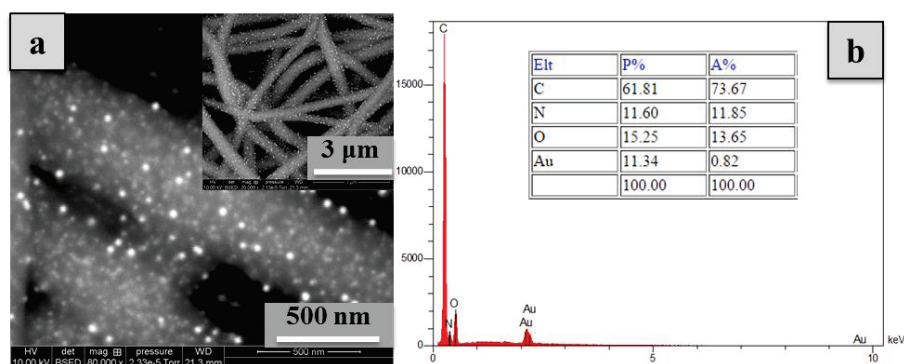


Figure 3.15 SEM image of PVP-Au NFs treated 2h under air at 200°C; Insert corresponds to a lower magnification.

### 3 Surface deposition

This route aims to deposit Au ions on the surface of as-spun polymer NFs and reduce Au subsequently to obtain the polymer-Au composite NFs. For this investigation, the Au concentration in the aqueous solution was fixed at 0.01M. As it was made for the “volume Au inclusion”, different polymers were tested before choosing the suitable one and solvent to fabricate the final composite NFs. Then, the thermal behavior will be discussed with the

stabilization temperature, TGA, and FT-IR results. Finally, the morphology and composition of the optimized samples are characterized.

### 3.1 Stability of different polymer nanofibers

Three different kinds of polymer NFs fabricated by ES with suitable solvent were studied. The Au salt was dissolved in H<sub>2</sub>O, EtOH, and DMF, respectively. Due to its natural property, PVP is completely dissolved in the three solutions. PVA NFs are partly dissolved with EtOH-Au and DMF-Au, while they cannot be stable with H<sub>2</sub>O-Au because of the high water solubility of PVA. Compared to these two kinds of NFs, PAN NFs show a higher stability in H<sub>2</sub>O-Au and in EtOH-Au solutions but, as expected, not in DMF-Au. After deposition of the Au solution on PAN NFs and followed with solvent evaporation at room temperature, the PAN mat keeps the same macroscopic shape as before checked by SEM, demonstrating that it is the best choice among these polymer NFs for surface deposition. As a consequence, the following parts about surface deposition are then focused on PAN NFs.

**Table 3.1 Stability of different polymer NFs in different solvents with Au ions.**

(×: completely dissolve; O: partly dissolve √: good stability)

	H <sub>2</sub> O-Au	EtOH-Au	DMF-Au
<b>PVP-EtOH</b>	×	×	×
<b>PVA-H<sub>2</sub>O</b>	×	O	O
<b>PAN-DMF</b>	√	√	×

### 3.2 Thermal behaviour of PAN-Au

The thermal behavior of pure PAN NFs was characterized by TGA (Figure 3.16). There are four weight loss steps for PAN NFs in air. The first step occurred below 180°C with the weight loss of 3.2% which is attributed to the release of absorbed solvent and moisture. From 180°C to 257°C, there is no obvious weight loss, and then PAN NFs start to degrade at 280°C. The SDTA curve exhibits a characteristic exothermic peak centered on 280°C which is attributed to cyclization reactions [134], which corresponds to the second weight loss, of 13.7% , between 257°C and 350°C. The main weight loss is the third step from 350°C to 700°C with 87.1% percentage weight loss, which was attributed to the volatilization of gaseous compounds in the oxidation and cyclization reactions. In this temperature range, the

PAN NFs decomposed dramatically. The last slightly weight loss with 0.6% occurred after 700°C, which can be assigned to a carbonization at higher temperature.

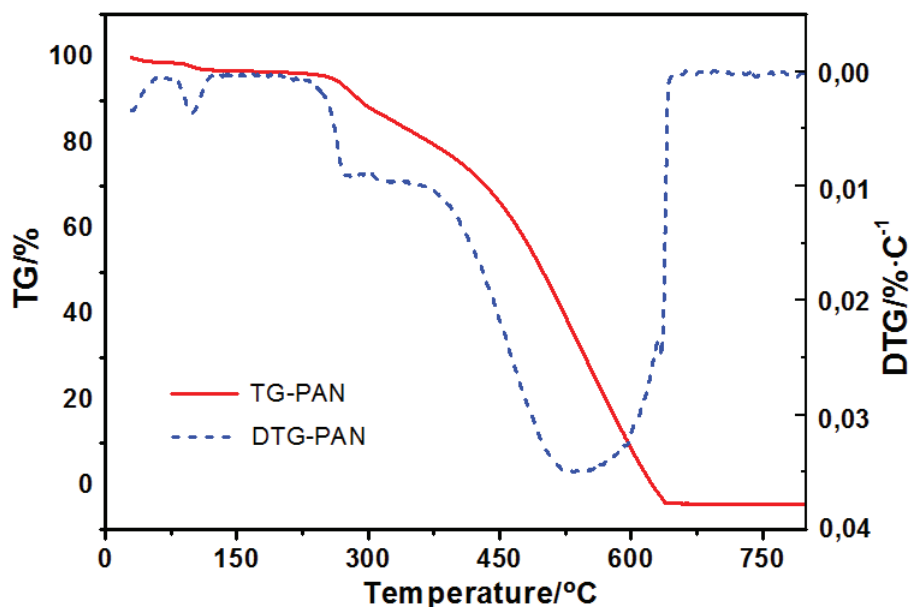


Figure 3.16 TGA and DTG thermograms (under air) for pure as-spun PAN NFs.

### 3.2.1 Stabilization temperatures

Figure 3.17 shows the effects of stabilization temperature on the chemical structure of as-spun PAN NFs treated 2h at different temperatures. The precursor as-spun PAN NFs displays characteristic vibrations at  $2926\text{ cm}^{-1}$  for  $\nu(\text{CH}_2)$ ,  $2244\text{ cm}^{-1}$  for  $\nu(\text{C}\equiv\text{N})$ ,  $1664\text{ cm}^{-1}$  for  $\nu(\text{C}=\text{O})$ , and  $1454\text{ cm}^{-1}$  for  $\delta(\text{CH}_2)$  as shown in Figure 3.17a. When the stabilization temperature is below  $150^\circ\text{C}$  (Figure 3.17b and Figure 3.17c), there is no significant difference between these curves. When the temperature rises  $200^\circ\text{C}$ , the peak at  $1454\text{ cm}^{-1}$  for  $\delta(\text{CH}_2)$  is reduced, as well as that at  $2244\text{ cm}^{-1}$  ( $\text{C}\equiv\text{N}$ ) to the detriment of new peaks at  $1378\text{ cm}^{-1}$ , and  $1591\text{ cm}^{-1}$  ( $\text{C}=\text{C}$ ,  $\text{C}=\text{N}$ ,  $\text{N}-\text{H}$  in the aromatic groups) corresponding to  $-\text{NH}$  bending combined with a  $-\text{CN}$  stretching vibration of the  $\text{C}(=\text{NH})-\text{NH}$ -group. In addition, the peak intensity of  $\text{C}\equiv\text{N}$  and is reduced. The formation of  $\text{C}-\text{O}$  ( $1590-1620\text{ cm}^{-1}$ ) and  $\text{C}=\text{O}$  ( $1730-1737\text{ cm}^{-1}$  and  $1170\text{ cm}^{-1}$ ) is also possible here and consistent with the reduction of the amount of nitrile groups, as previously reported [165]. Another band at  $804\text{ cm}^{-1}$  for  $\gamma(\text{C}=\text{C}-\text{H}$  in the aromatic rings) appeared. These chemical modifications are due to dehydrogenation and partial cyclization reactions in the stabilization stages. The stabilization temperature above  $200^\circ\text{C}$  leads to the disappearance of  $\text{C}\equiv\text{N}$  and  $\text{CH}_2$  groups, continuing to form new intermediates

leading to reactions of cyclization around 280-320°C. Even after treatment at 500°C (Figure 3.17h), two peaks located at 1594  $\text{cm}^{-1}$  and 1272  $\text{cm}^{-1}$  remain on the spectrum testifying the presence of organic compounds, thus a uncomplete PAN decomposition.

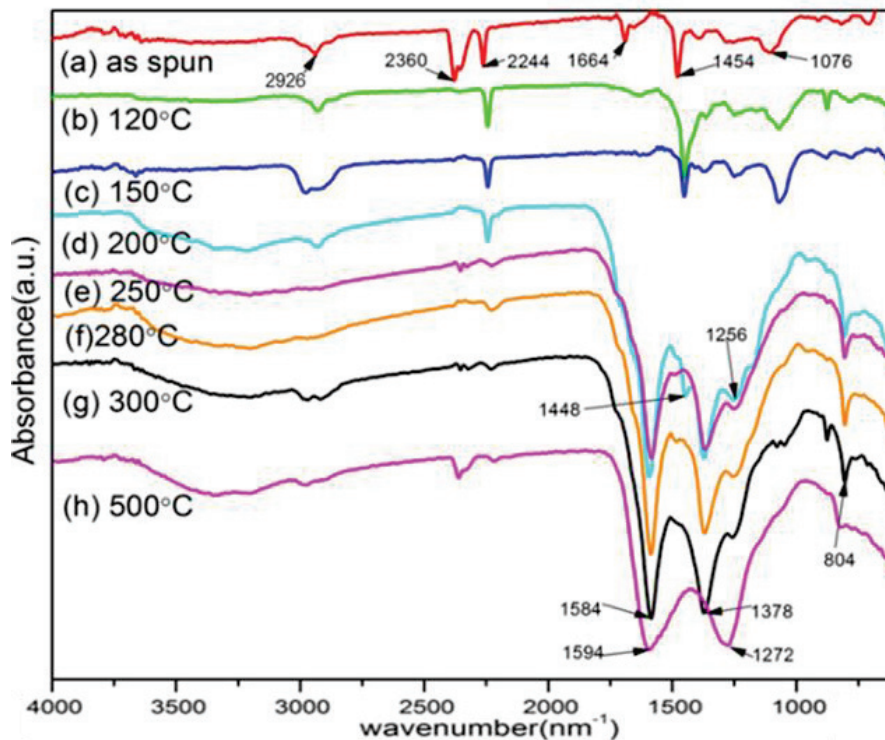


Figure 3.17 FT-IR spectra of as-spun PAN NFs stabilization at different temperatures: (a) as-spun; (b) 120°C; (c) 150°C; (d) 200°C; (e) 250°C; (f) 280°C; (g) 300°C; and (h) 500°C, respectively.

### 3.2.2 Au deposition on PAN nanofibers

This route aims to deposit Au on the surface of as-spun NFs and, as discussed before, taking into account the previous results, PAN NFs were stabilized under air at different temperatures, from 200 to 280°C, before Au deposition and treatment at 200°C to reduce  $\text{Au}^{3+}$  and  $\text{Au}^+$  ions into  $\text{Au}^0$  (Figure 3.18). By observing the filaments after reduction at 200°C, the filaments have a cylindrical shape, as before treatment, and support bright particles. A reduction at 200°C is enough to form Au NPs as observed in the previous part with the “volume inclusion” of Au.

The two differences we can notice between samples (Figure 3.18) are the following ones:

- (a) the filaments diameter decreases when the temperature rises;
- (b) the homogeneity in size and distribution of particles depends on the sample.

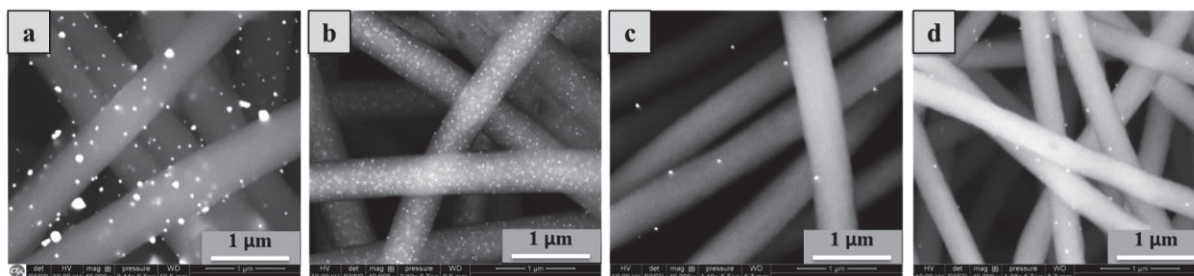


**Figure 3.18 SEM images of PAN-Au composite NFs obtained from Stabilization (ii) with different stabilization temperatures: (a) room temperature (not stabilized); (b) 200°C; (c) 250°C; (d) 280°C before deposition of 0.01M Au ions and a reduction at 200°C in air.**

Only the non-woven mat stabilized at 200°C presents very thin particles, with a narrow size distribution, and a high homogeneity of the particle distribution. Moreover, it seems that a non-negligible part of the particles is in the volume of filament not only on its surface (observation made possible by using SEM with a high voltage of 10 kV). Consequently, Au must diffuse easily to lead to this high homogeneity. We can wonder if the chemical groups (like carbonyl groups) formed after PAN stabilization at 200°C cannot play a favorable role by interacting with species like  $\text{AuCl}_3$  and/or  $\text{AuCl}$ , as a ligand could do (Figure 3.17). However, stabilization at higher temperature than 200°C does not enhance the good particle distribution. The only chemical difference between samples stabilized at 200°C and the others is that  $\text{C}\equiv\text{N}$  and  $\text{CH}_2$  groups remain present at 200°C. The lower homogeneity of Au distribution of samples stabilized at high temperature (above 200°C) could be explained by the absence of this nitrile group. It is thus possible to assume that this group can help fold to diffuse inside the filaments. It is well known that  $\text{AuCl}_3$ , involved in reactions (2)-(5) presented in section 2.4 of this chapter, is a Lewis acid. The interaction between this acid and the lone pair of electrons of the nitrile group is thus feasible and explain Au mobility through the filament. As observed on the corresponding TGA curve (Figure 3.16), it is possible that the solvent evaporation (below 150°C) forces the salt to stay onto the filament surface. This hypothesis would need to be verified with other experiments.

A stabilization of PAN NFs at 200°C seems to be the best choice. The following part is aimed to optimize the working conditions of the surface deposition method to precisely control the final filament structure and composition.

### 3.3 Optimization of the surface deposition method

#### 3.3.1 Au amount

The amount of Au deposited on the filament surface depends on several factors. The most influential factors are the initial concentration of Au ions in the raw aqueous solution, and the number of deposits that can be done on each sample before reduction of ions. These two factors are discussed separately hereafter.

#### Au ions concentration in the raw aqueous solution

In this study, the deposition of an aqueous solution, with Au concentration ranging between 0.01M and 1M, was performed on PAN NFs stabilized under air at 200°C beforehand. The obtained structures were then observed by SEM (Figure 3.19) after reduction under air at 200°C for 2 h. For concentrations of 0.01M and 0.1M, the resulting samples present similarities in terms of filament integrity and homogeneity. By SEM, the second sample (0.1M) seems to contain more particles but the difference is not really obvious by comparing the two corresponding pictures (Figure 3.19a and Figure 3.19b). The highest Au concentration tested led to filament destruction and the crystallization of Au polyhedral whose size exceeds 500nm. This is the signature of a strong corrosive effect of  $\text{HAuCl}_4$  with a high concentration.

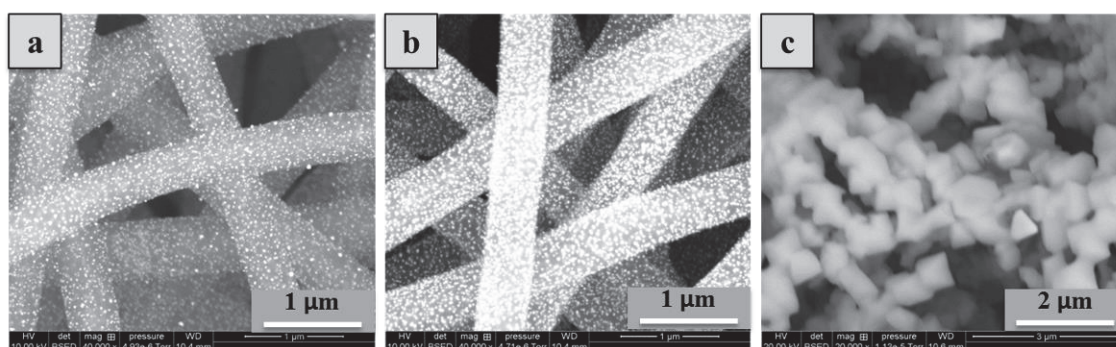


**Figure 3.19** SEM images of PAN-Au composite NFs fabricated by surface deposition (ii) with different Au concentration solutions and then heat treated in air at 200°C for 2 h: (a) 0.01M; (b) 0.1M; (c) 1M.

In order to prevent the PAN filaments from this strong corrosive effect, the lowest concentration (0.01M) had been kept for the following experiments concerning the influence of the number of deposits that can be done on each sample before reduction.

#### Number of Au deposits

This number of deposits before reduction was varied from one to five. For each sample, each deposit is about 2 to 10 drops of solution (0.01M) depending on the sample volume. Drops were deposited until the last drop allowed covering the whole surface of the sample. One can notice that all the samples were produced with the same duration of electrospinning, ensuring a repeatable sample thickness. For samples prepared with 3 and 5 deposits, a time of several minutes was necessary between each deposition in order to wait for the sample drying. After the conventional reduction under air at 200°C, the quantity of Au particles formed at the surface of the filaments clearly increases with the number of deposits (as shown in Figure 3.20). The morphology of the as-obtained filaments seems to remain unchanged with 1 and 3 deposits, but is affected after 5 deposits. This modification could be linked to the phenomenon previously observed by using a high concentration of Au in the aqueous solution (as shown in Figure 3.19c).

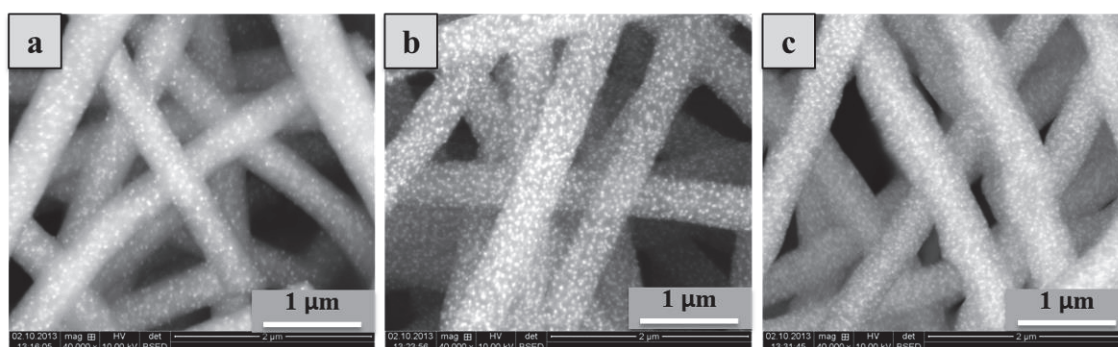


**Figure 3.20** SEM images of PAN-Au composite NFs fabricated by surface deposition (ii) with 0.01M Au solution at different deposition times and then heat treated in air at 200°C for 2 h: (a) 1 time; (b) 3 times; (c) 5 times.

In order to study the influence of the reducing method used to form Au NPs, a single deposit was used for the results presented hereafter.

### 3.3.2 Reducing method

Up to now, all the samples presented in this manuscript, and containing Au NPs (one deposition of Au on PAN stabilized at 200°C, with a concentration of 0.01M), were obtained after *in situ* reduction by thermal treatment. Here, this last reducing method is compared to two others, well known for the synthesis of Au NPs. These two reducing methods are linked to the use of citrate ions and hydrazine. The citrate is directly introduced inside an aqueous solution to obtain a concentration of 0.01M. The sample of PAN-Au is then immersed in the citrate solution for 2h before being washed at least three times with pure water and finally dried at ambient air. In case of using hydrazine, PAN-Au filaments are fixed in air above the surface of liquid hydrazine and kept until a changing of colour is observed. Samples obtained with the three reducing methods are compared by SEM in Figure 3.21. The three reducing methods lead to the Au NPs formation, but the thinnest particles and the highest distribution are obtained after calcination. The homogeneity of the sample reduced by citrate is the lowest, and we can wonder if a non-negligible amount of the particles observed on the filaments surface was not fabricated in the volume of the reducing solution. In case of hydrazine, the homogeneity of the sample is better and the particle size distribution seems to be narrower than the last sample.

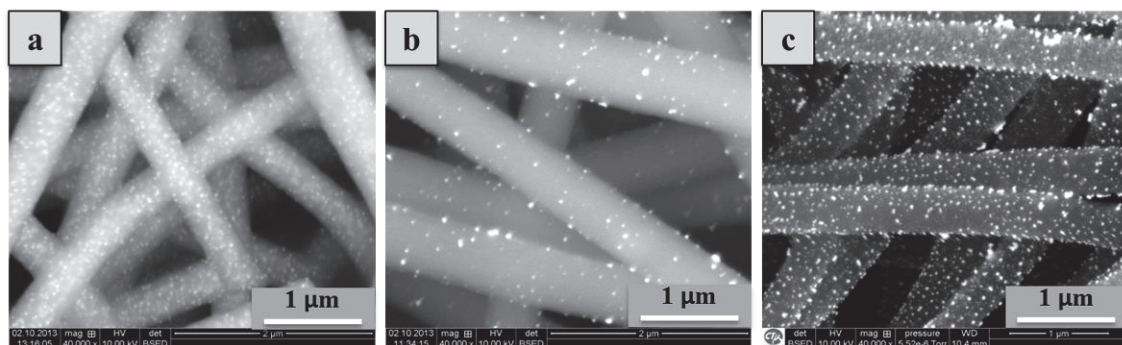


**Figure 3.21** SEM images of PAN-Au composite NFs fabricated by surface deposition (ii) with 0.01M Au solution followed with different reduction methods: (a) heating at 200°C; (b) citrate; (c) hydrazine.

The thermal reduction of Au was performed at 200°C as optimized beforehand. This sample is the best one to reach a highest homogeneity and the thinnest particles, even if the particles content seems to be lower at the surface than that of the sample reduced with hydrazine. To complete the study on these composite filaments, a further study was carried out on their morphology and their composition.

### 3.4 Morphology and composition of PAN-Au composite nanofibers

The morphology and composition were studied on composite NFs obtained after thermal reduction (200°C under air) of Au deposited (1 deposit with Au solution concentration of 0.1M) on PAN filaments previously stabilized under air at 200°C. This study was performed simultaneously to previous ones, which explains why the raw deposited solution contains 0.1M of Au instead of 0.01M as presented above. The use of solutions between 0.01M and 0.1M normally leads to similar structures, as seen in Figure 3.19. The thermal behaviour of the sample was first verified by heating the filaments up to 500°C (as shown in Figure 3.22). A logical decrease of the filament diameter is observed when temperature rises from 200 to 400°C, with a very slow particle size modification. However, the filament morphology does not remain anymore with a heating at 500°C. This temperature is corresponding to the fastest decomposition rate of PAN (as shown in Figure 3.16), and could also be coherent with melting of Au NPs [166].

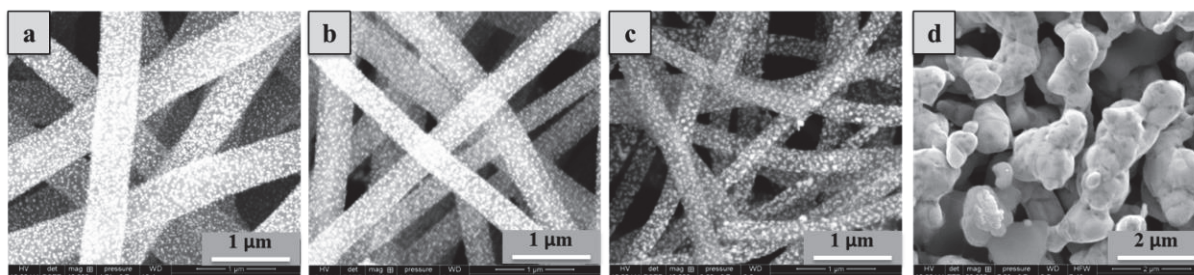


**Figure 3.22** SEM images of PAN-Au composite NFs fabricated by surface deposition (ii) with 0.1M of Au solutions and then heat treated in air at different temperatures for 2 h: (a) 200°C; (b) 300°C; (c) 400°C; (d) 500°C.

The crystal structures of Au NPs formed after reduction at 200°C of the PAN-Au composite NFs were determined by XRD ( $2\theta$ , range 10°-90°) as shown in Figure 3.23. Five obvious diffraction peaks at  $2\theta$  values of 38.18°, 44.39°, 64.58°, 77.55°, and 81.72° were observed, corresponding to (111), (200), (220), (311), and (222) crystal planes of the face centered cubic (fcc) crystalline Au (JCPDS No. 00-004-0784), respectively. The diffraction peak (111) is much stronger than the other, indicating that Au were mainly dominated by the crystal facet (111) and thus, the growth direction was mostly oriented parallel to the [111] direction [140]. The average crystallite size ( $D$ ) of Au NPs was around 15 nm, which was estimated by full width half maximum (FWHM) of the main peak (111) from the Scherrer's Formula [141]. Compared to the strong diffraction peaks discussed before, there are two weak and broad peaks located at around 16° and 25° according to PAN.

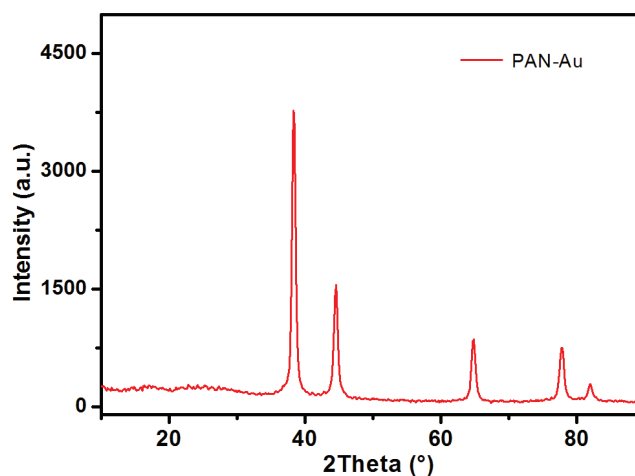


Figure 3.23 XRD pattern of PAN-Au composite NFs prepared by stabilization PAN NFs at 200°C and then deposition Au ions with concentration of 0.1M followed with calcination at 200°C for Au reduction.

Figure 3.24a and

Figure 3.24b show TEM and HR-TEM images of PAN-Au composite NFs fabricated with combination of stabilization, deposition, and reduction. According to the size distribution of

Figure 3.24c, the average Au NPs size is around 10 nm. With a surface deposition of Au on the stabilized PAN NFs, the Au NPs are homogeneously dispersed inside as well as outside the filament. This is a facile way to produce polymer-Au composite NFs. The stabilized PAN NFs at 200°C have the ability to absorb the Au ions in the volume of PAN fiber. All these experiments should be very useful for the fabrication of inorganic filaments containing Au NPs (Chapter 4 and 5).

Figure 3.24 (a) TEM images and (b) HR-TEM images of PAN-Au with stabilization at 200°C and then deposition Au ions followed with calcination reduction at 200°C; (c) size distribution of Au particle size of PAN-Au composite NFs.

## 4 Conclusions

According to the results of this third Chapter, the polymer-Au composite NFs are possible to achieve via different polymers by volume inclusion and surface deposition of Au ions. Among different Au reduction methods, calcination at 200°C is the most simplest and efficient way to obtain polymer-Au composite NFs with uniform size of Au around 10 nm

dispersed homogenously in the volume of polymer NFs. This is a facile way to fabricate these composite NFs containing Au NPs whose content and location are controllable. The optimized conditions for Au NFs are studied showing that PVP is the best choice for the starting polymer and the suitable calcination process conditions are heating in air at 500°C for 2 h. Continuous polycrystalline Au NFs with a diameter around 60 nm were obtained via ES followed by subsequent thermal annealing. Au ions were added into ES solution directly as the Au raw material, reduced and transformed in Au NPs during calcination. We showed that the morphology and crystal structure of Au NFs are governed by thermal treatment conditions. For future work, it could be interesting to tune the electric conductivity of Au NFs by controlling their grain structure for electronic applications.

## CHAPTER IV CHARACTERIZATION AND PHOTOCATALYTIC ACTIVITY OF TiO<sub>2</sub>-Au COMPOSITE NANOFIBERS

### 1 Introduction

TiO<sub>2</sub> based materials have attracted significant attention for photocatalysis due to their unique electronic and optical properties. Moreover, they also have long-term stability, strong oxidizing ability, and abundant, inexpensive and nontoxic properties [167]. In particular, by means of light irradiation, they can oxidize a wide range of organic pollutants. This property has been already used in many areas, such as air, water purification, sterilization, soil proof, and deodorization applications. However, TiO<sub>2</sub> based materials have some limitations as photocatalysts due to their specific electronic properties [168].

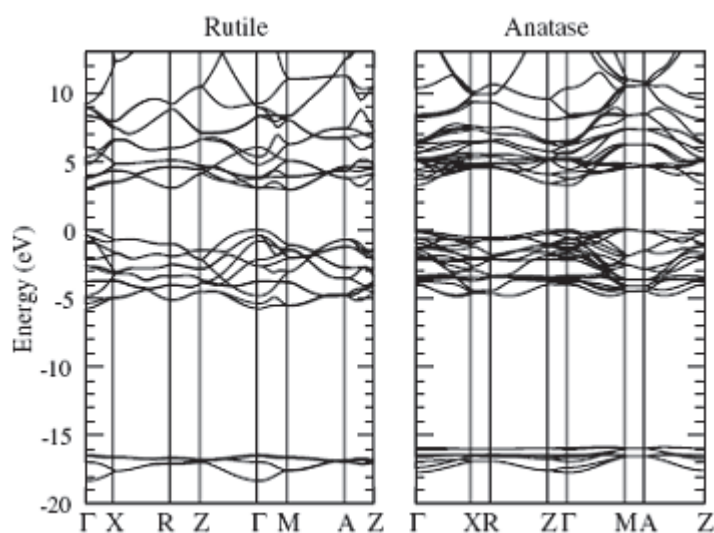


Figure 4.1 Electronic structure of anatase and rutile TiO<sub>2</sub>

Figure 4.1 shows the electronic structure of anatase and rutile TiO<sub>2</sub> without doping. The maximum of the valence band is taken as the zero of energy. The corresponding band gap energy around 3.2 eV ( $\lambda=384$  nm) implies that TiO<sub>2</sub> based materials mainly absorb in the UV light wavelength range that only represents only 5% of the total solar light emission. As a consequence, without additional materials, they exhibit a very low solar light harvesting thus limiting expected oxidation reactions. It has to be noticed that such reactions are also dependent of the recombination rate of photoexcited electron-hole ( $e^-/h^+$ ) pairs. To improve their photocatalytic performance, two complementary strategies are adopted by combining an

extension to the visible domain of TiO<sub>2</sub> based materials absorption and a way to reduce the recombination of (e<sup>-</sup>/h<sup>+</sup>) pairs. Some physical and chemical modifications, like modify the particle size, morphology, phase composition, surface modification and the use of elemental doping, have been studied in the past to improve photocatalytic performances. More recently, the association of TiO<sub>2</sub> with noble NPs, in particular gold for its chemical stability, has been considered and largely studied as one of the most promising catalysts for photocatalytic reactions. However, mechanisms implied during photocatalytic experiments on TiO<sub>2</sub>-Au based materials are still not understood and need again specific studies. In order to bring new elements to the understanding in research field, we have chosen to work on TiO<sub>2</sub>-Au composite NFs. In order to conduct photocatalytic experiments on large quantities of matter, the choice of working on NFs, which are considered as bridges between the *nano* and *meso* scale was natural.

In this chapter, TiO<sub>2</sub>-Au composite NFs were fabricated by ES with three different routes of introducing Au ions:

**Volume inclusion (i):** Au precursor was dissolved in the PVP/TTIP (titanium isopropoxide) solution (9:30) according to the content of Au in the final TiO<sub>2</sub>-Au composites, 2wt%, 4wt%, and 8wt%, respectively. Then a calcination step at 500°C for 2 h is performed. The samples of pure TiO<sub>2</sub> NFs and TiO<sub>2</sub>-Au with different Au contents were named as TiO<sub>2</sub>-Au-0wt%, TiO<sub>2</sub>-Au-2wt%, TiO<sub>2</sub>-Au-4wt%, and TiO<sub>2</sub>-Au-8wt%, respectively. Meanwhile, the sample of TiO<sub>2</sub>-Au-4wt% also named as TiO<sub>2</sub>-Au-i in order to compare with other two Au introducing routes.

**Surface deposition (ii):** depositing the Au aqueous solution with the concentration of 0.1M on the surface of PVP/TTIP composite NFs (with or without stabilization at 200°C for 2 h in ambient air). Then a calcination step at 500°C for 2 h is performed. The final sample was named as TiO<sub>2</sub>-Au-ii.

**Surface deposition (iii):** the third way is to introduce Au ions on the surface of already calcined TiO<sub>2</sub> NFs, and then reduce Au by heating at 200°C in air. The final sample was named as TiO<sub>2</sub>-Au-iii.

It has to be noticed that a particular attention is brought to annealing treatments that are essential since they contribute the polymer parts removal and the in-situ reduction of Au ions to Au NPs.

In the first section, we will present a preliminary study dedicated to TiO<sub>2</sub> NFs without Au. The influence of the Ti precursor concentration in the initial spinnable polymeric solution and of the post annealing treatments temperatures is evaluated. TiO<sub>2</sub>-Au composite NFs are then presented. Based on the three different approaches, the influence of experimental parameters, including the concentration of Ti precursor, the thermal temperatures during the annealing processes, and the Au concentrations has also been evaluated. The morphologies and composition of each sample are studied by electronic microscopy. In the last section, the photocatalytic performances of those samples, which can be varied with irradiation light, the ratio of anatase and rutile phases in TiO<sub>2</sub> and Au contents, are given and discussed.

## **2 Influence experimental parameters for TiO<sub>2</sub> nanofibers**

The synthesis of TiO<sub>2</sub> NFs is to mix the TTIP precursor directly with the polymer solution prior to ES. In a typical procedure, an amount of TTIP was dissolved in a volume of acetic acid and EtOH, and then mixed with the ES solution of 7 wt% PVP–EtOH, to get the weight ratio of PVP:TTIP to be 9:30, 9:10, and 9:3, respectively. To ensure good mixture homogeneity, the resulting solution was then stirred at room temperature for 2 h. After a typical ES process with conditions of 10 kV, 10 cm, 1.5 mL·h<sup>-1</sup>, the as-spun PVP–TTIP composite NFs were obtained and treated at different temperatures in air for 2 h. Among all the previous parameters, the Ti precursor concentration and the annealing treatment temperatures are two important parameters that require a specific study. The related final samples heat treated at 500°C with different concentration of TTIP were named as TiO<sub>2</sub>-9:3, TiO<sub>2</sub>-9:10, and TiO<sub>2</sub>-9:30, respectively. And the samples with the ratio of PVP:TTIP at 9:30 were heat treated at different temperatures were named as TiO<sub>2</sub>-500°C, TiO<sub>2</sub>-600°C, TiO<sub>2</sub>-700°C, and TiO<sub>2</sub>-800°C, respectively.

### **2.1 Concentration of titanium precursor**

After optimization of the main electrospinning parameters, samples of TiO<sub>2</sub> NFs obtained from calcined as-spun PVP-TTIP composite NFs in air at 500°C for 2 h but with different Ti precursor concentration have been firstly characterized by SEM. As shown in Figure 4.2, the corresponding SEM images exhibit clearly that the diameter homogeneity, which is a key objective of good electrospinning experiment, is reached for the higher concentration of TTIP.

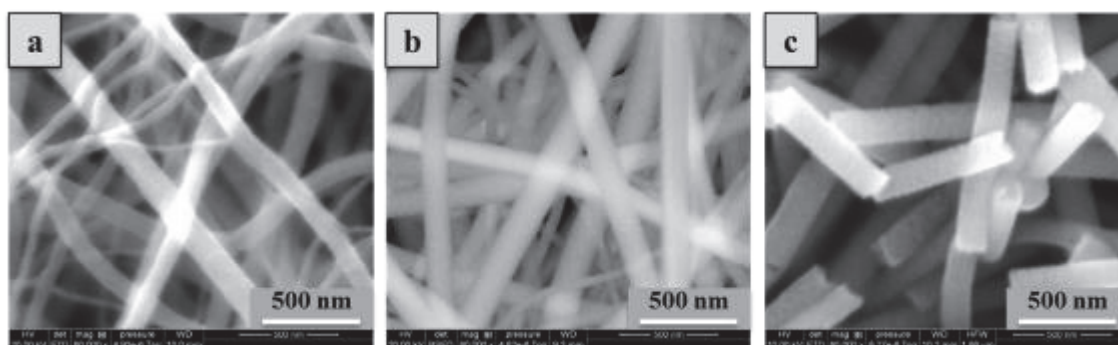


**Figure 4.2** SEM images of  $\text{TiO}_2$  NFs obtained from calcined the as-spun PVP-TTIP composite NFs in air at  $500^\circ\text{C}$  for 2 h with different concentration of PVP : TTIP : (a) 9:3; (b) 9:10; (c) 9:30.

Surprisingly, for smaller concentration, a similar behavior is observed with diameters widely dispersed, ranging from 50 nm to 150 nm (as shown in Figure 4.2a). This is probably due a non-homogeneous dispersion of the Ti precursor before the electrospinning process. After the calcination, the NFs containing higher concentration (PVP:TTIP is 9:30) of TTIP are more homogeneous with a mean diameter of  $164 \pm 21$  nm and a mesoporous surface. We can suppose that during the calcination step, the final shape of  $\text{TiO}_2$  fibers is ruled by Ti precursor concentration if this latter is large but only by the PVP decomposition if this latter is small. As a consequence, the final NFs shape is quite homogeneous for large quantity of initial Ti precursor but is more influenced by the Ti precursor dispersion for small Ti content, leading to dispersed diameter. In this case, the fibers are also clearly shorter than as-spun composite NFs, which indicate that materials became brittle due to formation of  $\text{TiO}_2$  and calcinations. It is obvious that this last sample corresponds better to what we are expected for further photocatalysis experiment. The specific surface area for  $\text{TiO}_2$ -9:30 is  $17 \text{ m}^2 \cdot \text{g}^{-1}$  with pore size of 5 nm checked by BET. It is more reproducible and offers an interesting porosity that could improve significantly the volume to surface available for reactions.

## 2.2 Thermal treatment temperatures

Starting from this last sample with an optimized concentration Ti precursor, the influence of the post-annealing treatment conditions has been studied. In particular, different calcination temperatures from  $500^\circ\text{C}$  to  $800^\circ\text{C}$  in air for 2 h have been performed on this sample. For each temperature, a corresponding SEM images are shown in Figure 4.3. When increasing temperature, the NFs morphology seems to change and in particular the surface that is clearly rougher. This point has to be related to the intrinsic polycrystalline structure of those NFs that

are composed of TiO<sub>2</sub> NPs growing under constrained conditions (high temperature) and dimensions (only 1D is unlimited).

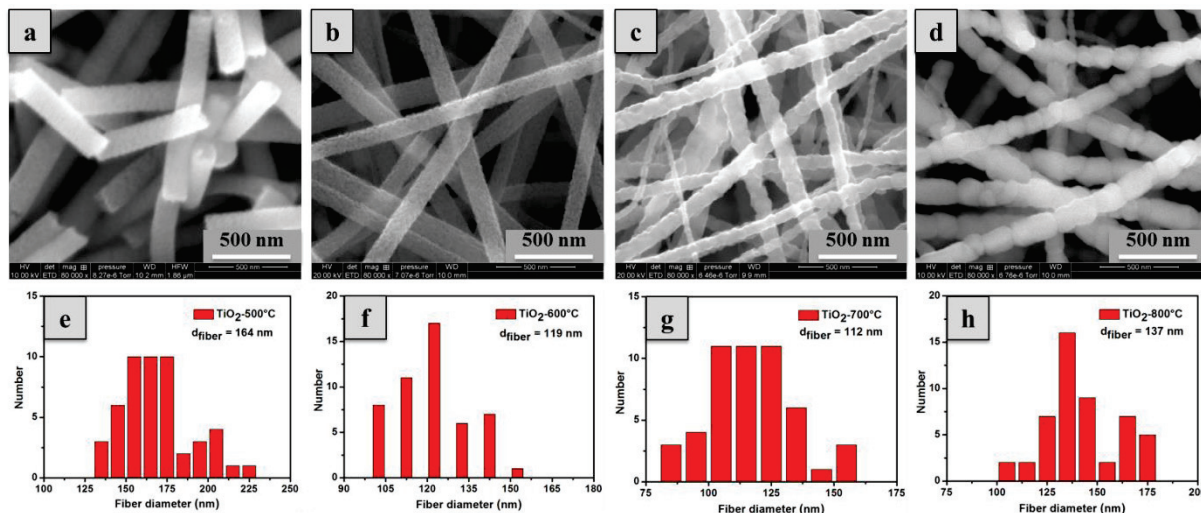


**Figure 4.3** SEM of TiO<sub>2</sub> NFs obtained with different calcination temperatures: (a) 500°C; (b) 600°C; (c) 700°C; and (d) 800°C; (e), (f), (g), and (h) are the corresponding size distributions of fiber diameter.

The fiber diameter of these samples annealed at 500°C, 600°C, 700°C and 800°C are 164 nm, 119 nm, 112 nm, and 137 nm, respectively, as estimated with the corresponding size distributions (Figure 4.3e to h). We propose that in a first step at 500°C PVP decomposition leaves porous fibers made of very small TiO<sub>2</sub> nanoparticles. From 600°C to 700°C, no changes in mean diameter are observed but the surface roughness increases accordingly to the nanoparticles size growth and aggregation. When the annealing temperature reached 800°C, (Figure 4.3d) NF is made of a linear assembly of large TiO<sub>2</sub> NPs. NPs diameter overcomes the NF diameter, and the mean NFs diameter consequently increases (137 nm). This typical behavior indicates that by continuing the temperature increase, the NFs morphology should evolve to necklace shape and probably a discontinuity of fiber.

### 2.3 Morphologies and composition of TiO<sub>2</sub> nanofibers

TiO<sub>2</sub> have three different phases of anatase, rutile, and brookite. The commercial P25 has the ratio of Anatase : Rutile is of 80:20. Temperature is the key factor to form different structures of TiO<sub>2</sub>. The ratio between anatase and rutile is Rietveld refinement analysis by software of Brass based on the XRD data. The refinement details of TiO<sub>2</sub> calcined at 500°C is shown in Figure 4.4. The ratio of Anatase : Rutile is 98:2 for 500°C, which is almost pure

anatase at this temperature. The results of  $\text{TiO}_2$  heated at different temperatures from  $500^\circ\text{C}$  to  $800^\circ\text{C}$  are listed in Table 4.1. Anatase is the stable phase at low temperature and rutile is the stable phase at high temperature. It is clear seen that the rutile component increases as the temperature increase, from 2% to 88 % with the temperature from  $500^\circ\text{C}$  to  $800^\circ\text{C}$ .

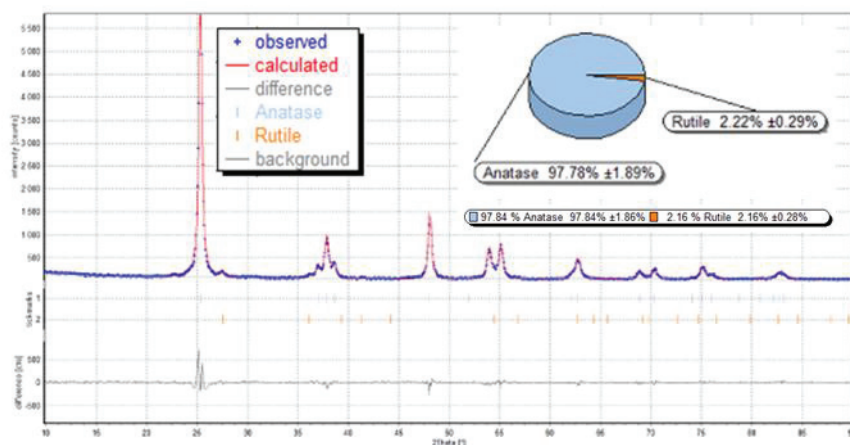
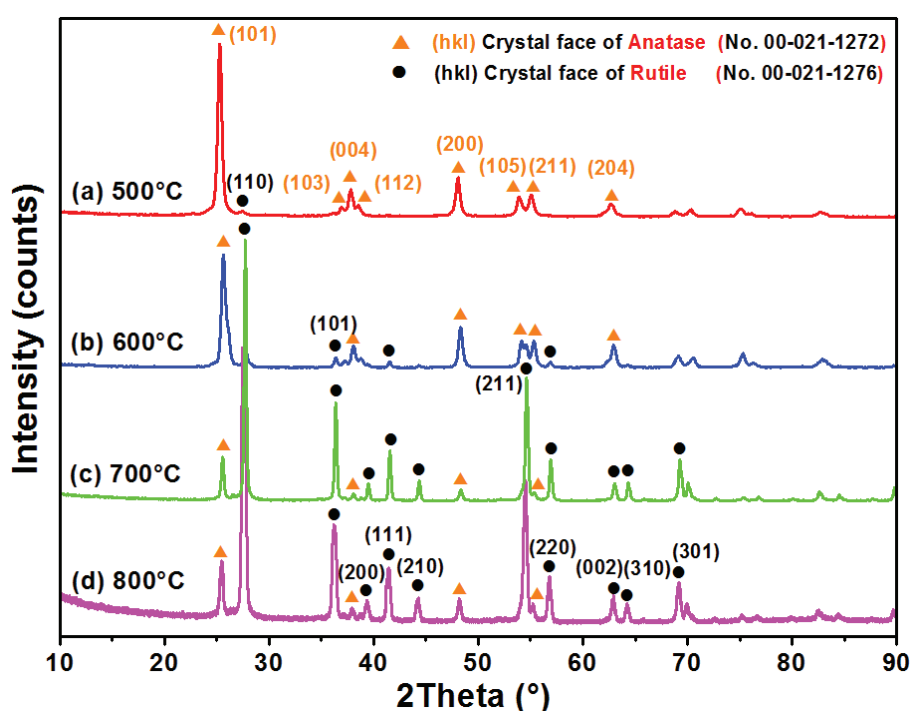


Figure 4.4 Rietveld refinement details by software of Bass based on XRD data of  $\text{TiO}_2$  obtained by calcined at  $500^\circ\text{C}$ .

The crystal structures of pure  $\text{TiO}_2$  samples were determined by XRD. Figure 4.5 displays XRD patterns of  $\text{TiO}_2$  NFs samples obtained from different calcination temperatures from  $500^\circ\text{C}$  to  $800^\circ\text{C}$ . As shown in Figure 4.5a, the XRD patterns of the sample  $\text{TiO}_2$  can be well-indexed to anatase (JCPDS Card No. 00-021-1272), with the lattice parameters  $a = 3.7852 \text{ \AA}$ ,  $b = 3.7852 \text{ \AA}$ , and  $c = 9.5139 \text{ \AA}$ . Peaks at  $2\theta = 25.3^\circ, 36.9^\circ, 37.8^\circ, 38.6^\circ, 48.1^\circ, 53.9^\circ, 55.6^\circ,$  and  $62.7^\circ$  are indexed to the (101), (103), (004), (112), (200), (105), (211), and (204) planes of Anatase, respectively. When checking carefully, a very weak peak can be found at  $27.4^\circ$ , which is attributed to the (110) planes of rutile (JCPDS Card No. 00-021-1276). As the temperature increase to  $600^\circ\text{C}$ , new peaks appear at  $2\theta = 27.4^\circ, 36.1^\circ, 41.2^\circ,$  and  $56.6^\circ$ , respectively indexed as the (110), (101), (111), and (220) planes from Rutile,. The intensity of Anatase main peak decreases, the sample is a mixture of Anatase and Rutile with the ratio of 84:16. It exhibits a similar change at  $700^\circ\text{C}$  and  $800^\circ\text{C}$ . The average crystal sizes from  $\text{TiO}_2$  were determined using the three strongest peaks from each sample using Scherrer's equation, with the value of 27 nm, 21 nm, 27 nm, and 22 nm for samples obtained from  $500^\circ\text{C}, 600^\circ\text{C}, 700^\circ\text{C},$  and  $800^\circ\text{C}$ , respectively, as shown in Table 4.1.

Table 4.1 Diameters, crystallite size and phase ratio A. of TiO<sub>2</sub> obtained from different calcination temperatures.

	Average Diameter / nm	Crystallite Size / nm	Anatase : Rutile / %
500°C	164 ± 21	27	98 : 2
600°C	119 ± 13	21	84 : 16
700°C	112 ± 17	27	13 : 87
800°C	137 ± 18	22	12 : 88

Figure 4.5 XRD patterns of TiO<sub>2</sub> NFs obtained with different calcination temperatures: (a) 500°C; (b) 600°C; (c) 700°C; and (d) 800°C.

## 2.4 Conclusions

As discussed above, the initial concentration of TTIP precursor influences morphology and diameter of pure TiO<sub>2</sub> NFs. The lower the ratio of PVP : TTIP, the more uniform the diameter of TiO<sub>2</sub> NFs. In order to fabricate TiO<sub>2</sub> NFs with large specific surface area and uniform diameters, an optimized concentration of PVP : TTIP at 9:30 and an optimal calcination temperature at 500°C in air for 2 h has been identified, thus resulting in pure TiO<sub>2</sub> NFs with uniform diameter of 164 nm. Those results constituted the basic elements for the formation of TiO<sub>2</sub>-Au composite NFs presented in the next section.

### **3 Influence experimental parameters for TiO<sub>2</sub>-Au composite nanofibers**

This preliminary study based on TiO<sub>2</sub> without gold precursor addition was necessary to understand the influence of experimental parameters on the resulting NFs final shape. At the beginning of this chapter, we have presented in details the different strategies to synthesize HMMOC materials starting with ES solution, the related ES process and the corresponding annealing treatment (volume inclusion (i), surface deposition (ii) and surface deposition (iii)). In this part, we compare morphology and structure from TiO<sub>2</sub>-Au NFs obtained with those three different methods.

#### **3.1 Gold salt concentrations**

The first study has been conducted following the volume inclusion (i), e.g. by directly mixing gold salt into the ES polymeric solution before the ES process. Obviously, the influence of the gold salt concentration is the starting point of this study.

Au content has been fixed to 2wt%, 4wt%, 8wt% and has been measured by ICP on TiO<sub>2</sub>-Au samples, annealed under air atmosphere at 500°C for 2 h. For the TiO<sub>2</sub>-Au-2wt%, TiO<sub>2</sub>-Au-4wt%, and TiO<sub>2</sub>-Au-8wt% samples, Au content by are 2.02%, 4.32%, 7.99% in weight, as measured by ICP. Compared to the calculated results based on the initial weight of Ti and Au precursors of 5.6%, 8.2%, and 15.1%, the ICP results are almost two times lower. This might due to the ICP sample preparing process. When dissolve the TiO<sub>2</sub>-Au composite NFs with aqua regia, Au NPs are well-dispersed inside and outside of TiO<sub>2</sub> NFs, the centrifugation cannot break the composite totally, and as a consequence, a certain amount of Au NPs inside the TiO<sub>2</sub> matrix still remains and cannot dissolve into the solution for ICP test. This last comment should allow us to evaluate the proportion of gold atoms inside and at the surface of the fiber but porosity from sample probably play also an important role in the sample preparation for ICP that render impossible this evaluation (a specific surface area of 33 m<sup>2</sup>·g<sup>-1</sup> with a pore size of 5 nm for TiO<sub>2</sub>-Au-4 wt% was measured by BET).

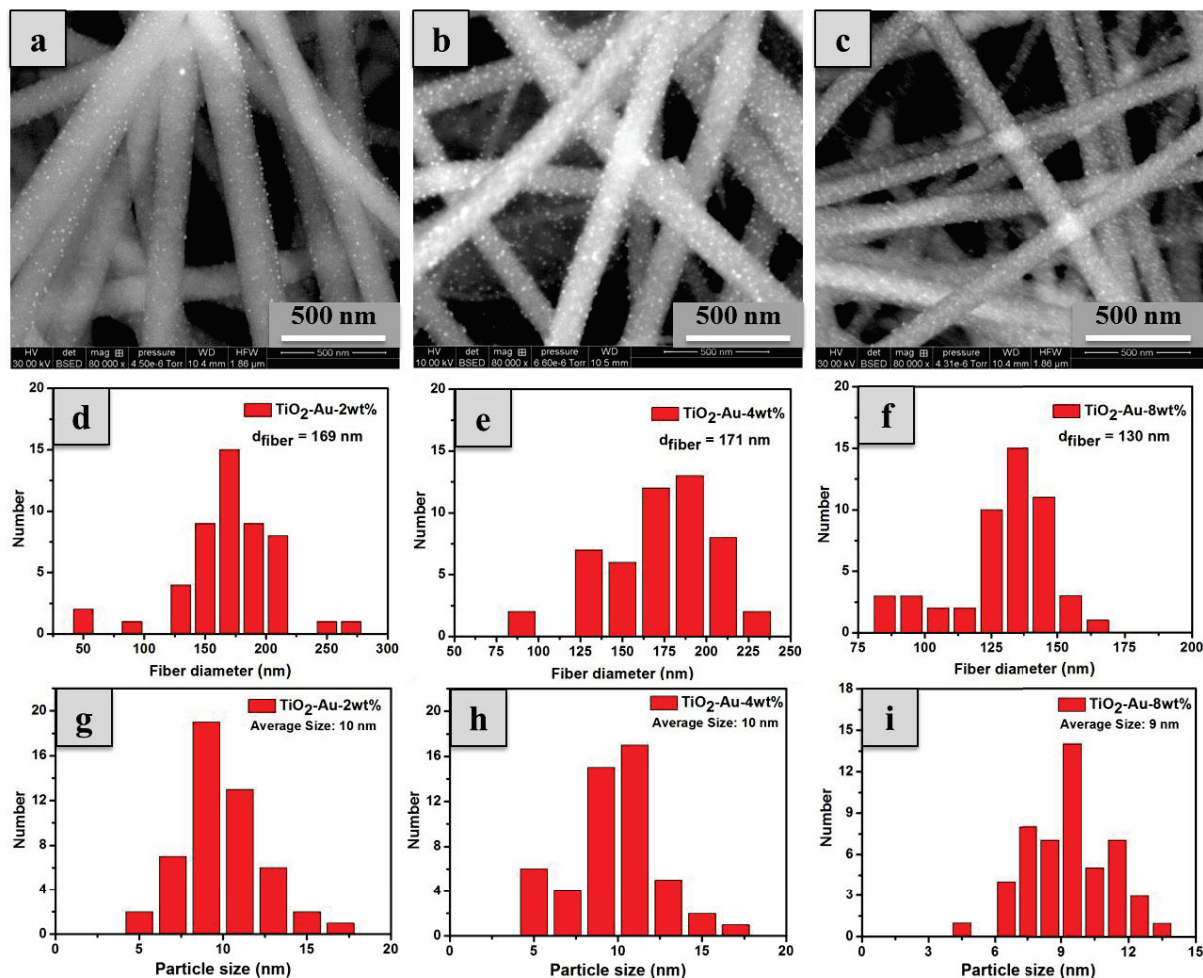


**Figure 4.6** SEM images of TiO<sub>2</sub>-Au composite NFs fabricated from volume inclusion (i) with different Au contents: (a) 2wt%; (b) 4wt%; (c) 8wt% ; (d), (e), (f) and (g), (h), (i) are the size distributions of TiO<sub>2</sub>-Au fiber diameter and Au NPs size for sample (a), (b), and (c), respectively.

The influence of gold content on NFs morphology has been studied by SEM and is shown in Figure 4.6. All the samples keep the fiber morphology with homogeneously dispersed bright dots, which are identified to Au NPs: the number of these bright particles on the fibers is directly related to the amount of gold precursor. The fiber mean diameter TiO<sub>2</sub>-Au-2wt%, TiO<sub>2</sub>-Au-4wt%, and TiO<sub>2</sub>-Au-8wt% samples have been measured to 169 nm, 171 nm, and 130 nm, respectively. Samples with a gold content of 2wt% and 4wt%, fiber diameter remains quite similar compared to pure TiO<sub>2</sub> of 164 nm (Figure 4.3a). Introducing a low concentration of Au ions into the ES solution with PVP and TTIP precursor, the fiber diameter only slightly changes after calcination in air at 500°C for 2 h. But for larger concentrations, typically, for TiO<sub>2</sub>-Au-8wt%, the diameter decreases from 170 nm to 130 nm. Introducing such a concentration of gold ions in the ES solution, ionic strength, viscosity and therefore spinnability of the precursor solution is modified, which has an impact on composite NFs size.

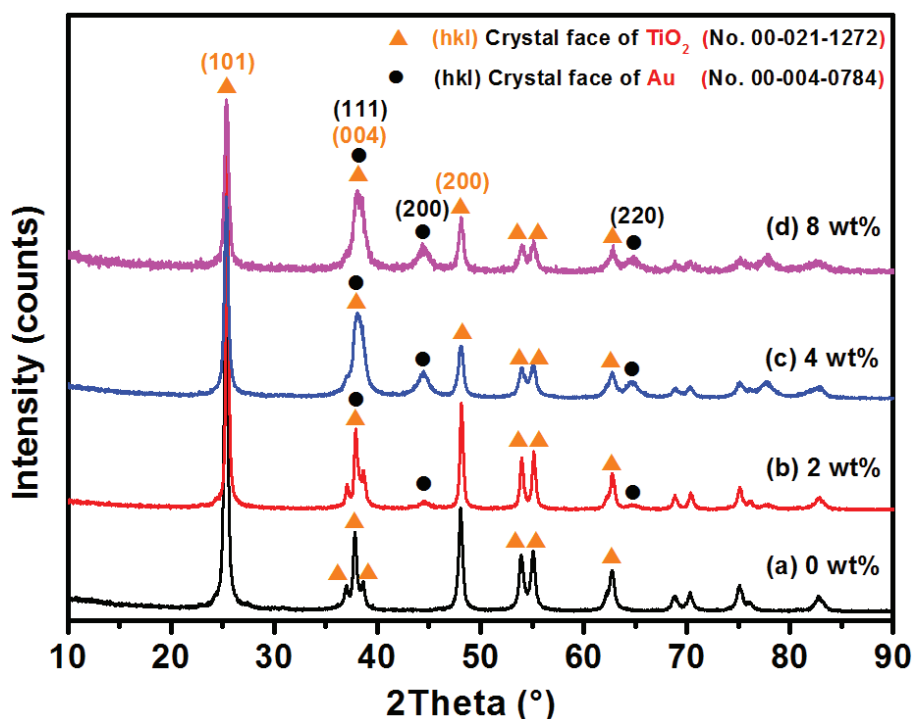
Another reason is the relative proportions of TTIP precursor and polymer decrease while the Au ions concentration increases. With the subsequent annealing to remove the polymer, TiO<sub>2</sub> fiber diameter decreases. These factors can make the fiber diameter from final products vary.

The size distribution of Au NPs for all the three samples follows a normal distribution with an average size around 10 nm. This uniform size of Au NPs is benefit from the *in situ* reduction of Au ions to Au NPs at low temperature before the formation of TiO<sub>2</sub> crystallite. As we discussed in Chapter 3 for different reduction methods, heating is quite effective to reduce Au ions to form Au NPs. The reduction mechanism is probably due to oxidation of terminal hydroxyl groups from PVP as observed in hydrothermal synthesis of Au NPs [169] or directly oxidation of the polymer backbone at high temperature, due to the high redox potential of HAuCl<sub>4</sub> ( $E^\circ=0.93$  V/ENH at 298K), The heating rate and different type of polymer matrix can influence the Au reduction. For these samples, the heating rate is fixed at 1 °C·min<sup>-1</sup> and the polymer matrix is PVP. The Au contents in the final sample can be varied by the concentration and volume of Au aqueous solution added into the ES solution.

The fibers diameter, the TiO<sub>2</sub> crystallite gold NPs mean sizes of TiO<sub>2</sub>-Au composite NFs obtained from different Au concentrations have been listed in Table 4.2. The average sizes of Au NPs in the three samples are 10.0 ± 2.2 nm (TiO<sub>2</sub>-Au-2wt%), 9.8±2.6 nm (TiO<sub>2</sub>-Au-4wt%) and 9.3±1.8 nm (TiO<sub>2</sub>-Au-8wt%), respectively, by SEM image analysis with software Nano Measurer. The crystallite sizes of TiO<sub>2</sub> were determined by XRD measurements of the strongest peaks (101) of anatase (JCPDS Card No. 00-021-1272) using Scherrer's equation (Figure 4.7). A mean value of 27 nm, 34 nm, 19 nm, and 18 nm has been obtained for TiO<sub>2</sub> crystallites of the samples TiO<sub>2</sub>-Au-0wt%, TiO<sub>2</sub>-Au-2wt%, TiO<sub>2</sub>-Au-4wt%, and TiO<sub>2</sub>-Au-8wt%, respectively. For the determination of Au crystallite mean sizes, we have followed the same experimental XRD analysis but with the second strongest peaks (200) of cubic gold (JCPDS Card No. 00-004-0784) using Scherrer's equation, and we have obtained a value of 8 nm, 8 nm, and 11 nm for Au crystallites from samples TiO<sub>2</sub>-Au-2wt%, TiO<sub>2</sub>-Au-4wt%, and TiO<sub>2</sub>-Au-8wt%, respectively. We have to precise that the choice of the second strongest peak of Au (200) has been motivated by the fact that the strongest one (111) coincides with the second strongest one of TiO<sub>2</sub> (004), thus conducting to a less accuracy to distinguish them.

**Table 4.2 Au contents, average fiber diameters, Au NPs size, and crystallite size of TiO<sub>2</sub>-Au composite NFs obtained from different Au concentrations.**

TiO <sub>2</sub> -Au	Au Contents / %			Fiber Diameter / nm	Crystallite Size TiO <sub>2</sub> / nm	NPs Size Au / nm	Crystallite Size Au / nm
	ICP wt%	Calculation					
		wt%	mol%				
0 wt%				170 ± 21	27		
2 wt%	2.02	5.6	2.3	169 ± 39	34	10.0 ± 2.2	8
4 wt%	4.32	8.2	3.5	171 ± 31	19	9.8 ± 2.6	8
8 wt%	7.99	15.1	6.7	130 ± 20	18	9.3 ± 1.8	11

**Figure 4.7 XRD patterns of TiO<sub>2</sub>-Au composite NFs fabricated with different Au concentrations: (a) 0wt% ; (b) 2wt%; (c) 4wt%; (d) 8wt%.**

The crystal structures of TiO<sub>2</sub>-Au samples with different Au contents were determined by XRD (Figure 4.7). As shown in Figure 4.7a, by studying a sample realized in the same conditions but without addition of gold ions in the preparation, the pure TiO<sub>2</sub> XRD patterns can be easily indexed to anatase (JCPDS Card No. 00-021-1272), with lattice parameters  $a = 3.7852 \text{ \AA}$ ,  $b = 3.7852 \text{ \AA}$ , and  $c = 9.5139 \text{ \AA}$ . Peaks at  $2\theta = 25.3^\circ$ ,  $36.9^\circ$ ,  $37.8^\circ$ ,  $38.6^\circ$ ,  $48.1^\circ$ ,  $53.9^\circ$ ,  $55.6^\circ$ , and  $62.7^\circ$  are indexed to the (101), (103), (004), (112), (200), (105), (211), and (204) planes, respectively. Figure 4.7 b shows the XRD pattern of the sample TiO<sub>2</sub>-Au-2wt%,

where two more small and weak peaks centered at  $2\theta = 44.4^\circ$  and  $64.6^\circ$  corresponding to the (200) and (220) planes of the cubic gold phase (JCPDS Card No. 00-004-0784). For the sample of TiO<sub>2</sub>-Au-4wt% shows in Figure 4.7 c, the two peaks at  $2\theta = 36.9^\circ$  and  $38.6^\circ$  corresponding to the (103) and (112) planes of anatase (JCPDS Card No. 00-021-1272) were disappeared, probably hidden by the strongest peak at  $2\theta = 38.2^\circ$  of the (111) planes of the gold phase. This is not surprising since the amount of gold increases from 2wt% to 8wt%. It has to be noticed that all those XRD patterns exhibit very thin peaks thus showing that all the samples of TiO<sub>2</sub>-Au with different contents are well crystallized.

### 3.2 Annealing temperature

The second study is dedicated to the influence of the annealing temperature. The other experimental parameters are kept constant following the volume inclusion (i) method. The gold content is fixed as PVP : Au of 6:1. The calcination is with heating rate of  $1^\circ\text{C}\cdot\text{min}^{-1}$  and holding time is 2 h.

Figure 4.8 shows SEM images of as-spun PVP -TTIP-Au composite without further heat treatment (Figure 4.8a), and TiO<sub>2</sub>-Au samples after heat treatment at 200°C and 500°C under air atmosphere for 2h. The as-spun sample exhibits fibers having a smooth surface similarly to pure polymer fibers. For as-spun composite NFs at room temperature, there are no distinguishable bright dots (Figure 4.8a). At room temperature, only Au ions are present into the as-spun NFs and homogeneously dispersed in the polymer. After treated at 200°C, the fibers diameter slightly changes and many bright dots appear well-dispersed onto the fiber, proving the presence of Au NPs. With a heating temperature lower than 200°C, the Au ions can be reduced to form Au NPs due to the decomposition of Au precursor as discussed in section 2.2.2 of Chapter 3. When the temperature reaches 500°C, all the polymer is removed by decomposition and TiO<sub>2</sub> is formed with Au NPs. The diameter of TiO<sub>2</sub>-Au composite NFs were 170 nm with Au NPs around 10 nm. The fiber diameters are homogenous with well-dispersed and uniform Au NP.

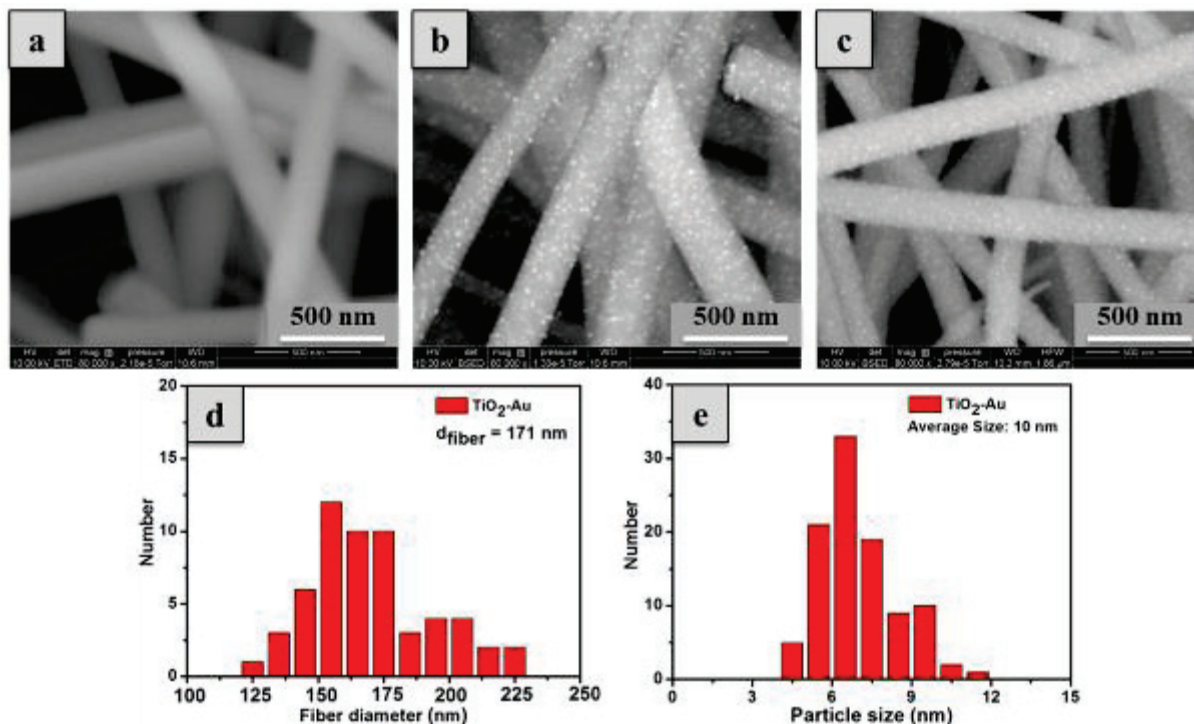


Figure 4.8 SEM images of PVP-TTIP as-spun composite NFs and treated with different temperatures in air for 2 h:(a) as-spun; (b) 200°C; (c) 500°C; (d) and (e) are the size distributions of TiO<sub>2</sub> fiber diameter and Au NPs size for (c).

This calcination process is not only removing the polymer part and form metallic oxide NPs, but also contribute to the transformation of Au ions to Au NPs by in-situ reduction. Nevertheless, this heat treatment has to be confined in limited regime of temperature, e.g. inferior to 500°C, because for temperature above this limit, gold NPs could eventually diffuse and form larger aggregates that would modify the fibers morphology.

### 3.3 Versatile experimental routes

Besides the volume inclusion (i) method to fabricate TiO<sub>2</sub>-Au composite NFs, two Gold introducing routes surface deposition (ii) and surface deposition (iii) are also studied. We remind the following three designed TiO<sub>2</sub>-Au composite NFs fabrication routes: volume inclusion (i): Au ions are dispersed in ES solution before ES process; surface deposition (ii): Au ions are deposited onto the as-spun NFs process before calcination; surface deposition (iii): the oxide NFs obtained after calcination is impregnated wild gold salt solution calcinations and further reduced.

In order to compare the three methods, the heat treatment temperature is kept constant at 500°C in air for 2h to obtain TiO<sub>2</sub> NFs. For the surface deposition routes (ii) and (iii), the concentration of gold is fixed with 0.1M and reduction temperature of transforming Au ions

to Au NPs is 200°C in air for 2h. Figure 4.9 shows the SEM images of resulting TiO<sub>2</sub>-Au composite NFs fabricated following those three experimental Au introduction. On Figure 4.9a, we show the same sample of TiO<sub>2</sub>-Au-4wt% (noted TiO<sub>2</sub>-Au-i) obtained with volume inclusion (i) method as described in the previous part. The samples obtained from surface deposition (ii) and surface deposition (iii), noted respectively TiO<sub>2</sub>-Au-ii (Figure 4.9b) and TiO<sub>2</sub>-Au-iii (Figure 4.9c) seem to have totally different morphologies and structures.

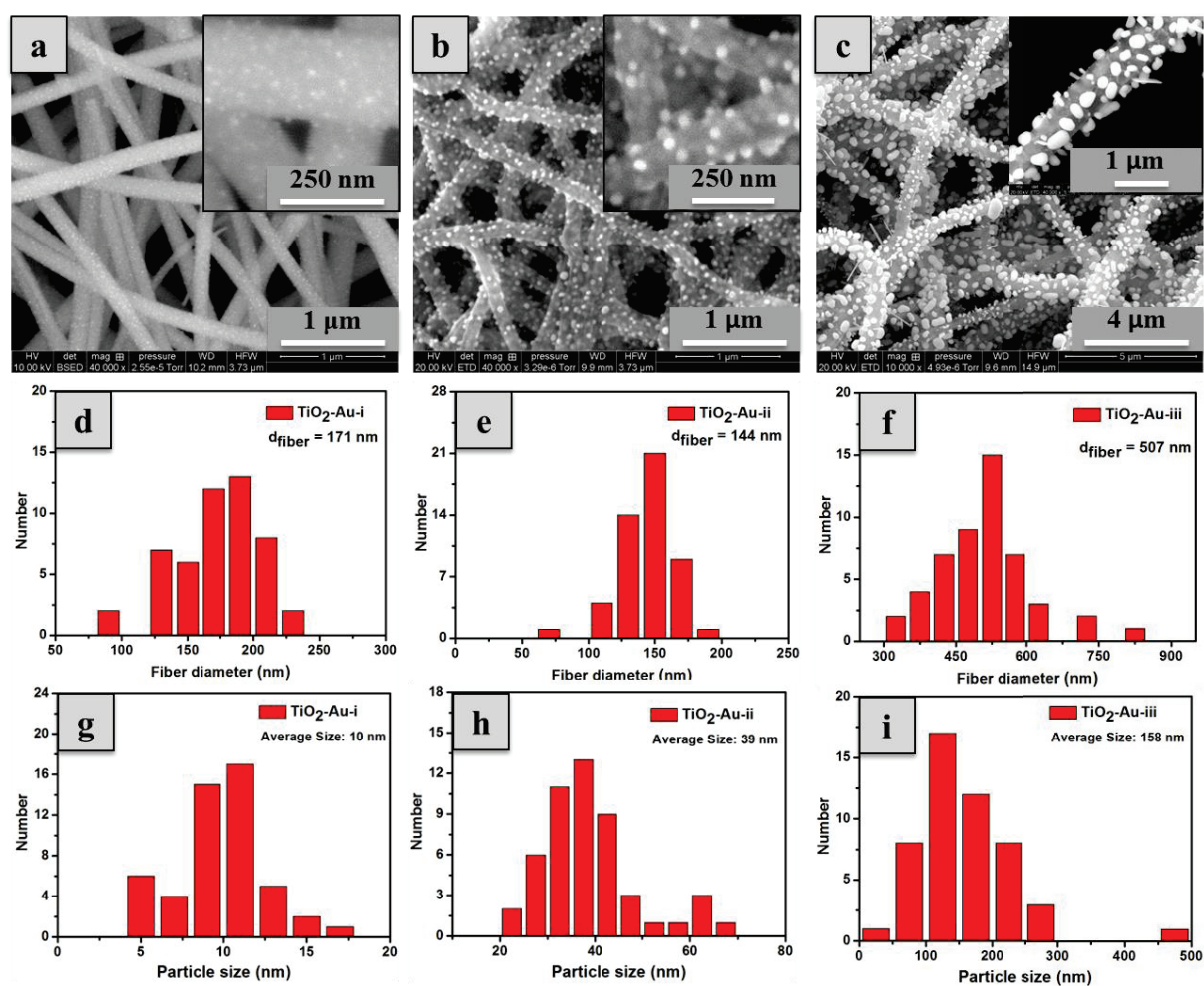


**Figure 4.9** SEM images of TiO<sub>2</sub>-Au composite NFs fabricated from different Au introducing routes: (a) volume inclusion (i); (b) surface deposition (ii); (c) surface deposition (iii); (d), (e), (f) and (g), (h), (i) are the size distributions of TiO<sub>2</sub>-Au fiber diameter and Au NPs size for sample (a), (b), and (c), respectively.

According to the size distribution results, the average diameters of TiO<sub>2</sub>-Au-i, TiO<sub>2</sub>-Au-ii, and TiO<sub>2</sub>-Au-iii nanofibers are 171 nm, 144 nm, and 507 nm, respectively. The average Au NPs size for TiO<sub>2</sub>-Au-i, TiO<sub>2</sub>-Au-ii, and TiO<sub>2</sub>-Au-iii, measured on SEM image analysis with the software NanoMeasurer, are 10 nm, 39 nm, and 158 nm, respectively (see Table 4.3).

**Table 4.3 Average diameters, Au NPs size, and crystallite size of TiO<sub>2</sub>-Au composite NFs obtained from different Au introducing routes.**

	Fiber Diameter / nm	Crystallite Size TiO <sub>2</sub> / nm	NPs Size Au / nm	Crystallite size Au / nm
<b>TiO<sub>2</sub></b>	170 ± 21	27		
<b>TiO<sub>2</sub>-Au-i</b>	171 ± 31	19	9.8 ± 2.6	8
<b>TiO<sub>2</sub>-Au-ii</b>	144 ± 19	20	38 ± 10	20
<b>TiO<sub>2</sub>-Au-iii</b>	507 ± 94	24	158 ± 74	27

Those values are also determined by XRD (as shown in Figure 4.10) with the second strongest peak of (200), using Scherrer's equation, giving the value of 8 nm, 20 nm, and 27 nm for Au crystallite of the samples TiO<sub>2</sub>-Au-i, TiO<sub>2</sub>-Au-ii, and TiO<sub>2</sub>-Au-iii, respectively. For the sample TiO<sub>2</sub>-Au-i, the size of Au NPs is uniform and the latter are dispersed homogeneously inside and outside the TiO<sub>2</sub> NFs. For the sample TiO<sub>2</sub>-Au-ii, which is obtained by depositing Au ions on the surface of as-spun PVP-TTIP composite NFs, the Au NPs size are larger, uniform and mainly inserted into the surface of TiO<sub>2</sub> NFs. This can be explained by the fact that during the calcination process Au ions are first reduced to form Au NPs and secondly the resulting Au NPs can aggregate and start slightly to diffuse onto the amorphous surface of the as-spun composite polymer NFs. For TiO<sub>2</sub>-Au-iii sample, larger Au particles with non-homogeneous shapes, including NPs, NRs, and nanoflakes decorate the surface of TiO<sub>2</sub> NFs. Au crystals are composed of well-defined facets with randomly oriented crystalline planes. In this case, we suggest that the TiO<sub>2</sub> crystals play the role of growth seed for Au NPs growth during the reduction process of Au ions. This reaction is probably sufficiently slow to participate to the growth of Au structures. The final shape of Au NPs mainly depends on TiO<sub>2</sub> seed that is not shaped at will. The crystallite mean sizes of TiO<sub>2</sub> were determined by XRD with the strongest peaks of (101) using Scherrer's equation, giving the value of 27 nm, 19 nm, 20 nm, and 24 nm for the pure sample TiO<sub>2</sub> NFs, TiO<sub>2</sub>-Au-i, TiO<sub>2</sub>-Au-ii, and TiO<sub>2</sub>-Au-iii, respectively. Even if those mean sizes are quite homogeneous versus the experimental routes, it should also be interesting to study for each sample the crystallographic planes of TiO<sub>2</sub> NPs (or seeds) at the early stage of the calcination process.

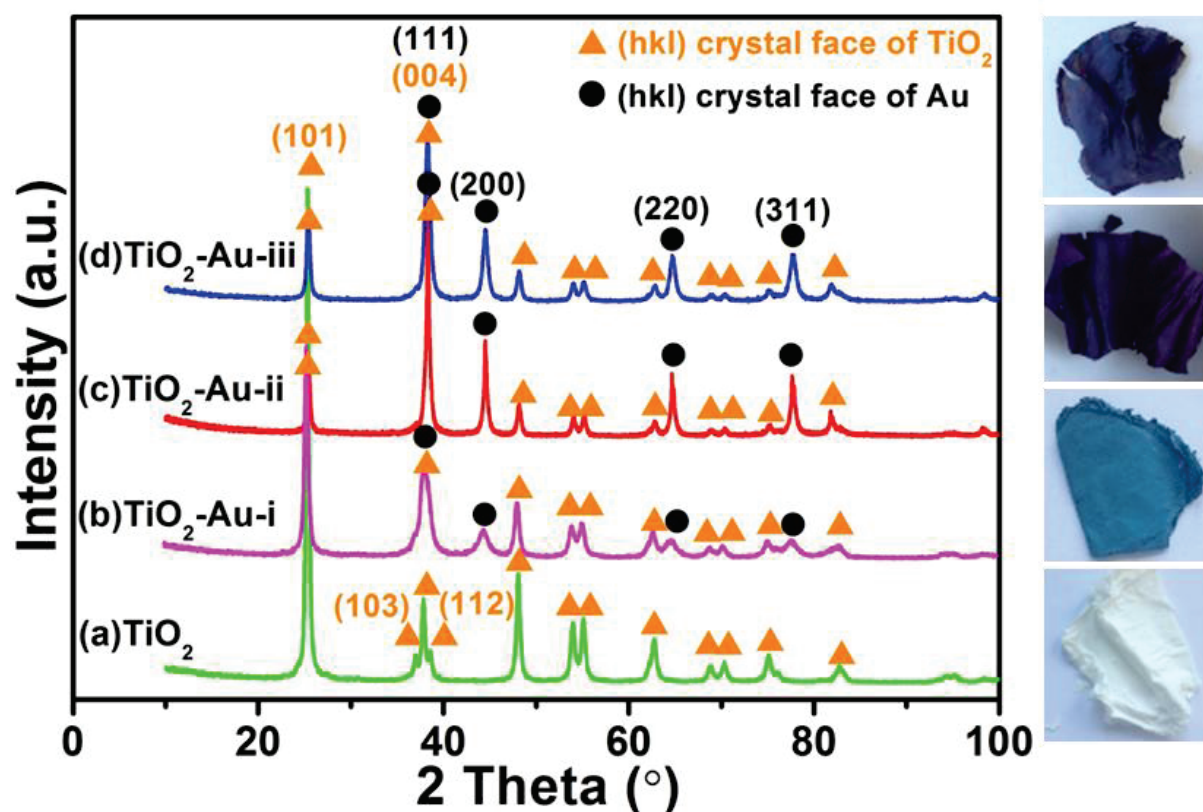


Figure 4.10 XRD patterns of  $\text{TiO}_2$ -Au composite NFs fabricated with different Au introducing routes: (a)  $\text{TiO}_2$ ; (b)  $\text{TiO}_2$ -Au-i; (c)  $\text{TiO}_2$ -Au-ii; (d)  $\text{TiO}_2$ -Au-iii.

Concerning the crystallographic structures obtained for each sample at the end of the experimental procedure introducing XRD patterns (Figure 4.10) exhibit peaks of Au (typically at  $38.2^\circ$ ,  $44.4^\circ$ , and  $64.6^\circ$  corresponding to the (111), (200), and (220) planes of the cubic gold phase, JCPDS Card No. 00-004-0784) and  $\text{TiO}_2$  (Anatase phase, JCPDS Card No. 00-021-1272). For each sample, we have added in the inset, its corresponding optical pictures exhibiting various colorations. It is well-known that this coloration is mainly due to the presence of Au NPs that enlarge the absorbance range of the resulting NFs from UV to visible light domain. For pure  $\text{TiO}_2$  NFs, it is not surprising to find the white color of pure  $\text{TiO}_2$ . The color of sample  $\text{TiO}_2$ -Au-i changed from white to blue to well-dispersed Au NPs with uniform size around 10 nm. The sample of  $\text{TiO}_2$ -Au-ii is purple, due to Au NPs size around 38 nm. For the sample of  $\text{TiO}_2$ -Au-iii, the color turns to dark blue because Au NPS are larger with non-uniform shape and sizes.

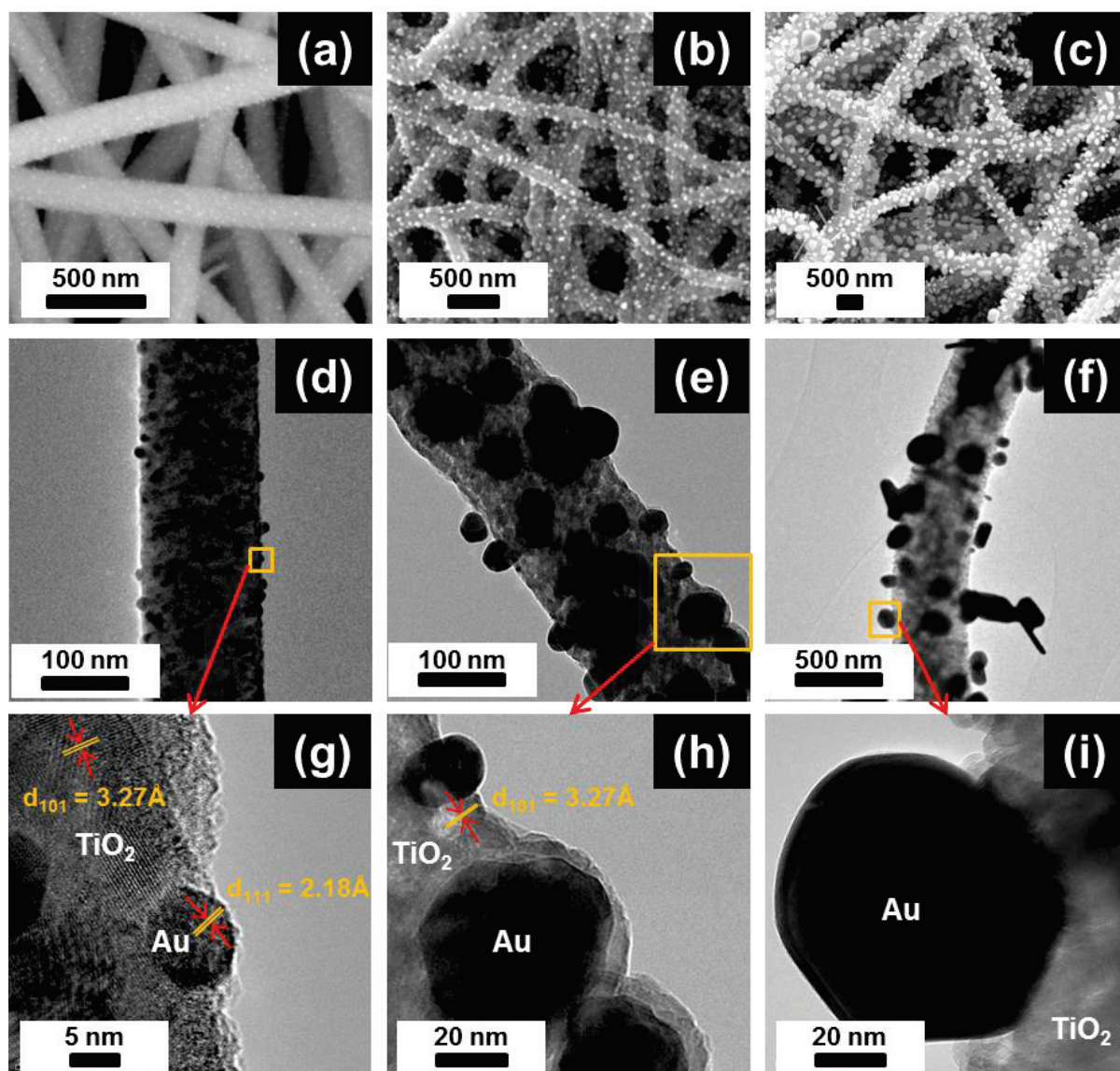
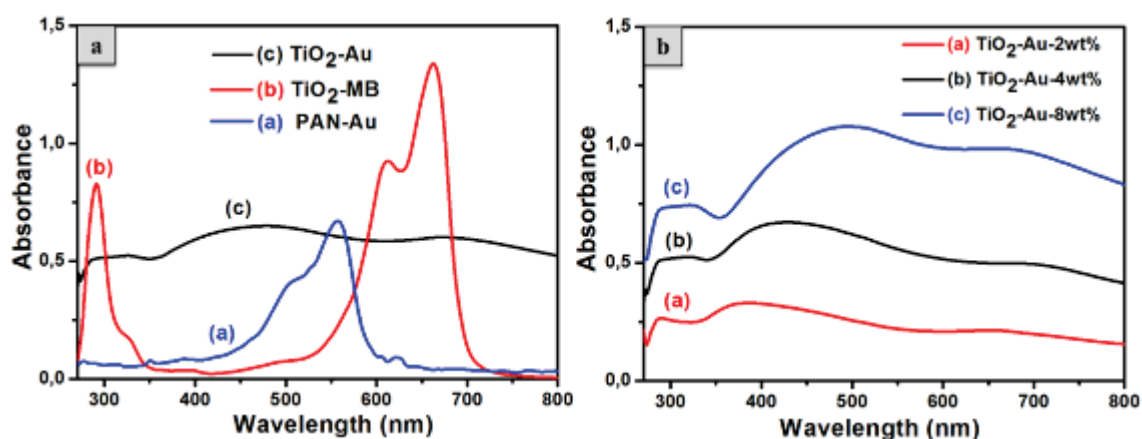


Figure 4.11 TEM & HR-TEM images of TiO<sub>2</sub>-Au NFs fabricated from different Au introducing routes: (a), (d) volume inclusion (i); (b), (e) surface deposition (ii); (c), (f) surface deposition (iii), respectively.

The different morphologies and detailed structures of TiO<sub>2</sub>-Au composite NFs obtained from the three different introducing routes are studied by electron microscopy in conventional mode (TEM) and high resolution one (HRTEM). TiO<sub>2</sub>-Au-i, TiO<sub>2</sub>-Au-ii, and TiO<sub>2</sub>-Au-iii samples are shown on Figure 4.11 a, b, and c respectively. For the sample TiO<sub>2</sub>-Au-i obtained from ES directly, the Au NPs are homogeneously dispersed in the volume of TiO<sub>2</sub> NFs with uniform size around 10 nm. Both Au and TiO<sub>2</sub> are well crystallized. On Figure 4.11d, Moire fringes can be observed, confirming the high level of TiO<sub>2</sub> crystallinity. The interface of TiO<sub>2</sub>-Au reveals that the lattices of Au and TiO<sub>2</sub> are in close contact, indicating that strong interactions between Au and TiO<sub>2</sub> have been established during the mild annealing process.

The crystallographic plane of (111) of gold (JCPDS No. 00-004-0784) is clearly observed with the corresponding lattice distances at 2.18 Å. Moreover, the crystallographic plane (101) of anatase (JCPDS Card No. 00-021-1272) with the corresponding lattice distances 3.27 Å is also present confirming the tetragonal structure of TiO<sub>2</sub> (Anatase phase).

As shown in Figure 4.12a, the curve (a) of PAN-Au composite NFs has a broad adsorption peak around 560 nm due to gold particles whereas PAN polymer has no adsorption of the UV-visible light. This is typical plasmon bands from gold NPs. From this peak we can conclude to the presence Au NPs within the PAN polymer NFs, which are similar in size and location for TiO<sub>2</sub>-Au composite NFs, just changing the matrix from polymer PAN to metallic oxide TiO<sub>2</sub>. For curve (b) in Figure 4.12a, there are characteristic adsorption peaks located at ~300 nm for TiO<sub>2</sub>, and ~ 613 nm, ~ 663 nm for MB molecular. With the ES technique and subsequence thermal treatment, TiO<sub>2</sub>-Au composite NFs are obtained. This composite sample can be considered as the mixture of TiO<sub>2</sub> NFs and Au NPs with the same dimension. To disperse TiO<sub>2</sub>-Au composite NFs in aqueous solution, the obtained curve is shown in Figure 4.12a curve (c). The typical sharp peak of TiO<sub>2</sub> located at ~300 nm become broader with low intensity, while the absorption peak of Au around 560 nm disappeared with a broader adsorption peak around 425 nm.



**Figure 4.12** (a) UV-visible absorption spectra of PAN-Au NFs, TiO<sub>2</sub> NFs dispersed in MB aqueous solution, and TiO<sub>2</sub>-Au composite NFs; (b) TiO<sub>2</sub>-Au NFs with different Au contents: TiO<sub>2</sub>-Au-2wt%, TiO<sub>2</sub>-Au-4wt%, TiO<sub>2</sub>-Au-8wt%.

The base line of sample TiO<sub>2</sub>-Au composite is at higher level with the value around 0.47, which can be attributed to the scattering of light from particles coming from the NFs. This scattering influence is treated as the background to study the effect of Au contents in TiO<sub>2</sub> NFs as shown in Figure 4.12b. The UV-visible absorption spectra of samples TiO<sub>2</sub>-Au-2wt%, TiO<sub>2</sub>-Au-4wt%, and TiO<sub>2</sub>-Au-8wt% are shown as curves (a), (b), and (c), respectively. All the

peaks around ~300 nm for TiO<sub>2</sub> is wide, as increasing the Au contents, the absorption peak become wider with increasing intensity, which could be due to heterogeneous plasmon coupling between metallic particles and with the matrix. As increasing the Au contents, the broader peak around 380 nm of TiO<sub>2</sub>-Au-2wt% have a red-shift to 425 nm for TiO<sub>2</sub>-Au-4wt%, and 500 nm for TiO<sub>2</sub>-Au-8wt%. All these plasmon bands were notable broader than those of Au NPs within PAN polymer NFs, which was due to plasmon coupling. The absorption peak position have a red-shift as the Au contents increased, the distance between each Au NPs decreased while is little change for the matrix of TiO<sub>2</sub> NFs. The visible light absorption rising from the surface plasmon resonance effect of Au NPs is capable of enhancing the photocatalytic activities of the TiO<sub>2</sub> NFs.

### 3.4 Conclusions

TiO<sub>2</sub>-Au composite NFs with Au NPs uniform in size and homogenously dispersed can be fabricated by a facile and controllable method of combination ES with subsequent thermal treatment for *in situ* Au reduction. The experimental parameters of thermal temperatures and Au concentration were studied based on Au introducing route of volume inclusion (i). For the influence of thermal temperatures, the Au NPs form at low temperature below 200°C with uniform size of 10 nm. At 500°C, all the polymer components were removed, meanwhile, the formation of TiO<sub>2</sub>-Au composite NFs with diameter of 171 nm and Au NPs size of 10 nm are obtained after calcination. The initial concentration of Au aqueous solution can adjust the final Au contents in the composite with the same size of Au NPs around 10 nm. The higher the concentration, the more Au NPs we obtain, dispersed in TiO<sub>2</sub> NFs. Three different Au introducing routes can fabricate different nanostructures of TiO<sub>2</sub>-Au composite NFs. The key point for these introducing routes is the starting point for introducing Au ions. Volume inclusion (i), surface deposition (ii), and surface deposition (iii) are introducing Au with solution, polymer, and crystallite TiO<sub>2</sub>, these different phases lead different size, structures and location of Au.

## 4 Photocatalytic performance

Considering the previous study dedicated to the morphology and structure of TiO<sub>2</sub>-Au NFs samples obtained with the three different routes, we follow the same strategy in order to investigate the photocatalytic performances of each sample as a function of experimental parameters like TTIP concentration, the balance between anatase and rutile phase and Au NPs sizes and shapes.

### 4.1 Influence of concentration of titanium precursor

The photocatalytic performance of pure TiO<sub>2</sub> NFs obtained with different concentration of TTIP was evaluated by photodegradation of methylene blue (MB). This material, normally used in the dye industries, is used as benchmark in many photocatalytic experiments, Figure 4.13 shows the absorption spectra of MB solution under UVA light irradiated photocatalysis of TiO<sub>2</sub>-9:3 (a), TiO<sub>2</sub>-9:10 (b), and TiO<sub>2</sub>-9:30 NFs (c). The characteristic absorption double peaks of the MB molecules in water located at ~ 613 nm and ~ 663 nm weakened gradually with time and almost fully degraded after ~ 40 min. There is no significant difference among these three samples, although their average diameter and mesoporous surface are different. During the photocatalytic experiment preparation, the ultrasonic bath used to make well dispersed NFs in water for each samples before photocatalysis experiment is probably responsible of this first smoothing result. This ultrasonic process, by reducing the NFs length could weaken the influence of the morphology.

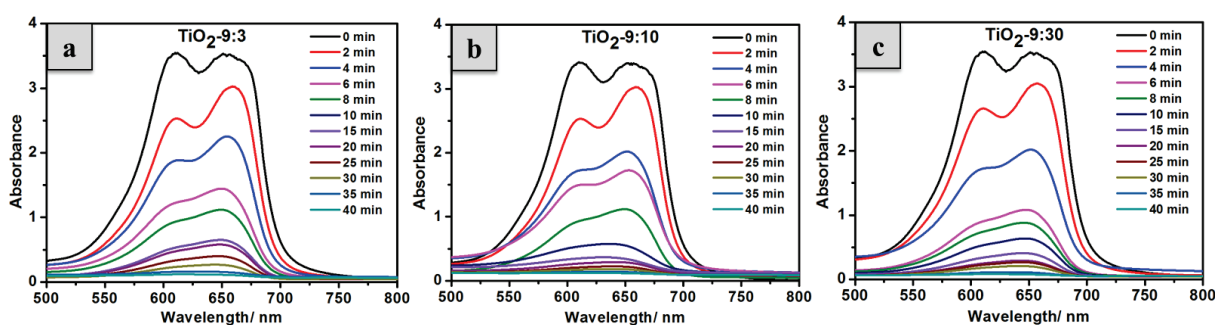


**Figure 4.13** UV-Vis absorption spectra of MB aqueous solution in photodegradation process under irradiation of UVA light in the presence of TiO<sub>2</sub> NFs obtained by heat treatment of PVP-TTIP as-spun composite NFs prepared with different concentration of TTIP by ES: (a) 9:3; (b) 9:10; (c) 9:30.

As a further confirmation, Figure 4.14 shows the degradation rate toward MB dye by using pure TiO<sub>2</sub> NFs prepared with different concentration of TTIP. For the three samples, similar photocatalytic activities of the MB are observed that indicates the slight influences of the concentration of TTIP on the photocatalysis performance, although the fibers morphology and diameter have changed. According to the curves, there are two clearly behavior can be obvious. Before 10 mins, the degradation of MB is rapidly, while it slows down after 10 mins. This can be explained with two key points determine the reaction time of photocatalysis: diffusion time of dye transport from the solution to the surface of catalyst, and the absorption time of catalyzed reaction with dye molecule. At the beginning of the photocatalytic process dye concentration is high, and limiting factor is thus the reaction time. As the photocatalysis reaction carry on, the concentration of dye decreases due to the photocatalytic degradation. In this case, the limiting factor for the kinetic is the diffusion of dye from the solution to the catalysts, which seem to occur after 10 min.

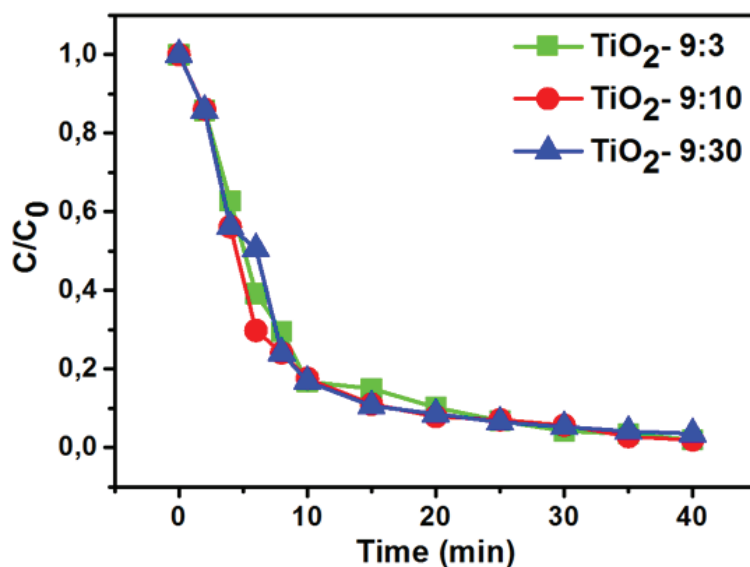
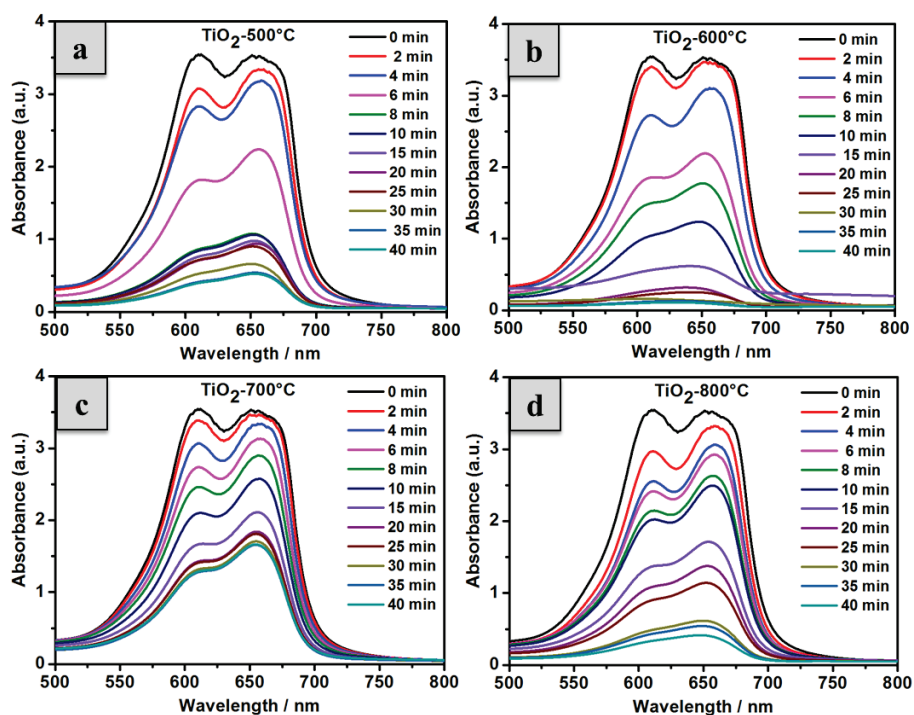


Figure 4.14 Variation of normalized  $C/C_0$  (a) of MB concentration as a function of UV light irradiation time for TiO<sub>2</sub>-9:3, 9:10, and 9:30.

## 4.2 Influence of anatase and rutile phase

Figure 4.15 shows the absorption spectra of MB solution under UVA light irradiated photocatalysis of TiO<sub>2</sub>-500°C (a), TiO<sub>2</sub>-600°C (b), TiO<sub>2</sub>-700°C (c), and TiO<sub>2</sub>-800°C NFs (d). The characteristic absorption double peaks of the MB molecules in water located at ~ 613 nm and ~ 663 nm weakened gradually with time and almost fully degraded after ~ 40 min for samples of TiO<sub>2</sub>-500°C and TiO<sub>2</sub>-600°C (Figure 4.15a and b). In the first 10 mins, the absorbance of sample TiO<sub>2</sub>-500°C is much lower than the other three samples and the reaction time is determined by the absorption of dye reacting with the catalyst. As a consequence, it is quite reasonable to say that the degradation efficiency of samples TiO<sub>2</sub>-500°C is better than for the other samples. This can be attributed to the phase ratio between Anatase and Rutile (A/R) in these samples. Indeed, the main phase of sample TiO<sub>2</sub>-500°C is anatase with a ratio A/R is 98:2, while this ratio is only of 13:87 and 12:88 for sample TiO<sub>2</sub>-700°C and TiO<sub>2</sub>-800°C, respectively. Sample TiO<sub>2</sub>-600°C with a ratio A/R around 84:16 gives comparable photocatalytic performance to the one of the sample TiO<sub>2</sub>-500°C. Those results are not in agreement with the common idea that a mixture of anatase and rutile can enhance photocatalytic behavior by facilitating the electron transfer between those two phases for photo-oxidative reaction [170], [171].



**Figure 4.15** UV-Vis absorption spectra of MB aqueous solution in photodegradation process under irradiation of UVA light in the presence of TiO<sub>2</sub> NFs obtained with different temperatures: (a) 500°C; (b) 600°C; (c) 700°C; (d) 800°C.

As a further confirmation, Figure 4.16 shows the corresponding degradation rate toward MB dyes by using pure TiO<sub>2</sub> NFs prepared with different temperatures. The variation of normalized  $\ln(C/C_0)$  is divided in two parts: within 20 mins and more than 20 mins. The catalytic reduction reactions confirm to the pseudo-first-order kinetics within 20 mins and more than 20 mins separately. The photocatalytic efficiency could also be estimated based on the equation:  $K = -\ln(C/C_0)/t$ , where  $K$  is the reaction rate constant,  $C/C_0$  is the ratio of absorbance values corresponding to the characteristic peaks of different dyes before and after photocatalysis and  $t$  is the reaction time [172]. The reaction rate constants  $k$  within 20 mins are 0.1338, 0.1329, 0.0035, and 0.0491  $\text{min}^{-1}$  for TiO<sub>2</sub>-500°C, TiO<sub>2</sub>-600°C, TiO<sub>2</sub>-700°C, and TiO<sub>2</sub>-800°C respectively. The catalytic activity of TiO<sub>2</sub>-500°C NFs is superior to the ones obtained with others annealing temperatures. This is explained by the fact that the calcination temperature can vary both the morphology and A/R phase ratio of TiO<sub>2</sub>.

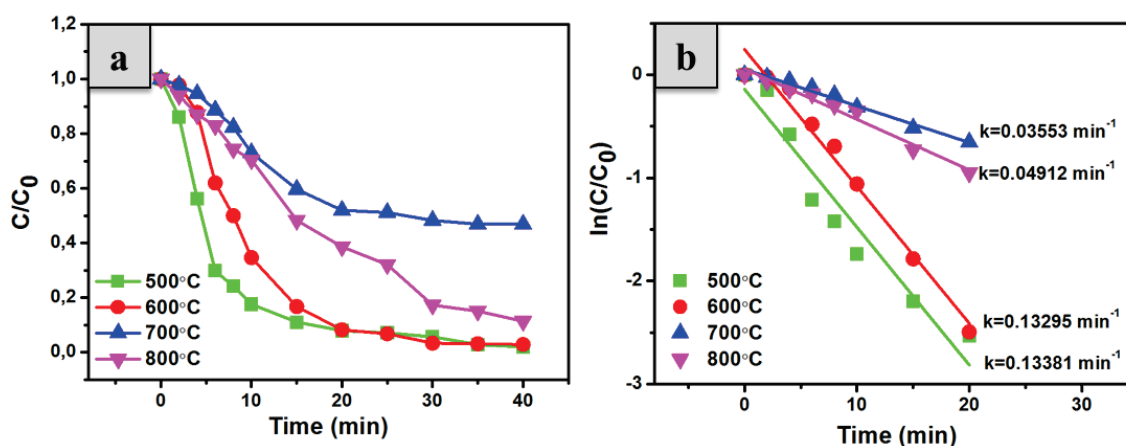


Figure 4.16 (a) Variation of normalized  $C/C_0$  and (b) variation of normalized  $\ln(C/C_0)$  of MB concentration as a function of UV light irradiation time for TiO<sub>2</sub> heated at 500 °C, 600 °C, 700 °C and 800°C, respectively.

However, we observe that after 20 mins, whatever the samples, the photocatalytic activity remains constant without further evolution. There is no more significant difference among these catalysts after reaction with dyes under UVA irradiation. This might be due to the absorption of MB dyes on the surface of catalysts during the reactions and the remaining concentration of dyes in the solution. Indeed, as extending the duration experiment, the reacting rate is mainly related to the concentration of dyes than to the reacting activity sites of catalysts. The reaction rate is limited by the remaining concentration of dyes in the solution.

### 4.3 Influence of Au nanoparticles

By comparison with the previous result, the presence of the TiO<sub>2</sub>-Au catalysts in the solution seems to cause a rapid discoloration of MB solution from bright yellow to colorless. As a consequence, the intensity of the characteristic absorption peaks of MB at ~ 613 nm and ~ 663 nm quickly decreases in the first 5 mins, which is 5 times quicker than in the case of pure TiO<sub>2</sub> NFs under the same test conditions. The photocatalytic behavior shown in Figure 4.17 indicates that after 20 mins of photocatalytic reaction, the MB molecules could be fully degraded using the TiO<sub>2</sub>-Au. All the catalysts of TiO<sub>2</sub>-Au composite NFs have better photocatalytic activities than the one of pure TiO<sub>2</sub> NFs.

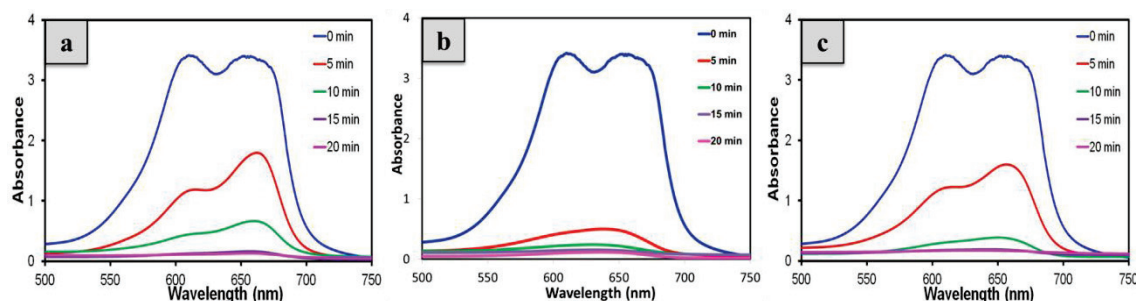


Figure 4.17 UV-Vis absorption spectra of MB aqueous solution in photodegradation process under irradiation of UVA light in the presence of TiO<sub>2</sub>-Au composite NFs with different Au contents: (a) TiO<sub>2</sub>-Au-2wt%; (b) TiO<sub>2</sub>-Au-4wt%; (c) TiO<sub>2</sub>-Au-8wt%.

The catalytic activity of TiO<sub>2</sub>-Au samples are closely related to the Au NPs contents in TiO<sub>2</sub>-Au hybrid NFs. As the Au content increasing, the number of Au NPs in TiO<sub>2</sub> support increases resulting the higher total catalytic capacity, that's why TiO<sub>2</sub>-Au-4wt% has better photocatalytic performance than TiO<sub>2</sub>-Au-2wt%. Smaller Au NPs show higher catalytic activity, as demonstrated previously [173]. Due to the small size of Au NPs (around 10 nm), the fraction of coordinately unsaturated surface atoms is highly catalytically active. However, the Au content is not the higher the performance the better. The Au content increases from 4wt% to 8wt%, the photocatalytic performance decreases. This can be attributed to the recommendation of h<sup>+</sup>/e<sup>-</sup> pairs by Au NPs as the active sites. So there should be optimized balance between the positive affection of offer active sites and negative affection of recommendation of h<sup>+</sup>/e<sup>-</sup> pairs by Au NPs to functionalize the TiO<sub>2</sub> NFs. Among these three different Au contents, Therefore, TiO<sub>2</sub>-Au-4wt% is the best sample for photocatalysis performance of MB.

TiO<sub>2</sub>-Au-4wt% contains more Au NPs than TiO<sub>2</sub>-Au-2wt%, thus generating more active oxygen vacancy electron pairs, and then better photocatalytic performance. However, the catalyst of TiO<sub>2</sub>-Au-8wt%, with the highest Au contents has worst performance compared to TiO<sub>2</sub>-Au-4wt%. It can be explained for the two roles of Au NPs in TiO<sub>2</sub>: generate oxygen vacancy/electron pairs and recombination center to gather the vacancy/electron pairs. So, when the Au NPs concentration is higher than a critical value, the recombination effect plays the main role, which would limit the photocatalysis efficiency. Gold NPs are also strong UV absorbers, and it cannot be excluded that if gold exceed a certain amount, it will screen absorption from TiO<sub>2</sub> and thus lower photo-activity from the Au-TiO<sub>2</sub> NFs, which would explain a lowering of the catalytic activity for TiO<sub>2</sub>-Au-8wt% fibers.

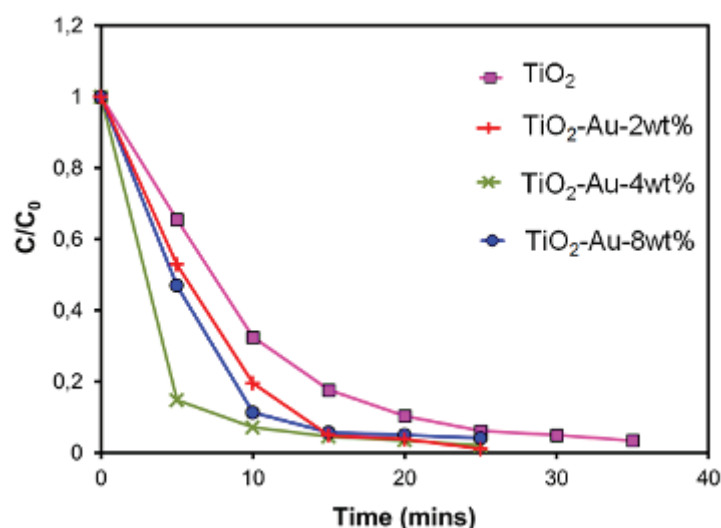


Figure 4.18 Variation of normalized  $C/C_0$  of MB concentration as a function of UV light irradiation time for pure TiO<sub>2</sub> NFs and TiO<sub>2</sub>-Au composite NFs with different Au contents: (a) 2wt%; (b) 4wt%; (c) 8wt%.

#### 4.4 Influence of experimental routes

In order to determine the more efficient experimental procedure to get photocatalysts with the highest performances, we only compare results obtained with samples TiO<sub>2</sub>-Au-i, TiO<sub>2</sub>-Au-ii and of course pure TiO<sub>2</sub> NFs. Due to its large dispersion in Au NPs sizes and shapes, the sample of TiO<sub>2</sub>-Au-iii is not selected. Indeed, large and inhomogeneous Au NPs are not suitable for plasmon resonance or to generate oxygen vacancy/electron pairs.

As shown in Figure 4.19, the photocatalytic performance of TiO<sub>2</sub>-Au-ii composite NFs is close to the pure TiO<sub>2</sub> NFs. In this case, we see clearly that even for small Au NPs (38 nm) onto the fiber surface (Insert Figure 4.19) there are no sufficient interactions between TiO<sub>2</sub>

and Au that could enhance the photocatalytic effect. In others words, the common surface of matter shares by the two components (Au and  $\text{TiO}_2$ ) is clearly too reduced. As a consequence, this catalyst is quite similar from pure  $\text{TiO}_2$  in the solution with some useless large Au NPs. Concerning the  $\text{TiO}_2$ -Au-i composite NFs catalyst, the photocatalytic activity is highly enhanced within the first 10 min compared to pure  $\text{TiO}_2$  and  $\text{TiO}_2$ -Au-ii samples. This sample contains smaller Au NPs (10 nm) located in the volume of  $\text{TiO}_2$  fibers. In this case, the interface between  $\text{TiO}_2$  and Au is really important and sufficient for the electron transfer and to enhance the photocatalytic performance.

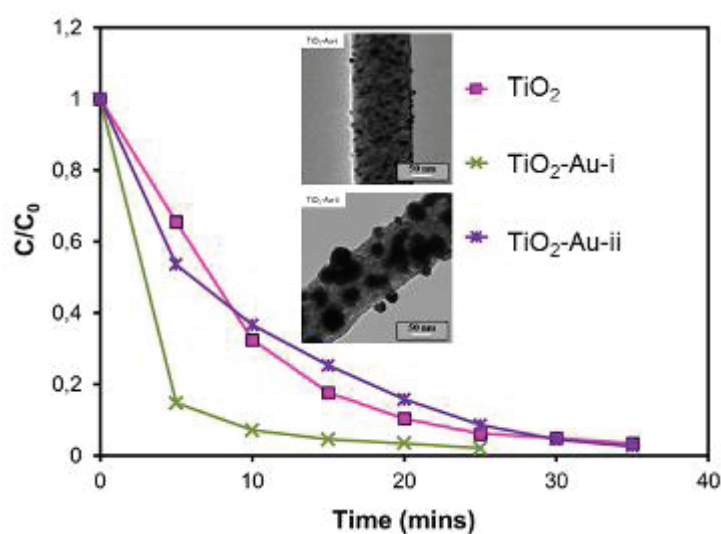


**Figure 4.19** Variation of normalized  $C/C_0$  of MB concentration as a function of UV light irradiation time for  $\text{TiO}_2$ -Au composite NFs obtained from different Au introducing routes: pure  $\text{TiO}_2$  NFs,  $\text{TiO}_2$ -Au-i, and  $\text{TiO}_2$ -Au-ii.

#### 4.5 Comparison with P25

In order to evaluate the real photocatalytic performance of electrospun  $\text{TiO}_2$  and  $\text{TiO}_2$ -Au composite NFs, we have compared the previously discussed results with those obtained in the same condition with commercial catalysts named “P25” (as shown in Figure 4.20). The composition of P25 is anatase and rutile crystallites with the reported ratio typically of 70:30 or 80:20, which is not exactly crystalline composition. P25 is used widely as a de-facto standard titania photocatalysts because of its relatively high levels of activity in many photocatalytic reaction systems and it is not easy to find a photocatalyst showing activity higher than that of P25 [174].

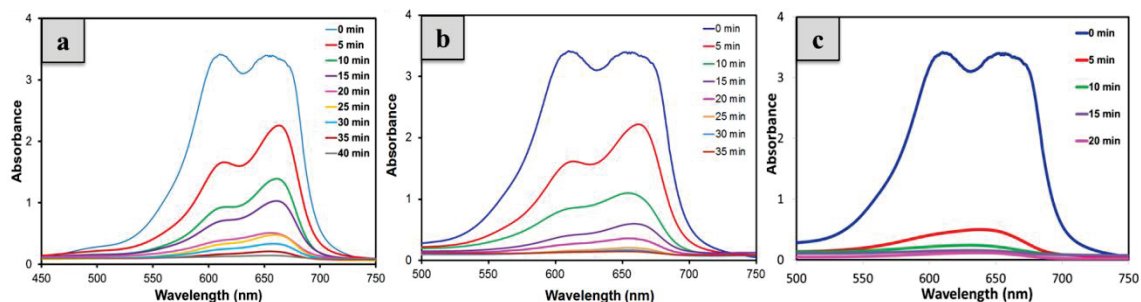


**Figure 4.20** UV-Vis absorption spectra of MB aqueous solution in photodegradation process under irradiation of UVA light in the presence of different catalysts: (a) P25; (b) TiO<sub>2</sub> NFs; (c) TiO<sub>2</sub>-Au.

As we discussed in Figure 4.14, there are two important factors of diffusion rate and absorption rate during the degradation process of MB. At the beginning, the absorption rate of the catalysts to react with the dye is the determine factor, which plays more important influence than the diffusion rate of the dye transport from the solution to the catalysts. With the photocatalysis process carried on, the concentration of dye decrease as the dye decomposed by catalyst. In this case the diffusion rate comes to be the determine factor for the photocatalytic activity. The degradation with TiO<sub>2</sub>-Au composite NFs is obviously faster than P25 within an interval of 5 min, while pure TiO<sub>2</sub> NFs is quite similar to P25. After 10 min, TiO<sub>2</sub>-Au composite NFs have already decomposed the MB entirely and color solution changes from blue to transparent. In addition, the performance of P25 and pure TiO<sub>2</sub> NFs are very similar, demonstrating that the morphology is not necessarily a key parameter to enhance photocatalytic performances. Obviously, this last comment has to be relativized in regard to the specific surface area that is quite different from one sample to another.

During this first step, the concentration of MB dye is still high and offers more chance for the dye molecule to adsorb on the catalyst. So the adsorption rate of MB molecule is a critical factor at the early stage of the reaction. Due to the absence of Au additions of TiO<sub>2</sub>-Au composite catalysts, it offers more activity sites for reactions and can attract more molecules of dye, which related to the excellent performance for degradation of MB. As the reaction is proceeding, the concentration of MB decrease due to degradation by the catalysts, there are less residued MB molecules in the aqueous solution. The chance for adsorbing the MB molecules is the determining factor and it is all the same for each sample. So the photocatalytic performance of P25 and pure TiO<sub>2</sub> NFs are close to each other at the end with the totally degradation time of 40 mins and 35 mins, respectively.

**Table 4.4 Specific surface area, crystallite size and Anatase / Rutile ratio of P25, TiO<sub>2</sub> and TiO<sub>2</sub>-Au with different photocatalytic performance.**

	Specific surface area / m <sup>2</sup> ·g <sup>-1</sup>	Crystallite Size / nm	Anatase : Rutile / %	Photocatalytic / min
P25	50 ± 15	21	80 : 20	40
TiO <sub>2</sub>	17	27	98 : 2	35
TiO <sub>2</sub> -Au	33	19	98 : 2	15

As shown in Table 4.4, the crystallite size and A/R ratio of pure TiO<sub>2</sub> and TiO<sub>2</sub>-Au composite NFs are similar, but they have totally different activity for decomposing MB. The catalysts of TiO<sub>2</sub>-Au composite NFs are better than P25, although their specific surface area measured by BET is smaller than 50 m<sup>2</sup>·g<sup>-1</sup> for P25, with 33 m<sup>2</sup>·g<sup>-1</sup> for TiO<sub>2</sub>-Au. The specific surface area is an important factor for catalysts, but it is not the only influent factor determining the catalyst efficiency. Presence of Au NPs plays here an even more important role than specific surface area, crystallite size and A/R ratio affects.

As shown in Figure 4.21, the linear relationships between ln(C/C<sub>0</sub>) and the reaction time (t) are obtained in the reduction reaction catalyzed by the different catalysts among P25, pure TiO<sub>2</sub> and TiO<sub>2</sub>-Au, where C and C<sub>0</sub> are the MB concentration at time t and 0, respectively. The catalytic reduction reactions confirm to the pseudo-first-order kinetics. The reaction rate constants k, calculated from the rate equation ln(C/C<sub>0</sub>)=kt, are 0.0786, 0.0976, 0.1829 min<sup>-1</sup> for P25, pure TiO<sub>2</sub> and TiO<sub>2</sub>-Au, respectively. This approves that the catalytic activities of pure TiO<sub>2</sub> and TiO<sub>2</sub>-Au composite NFs are better than commercial P25 NPs.

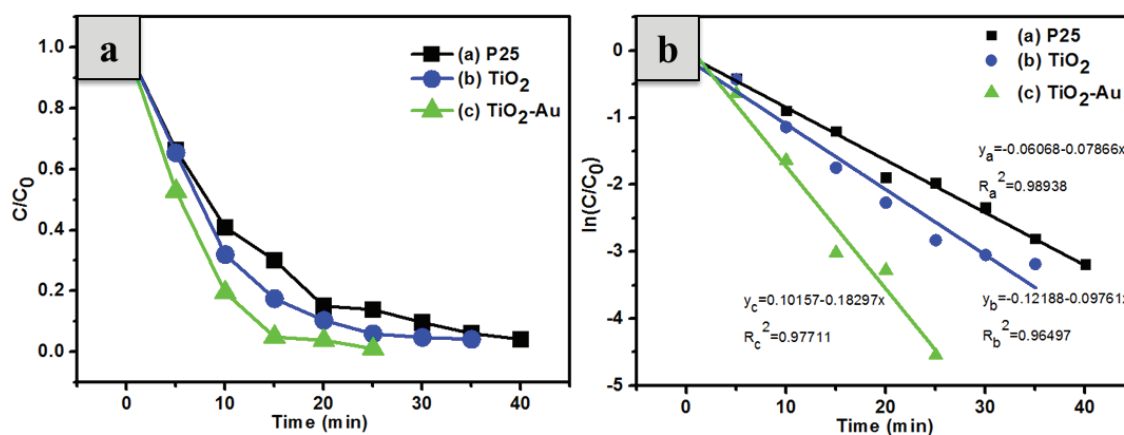


**Figure 4.21 (a) Variation of normalized C/C<sub>0</sub> and (b) variation of normalized ln(C/C<sub>0</sub>) of MB concentration as a function of UV light irradiation time for P25, TiO<sub>2</sub>, and TiO<sub>2</sub>-Au, respectively.**

#### 4.6 Photocatalysis under different wavelength irradiations

Compared with the tests under UVA irradiations, different wavelength light have been chosen for photocatalysis experiments with the TiO<sub>2</sub>-Au composite NFs, which has the best photocatalytic performance under UVA to degrade the MB dye molecules. Due to the fact that TiO<sub>2</sub> can only absorb the UV light and cannot react in the visible range, and that functionalization with Au can extend the absorption range from UV to visible range, we performed similar experiments with visible light sources. Tested wavelengths have been chosen as 360 nm in the UV range, 528 nm in the visible range, and 360 nm with 528 nm to offer UV and visible light together. As shown in Figure 4.22a, TiO<sub>2</sub>-Au catalyzes degradation of MB dyes under irradiation with the 360 nm light source, is observed by a decrease of MB molecular absorption peaks. If the light is changed from UV range to visible range, the degradation rate of TiO<sub>2</sub>-Au catalysts toward to MB slows down but it still has some photocatalysis effects. This can be attributed to the presence of gold NPs, band gap from pure TiO<sub>2</sub> only allowing UV light absorption. Still this effect is limited since reaction rate slows down compared to irradiation under pure UV light at 360 nm.

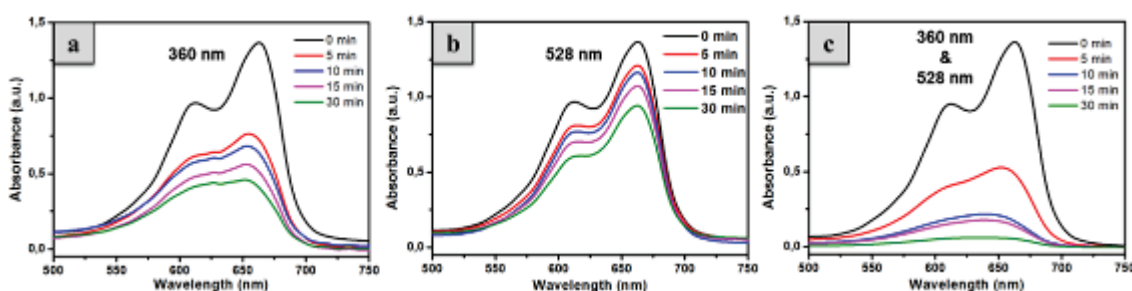


Figure 4.22 UV-Vis absorption spectra of MB aqueous solution in photodegradation process under different wavelength irradiations in the presence of TiO<sub>2</sub>-Au composite NFs: (a) 360 nm; (b) 528 nm; (c) 360 nm & 528 nm.

The irradiated lights under both 360 nm in UV range and 528 nm in visible range obviously enhance the photocatalytic performance. The color of the solution changes rapidly from blue to transparent in the first 5 mins and the degradation of MB is totally finished within 30 mins. This indicates the photocatalytic activity under UV light and visible light together is better than the irradiation under UV light or visible light separately. It proves that with the functionalization with Au, the reaction range of TiO<sub>2</sub> catalysts is enlarged from UV range to visible range. The more details about the linear relationships between  $\ln(C/C_0)$  and the reaction time (t) are shown in Figure 4.22a and b. The catalytic reduction reactions confirm to the pseudo-first-order kinetics. The reaction rate constants k as shown in Figure

4.23, calculated from the rate equation  $\ln(C/C_0)=kt$ , are 0.0115, 0.0322, and 0.0979  $\text{min}^{-1}$  for 360 nm, 528 nm and 360 nm & 528 nm, respectively.

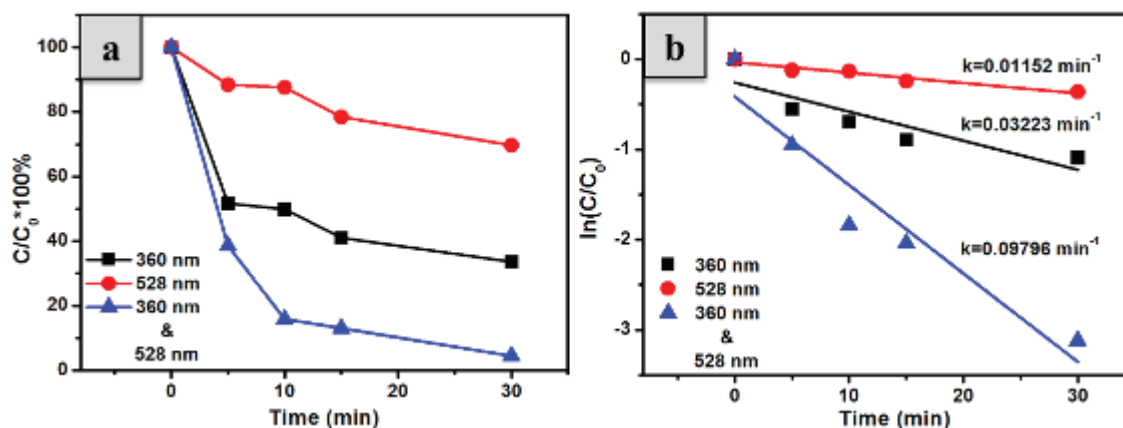


Figure 4.23 (a) Variation of normalized  $C/C_0$  and (b) variation of normalized  $\ln(C/C_0)$  of MB concentration as a function of different wavelength light irradiation time for 360 nm, 528 nm, and 360 nm & 528 nm, respectively.

#### 4.7 Photocatalytic mechanisms

Based on the experimental results, the possible photocatalytic mechanism of photocatalytic degradation of MB over the optimal sample  $\text{TiO}_2$ -Au composite NFs under UV irradiation and visible irradiation are elucidated schematically in Figure 4.24.  $\text{TiO}_2$  is “mixed” crystalline, anatase and rutile phase  $\text{TiO}_2$  particles have different conduction bands, valence bands and Fermi levels. As shown in Figure 4.24a, under a UV irradiation, the photogenerated electrons ( $e^-$ ) from VB, have excitation with the energy of UV, then transited to the CB and also produced hydroxyl radicals ( $\text{OH}\cdot$ ) in the solution by capture of an electron. The conduction band electrons ( $e^-$ ) transfer from  $\text{TiO}_2$  to Au NPs, and reacted with the dissolved oxygen molecules ( $\text{O}_2$ ) of Au to yield superoxide radical anions ( $\cdot\text{O}_2^-$ ). And then the  $\cdot\text{O}_2^-$  radicals can further react with  $\text{H}^+$  and the trapped  $e^-$  to produce  $\text{H}_2\text{O}_2$  in aqueous solution.

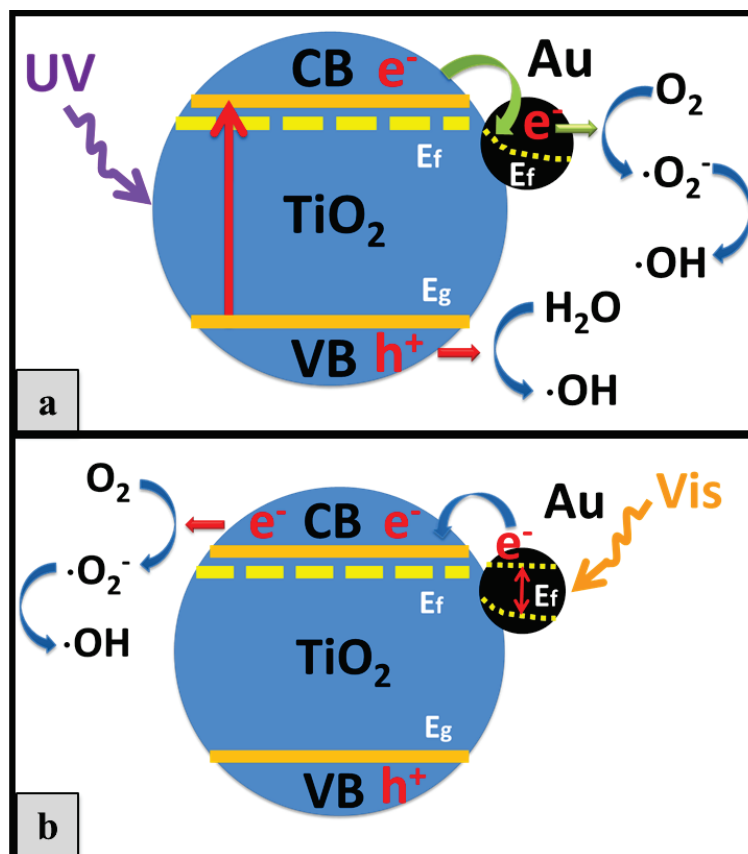


Figure 4.24 Schematic diagrams of the (a) UV irradiation and (b) visible irradiation photocatalytic degradation of MB with TiO<sub>2</sub>-Au composite NFs.

As shown in Figure 4.24b, under a visible irradiation, a charge carrier has been produced by the surface plasmon resonance effect of Au NPs into the TiO<sub>2</sub> NFs. Meanwhile there is an intense electric field at the surface of Au NPs which can separate the holes and electrons so as to avoid their recombination. The electrons transfer from an excited Au NP to a TiO<sub>2</sub> particle due to the photogenerated electrons with a more negative potential compared with the conduction band level of TiO<sub>2</sub>. As reported in the literature [175] that the migration rate is very fast less than 240 fs, thus the photogenerated electron-hole pairs can be effectively separated. The photogenerated electrons ( $e^-$ ) is injected into the CB of TiO<sub>2</sub>, the dissolved oxygen molecules ( $O_2$ ) reacted with conduction band electrons ( $e^-$ ) to yield superoxide radical anions ( $\cdot O_2^-$ ). And then the  $\cdot O_2^-$  radicals can further react with  $H^+$  and the trapped  $e^-$  to produce  $H_2O_2$  in aqueous solution. The formed  $H_2O_2$  is on protonation generated the hydroperoxy radicals ( $HO_2\cdot$ ) producing hydroxyl radicals ( $OH\cdot$ ) by capture of an electron, which are strong oxidizing agents to decompose the organic dye [176], [177]. The reactants are decomposed by the forming  $\cdot O_2^-$  and  $OH\cdot$  radicals. Meanwhile, it is found by other researchers that  $OH\cdot$  is the major active species responsible for the photocatalytic oxidation

reaction, especially for the bi-phase structure (anatase and rutile) from  $\text{TiO}_2$  with the photoluminescence technique using coumarin as a probe molecule to quantitatively characterize the  $\text{OH}\cdot$  production on  $\text{TiO}_2$  in aqueous solution [178]. This is beneficial for enhancing the formation rate of  $\text{OH}\cdot$ . We can also assume that Au- $\text{TiO}_2$  being active under both UV and moderately under visible light, combination of both logically lead us to the observed enhanced photocatalytic properties, which is an indication that we obtained a material with an extended light photo-activity range.

## 5 Conclusions

In this chapter, TiO<sub>2</sub> and TiO<sub>2</sub>-Au composite NFs were fabricated based on ES. Critical experimental parameters like concentration of Titanium precursor TTIP, thermal annealing temperatures, and Au inclusion routes were investigated. The initial concentration of TTIP can affect the fiber diameter and morphology of TiO<sub>2</sub>. The concentration of PVP:TTIP 9:30 is optimized to fabricate TiO<sub>2</sub> NFs with uniform diameter and porous surface. Calcination is another important factor to control the morphology and composition of TiO<sub>2</sub> NFs. Variable temperatures allowed us to obtain TiO<sub>2</sub> materials with different Anatase/Rutile ratio and different crystalline size. As the temperature increases from 500°C to 800°C, anatase, the low temperature stable phase transforms into rutile with the growth of crystals, which would influence the specific surface area and morphology of final NFs. Thermal treatment in air at 500°C for 2h is the best condition for calcination process to fabricate TiO<sub>2</sub> NFs with a ratio of Anatase/Rutile of 98:2, average diameter of 164 nm. By using the volume inclusion (i) method, Au is introduced at the beginning of the solution formulation and is dispersed homogeneously within PVP-TTIP ES solution. With the subsequent thermal treatment in air, Au NPs are formed at lower temperature with uniform size around 10 nm at 200°C, before the decomposition of polymer and formation of metallic oxide. The final TiO<sub>2</sub>-Au composite NFs were obtained at 500°C. The heating process plays an important role to get the target samples including the *in-situ* reduction of Au ions to form Au NPs, decomposition of PVP, and formation of TiO<sub>2</sub>. The chloroauric solution concentration introduced into the ES solution tunes the Au NPs content in the final product, although the size of Au NPs remains stable, around 10 nm in diameter. TiO<sub>2</sub>-Au composite NFs were obtained by three different Au “introducing” routes. The schematic diagram (Figure 4.25) illustrates the formation of TiO<sub>2</sub>-Au composite NFs using the three introducing experimental methods developed in this study. The gold volume inclusion (i) route leads to TiO<sub>2</sub>-Au composite NFs with homogeneous and uniform Au NPs dispersed in the volume of a TiO<sub>2</sub> matrix NF. Surface deposition (ii) can get Au NPs with nonuniform size located on the surface of TiO<sub>2</sub> NFs. Whereas gold surface deposition introducing route (iii) fabricates TiO<sub>2</sub>-Au composite NFs with several Au large nanostructures including NPs, NRs, and nanoflakes. The Au content can be adjusted by varying the concentration of HAuCl<sub>4</sub> aqueous solution. The first route of volume inclusion (i) is the best choice to fabricate TiO<sub>2</sub>-Au composite NFs with homogeneously deposited and uniform Au NPs size. Uniformly sized Au NPs (~10 nm) were then decorated on the surface of the TiO<sub>2</sub>-Au NFs as reaction sites for improving the photocatalysis performance.

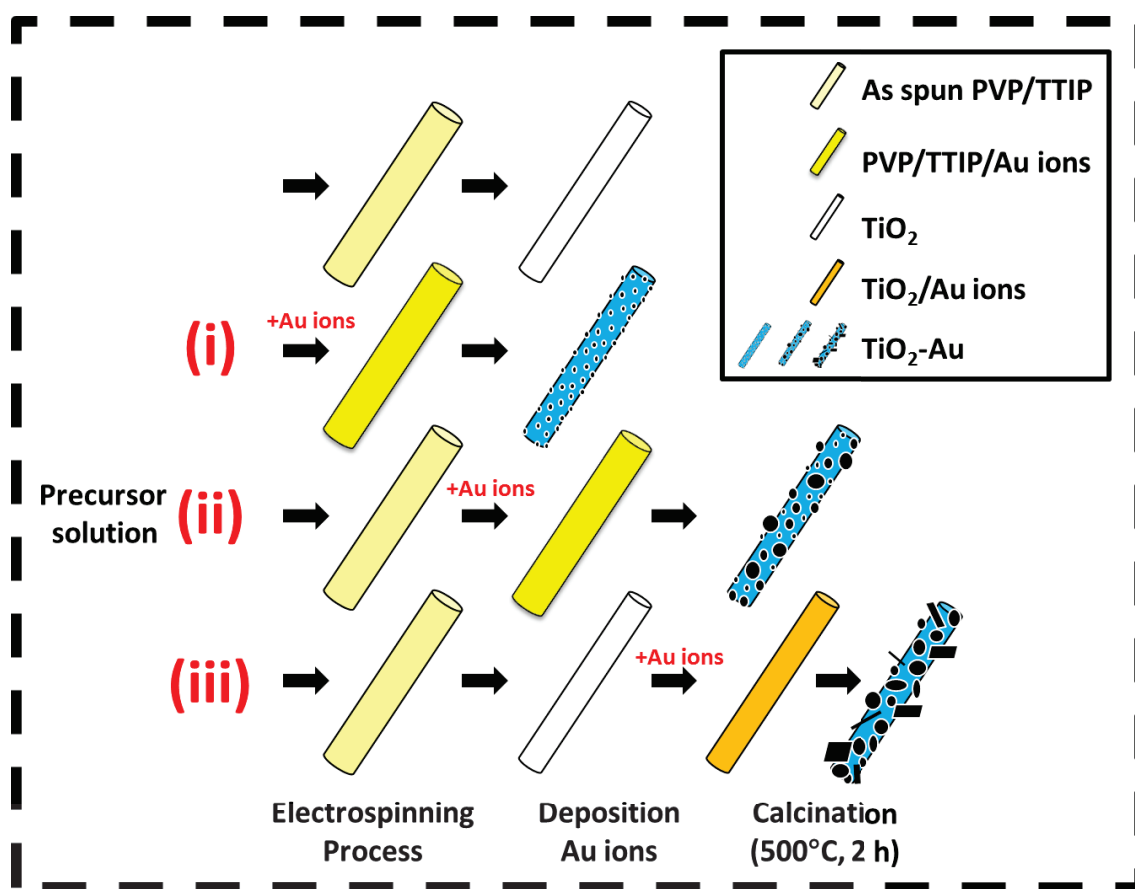


Figure 4.25 Schematic diagram illustrating the formation of TiO<sub>2</sub>-Au composite NFs.

The photocatalytic results demonstrate the excellent response of the TiO<sub>2</sub>-Au composite NF catalyst, particularly the TiO<sub>2</sub>-Au-4wt% catalyst, which exhibits ~3 times higher reaction rate and significantly improved degradation of MB aqueous solution than the pure TiO<sub>2</sub> NFs and the commercial catalysts of P25. In addition, the different irradiation wavelength has different photocatalytic performance. TiO<sub>2</sub>-Au composite catalyst under the mixture of UV light (360 nm) and visible light (528 nm) can obviously enhance the photocatalytic performance than the UVA irradiation. The photocatalytic mechanism of TiO<sub>2</sub>-Au composite NFs under UV light and visible light has been discussed. This study will benefit for the design and construction of TiO<sub>2</sub>-based composite catalyst with high performance to improve the photocatalytic activity of TiO<sub>2</sub> for various applications.

## CHAPTER V CHARACTERIZATION AND GAS SENSING ACTIVITY OF WO<sub>3</sub>-Au COMPOSITE NANOFIBERS

### 1 Introduction

Among previous studies on WO<sub>3</sub>-based sensors, many are focused on the detection of NO, NO<sub>2</sub>, H<sub>2</sub>, H<sub>2</sub>S and NH<sub>3</sub> [141], [143], [179], and only a few studies have investigated the gas-sensing performance toward VOCs, such as *n*-butanol, methanol, ethanol and acetone [144]. VOCs are numerous, varied, ubiquitous and some of them dangerous to human health or harmful to the environment [180]. Therefore, it is necessary to fabricate sensitive and selective gas-sensing materials for the VOCs detection. The catalytic functionalization of noble metal NPs onto oxide NFs has been introduced to promote gas sensing reactions by reducing the activation energy, and thereby increasing the sensing response and selectivity while also decreasing the maximum working temperature of the sensors. Particularly, *n*-butanol, which is often used in perfumes and fragrances, repellents, petroleum refineries and frequently used as a solvent for paints, coatings and natural synthetic resins, have been rarely studied comparing to others [181]. Long-term exposure to *n*-butanol may be hazardous as it acts as a depressant to the central nervous system. Noble metals such as Pd, Pt and Au are known to be used as catalysts for gas activation [150]. Therefore, the WO<sub>3</sub> NFs functionalized by Au NPs is an effective method for enhancing the sensing response of WO<sub>3</sub> NFs and ES is a highly attractive method for the large scale synthesis of such composite NFs. For all these reasons, we have focused our efforts to develop a facile approach to fabricate WO<sub>3</sub>-Au composite NF gas sensors by ES for the sensitive and selective detection of volatile *n*-butanol, and to understand the mechanisms behind the enhanced performance of the WO<sub>3</sub>-Au composite NFs.

In this chapter, the first research point is focusing on the calcination atmosphere, which plays a crucial role on the morphologies and compositions of WO<sub>3</sub> NFs. The products obtained from three different starting polymers (such as PVP, PVA, PAN) and calcination atmospheres (including air, reducing gas H<sub>2</sub>, inert gas N<sub>2</sub>) were investigated by SEM combined with EDS to determine their morphologies and components. The section 2 and 3 are focused on the influence experimental parameters of WO<sub>3</sub> and WO<sub>3</sub>-Au NFs, including the different starting polymers, calcination atmosphere and temperatures, Au addition routes and Au concentration. The morphologies and compositions of related WO<sub>3</sub> and WO<sub>3</sub>-Au

composite NFs were described in section 4 and 5, respectively. The gas-sensing performance of Au-functionalized  $\text{WO}_3$  composite NFs toward different gases (methanol, ethanol, acetone and *n*-butanol) has been investigated in section 6. And it was focused on *n*-butanol due to its excellent sensitivity compared to other gases, such as operating temperatures, response ( $T_{\text{res}}$ ) and recovery ( $T_{\text{rec}}$ ) times, and stability. Meanwhile the mechanism of gas sensing was discussed. The conclusions and respective of  $\text{WO}_3$ -Au composite NFs as gas sensor materials were mentioned in the final section.

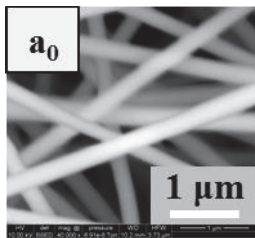
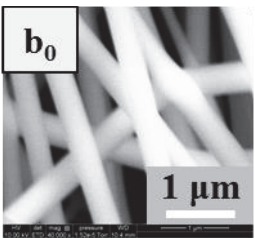
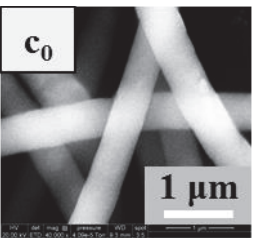
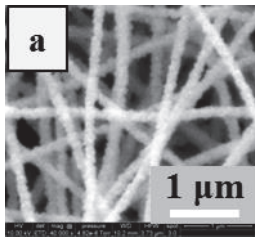
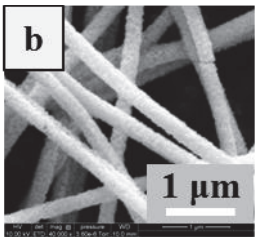
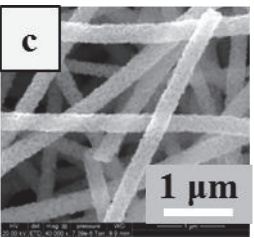
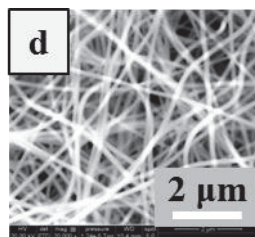
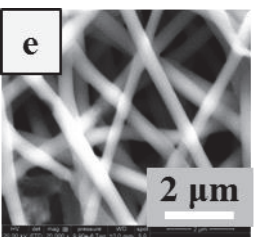
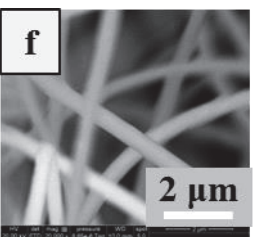
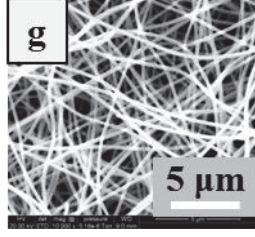
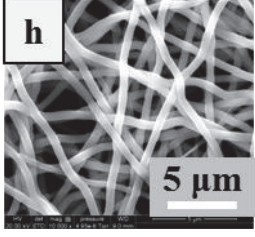
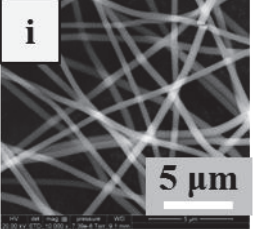
## **2 Influence experimental parameters for $\text{WO}_3$ nanofibers**

In Table 5.1, all the polymer-AMT (Ammonium metatungstate hydrate) as-spun composite NFs obtained after a typical ES process by dissolving an amount of AMT in polymer-solvent ES solutions (including PVP-EtOH, PVA- $\text{H}_2\text{O}$ , and PAN-DMF), were calcined in air at  $500^\circ\text{C}$  for 2 h in air,  $\text{H}_2$ , and  $\text{N}_2$ , respectively. The optimized ES conditions are showing in after calcination, target products had morphologies and compositions depending on the starting polymers and calcination atmospheres; and the related products were investigated by SEM combined with EDS. The average diameters of the composite NFs were determined with Nano measurement software based on 50 fibers.

### **2.1 Influence of starting polymers**

The as-spun polymers-AMT composite NFs (including PVP-AMT, PVA-AMT, and PAN-AMT as shown in Table 5.1 images a0, b0, and c0) are continuous and have smooth surface due to the natural properties of polymer with the average diameters of 286 nm, 453 nm, and 548 nm, respectively. With the same ES conditions, by choosing PVP as the starting polymer we can obtain NFs more tenuous than with PVA and PAN. After the calcination in different atmospheres such as air,  $\text{H}_2$ , and  $\text{N}_2$ , the average diameter of the samples treated in air decreased dramatically to 170 nm, 258 nm, and 271 nm for PVP, PVA, and PAN, respectively, as shown in Table 5.1 images a, b, and c. This is due to the decomposition of polymer components in air. Meanwhile, the surface of fiber became rough as the formation of  $\text{WO}_3$ , which was determined later by EDS and XRD results.

Table 5.1 Diameters and components of WO<sub>3</sub> NFs fabricated from different polymers and atmospheres.

Sample	PVP-AMT			PVA-AMT			PAN-AMT			Products	
SEM of As-spun NFs										Polymers -AMT	
SEM of Calcined NFs (500°C, 2h)	air										WO <sub>3</sub>
	H <sub>2</sub>										WC & WC with oxygen for PAN
	N <sub>2</sub>										Mixture of WO <sub>3</sub> , WC with nitrogen for PAN
ES Conditions		/ kV	/ cm	/ mL·h <sup>-1</sup>	/ kV	/ cm	/ mL·h <sup>-1</sup>	/ kV	/ cm	/ mL·h <sup>-1</sup>	
		10	10	0.2	10	10	0.2	6.5	10	0.2	
Atmosphere		air	H <sub>2</sub>	N <sub>2</sub>	air	H <sub>2</sub>	N <sub>2</sub>	air	H <sub>2</sub>	N <sub>2</sub>	
EDS Result Atom %	W	33,12	25,28	18,80	31,39	18,81	12,46	26,24	5,71	3,09	
	O	66,88	0	31,00	68,61	0	29,37	73,76	3,99	18,53	
	C	0	74,72	50,20	0	81,19	58,17	0	90,30	66,65	
	N							0	0	11,73	
As-spun NFs Diameter / nm		286 ± 30			412 ± 42			548 ± 36			
Calcined NFs Diameter / nm		170 ± 15	154 ± 25	228 ± 18	315 ± 42	440 ± 51	453 ± 77	271 ± 28	526 ± 71	433 ± 51	

## 2.2 Influence of calcination process

### 2.2.1 Atmosphere

Annealing under air, H<sub>2</sub> or N<sub>2</sub> lead to different results, under air a total oxidation would mainly lead to WO<sub>3</sub>, all the other oxides (CO<sub>x</sub> and NO<sub>x</sub> being volatile), whereas annealing under H<sub>2</sub> would lead to a reduced state of matter, mainly carbon (C), metallic tungsten (W) and their compound (WC). Under nitrogen, precursors undergo decomposition, producing eventually CO<sub>x</sub> and NO<sub>x</sub> with oxygen intrinsically present in the precursors. With the thermal treatment in H<sub>2</sub> atmosphere, PVP-AMT composite NFs kept reducing in diameter from 286 nm to 154 nm and still kept the smooth surface as shown in Table 5.1 image d, which could be attributed to the absence of oxygen and only tungsten (W) and residue carbon (C) are present according to EDS results. There were no significant peaks for tungsten carbide (WC) with the XRD spectra of this sample, which means the sample was a mixture of W, C and perhaps have some amorphous WC at this temperature. If increasing the heating temperature, well-crystallized WC NFs can be fabricated with this experimental route. For PVA-AMT composite NFs heated in H<sub>2</sub> atmosphere was the similar situation as shown in Table 5.1 image e. The calcined sample also included tungsten and residue carbon to compose WC. The difference for this sample was about the average diameter, it was almost remaining the original size from 453 nm to 440 nm. Under air, if carbon and nitrogen are totally removed, and WO<sub>3</sub> is the only compound remaining, atomic ratio for tungsten and oxygen should be 25% and 75% respectively. Under H<sub>2</sub>, carbon and tungsten are expected with an atomic ratio depending on Polymer/AMT ratio. For PAN-AMT samples as shown in image f of Table 5.1, the atomic percentages of tungsten and oxygen were 5.71% and 3.99%, which might because the W-O bond of AMT was not totally decomposed in H<sub>2</sub>. The major component is carbon with an atomic fraction of 90.3%. Nitrogen is no more observed, which indicates that all the cyano groups (C≡N) from PAN are removed during calcination and released as CO<sub>x</sub> and NO<sub>x</sub> gases. After calcination in N<sub>2</sub>, all the samples remained smooth and they were a mixture of tungsten, oxygen, carbon and nitrogen (only for PAN with a 11.73 % proportions). The average diameters were “slightly” lower from 286 nm, 488 nm, and 548 nm, to 228 nm, 453 nm, and 433 nm for PVP-AMT, PVA-AMT, and PAN-AMT, respectively, as shown in Table 5.1 images g, h, and i. Comparing these three atmospheres, air is the best choice for obtaining porous and continuous WO<sub>3</sub> NFs with large specific surface area, so all the treatments were taken place in air and the detail information of fabricating WO<sub>3</sub> NFs will be discussed in the next section.

### 2.2.2 Calcination temperatures

Calcination temperature is an important experimental parameter, which influence morphology and structures of final products. As shown in Figure 5.1, as-spun PAN-AMT composite NFs treated with different temperatures have different morphologies. In Figure 5.1a, when thermal treatment temperature was as low as 200°C, before decomposition of polymer and formation of metallic oxide occurs, sample remains smooth similar to the as-spun NFs, due to the natural properties of polymer. When heating temperature is set to 500°C, as shown in Figure 5.1b, fiber morphology changes from smooth to rough and became very porous, this can be attributed to the polymer removal. The subsequent gas release makes fiber porous and induces the formation of WO<sub>3</sub> particles on the rough surface. As increasing the temperature to 600°C, diameter of fibers decreases and the fibers became denser with several large blocks insert the fiber. This is because as the temperature increased, the WO<sub>3</sub> particles gather together and sinter as larger particles. In order to get porous samples with large specific surface area, the optimism final treatment temperature is fixed at 500°C.

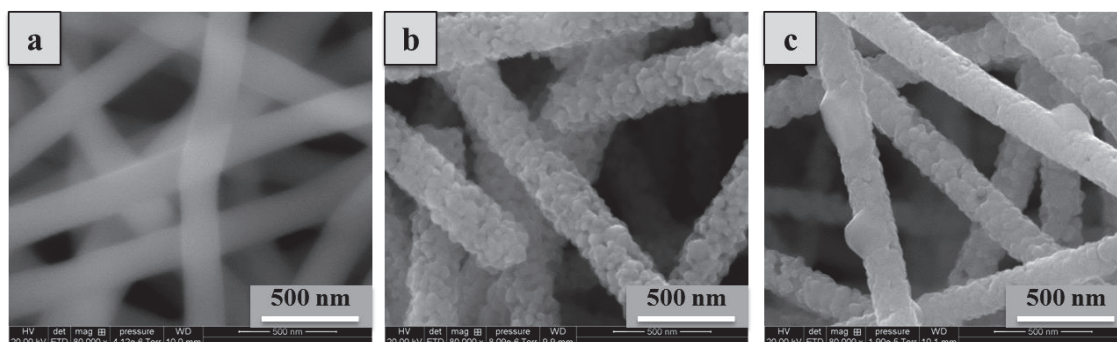


**Figure 5.1** SEM images of samples obtained from different calcination temperatures of PAN-AMT composite NFs in air for 2 h: (a) 200°C; (b) 500°C; (c) 600°C

### 2.3 Conclusions

The influence experimental parameters of WO<sub>3</sub> NFs including the starting polymers, calcination atmospheres, calcination temperatures have been investigated in this section. WO<sub>3</sub> NFs can be obtained from three starting polymers of PVP, PVA, PAN with different morphologies by calcination in air at 500°C. When polymer-AMT composite treatment is performed under H<sub>2</sub> atmosphere WC NFs can also be fabricated.

### 3 Morphology and composition of WO<sub>3</sub> nanofibers

The crystal structures of samples calcined from three starting polymers were determined by XRD as shown in Figure 5.2. It displays XRD patterns of WO<sub>3</sub> products. The XRD pattern of the three samples can be well-indexed to tungsten oxide (JCPDS Card No.32-1395), with lattice parameters  $a = 7.309 \text{ \AA}$ ,  $b = 7.522 \text{ \AA}$ , and  $c = 7.678 \text{ \AA}$ . Peaks at  $2\theta = 23.1^\circ$ ,  $23.6^\circ$ ,  $24.4^\circ$ ,  $33.6^\circ$ , and  $34.1^\circ$  are indexed to the (002), (020), (200), (-202) and (202) planes of WO<sub>3</sub>, respectively. The average sizes of WO<sub>3</sub> nanocrystalline were determined by the three strongest peaks of (002), (020), (200) using Scherrer's equation, with the value of 25 nm, 27 nm, and 59 nm for samples obtained from PVP-AMT, PVA-AMT, and PAN-AMT, respectively, as shown in Table 5.2.

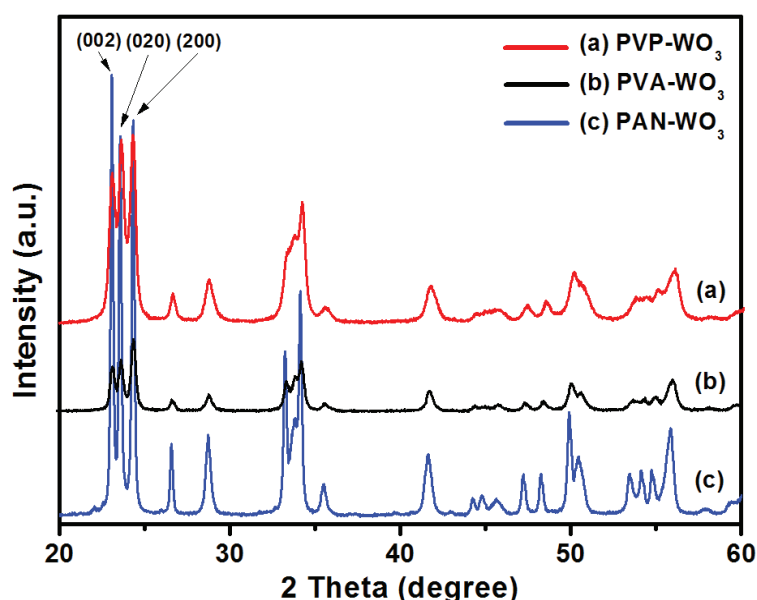
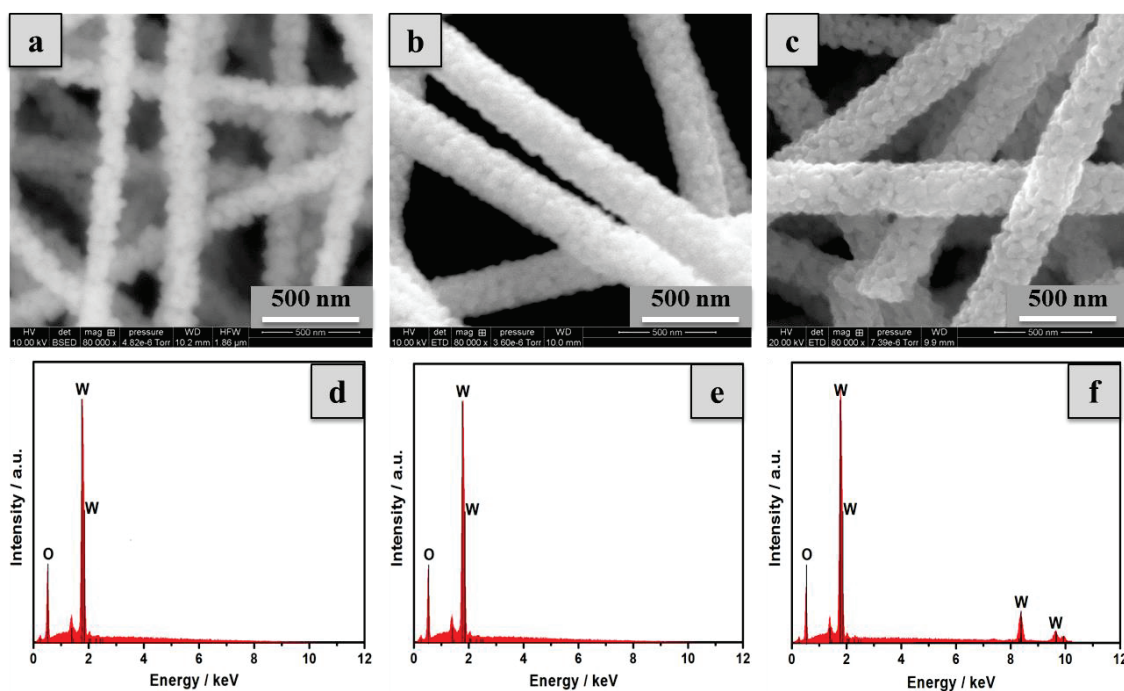


Figure 5.2 XRD patterns of WO<sub>3</sub> NFs fabricated with three different starting polymers calcination in air at 500°C for 2 h: (a) PVP-WO<sub>3</sub>; (b) PVA-WO<sub>3</sub>; (c) PAN-WO<sub>3</sub>

As shown in Figure 5.3, the morphologies of WO<sub>3</sub> NFs obtained from three different starting polymers were investigated by SEM. It can be observed that the 1D morphology of WO<sub>3</sub> NFs remains after the heat treatment. The sample fabricated from PVP-AMT composite NFs has the smallest diameter 170 nm compared with 258 nm and 271 nm obtained from PVA-AMT and PAN-AMT composite NFs. The smooth and continuous surface of the as-spun polymer-composite NFs become rough after the annealing process, due to the crystal growth of WO<sub>3</sub> and the decomposition of polymers.

**Table 5.2** Diameters, crystallite size and their specific surface area of WO<sub>3</sub> NFs fabricated with different polymers

	as-spun Diameter / nm	WO <sub>3</sub> Diameter / nm	Crystallite Size / nm	Specific Surface Area m <sup>2</sup> ·g <sup>-1</sup>	Mean Pore Diameter / nm
PVP-AMT	286 ± 30	170 ± 15	25	10.1	22.8
PVA-AMT	412 ± 42	315 ± 42	27	3.0	34.6
PAN-AMT	548 ± 36	271 ± 28	59	5.4	34.2



**Figure 5.3** SEM images of WO<sub>3</sub> NFs obtained from three polymers-AMT composite NFs after calcination at 500°C in air for 2h: (a) WO<sub>3</sub> NFs obtained from calcined PVP-AMT as-spun NFs; (b) WO<sub>3</sub> NFs obtained from calcined PVA-AMT as-spun NFs; (c) WO<sub>3</sub> NFs obtained from calcined PAN-AMT as-spun NFs; (d), (e), (f) were the EDS spectra of the samples above, respectively.

The average diameters, crystallite size and their specific surface area of WO<sub>3</sub> NFs fabricated with three different polymers are summarized in Table 5.2. The formation and growth of WO<sub>3</sub> NFs were just caused by decomposition at high temperatures, and its self-nucleation was restrained by the surrounded polymers. Investigated with BET, the typical polycrystalline structures has generated a porosity characterized by a specific surface area of 10.1 m<sup>2</sup>·g<sup>-1</sup>, 3.0 m<sup>2</sup>·g<sup>-1</sup>, and 5.4 m<sup>2</sup>·g<sup>-1</sup> with a mean pore size of 22.8 nm, 34.6 nm, and 34.2 nm for samples obtained from PVP-AMT, PVA-AMT, and PAN-AMT, respectively.

Compared with the three samples, the WO<sub>3</sub> NPs are the smallest sample obtained from PVA-AMT as shown in Figure 5.3 b, which are denser with the smallest specific surface area

of  $3.0 \text{ m}^2 \cdot \text{g}^{-1}$  than the others due to the natural properties of PVA. It just has one side chain of hydroxyl (-OH) which could be easily removed as  $\text{H}_2\text{O}$  steam during the decomposition. While the polymer PVP has branches of carbon-nitrogen single bond (C-N) and five bonds ring () with a carbonyl (C=O), PAN has a side chain of cyano groups ( $\text{C}\equiv\text{N}$ ). The functional groups were decomposed and released as gases of  $\text{CO}_x$ , and  $\text{NO}_x$ . During the release of these gases, fibers become more and more porous as shown in Figure 5.3 a and c.

## 4 Influence experimental parameters for $\text{WO}_3$ -Au composite nanofibers

### 4.1 Influence parameter of different starting polymers

For different starting polymers, PVP-AMT, PVA-AMT, PAN-AMT composite NFs were stabilized at  $200^\circ\text{C}$  before depositing (ii) Au ions on the fiber surface, then polymer part is removed; oxide particles are formed and meanwhile reduced the Au ions to Au NPs.

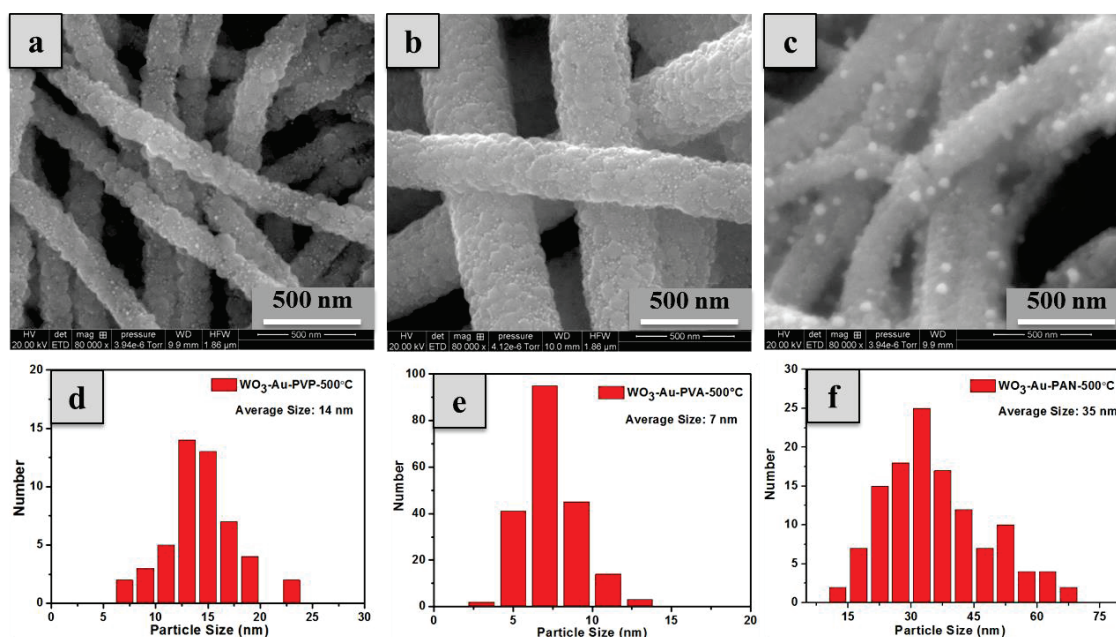


**Figure 5.4** SEM images  $\text{WO}_3$ -Au composite NFs obtained with calcination from stabilization of three different starting polymer-AMT composite NFs and then deposition (ii) Au NPs with 0.1M concentration of gold aqueous solutions followed with calcination in air at  $500^\circ\text{C}$  for 2 h: (a) PVP-AMT; (b) PVA-AMT; (c) PAN-AMT; and (d), (e), (f) are the size distributions of Au particle size

For PVP and PVA as starting polymers, the Au NPs were homogeneously distributed on the surface of fiber with uniform size, while for PAN starting polymer the final samples contained larger Au NPs. With images analysis, the Au NPs average size of these three samples (as

shown in Figure 5.4 (d), (e), and (f)) were 14 nm, 7 nm and 35 nm for starting polymers of PVP-AMT, PVA-AMT and PAN-AMT, respectively.

## 4.2 Influence parameters during calcination process

### 4.2.1 Atmosphere

As shown in Figure 5.5, SEM images of WO<sub>3</sub>-Au composite NFs obtained from pretreated the polymer-AMT composite NFs in N<sub>2</sub> at 500°C for 2 h, and deposited Au ions on the surface samples, and then calcined in air at 500°C for 2 h. The thermal treatment in N<sub>2</sub> was in order to get the mixture of WO<sub>3</sub>, WC with nitrogen and the SEM images of these samples were shown in Table 5.1 (g), (h), (i), respectively.

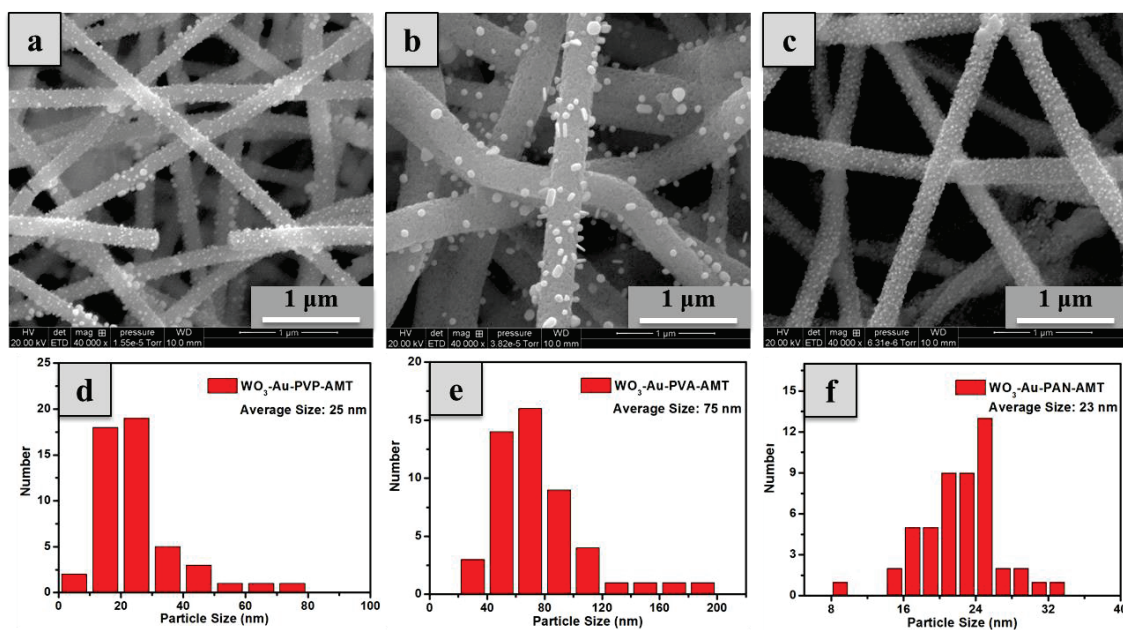


**Figure 5.5** SEM images WO<sub>3</sub>-Au composite NFs obtained with calcination three different starting polymers with AMT composite NFs in N<sub>2</sub> at 500°C for 2 h and then deposition (ii) Au NPs with 0.1M concentration of Au aqueous solutions followed with calcination in air at 500°C for 2 h: (a) PVP-AMT; (b) PVA-AMT; (c) PAN-AMT; and (d), (e), (f) are the size distributions of Au particle size

With the smooth surface of amorphous fibers, depositing Au ions and then heating in air to reduce Au ions and form Au NPs and transform the WC to WO<sub>3</sub>, and removing the nitrogen residue. All the Au NPs were decorated the fiber surface. Figure 5.5a, b and c are SEM images for PVP-AMT, PVA-AMT, and PAN-AMT, respectively. According to the image analysis with software of Nanomeasure, the size distribution of Au NPs on these three

samples are  $25 \pm 14$  nm,  $75 \pm 32$  nm, and  $23 \pm 4$  nm for PVP-AMT, PVA-AMT, and PAN-AMT, respectively (as shown in Figure 5.5 d, e, and f). For Figure 5.5 b, the PVA-AMT samples, the Au have several nanostructures including NPs, NRs and triangles, while for Figure 5.5 c the PAN-AMT samples had uniform size of Au NPs with the smallest standard deviation. Using different atmosphere provide another possibility to form  $\text{WO}_3$ -Au composite NFs with expected morphologies.

#### 4.2.2 Stabilization temperatures

The surface deposition (ii) Au addition route is addition Au aqueous solution on the surface of as-spun composite NFs. For polymer PVP and PVA, their solvents are EtOH and  $\text{H}_2\text{O}$ , respectively. Addition Au aqueous solution directly on the composite as-spun NFs, there is danger to dissolve the polymer part again and destroy the fiber morphology. So a prior stabilization is a necessary way to keep the fiber morphology while addition with Au ions. The temperature influence has been taken into consideration of PVP-AMT composite NFs. As shown in Figure 5.6a, Au ions were introduced on the surface of as-spun PVP-AMT NFs at room temperature without any prior heat treatment. After the calcination process, the polymer component and solvent decomposed and removed, meanwhile the Au ions reduced to Au NPs during the  $\text{WO}_3$  formation. The bright dots were considered as Au NPs, which are located inside and outside the fiber matrix. This last observation has been checked by 3D tomography combined with TEM.

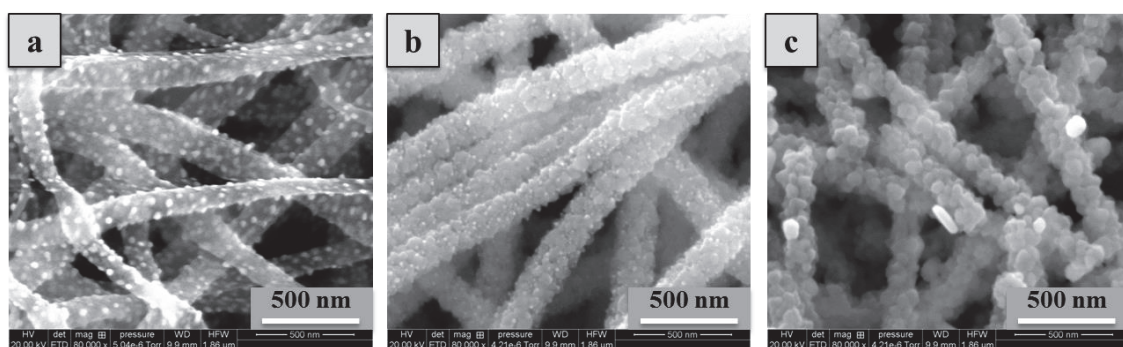


**Figure 5.6 SEM images of  $\text{WO}_3$ -Au composite NFs obtained from calcined PVP-AMT NFs with deposition (ii) Au by different stabilization temperatures followed with calcination in air at  $500^\circ\text{C}$  for 2h: (a) stabilization at room temperature on the as-spun PVP-AMT NFs; (b) stabilization at  $200^\circ\text{C}$  addition on the PVP-AMT pre-treated NFs; (c) stabilization at  $500^\circ\text{C}$  to form  $\text{WO}_3$  NFs before addition Au**

Figure 5.6 b shows sample realized with a prior stabilization temperature at 200°C before addition Au ions. The matrix part of the fiber kept similar to typical WO<sub>3</sub> NFs obtained from PVP-AMT NFs. The bright dots are Au NPs deposited homogeneously on the surface of fiber matrix, which can be attributed to the stabilization at 200°C of composite polymers. Because of the stabilization, the PVP-AMT composite NFs do not further decompose when the temperature is below 200°C during the calcination. Meanwhile, Au ions can be reduced to Au NPs during the heating below 200°C. That explains why the size of the Au NPs was homogenous and well-dispersed in fiber matrix. As shown in Figure 5.6 c, when the stabilization temperature is increased up to 500°C, WO<sub>3</sub> crystalline are already formed before addition of Au. In this case, conditions are similar to surface deposition (iii) Au addition routes. Large WO<sub>3</sub> NPs were obtained and big Au particles are sporadically scattered along the fiber matrix. As the Au ions addition takes place after stabilization at 500°C, Au ions can hardly penetrate within the fiber matrix. With a stabilization temperature at 200°C, fiber matrix just started to decompose, and several organic groups and ligands remain and react with Au ions. As a consequence, a prior stabilization at 200°C gives the more suitable results for further experiments, it can not only solidify the polymer by keeping fiber morphology, but also has a good ability to absorb Au ions and reduces it homogeneously

### 4.3 Influence parameters of Au addition

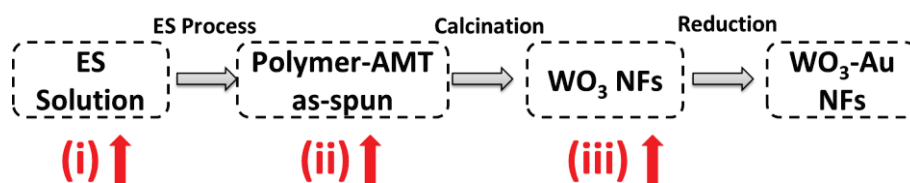


Figure 5.7 Schematic of three different Au addition routes

As shown in Figure 5.7, a schematic view of three different Au addition routes: volume inclusion (i), surface deposition (ii), and surface deposition (iii). A more detailed description about these routes has been explained in Chapter 2 section 2.1.1. For different Au addition routes, there are still many factors that can determine the morphology and composition of the final products such as stabilization temperatures, and Au aqueous concentrations. In the following part, stabilization temperatures for PVP-AMT composite NFs, different Au addition routes for PVA-AMT composite NFs, and various Au concentrations for PVA-AMT composite NFs have been researched.

### 4.3.1 Au addition routes

PVA-AMT composite NFs were chosen to compare the influence of three different Au addition routes. As shown in Figure 5.8 a, volume inclusion (i) is the first route allowing to add Au ions directly into ES solution. In this case, porous  $\text{WO}_3$  NFs with large and small Au NPs on the surface are observed. Before calcination, Au ions were well dispersed with polymer and solvent in as-spun composite NFs. During the calcination process, Au ions reduced to Au NPs at lower temperature below  $200^\circ\text{C}$ , as temperature increases, the polymer part start to decompose and form  $\text{WO}_3$  oxide matrix with several thermal decomposition gas products, which not only make the fiber become porous, but also provide access to Au atoms or clusters gather together and form larger particles, which makes the size of Au NPs are uniform. Volume inclusion (i) Au addition route is not suitable for fabricating homogenous  $\text{WO}_3$ -Au NFs like  $\text{TiO}_2$ -Au NFs introduced in Chapter 4, which might due to the retraction of the formation of these two metallic oxide matrix and the reduction of Au ions to NPs are different during the calcination. It needs more experiments to figure out the real reason.

In Figure 5.8 b, it is the second Au addition route of deposition (ii), which is similar with PVP-AMT stabilization at  $200^\circ\text{C}$  as discussed above in section 3.2.2. The bright dots observed on the NF surface could correspond to Au NPs. Indeed, this hypothesis is strengthened by XRD results and by the number of bright dots that is larger for the sample of  $\text{WO}_3$ -Au. Au NPs could be easily and firstly formed at high-temperature treatment on the surface of NFs, and then they may act as seeds or nucleation centers for the  $\text{WO}_3$  crystallization and growth on the surface of NFs. Figure 5.8 c show the third way of Au addition route, surface deposition (iii) where Au ions were deposited on the surface of  $\text{WO}_3$  oxide NFs and then followed with calcination to reduce Au ions into Au NPs. It is clear that many different bright nanostructures (NPs, NRs, and nanoflakes) seem to grow on the surface of NFs. The different formation of Au nanostructures come from the thermal treatment, at low temperatures Au ions reduced to form Au nanoseeds, the crystallized  $\text{WO}_3$  play a role as matrix and nuclear growth seed. As increasing the temperature, the Au nanoseeds grow and decorate on the surface of  $\text{WO}_3$  NFs and form different structures. Above all the Au addition techniques, the deposition (ii) one, with prior thermal stabilization is the best to obtain  $\text{WO}_3$ -Au composite NFs to further gas sensors experiments..

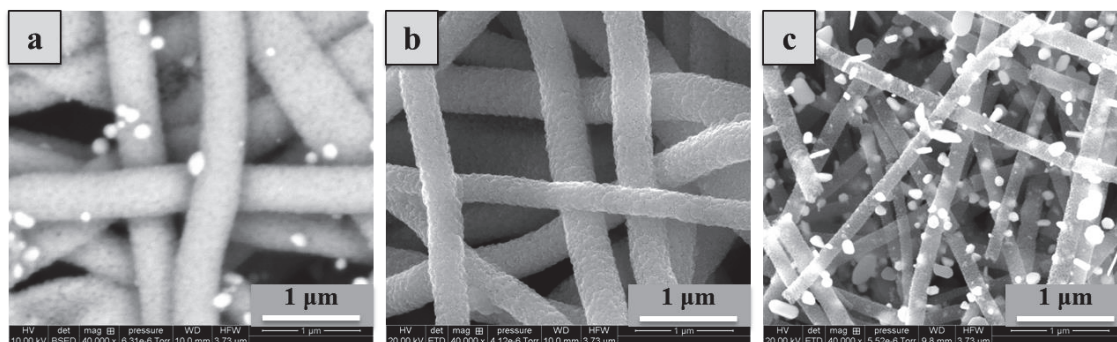


**Figure 5.8 SEM images of WO<sub>3</sub>-Au composite NFs obtained from calcined PVA-AMT NFs with three Au addition routes followed with calcination in air at 500°C for 2h: (a) volume inclusion (i) addition Au ions into PVA-AMT ES solution directly before ES; (b) surface deposition (ii) addition Au ions on the surface of PVA-AMT NFs with stabilization after ES; (c) surface deposition (iii) addition Au ions on the surface of WO<sub>3</sub> NFs after calcination**

### 4.3.2 Au concentrations

Three concentrations of Au aqueous solution (including 0.001M, 0.01M, and 0.1 M as shown in Figure 5.9 a, b, and c, respectively) were used to deposit Au ions on the surface of PVA-AMT stabilized NFs with Au addition route deposition (ii) followed with calcination in air at 500°C for 2 h. As the concentration of Au aqueous solution is increasing, the amount of bright dots increased. Varying the initial concentration of Au aqueous solution can adjust the final contents of Au with WO<sub>3</sub>-Au composite NFs. The Au NPs of three samples realized with three different Au ions concentrations (as shown in size distribution of Figure 5.9 d, e, and f), are 9 nm, 8 nm, and 7 nm, respectively for 0.001M, 0.01M, and 0.1 M, respectively. More details about the sample morphologies and Au contents will be discussed in section 5 where morphologies and composition of WO<sub>3</sub>-Au composite NFs were investigated with XRD, TEM, and ICP analysis results.

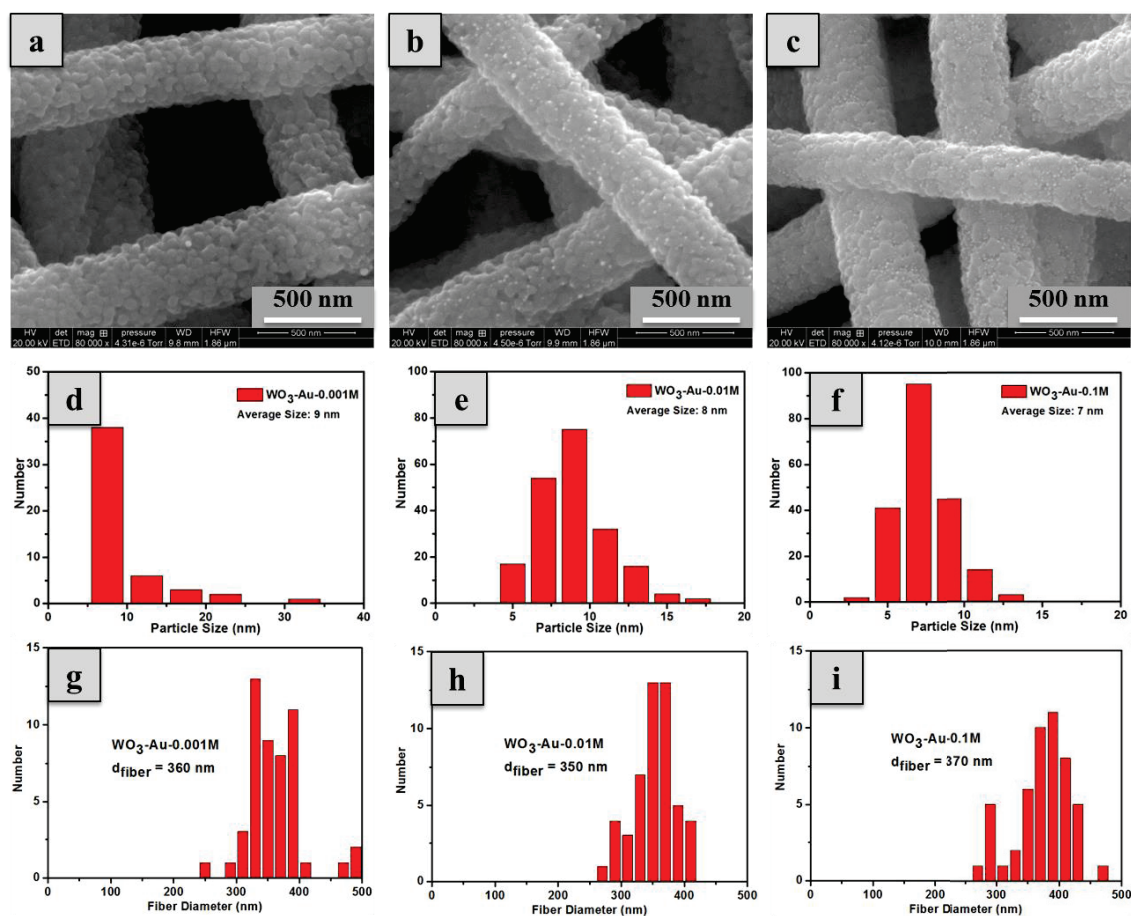


**Figure 5.9** SEM images WO<sub>3</sub>-Au composite NFs obtained with calcination from stabilization of PVA-AMT composite NFs and then deposition (ii) Au NPs with three different concentrations of gold aqueous solutions followed with calcination in air at 500°C for 2 h: (a) 0.001M; (b) 0.01M; (c) 0.1M; (d), (e), (f) are the size distributions of Au particle size; and (g), (h), (i) are the size distributions of fiber diameter

#### 4.4 Conclusions

This section describes the influence of experimental parameters for WO<sub>3</sub>-Au composite NFs, including different starting polymers, calcination atmosphere, stabilization temperature, Au addition routes, and different Au concentrations. PVA-AMT composite NFs as the matrix and Au addition routes of deposition (ii) combined with a prior stabilization at 200°C and followed with calcination in air at 500°C for 2 h seem the best experimental procedure to form WO<sub>3</sub>-Au composite NFs with uniform Au NPs on the surface. Au contents can be adjusted by tuning the initial concentration of Au aqueous solution. The structures of Au are also influenced by calcination temperatures and atmosphere.

## 5 Morphologies and composition of WO<sub>3</sub>-Au composite nanofibers

The crystal structures of the samples were determined by XRD. Figure 5.10 displays XRD patterns of the as-prepared WO<sub>3</sub> and WO<sub>3</sub>-Au composite products. As shown in Figure 5.10 a, the XRD pattern of the sample WO<sub>3</sub> can be well-indexed to tungsten oxide (JCPDS Card No. 32-1395), with lattice parameters  $a = 7.309 \text{ \AA}$ ,  $b = 7.522 \text{ \AA}$ , and  $c = 7.678 \text{ \AA}$ . In comparison, the XRD pattern of the sample WO<sub>3</sub>-Au-0.1M (Figure 5.10 b) shows the diffraction peaks of both WO<sub>3</sub> and cubic gold with lattice parameters  $a = 4.0786 \text{ \AA}$  (JCPDS No. 04-0784). In Figure 5.10 b, peaks at  $2\theta = 23.1^\circ$ ,  $23.6^\circ$ ,  $24.4^\circ$ ,  $33.6^\circ$ , and  $34.1^\circ$  are indexed to the (002), (020), (200), (-202) and (202) planes of WO<sub>3</sub>, respectively. Additionally, the three more peaks at  $2\theta = 38.2^\circ$ ,  $44.4^\circ$ , and  $64.6^\circ$  correspond to the (111), (200) and (220) planes of the cubic gold phase (JCPDS No. 04-0784).

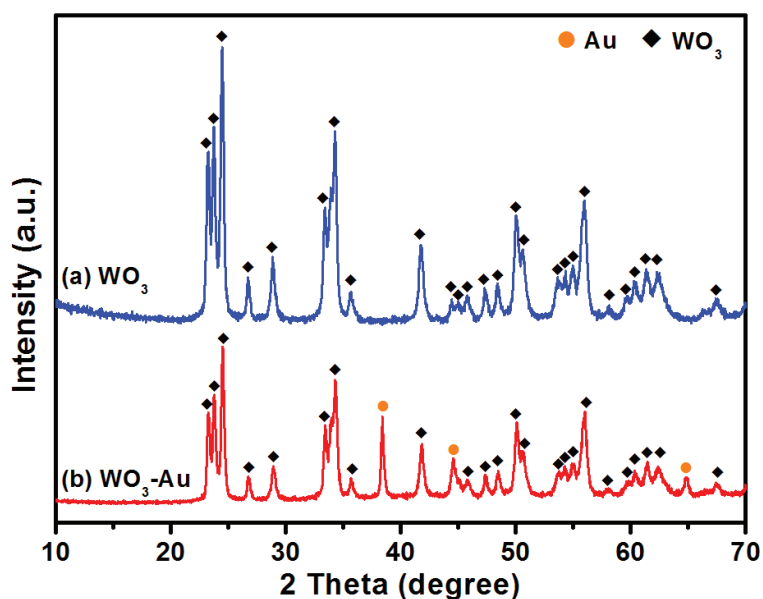
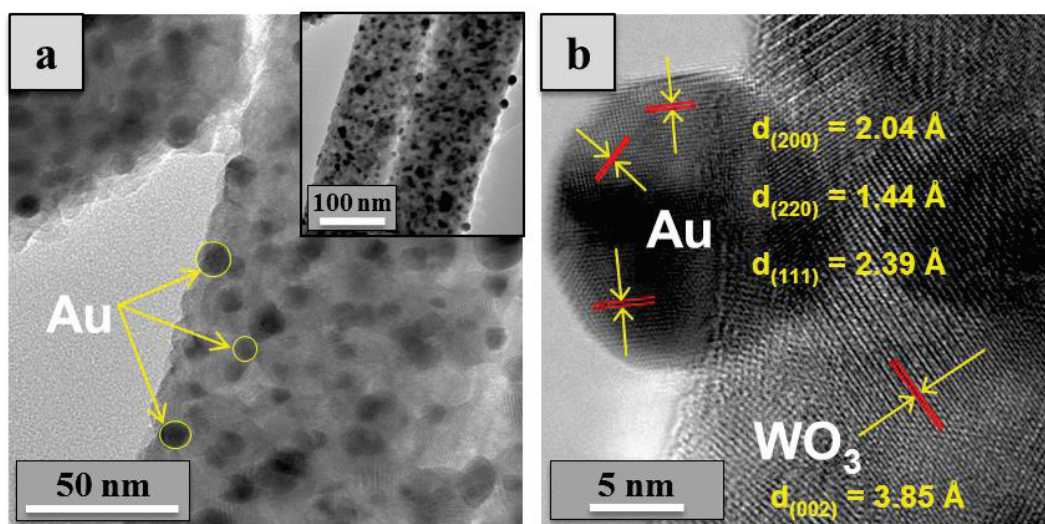


Figure 5.10 XRD patterns of (a) WO<sub>3</sub> NFs and (b) WO<sub>3</sub>-Au composite NFs obtained with calcination from stabilization of PVA-AMT composite NFs and then deposition (ii) Au NPs of 0.1M gold aqueous solutions followed with calcination in air at 500°C for 2 h

Figure 5.11 shows TEM images of WO<sub>3</sub>-Au-0.1M composite NFs. From Figure 5.11 a, it can be observed that the prepared WO<sub>3</sub> NF is well-decorated with Au NPs with an average particle size of  $\sim 7 \text{ nm}$ . A typical HRTEM image of the WO<sub>3</sub>-Au composite NF is shown in Figure 5.11 b. The crystallographic planes (111), (200), and (220) of gold (JCPDS No. 04-0784) are clearly observed with the corresponding lattice distances measured as  $2.39 \text{ \AA}$ ,  $2.04 \text{ \AA}$ , and  $1.44 \text{ \AA}$ , respectively. Corresponding tabulated lattice distances are  $2.36 \text{ \AA}$ ,  $2.04 \text{ \AA}$ , and

1.44 Å, respectively. Moreover, the crystallographic plane (002) of  $\text{WO}_3$  is also present with the value of 3.85 Å, confirming the orthorhombic structure of  $\text{WO}_3$  (JCPDS No. 00-032-1395) with the corresponding tabulated lattice distance is 3.84 Å. Previous studies by Jiang et al. have shown that the interaction energies of Ag, Pd or Pt NPs deposited on  $\alpha\text{-Fe}_2\text{O}_3$  were much higher with a porous/rough surface than with a smooth one, leading to an easier deposition on the  $\alpha\text{-Fe}_2\text{O}_3$  surface [182], [183]. In our case, the route of surface deposition (ii) can obtain  $\text{WO}_3\text{-Au}$  composite NFs with well deposited Au NPs.



**Figure 5.11** (a) TEM images of  $\text{WO}_3\text{-Au-0.1M}$  composite NFs obtained with calcination from stabilization of PVA-AMT composite NFs and then deposition (ii) Au NPs of 0.1M gold aqueous solutions followed with calcination in air at 500°C for 2 h; (b) High-resolution TEM image of Au NPs embedded  $\text{WO}_3$  NFs showing the Au and  $\text{WO}_3$  lattices

The size measurements of the as-prepared  $\text{WO}_3$  NFs and the decorated Au NPs are summarized in Table 5.3. The average diameters of the  $\text{WO}_3$ ,  $\text{WO}_3\text{-Au-0.001M}$ ,  $\text{WO}_3\text{-Au-0.01M}$ , and  $\text{WO}_3\text{-Au-0.1M}$  composite NFs are 315 nm, 360 nm, 350 nm, and 370 nm, respectively (as seen in Figure 5.9 size distributions of fiber diameter). After functionalization with Au NPs, the mean diameter of the NFs increases slightly from 315 nm to 350 nm, which may be due to the presence of Au NPs on the surface of  $\text{WO}_3$  NFs. Moreover, for pure  $\text{WO}_3$  NFs, formation and growth is caused by decomposition at high temperatures, and its self-nucleation is restrained by the surrounding polymer(s). Whereas in presence of  $\text{HAuCl}_4$ , Au NPs can be easily and firstly formed at an intermediate temperature on the surface of NFs, and then they may act as seeds or nucleation centres for the further  $\text{WO}_3$  crystallization and growth on the surface of NFs. This may result in a broadening of NF diameter. Moreover, the

gold aqueous solution may have introduced water into the fibers. This water is then released as steam, thus increasing the fiber porosity.

The gold contents of WO<sub>3</sub>-Au-0.001M, WO<sub>3</sub>-Au-0.01M and WO<sub>3</sub>-Au-0.1M composite NFs were measured by ICP as 0.13%, 0.47% and 1.65%, respectively (shown in Table 5.3). The slightly discrepancy between the theoretical concentrations and the experimental gold contents may be attributed to small impregnated volume variations. The average sizes of Au NPs in the three samples are 9 nm (WO<sub>3</sub>-Au-0.001M), 8 nm (WO<sub>3</sub>-Au-0.01M) and 7 nm (WO<sub>3</sub>-Au-0.1M), respectively, by SEM image analysis with software Nano Measurer (as seen in Figure 5.9 size distributions of Au particle size).

**Table 5.3 Measurement results of the mean diameter of fiber and Au NP size of WO<sub>3</sub>-Au composites NFs**

	WO <sub>3</sub>	WO <sub>3</sub> -Au-0.001M	WO <sub>3</sub> -Au-0.01M	WO <sub>3</sub> -Au-0.1M
Fiber diameter / nm	315 ± 42	360 ± 45	350 ± 32	370 ± 43
Au particle size / nm		9 ± 5	8 ± 2	7 ± 2
Au contents		0.13%	0.47%	1.65%

A simple image analysis allowed us to check that composition obtained by ICP was in qualitative agreement with the number of NPs observed by SEM on the WO<sub>3</sub> NFs, indicating that gold NPs are mostly located on the fiber surface. For example, on a section of fiber of diameter  $D$  and length  $L$ , a rough estimation of the gold content can be made by measuring the gold nanoparticles diameter  $d_i$ . The gold content is then estimated using the following equation:

$$\%Au = \frac{4 \frac{\rho_{Au}}{M_{Au}} \sum d_i^3}{3 \frac{\rho_{WO_3}}{M_{WO_3}} D^2 L}$$

$\rho$  and  $M$  are the volumetric mass density and molecular weight of gold and tungsten oxide, respectively. Calculation made on Figure 5.9 b and Figure 5.9 c on about hundred particles gave a content of 0.44% and 0.8% on samples WO<sub>3</sub>-Au-0.01M and WO<sub>3</sub>-Au-0.1M respectively, which is in a good qualitative agreement with ICP measurement, taking into account the rough approximation made on particles size and shape and sample homogeneity. More importantly, this indicates that most of the gold content is indeed located on the fiber surface and not impregnated within the fiber porosity.

The ICP results show that the final Au content could be tuned by adjusting the initial concentration of the gold aqueous solution and the impregnated volume. This is important as

the content of the noble metal largely influences the gas-sensing performance as seen in previous studies [41]. In the proposed method, the first thermal stabilization at 200 °C plays an important role in keeping the fiber structure intact. Without this preliminary step, the polymer PVA would be partly dissolved by water of the Au aqueous solution thus leading to the structural destruction of the NFs. Moreover, as Au ions can be dissolved in water, they are more easily dispersible onto the WO<sub>3</sub> surface. Finally, the thermal treatment process allows the Au ions to be reduced and transformed into Au NPs. This simple annealing treatment allows for the decoration of Au NPs and the transformation to WO<sub>3</sub> to be simultaneously achieved at the same low temperature. All these advantages demonstrate that the proposed synthesis strategy is a facile and effective method for producing well-controlled WO<sub>3</sub>-Au composite NFs.

## **6 Gas-sensing performance**

### **6.1 Operating temperature**

It is well known that the operating temperature highly influences the response of semiconductor-based gas sensors, as it governs the mobility of electrons and the electrical conductivity from the metallic oxide material [184], [185]. Therefore, the responses of the WO<sub>3</sub> and WO<sub>3</sub>-Au composites NFs toward 100 ppm of *n*-butanol were tested at different operating temperatures in order to find the optimum operating temperature of these sensors, as a compromise between electrical conductivity and molecules desorption. Figure 5.12 a shows the variation in responses of the WO<sub>3</sub> sensors, which obtained from PVP-AMT, PVA-AMT, and PAN-AMT, toward 100 ppm of *n*-butanol with increasing operating temperatures. The response curves of these sensors show a typical bell-shape in the entire temperature range from 175 to 325 °C. Further observation of Figure 5.12 a, it reveals that all WO<sub>3</sub> sensors exhibit a lower optimum operating temperature at 300 °C. The maximum response values of these three sensors toward 100 ppm of *n*-butanol at 300 °C are 6.9, 7.3, and 8.5 for WO<sub>3</sub> obtained from PVP, PVA, and PAN, respectively.

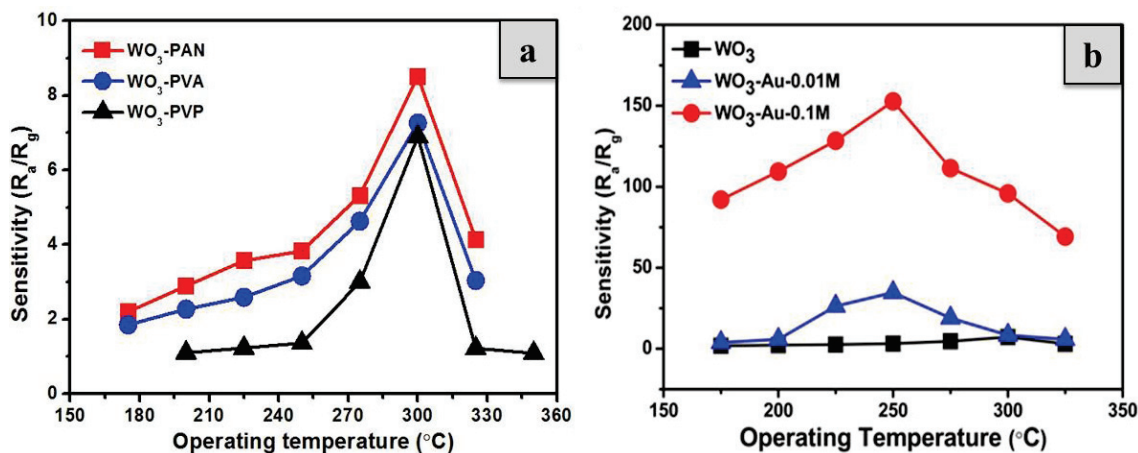


Figure 5.12 The variation in responses of WO<sub>3</sub>, WO<sub>3</sub>-Au sensors toward 100 ppm of *n*-butanol as a function of the operating temperature: (a) WO<sub>3</sub> obtained from different polymers; (b) WO<sub>3</sub>, WO<sub>3</sub>-Au-0.01M and WO<sub>3</sub>-Au-0.1M.

Figure 5.12b shows the variation in responses of the WO<sub>3</sub>, WO<sub>3</sub>-Au-0.01M, and WO<sub>3</sub>-Au-0.1M composite NF sensors toward 100 ppm of *n*-butanol with increasing operating temperatures. The response curves of these sensors show a typical bell-shape in the entire temperature range from 175 to 325°C. Further observation of Figure 5.12b reveals that both WO<sub>3</sub>-Au sensors exhibit a lower optimum operating temperature at 250°C compared to pure WO<sub>3</sub> sensor which displays the highest response toward *n*-butanol gas at 300°C. The maximum response values of these three sensors toward 100 ppm of *n*-butanol are 7.3 for WO<sub>3</sub> at 300°C, 34.7 for WO<sub>3</sub>-Au-0.01M and 152.7 for WO<sub>3</sub>-Au-0.1M at 250°C. In comparison to the pure WO<sub>3</sub> sensor, the two WO<sub>3</sub>-Au sensors show much higher response toward *n*-butanol at a lower optimum operating temperature (250°C), indicating the double benefit of the Au decoration.

## 6.2 Response of the sensors

### 6.2.1 Selectivity --- response towards different gases

Selectivity is an important parameter of a gas sensor. A good gas sensor can selectively detect a particular gas when it is exposed to an environment containing multiple gases with similar physicochemical properties. The selectivity tests of the  $\text{WO}_3$ ,  $\text{WO}_3\text{-Au-0.01M}$  and  $\text{WO}_3\text{-Au-0.1M}$  sensors were carried out by comparing their response to *n*-butanol against other VOCs with nearly identical physicochemical properties, such as methanol, ethanol, and acetone. From Figure 5.13, it is noted that the both  $\text{WO}_3\text{-Au}$  sensors clearly exhibits the higher response toward a concentration of 100 ppm of all the six VOCs gases compared to pure  $\text{WO}_3$  sensor. Functionalized with Au NPs can improve the response and the Au content also has an important role for the performance. As shown in Table 5.4,  $\text{WO}_3\text{-Au-0.1M}$  exhibits the highest response toward volatile *n*-butanol gas, with  $S = 229.7$  at a concentration of 100 ppm. This is around 2 to 28 times higher than the response to other gases, indicating its excellent selectivity toward *n*-butanol vapor. In comparison, the selectivity of the pure  $\text{WO}_3$  sensor is much poorer than the  $\text{WO}_3\text{-Au}$  composite NF sensors as it could not distinguish the different organic vapors.

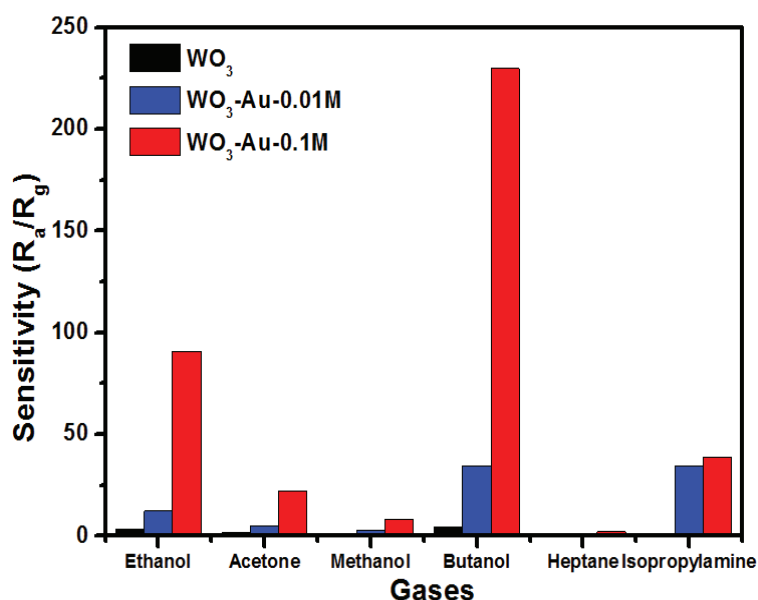


Figure 5.13 Selectivity of the  $\text{WO}_3$ ,  $\text{WO}_3\text{-Au-0.01M}$  and  $\text{WO}_3\text{-Au-0.1M}$  sensors toward 100 ppm of VOCs at 250 °C

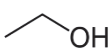
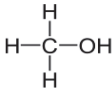
**Table 5.4 Selectivity of WO<sub>3</sub>, WO<sub>3</sub>-Au-0.01M and WO<sub>3</sub>-Au-0.1M sensors toward 100 ppm of various VOCs at 250 °C**

	Ethanol	Acetone	Methanol	Isopropylamine	Heptane	<i>n</i> -butanol
WO <sub>3</sub>	3.43	2	1.28	1.39	0.89	4.4
WO <sub>3</sub> -Au-0.01M	12.3	5.25	2.83	34.7	1	34.7
WO <sub>3</sub> -Au-0.1M	90.8	22.3	8.05	38.7	2.25	229.7

### 6.2.2 Properties of different gases

WO<sub>3</sub>-Au composite NF sensor has excellent selectivity toward *n*-butanol vapor could be attribute to the physico-chemical properties of these VOCs gases like density, boiling point, and functional group as shown in Table 5.5. Butanol has the lowest density of 0.810 g·cm<sup>-3</sup> among these gases. Due to the light ambient air, so the more heavier the more difficult to escape from the material surface, and then have more chance to react with sensor. For the boiling point of butanol is 117.70 °C, it is the highest among these VOCs gases. The operating temperature is 250 °C, so the higher boiling point, the higher reaction efficient. Meanwhile, the functional groups like hydroxyl (-OH), amino (-NH<sub>2</sub>) make the reaction with sensor easier. All the reasons discussed above, butanol exhibits the best performance with WO<sub>3</sub>-Au composite NF sensor.

**Table 5.5 Basic physico-chemical properties of different gases**

	Ethanol	Acetone	Methanol	Isopropylamine	Heptane	<i>n</i> -butanol
Skeletal Formula						
Molecular Formula	CH <sub>3</sub> CH <sub>2</sub> OH	CH <sub>3</sub> COCH <sub>3</sub>	CH <sub>3</sub> OH	C <sub>3</sub> H <sub>9</sub> N	C <sub>7</sub> H <sub>16</sub>	C <sub>4</sub> H <sub>10</sub> O
Molecular Weight / g·mol <sup>-1</sup>	46.07	58.08	32.04	59.11	100.21	74.12
Density / g·cm <sup>-3</sup>	0.789	0.790	0.792	0.722	0.684	0.810
Boiling Point /°C	98.40	56.53	64.70	31.00~35.00	98.42	117.70

The modulation model of depletion layer by oxygen adsorption is the most commonly accepted model to explain the sensing mechanism of metallic oxide based sensor [186]. According to literature, the response from a sensor increases with an increase in the alkyl (carbon-carbon) chain length from methanol (CH<sub>4</sub>O) to *n*-butanol (C<sub>4</sub>H<sub>10</sub>O). When the adsorbed oxygen species react with higher alkyl chain length alcohols such as *n*-butanol as

opposed to shorter ones such as methanol, the enhancement of gas sensitivity can be attributed to the higher increase in electron concentration (and therefore a higher increase in conductivity) [187]. Moreover, heavier molecules will vibrate and/or rotate less than lighter molecules, and therefore, they tend to have lower diffusivity. In this case gas molecules are more likely to react on the surface of metallic oxide sensing materials. As the number of carbons in the alkyl chain for *n*-butanol is larger compared to other alcohol molecules with smaller molecular weight (methanol 1, ethanol 2, and acetone 3 as shown in Table 5.5), therefore, this may explain why the response of the WO<sub>3</sub>-Au-0.1M sensor toward *n*-butanol is much higher than other gases. Another hypothesis could be that sensor has been optimized for *n*-butanol and not for other gases, therefore enhancing the response from the material to this specific VOCs.

**Table 5.6 Comparison of sensing performance of various WO<sub>3</sub> based sensors toward 100 ppm of different VOCs**

Sensor Materials	Gases	T (°C)	C (ppm)	<i>S</i> ( <i>R<sub>a</sub>/R<sub>g</sub></i> )	Refs
WO <sub>3</sub> nanofibers	C <sub>2</sub> H <sub>6</sub> O	250	100	3.43	[188]
<b>Au-WO<sub>3</sub> nanofibers</b>		<b>250</b>	<b>100</b>	<b>90.8</b>	<b>[188]</b>
Pt-WO <sub>3</sub> powder		190	100	40	[189]
Au-WO <sub>3</sub> nanofibers	CH <sub>4</sub> O	250	100	8.1	[188]
Ag-WO <sub>3</sub> nanoplates		200	100	1.2	[44]
Au-WO <sub>3</sub> nanofibers	C <sub>3</sub> H <sub>6</sub> O	250	100	22.3	[188]
Ag-WO <sub>3</sub> nanoplates		200	100	7.5	[44]
<b>Au-WO<sub>3</sub> nanofibers</b>	<b>C<sub>4</sub>H<sub>10</sub>O</b>	<b>250</b>	<b>100</b>	<b>229.7</b>	<b>[188]</b>
$\alpha$ -Fe <sub>2</sub> O <sub>3</sub> -ZnO-Au nanorods		225	100	113	[190]
$\alpha$ -Fe <sub>2</sub> O <sub>3</sub> -Au nanospindles		300	100	7.2	[190]

Table 5.6 compares the gas-sensing performance of pure WO<sub>3</sub> and WO<sub>3</sub>-Au-0.1M NF sensors prepared in this work with the best performance of previously reported sensors based on different nanostructures of oxide materials functionalized with noble metal NPs. The WO<sub>3</sub>-Au composite NFs sensor fabricated exhibit better sensing performance compared to Ag-WO<sub>3</sub> nanoplates [169], i.e. the response value increases from 1.2 to 8.1 and 7.5 to 22.3 toward methanol and acetone, respectively. Additionally, the response of the fabricated WO<sub>3</sub>-Au-0.1M NF sensor toward *n*-butanol is much higher compared to previous sensors based on  $\alpha$ -Fe<sub>2</sub>O<sub>3</sub>-ZnO-Au nanocomposites and  $\alpha$ -Fe<sub>2</sub>O<sub>3</sub>-Au nanospindles [43],[168]. All the above

comparisons indicate the good sensing capability of the WO<sub>3</sub>-Au composite NF sensor, not only toward *n*-butanol but also toward other gases (e.g. methanol, ethanol and acetone) compared to previous noble metal functionalized WO<sub>3</sub> nanostructures, including nanorods, nanoneedles or nanoplates modified with Au, Pt, or Ag NPs.

### 6.2.3 Sensitivity with gas concentrations

The dynamic response-recovery curves of the three sensors toward to 100 ppm *n*-butanol at 250 °C are given in Figure 5.14. It reveals the n-type sensing behaviors of all the fabricated sensors, whereby the output voltage of each of these sensors increases as the *n*-butanol gas is injected into the test chamber but gradually decreases as the sensors are exposed to air. However, it is clear that the increase in the output voltage upon exposure to *n*-butanol is greater for both WO<sub>3</sub>-Au sensors than for pure WO<sub>3</sub> sensor, indicating the higher response of the WO<sub>3</sub> functionalized with Au NPs. The response is highly enhanced as the Au content is increased further from 0.47% to 1.65% by weight. Furthermore, it can be observed from Figure 5.14 that the WO<sub>3</sub>-Au-0.01M and WO<sub>3</sub>-Au-0.1M sensors show 5 and 20 times higher response, respectively, compared to the pure WO<sub>3</sub> sensing material.

The content of noble metal has a significant influence on the sensing performance, thus we first investigated the response of the pure WO<sub>3</sub>, WO<sub>3</sub>-Au-0.01M, and WO<sub>3</sub>-Au-0.1M sensors as a function of *n*-butanol concentration (10, 20, 50, 100, 200, 500 ppm) at 250 °C. The results in Figure 5.15 show that the WO<sub>3</sub>-Au-0.1M composite NF sensor exhibits a high response of  $S = 63.6$  toward 10 ppm of *n*-butanol, whereas the response values of WO<sub>3</sub>-Au-0.01M composite NF and pure WO<sub>3</sub> sensors are 9.5 and 1.55, respectively. Increasing the *n*-butanol concentration to 100 ppm, the response significantly increases to 229.7 for WO<sub>3</sub>-Au-0.1M, 34.7 for WO<sub>3</sub>-Au-0.01M and 4.5 for pure WO<sub>3</sub>. For WO<sub>3</sub> and WO<sub>3</sub>-Au-0.01M sensors, the response initially rises quickly with increasing concentration of *n*-butanol before eventually reaching saturation at a higher concentration of *n*-butanol. In comparison, the pure WO<sub>3</sub> sensor experiences only a slight increase in response with increasing *n*-butanol concentration. This result demonstrates that the Au additive generates a promotion effect on the sensor response. Furthermore, it can be observed that different Au contents result in a large difference in the sensing response. The response of the WO<sub>3</sub>-Au-0.1M sensor keeps increasing sharply and reaches as high as 515.2 at an *n*-butanol concentration of 500 ppm, which is ~60 times higher compared to the response of pure WO<sub>3</sub> sensor ( $S = 8.5$ ) and also 8 times higher than the response of WO<sub>3</sub>-Au-0.01M sensor ( $S = 68.1$ ). All these results clearly

indicate the beneficial addition of Au NPs on the surface of WO<sub>3</sub> NFs.

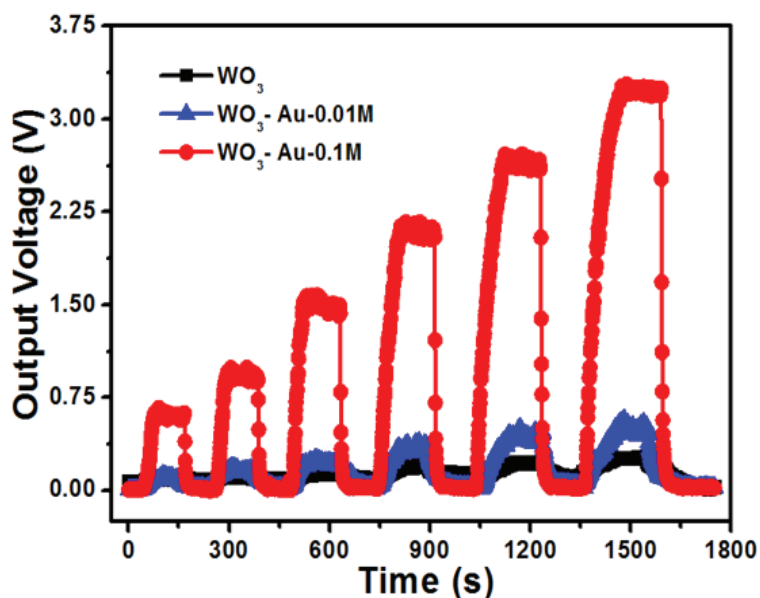


Figure 5.14 Dynamic response-recovery behaviors of the WO<sub>3</sub>, WO<sub>3</sub>-Au-0.01M and WO<sub>3</sub>-Au-0.1M sensors toward various concentrations of *n*-butanol at the optimum working temperature (250 °C)

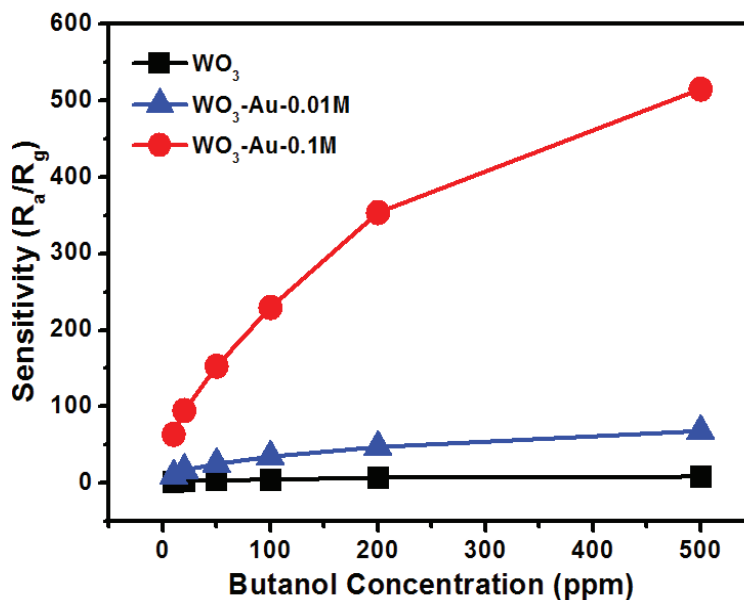


Figure 5.15 Response vs. concentration curves of the WO<sub>3</sub>, WO<sub>3</sub>-Au-0.01M and WO<sub>3</sub>-Au-0.1M sensors toward *n*-butanol at 250 °C

### 6.3 Response ( $T_{res}$ ) and Recovery ( $T_{rec}$ ) times

The details of response-recovery properties of the WO<sub>3</sub>-Au-0.1M composite NFs sensor

are shown in Figure 5.16. The variation in the voltage of the WO<sub>3</sub>-Au-0.1M sensor toward 10 ppm of *n*-butanol at 250 °C is shown in Figure 5.16 a. It presents a fast response and recovery time, of about 31 and 9s, respectively. Figure 5.16 b shows the response and recovery time curves of the WO<sub>3</sub>-Au-0.1M based sensor with different concentration of *n*-butanol at 250 °C. It can be observed that the response time increases as the *n*-butanol concentration is increased. In contrast, the recovery time the WO<sub>3</sub>-Au-0.1M sensor remains very (~13 s) fast, regardless of the concentration of *n*-butanol.

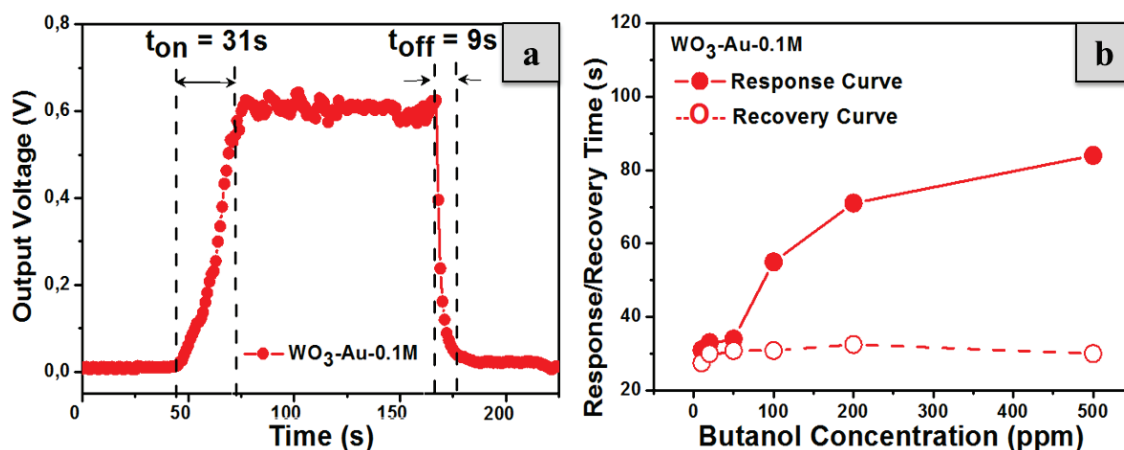


Figure 5.16 (a) The dynamic response-recovery behavior of the WO<sub>3</sub>-Au-0.1M sensor toward 10 ppm of *n*-butanol at 250 °C; (b) The response and recovery vs. concentration curves of the WO<sub>3</sub>-Au-0.1M sensor toward *n*-butanol at 250°C.

The response-recovery properties of the WO<sub>3</sub>-Au composite NF sensors were also compared to the pure WO<sub>3</sub> NF sensor, as depicted in Figure 5.17. The response time values of the WO<sub>3</sub>-Au-0.1M sensor toward 10, 20, 50, 100, 200 and 500 ppm of *n*-butanol are 31, 33, 34, 55, 71 and 84 s, respectively. These response values are significantly lower than those of pure WO<sub>3</sub> sensor (61, 76, 71, 76, 96 and 101 s, respectively). This shows that response time of the WO<sub>3</sub>-Au-0.1M sensor is accelerated for all the different concentration of *n*-butanol, which is reduced for 43 s compared to the pure WO<sub>3</sub> sensor toward 20 ppm of *n*-butanol. Moreover, the recovery time values of the WO<sub>3</sub>-Au-0.1M sensor toward 10, 20, 50, 100, 200 and 500 ppm of *n*-butanol are only slightly increased from 9 to 15 s as the concentration of *n*-butanol increases, which is highly accelerated compared to pure WO<sub>3</sub> sensors recovery time changing from 10 to 122 s.

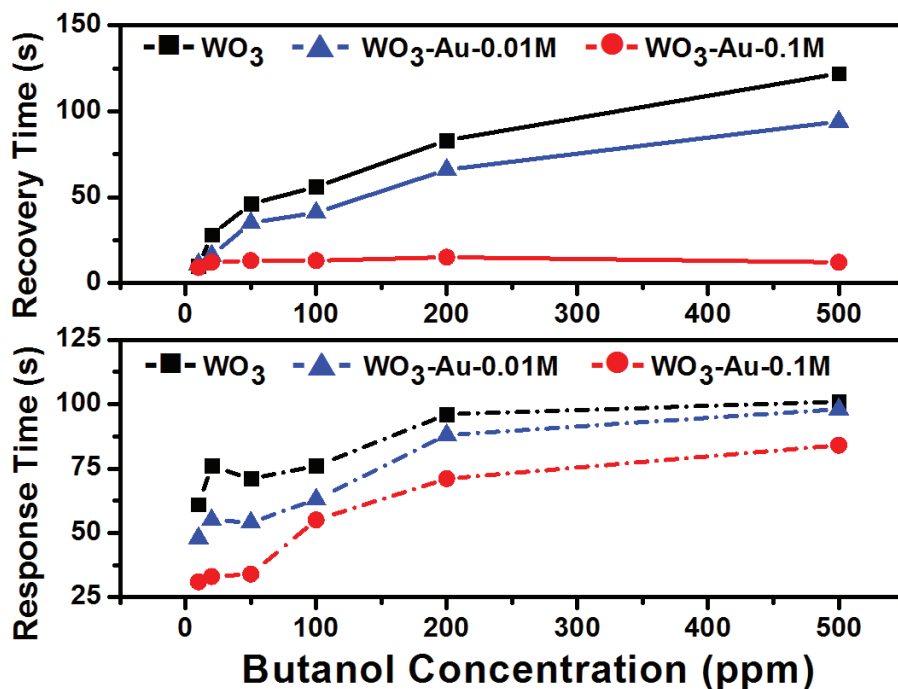


Figure 5.17 Response-recovery time vs. *n*-butanol concentration plots of  $\text{WO}_3$ ,  $\text{WO}_3\text{-Au-0.01M}$  and  $\text{WO}_3\text{-Au-0.1M}$  sensors at 250°C

## 6.4 Stability

The reproducibility of the response for this particular sensor toward 100 ppm of *n*-butanol was also investigated as shown in Figure 5.18 a. The output voltage value remains more or less similar with the continuous cycling tests. For practical applications, gas sensors not only need to exhibit high sensitivity and selectivity toward the target gases, but also good stability to ensure their long-term reliability. Figure 5.18 b shows the stability evaluation of the  $\text{WO}_3\text{-Au-0.1M}$  sensor toward 50 ppm of *n*-butanol over a total period of 30 days. It is clearly shown that the  $\text{WO}_3\text{-Au-0.1M}$  sensor exhibits excellent stability toward *n*-butanol gas as the *S* value remains equal to around 150 during the 30 days testing period.

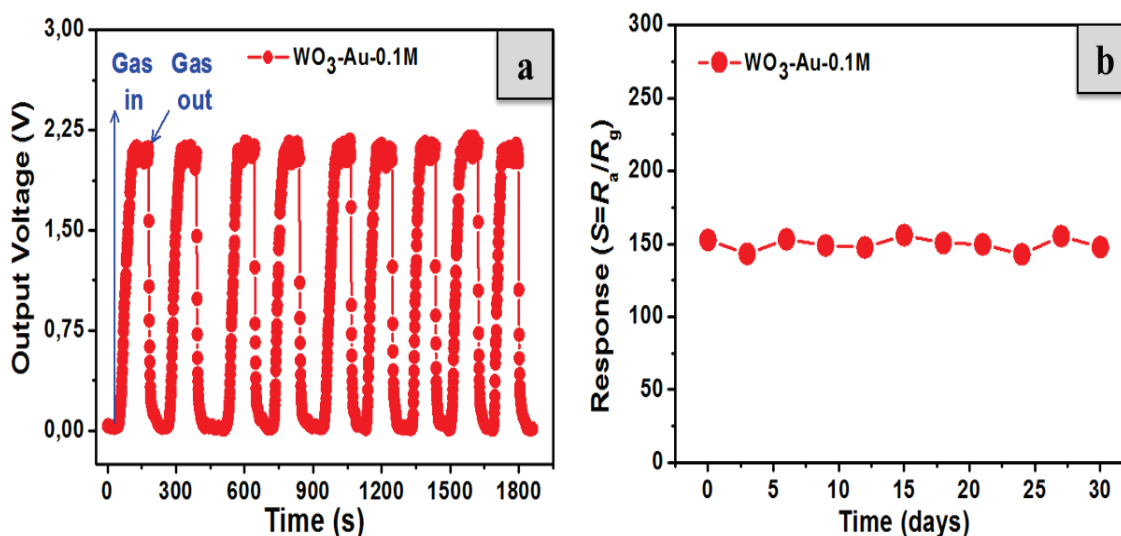
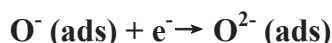
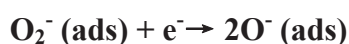
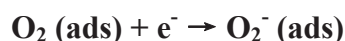


Figure 5.18 (a) Response of WO<sub>3</sub>-Au-0.1M sensor to cycling toward n-butanol (100 ppm) at 250 °C; (b) Stability evaluation of the WO<sub>3</sub>-Au-0.1M sensors toward 100 ppm of n-butanol over a period of 30 days

## 6.5 Sensing Mechanism

The sensing mechanisms of WO<sub>3</sub> and WO<sub>3</sub>-Au composite sensors are relatively different from each other due to the oxide crystals and metal NPs components. For pure WO<sub>3</sub> sensor, the gas-sensing mechanism is probably similar to other semiconductor oxide sensors [191]. Indeed, oxygen molecules are adsorbed on the surface of the WO<sub>3</sub> nanocrystals when the sensor is exposed to air and are ionized to O<sup>-</sup> or O<sup>2-</sup> by capturing free electrons from the conduction band of WO<sub>3</sub>. Thus, an electron depletion layer is formed by reducing the free charge carrier (electron) concentration. In our case, the *n*-butanol molecules reacts with the adsorbed oxygen species (O<sup>2-</sup>) on the surface of the WO<sub>3</sub> nanocrystals, according to the following equations, which release the trapped electrons back into the conduction band of WO<sub>3</sub>. As a consequence, the concentration of free electron increases and ultimately decreases the resistance of the WO<sub>3</sub> sensor.

**Air:**



***n*-butanol:**



By comparison, the enhanced response of the WO<sub>3</sub>-Au composite sensor toward *n*-butanol could be attributed to both chemical and electronic sensitization effects induced by the Au NPs. The adsorbed oxygen can diffuse faster to the surface vacancies and capture electrons from the conduction band of WO<sub>3</sub>. The amount of active oxygen ions (O<sup>-</sup> or O<sup>2-</sup>) increases significantly with the present of Au NPs, due to its better oxygen dissociation properties than WO<sub>3</sub>. In this case gold acts as a catalyst, reducing activation energy for the surface reaction. Due to both the increase in adsorbed oxygen and the molecules to ions rate of conversion, the degree of electron depletion at the Au/WO<sub>3</sub> interface is higher than that at the pure WO<sub>3</sub> surface. The loading of Au NPs on the surface of WO<sub>3</sub> NFs is expected to induce electronic sensitization, due to the differences in their work functions:  $\Phi(\text{Au})= 5.1 \text{ eV}$  and  $\Phi(\text{WO}_3) = 5.7 \text{ eV}$  [192], [193]. Furthermore, a Schottky barrier can be formed by the presence of Au NPs on the surfaces of the WO<sub>3</sub> nanocrystals [194], [195]. It generates a layer depleting electron region at the Au/WO<sub>3</sub> interface, which further increases the resistance of the sensor. The size of Au NPs probably plays also an important role since small NPs size, of a few nanometers, leads to an increase of the surface-to-volume ratio. The oxygen atoms have consequently more potential to adsorb on NPs and to react efficiently at constant volume inducing a high degree of electron depletion in the WO<sub>3</sub>-Au sensor, which also significantly enhance its resistivity. As a result, by combining the semiconductor and noble metal properties, WO<sub>3</sub>-Au sensors show higher sensitivity and faster response/recovery properties toward the target gases.

## 7 Conclusions

In this chapter, we presented WO<sub>3</sub> and WO<sub>3</sub>-Au composite NFs fabricated with ES. Important experimental parameters like starting polymer, calcination process factor, and Au addition routes were investigated. Calcination with different atmospheres can lead to different materials, form pure metallic oxide WO<sub>3</sub> NFs in air, tungsten carbide WC and C in H<sub>2</sub>, and the mixture of W, O, C composite in N<sub>2</sub>. The temperature and atmosphere control composition and structure from the sample. Thermal treatment in air at 500°C for 2h is the best calcination process to fabricate WO<sub>3</sub> NFs. Different starting polymers influence the specific surface area and mean pore size of samples. WO<sub>3</sub> NFs fabricated from PVP-AMT has the highest specific surface area of 10.1 m<sup>2</sup>·g<sup>-1</sup> with a smallest mean pore size of 22.8 nm. All the starting polymers including PVP-AMT, PVA-AMT, and PAN-AMT lead to WO<sub>3</sub> NFs followed with subsequent calcination process in air at 500°C for 2 h.

WO<sub>3</sub>-Au composite NFs were obtained by three different Au addition routes. The schematic diagram illustrates the formation of WO<sub>3</sub>-Au composite NFs by three Au addition routes is shown in Figure 5.19. The volume inclusion (i) Au addition routes lead to WO<sub>3</sub>-Au composite NFs with larger and uniformly distributed Au NPs on the fiber surface. Surface deposition (ii) can get homogenous Au NPs on the surface of WO<sub>3</sub> NFs with a previous stabilization process at 200°C before addition Au ions, and then followed with calcination in air at 500°C for 2 h. Surface deposition (iii) route leads to WO<sub>3</sub>-Au composite NFs with several Au nanostructures including NPs, NRs, nanoflakes. The Au contents can be adjusted by varying the concentration of Chloroauric acid aqueous solution. The second route of deposition (ii) is the best choice to fabricate WO<sub>3</sub>-Au composite NFs with homogeneously deposited and uniform size Au NPs. Uniformly sized Au NPs (5-10 nm) were then decorated on the surface of the WO<sub>3</sub> NFs as catalysts for improving the sensing response. The gas-sensing results demonstrate the excellent response of the WO<sub>3</sub>-Au composite NF sensor, particularly the WO<sub>3</sub>-Au-0.1M sensor, which exhibits ~ 60 times higher response and significantly improved selectivity toward *n*-butanol than the pure WO<sub>3</sub> sensor. In addition, they also show a decreased optimum operating temperature at 250°C compared to 300°C for pure WO<sub>3</sub> sensor. Furthermore, the Au-decoration also improves the response and recovery time of the WO<sub>3</sub> sensor by 5-43 s and 10-122 s, respectively. The enhanced response of the WO<sub>3</sub>-Au composite NF sensor toward *n*-butanol may be attributed to the excellent catalytic activity of Au NPs which enhances the oxygen molecule to ion conversion rate and the existence of multiple depletion layers at the surface of the WO<sub>3</sub>-Au composite NFs. This

effect results in a greater change in resistivity upon exposure to *n*-butanol. This study will be beneficial for the design and manufacturing of WO<sub>3</sub>-based composite gas sensors with high performance toward VOCs for diverse sensing applications.

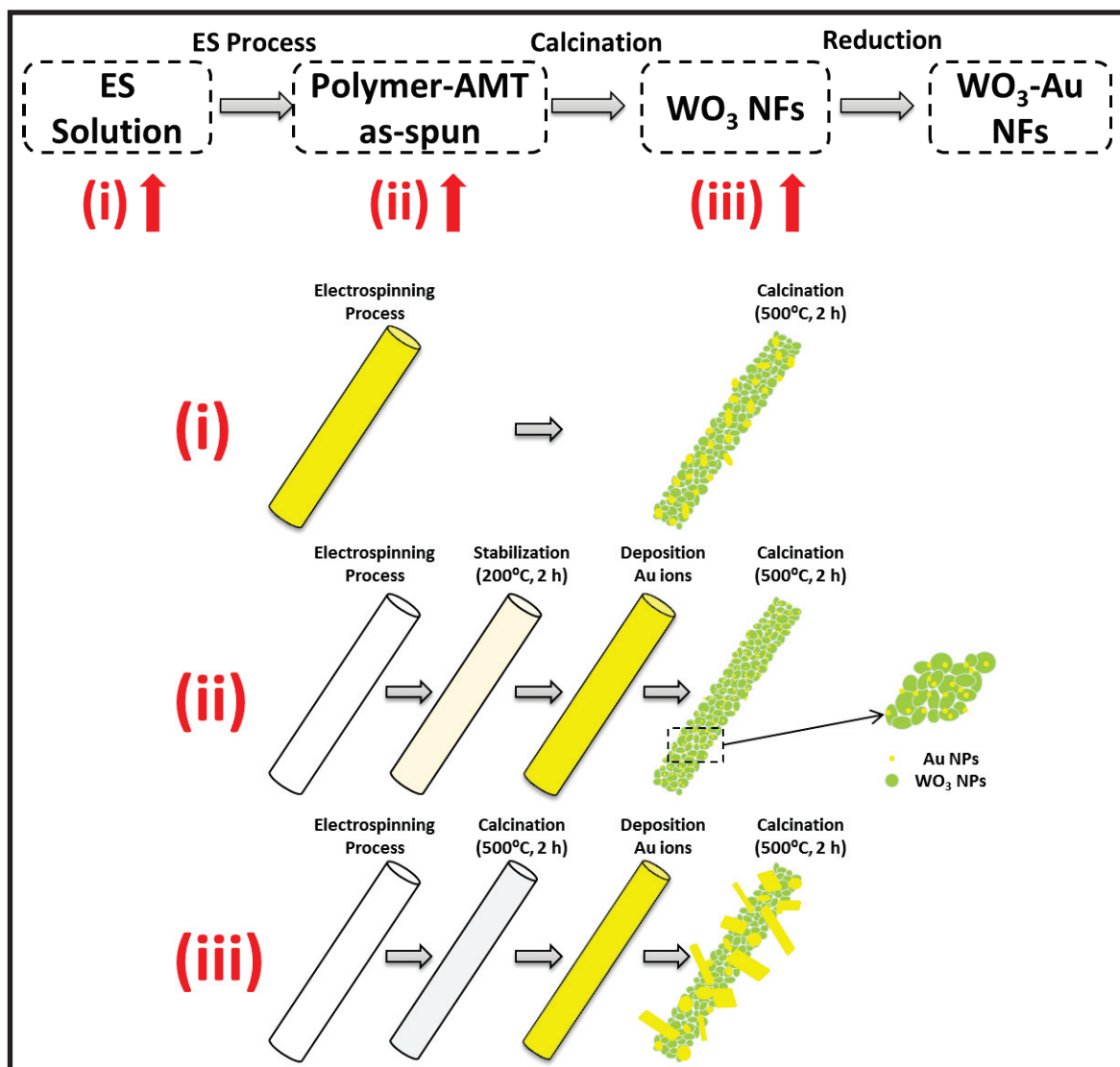


Figure 5.19 Schematic diagram illustrating the formation of WO<sub>3</sub>-Au composite NFs

## GENERAL CONCLUSION

In this thesis, we have studied the synthesis and characterization of hybrid metal-metallic oxide composite (HMMOC) nanofibers (NFs) obtained by electrospinning (ES) and their applications, especially photocatalytic degradation for methylene blue (MB) in an aqueous solution by TiO<sub>2</sub>-Au composite NFs and gas sensing of volatile organic compounds (VOCs) by WO<sub>3</sub>-Au composite NFs. The influence of polymer precursors (PVP, PVA, PAN), calcination process (atmosphere, temperature) and Au addition routes including volume inclusion (i), surface deposition (ii), and surface deposition (iii) have been investigated for the fabrication of three types of samples:

- a) polymer-gold composites
- b) metallic oxide NFs (TiO<sub>2</sub> or WO<sub>3</sub>)
- c) HMMOC (TiO<sub>2</sub>-Au or WO<sub>3</sub>-Au) NFs.

The surface morphologies and dimension of nanostructures are tuned with the employed processing route.

1) Based on various physico-chemical characterizations, the morphologies, compositions, and nanostructures of polymer-Au composite, metallic oxide, and HMMOC NFs have been studied. According to the results, the polymer-Au composite NFs can be achieved via different starting polymers by volume inclusion (i) or surface deposition (ii). Among various gold reduction methods, calcination at 200°C is the simplest and most efficient way to obtain polymer-Au composite NFs with uniform Au NPs, 10 nm in size, and homogeneously dispersed in the volume of polymer NFs. This is a facile way to fabricate composite NFs containing Au NPs with a controllable content and location, which are important characteristics for potential applications. In order to obtain pure Au NFs, optimized experimental conditions are studied showing that PVP is the best choice as starting polymer and the most suitable calcination process is in air at 500°C for 2 h. Au NFs with average diameter around 60 nm are then obtained.

2) TiO<sub>2</sub> NFs is also fabricated with ES. The influence of experimental parameters like titanium isopropoxide (TTIP) concentration and annealing treatment temperatures were

investigated. We have shown that the initial concentration of TTIP can affect the fiber diameter and morphology of TiO<sub>2</sub>. The relative concentration of PVP/TTIP 9:30 is optimized to fabricate TiO<sub>2</sub> NFs having a fairly uniform diameter and porous surface. The calcination process is another important factor to control the morphology and composition of TiO<sub>2</sub> NFs. Varying temperatures allowed to obtain TiO<sub>2</sub> having different Anatase/Rutile ratio and different TiO<sub>2</sub> crystal size. As temperature increases from 500°C to 800°C, anatase, the low temperature phase transforms to rutile as well as a significant crystal growth, which affects specific surface area and final morphology of NFs. Thermal treatment under air at 500°C for 2h has been identified as the best conditions to fabricate TiO<sub>2</sub> NFs with a Anatase/Rutile ratio of 98:2 and an average diameter of 164 nm.

Concerning the WO<sub>3</sub> NFs, the influence of experimental parameters like the polymer precursors and the calcination process are investigated. Different starting polymers can influence the specific surface area and the mean pore size of samples. For example, WO<sub>3</sub> NFs fabricated from PVP-AMT has the highest specific surface area of 10.1 m<sup>2</sup>.g<sup>-1</sup> with the smallest mean pore size of 22.8 nm. The annealing treatment realized with different atmospheres can lead to different types of materials: For example, under air pure metallic oxide WO<sub>3</sub> NFs are obtained, while tungsten carbide WC and C in H<sub>2</sub>, and the mixture of W, O, C composite in N<sub>2</sub> can be synthesized. All the starting polymers including PVP-AMT, PVA-AMT, and PAN-AMT can finally lead to WO<sub>3</sub> NFs when followed with a calcination process in air at 500°C.

3) TiO<sub>2</sub>-Au composite NFs were obtained from three different Au doing routes with subsequent thermal process. The calcination process plays an important role to get the targeted samples including the *in situ* reduction of Au ions to form Au NPs, decomposition of PVP, and formation of TiO<sub>2</sub>. The Au NPs are formed at lower temperature with uniform size around 10 nm at 200°C. The final TiO<sub>2</sub>-Au composite NFs were obtained at 500°C. The volume inclusion (i) Au addition route lead to TiO<sub>2</sub>-Au composite NFs with homogenous and uniform Au NPs dispersed within the volume of TiO<sub>2</sub> matrix NF whereas the surface deposition (ii) routes only generate Au NPs with non-uniform size located on the surface of TiO<sub>2</sub> NFs. The Surface deposition (iii) Au addition route allows synthesizing TiO<sub>2</sub>-Au composite NFs with several Au nanostructures including NPs, NRs, nanoflakes (non-uniform shapes). The Au contents can be adjusted by varying the concentration of the initial Au

aqueous solution. The first route of volume inclusion (i) appears to be the best choice to fabricate TiO<sub>2</sub>-Au composite NFs with homogeneously deposited and uniform size Au NPs. Uniformly sized Au NPs (~10 nm) decorate the TiO<sub>2</sub>-Au NFs surface and act as reaction sites for improving the photocatalysis performance.

The WO<sub>3</sub>-Au composite NFs are also obtained from the three different Au addition routes with subsequent thermal process. The volume inclusion (i) Au addition route allows obtaining WO<sub>3</sub>-Au composite NFs with larger and uniform Au NPs on the fiber surface. With a prior stabilization process at 200°C before Au ions addition, the surface deposition (ii) leads to homogenous Au NPs on the surface of WO<sub>3</sub> NFs, and then followed with calcination in air at 500°C for 2 h. Surface deposition (iii) Au addition route fabricate WO<sub>3</sub>-Au composite NFs with several Au nanostructures including NPs, NRs, nanoflakes. The Au contents can be adjusted by varying the concentration of the initial Au aqueous solution. The second route of surface deposition (ii) has then be identified as the best choice to fabricate WO<sub>3</sub>-Au composite NFs with homogeneously dispersed and uniform in size Au NPs. Uniformly sized Au NPs (5-10 nm) with WO<sub>3</sub> NFs is an efficient catalysts to improve the sensing response of volatile organic compounds.

The photocatalytic results demonstrate the excellent response from TiO<sub>2</sub>-Au composite NF catalysts, particularly the TiO<sub>2</sub>-Au-4wt% catalyst, which exhibits ~3 times higher reaction rate and significantly improves the degradation speed of MB aqueous solution compared to pure TiO<sub>2</sub> NFs and commercial P25 catalysts. In addition, using different irradiation wavelength leads to different photocatalytic performances. Indeed, under UV light (360 nm) combined with visible light (528 nm), photocatalytic performances of TiO<sub>2</sub>-Au composites can be enhanced compared to the use of pure UVA irradiation, which indicates that synthesized material has a photocatalytic activity range in the visible range. The photocatalytic mechanism of TiO<sub>2</sub>-Au composite NFs under UV light and visible light has been discussed. This study will benefit for the design and construction of TiO<sub>2</sub>-based composite catalysts with high photocatalytic activity.

The gas-sensing results demonstrate the excellent response of the WO<sub>3</sub>-Au composite NF sensors, particularly the WO<sub>3</sub>-Au-0.1M sensor, which exhibits ~60 times higher response and significantly improved the selectivity toward *n*-butanol than pure WO<sub>3</sub> sensors. In addition,

their optimum operating temperature (250°C) is significantly lower than pure WO<sub>3</sub> sensor (300°C). Furthermore, the surface decoration with gold nanoparticles also improves the response and recovery time compared to pure WO<sub>3</sub> sensor. This enhanced response of the WO<sub>3</sub>-Au composite NF sensor toward *n*-butanol may be attributed to the excellent catalytic activity of Au NPs which drastically improve the oxygen molecule to ion conversion rate and the existence of multiple depletion layers at the surface of the WO<sub>3</sub>-Au composite NFs. These results will be highly beneficial for the design and construction of WO<sub>3</sub>-based composite gas sensors with high performance toward VOCs for diverse sensing applications.

## LIST OF FIGURES

Figure 1.1 Energy bands in (a) conductors, (b) SC, and (c) insulators [2].....	26
Figure 1.2 Schematic of a silicon crystal lattice doped with impurities for <i>n</i> -type and <i>p</i> -type SC material[3]. .....	27
Figure 1.3 Electron-hole pair generation in a photo illuminated <i>n</i> -type SC nanoparticle. ....	27
Figure 1.4 Crystal structures of TiO <sub>2</sub> a) Rutile b) Anatase c) Brookite [7].....	29
Figure 1.5 TEM image of gold nano-objects. ....	32
Figure 1.6 Schematic of plasmon oscillation for a sphere, showing the displacement of the conduction electron charge cloud relative to the nuclei[25]. .....	33
Figure 1.7 Longitudinal Surface Plasmon Resonance mode and Normalized Cross sections in function of the Au nanorods shape. In insert Extinction spectra in function of the nanorods aspect ratio [28]. .....	34
Figure 1.8 Electric field contours for radius 30 nm Ag spheres in vacuum [29]. .....	34
Figure 1.9 SEM and TEM images of metal/TiO <sub>2</sub> nanostructures: (a)(Au core) /(TiO <sub>2</sub> shell) ; (b) (Cu NPs)/(TiO <sub>2</sub> NTs); (c) (Ag NPs)/(TiO <sub>2</sub> NTs); (d) (Au NPs)/(TiO <sub>2</sub> NTs) [1]. .....	36
Figure 1.10 SEM images of different WO <sub>3</sub> nanostructures.....	36
Figure 1.11 Schematic of two different ways for <i>in situ</i> photoreduction of NPs with polymer [49]. .....	40
Figure 1.12 Schematic illustration of the basic setup and process for electrospinning. ....	43
Figure 1.13 Three main steps of typical electrospinning process to produce metallic oxide nanofibers.....	43
Figure 1.14 General effect of increasing voltage on electrospinning process and fiber diameter[75]. .....	45
Figure 1.15 SEM images of poly (ethyleneoxide) fibers (each image shows a 20 μm wide area), together with viscosity value (in red). Evolution of the morphology of polymer fibers upon increase of solution viscosity. Adapted from [76]. .....	46
Figure 1.16 (a) General model of photocatalysis on TiO <sub>2</sub> . Reactions occur in three steps: (1) absorption of photons greater than the band gap energy to produce an electron-hole pair; (2) separation of charges and migration to the surface; (3) redox reactions with adsorbed reactants. (b) TiO <sub>2</sub> composite structure exhibiting a heterojunction and charge trapping on TiO <sub>2</sub> and the second component [117]. .....	54
Figure 1.17 Schematic of the Schottky barrier [118]. .....	55

Figure 1.18 Application map of photocatalysts [119]. ..... 56

Figure 1.19 Receptor transduce function of a semiconductor gas sensor: (a) surface, providing the receptor function, (b) microstructure of the sensing layer, providing the transducer function, and (c) element, enabling the detection of the change in output resistance of the sensing layer, here deposited on an interdigital microelectrode. Reprinted with permission from Reference [129]. ..... 57

Figure 2.1 Chemical structures of the three different precursors of metallic oxides. .... 64

Figure 2.2 Chemical structures of three different polymers. .... 65

Figure 2.3 the typical synthesis routes and processes of electrospinning with experiment factors. .... 66

Figure 2.4 Electrospinning setup: (a) high voltage supply, (b) syringe pump, (c) plastic syringe, (d) needle, (e) collector. .... 66

Figure 2.5 Synthesis processes and three different Au addition routes. .... 68

Figure 2.6 Different thermal treatment processes for three different addition routes. Red arrows indicate when gold ions are introduced in the system: (i) with co-spinning of gold ions and polymer solution, (ii) with deposition either before or after stabilization of polymer filaments and (iii) with deposition after filament calcination. .... 69

Figure 2.7 Schematic of Photocatalysis performance measurement system. .... 82

Figure 2.8 the sensor prepared process and gas-sensing measurement system. .... 84

Figure 2.9 Schematic giving more details about the sensing part of the detector (part c of Figure 2.8) ..... 85

Figure 3.1 SEM images of PVP-Au composite NFs fabricated with different Au contents by volume inclusion with ES and calcined at 500°C in air for 2h: (a) PVP-Au-3:1; (b) PVP-Au-6:1; (c) PVP-Au-9:1. .... 88

Figure 3.2 SEM images of polymer-Au composite NFs fabricated with different starting polymers by Direct ES and calcined at 200°C in air for 2h, respectively: (a) PVP-Au; (b) PVA-Au; (c) PAN-Au. .... 89

Figure 3.3 SEM images of as spun PVP-Au composite NFs fabricated by volume inclusion and then heated in different atmospheres at 500°C for 2 h: (a) as-spun; (b) air (high resolution in insert); (c) Ar-H<sub>2</sub>; (d) H<sub>2</sub>. .... 90

Figure 3.4 TGA of and DTG thermograms for pure PVP, PVP-Au precursor NFs. .... 91

Figure 3.5 FT-IR spectra of (a) PVP NFs and (b) PVP-Au precursor NFs prepared at different calcination temperatures:(c) 200°C; (d) 300°C; Calcination was performed in air. .... 92

Figure 3.6 FT-IR spectra of PVP-Au precursor NFs prepared at different calcination

temperatures: (a) as spun; (b) 400°C; (c) 500°C; Calcination was performed under air. ....	93
Figure 3.7 SEM images of PVP-Au composite NFs fabricated by volume inclusion (i) and then heat treated in air at different temperatures for 2 h: (a) 200°C; (b) 300°C; (c) 400°C; (d) 500°C.....	94
Figure 3.8 XRD patterns of as-spun PVP-Au composite NFs prepared at different calcination temperatures: (a) 200°C; (b) 300°C; (c) 400°C; (d) 500°C. ....	95
Figure 3.9 (a) HRTEM images of Au NFs prepared at 500°C in air for 2 h; (a-insert) SAED pattern of the Au NFs at 500°C; (b) HR-TEM image of Au NF at 500°C; (c) HR-TEM lattice images of Au NFs at 500°C.....	96
Figure 3.10 EDS spectrum of Au NFs obtained by calcined the volume inclusion (i) electrospun PVP-Au composite NFs in air at 500°C for 2 h and its elements compositions...	97
Figure 3.11 (a) EDS spectrum of sample obtained after 10 h electrospinning process and then calcined the as-spun PVP-Au composite NFs in air at 500°C for 2 h and its elements compositions; (b) Raman spectrum of Au NFs calcined at 500°C with stainless steel after ES process for 10 h. ....	97
Figure 3.12 Schematic of the designed spinning nozzle using an inert Pt wire inserted through a plastic tube.....	98
Figure 3.13 The SEM images and EDS spectrum of Au NFs fabricated with Pt wire calcined in air at 500°C for 2 h.....	98
Figure 3.14 TGA and SDTA of pure PVP NFs and PVP-Au Pt-wire NFs.....	99
Figure 3.15 SEM image of PVP-Au NFs treated 2h under air at 200°C; Insert corresponds to a lower magnification.....	100
Figure 3.16 TGA and DTG thermograms (under air) for pure as-spun PAN NFs. ....	102
Figure 3.17 FT-IR spectra of as-spun PAN NFs stabilization at different temperatures: (a) as-spun; (b) 120°C; (c) 150°C; (d) 200°C; (e) 250°C; (f) 280°C; (g) 300°C; and (h) 500°C, respectively.....	103
Figure 3.18 SEM images of PAN-Au composite NFs obtained from Stabilization (ii) with different stabilization temperatures: (a) room temperature (not stabilized); (b) 200°C; (c) 250°C; (d) 280°C before deposition of 0.01M Au ions and a reduction at 200°C in air.....	104
Figure 3.19 SEM images of PAN-Au composite NFs fabricated by surface deposition (ii) with different Au concentration solutions and then heat treated in air at 200°C for 2 h: (a) 0.01M; (b) 0.1M; (c) 1M.....	105
Figure 3.20 SEM images of PAN-Au composite NFs fabricated by surface deposition (ii) with 0.01M Au solution at different deposition times and then heat treated in air at 200°C for 2 h:	

(a) 1 time; (b) 3 times; (c) 5 times.....	106
Figure 3.21 SEM images of PAN-Au composite NFs fabricated by surface deposition (ii) with 0.01M Au solution followed with different reduction methods: (a) heating at 200°C; (b) citrate; (c) hydrazine.....	107
Figure 3.22 SEM images of PAN-Au composite NFs fabricated by surface deposition (ii) with 0.1M of Au solutions and then heat treated in air at different temperatures for 2 h: (a) 200°C; (b) 300°C; (c) 400°C; (d) 500°C.....	108
Figure 3.23 XRD pattern of PAN-Au composite NFs prepared by stabilization PAN NFs at 200°C and then deposition Au ions with concentration of 0.1M followed with calcination at 200°C for Au reduction.....	109
Figure 3.24 (a) TEM images and (b) HR-TEM images of PAN-Au stabilization with at 200°C and then deposition Au ions followed with calcination reduction at 200°C; (c) size distribution of Au particle size of PAN-Au composite NFs.....	109
Figure 4.1 Electronic structure of anatase and rutile TiO <sub>2</sub> .....	111
Figure 4.2 SEM images of TiO <sub>2</sub> NFs obtained from calcined the as-spun PVP-TTIP composite NFs in air at 500°C for 2 h with different concentration of PVP : TTIP : (a) 9:3; (b) 9:10; (c) 9:30.....	114
Figure 4.3 SEM of TiO <sub>2</sub> NFs obtained with different calcination temperatures: (a) 500°C; (b) 600°C; (c) 700°C; and (d) 800°C; (e), (f), (g), and (h) are the corresponding size distributions of fiber diameter.....	115
Figure 4.4 Rietveld refinement details by software of Bass based on XRD data of TiO <sub>2</sub> obtained by calcined at 500°C.....	116
Figure 4.5 XRD patterns of TiO <sub>2</sub> NFs obtained with different calcination temperatures: (a) 500°C; (b) 600°C; (c) 700°C; and (d) 800°C.....	117
Figure 4.6 SEM images of TiO <sub>2</sub> -Au composite NFs fabricated from volume inclusion (i) with different Au contents: (a) 2wt%; (b) 4wt%; (c) 8wt% ; (d), (e), (f) and (g), (h), (i) are the size distributions of TiO <sub>2</sub> -Au fiber diameter and Au NPs size for sample (a), (b), and (c), respectively.....	119
Figure 4.7 XRD patterns of TiO <sub>2</sub> -Au composite NFs fabricated with different Au concentrations: (a) 0wt% ; (b) 2wt%; (c) 4wt%; (d) 8wt%.....	121
Figure 4.8 SEM images of PVP-TTIP as-spun composite NFs and treated with different temperatures in air for 2 h:(a) as-spun; (b) 200°C; (c) 500°C; (d) and (e) are the size distributions of TiO <sub>2</sub> fiber diameter and Au NPs size for (c).....	123
Figure 4.9 SEM images of TiO <sub>2</sub> -Au composite NFs fabricated from different Au introducing	

routes: (a) volume inclusion (i); (b) surface deposition (ii); (c) surface deposition (iii); (d), (e), (f) and (g), (h), (i) are the size distributions of TiO <sub>2</sub> -Au fiber diameter and Au NPs size for sample (a), (b), and (c), respectively. ....	124
Figure 4.10 XRD patterns of TiO <sub>2</sub> -Au composite NFs fabricated with different Au introducing routes: .....	126
Figure 4.11 TEM & HR-TEM images of TiO <sub>2</sub> -Au NFs fabricated from different Au introducing routes: (a), (d) volume inclusion (i); (b), (e) surface deposition (ii); (c), (f) surface deposition (iii), respectively. ....	127
Figure 4.12 (a) UV-visible absorption spectra of PAN-Au NFs, TiO <sub>2</sub> NFs dispersed in MB aqueous solution, and TiO <sub>2</sub> -Au composite NFs; (b) TiO <sub>2</sub> -Au NFs with different Au contents: TiO <sub>2</sub> -Au-2wt%, TiO <sub>2</sub> -Au-4wt%, TiO <sub>2</sub> -Au-8wt%. ....	128
Figure 4.13 UV-Vis absorption spectra of MB aqueous solution in photodegradation process under irradiation of UVA light in the presence of TiO <sub>2</sub> NFs obtained by heat treatment of PVP-TTIP as-spun composite NFs prepared with different concentration of TTIP by ES: (a) 9:3; (b) 9:10; (c) 9:30. ....	130
Figure 4.14 Variation of normalized C/C <sub>0</sub> (a) of MB concentration as a function of UV light irradiation time for TiO <sub>2</sub> -9:3, 9:10, and 9:30. ....	131
Figure 4.15 UV-Vis absorption spectra of MB aqueous solution in photodegradation process under irradiation of UVA light in the presence of TiO <sub>2</sub> NFs obtained with different temperatures: (a) 500°C; (b) 600°C; (c) 700°C; (d) 800°C. ....	132
Figure 4.16 (a) Variation of normalized C/C <sub>0</sub> and (b) variation of normalized ln(C/C <sub>0</sub> ) of MB concentration as a function of UV light irradiation time for TiO <sub>2</sub> heated at 500 °C, 600 °C, 700 °C and 800°C, respectively. ....	133
Figure 4.17 UV-Vis absorption spectra of MB aqueous solution in photodegradation process under irradiation of UVA light in the presence of TiO <sub>2</sub> -Au composite NFs with different Au contents: (a) TiO <sub>2</sub> -Au-2wt%; (b) TiO <sub>2</sub> -Au-4wt%; (c) TiO <sub>2</sub> -Au-8wt%. ....	134
Figure 4.18 Variation of normalized C/C <sub>0</sub> of MB concentration as a function of UV light irradiation time for pure TiO <sub>2</sub> NFs and TiO <sub>2</sub> -Au composite NFs with different Au contents: (a) 2wt%; (b) 4wt%; (c) 8wt%. ....	135
Figure 4.19 Variation of normalized C/C <sub>0</sub> of MB concentration as a function of UV light irradiation time for TiO <sub>2</sub> -Au composite NFs obtained from different Au introducing routes: pure TiO <sub>2</sub> NFs, TiO <sub>2</sub> -Au-i, and TiO <sub>2</sub> -Au-ii. ....	136
Figure 4.20 UV-Vis absorption spectra of MB aqueous solution in photodegradation process under irradiation of UVA light in the presence of different catalysts: (a) P25; (b) TiO <sub>2</sub> NFs; (c)	

TiO <sub>2</sub> -Au .....	137
Figure 4.21 (a) Variation of normalized C/C <sub>0</sub> and (b) variation of normalized ln(C/C <sub>0</sub> ) of MB concentration as a function of UV light irradiation time for P25, TiO <sub>2</sub> , and TiO <sub>2</sub> –Au, respectively.....	138
Figure 4.22 UV-Vis absorption spectra of MB aqueous solution in photodegradation process under different wavelength irradiations in the presence of TiO <sub>2</sub> -Au composite NFs: (a) 360 nm; (b) 528 nm; (c) 360 nm & 528 nm. ....	139
Figure 4.23 (a) Variation of normalized C/C <sub>0</sub> and (b) variation of normalized ln(C/C <sub>0</sub> ) of MB concentration as a function of different wavelength light irradiation time for 360 nm, 528 nm, and 360 nm & 528 nm, respectively.....	140
Figure 4.24 Schematic diagrams of the (a) UV irradiation and (b) visible irradiation photocatalytic degradation of MB with TiO <sub>2</sub> -Au composite NFs.....	141
Figure 4.25 Schematic diagram illustrating the formation of TiO <sub>2</sub> -Au composite NFs. ....	144
Figure 5.1 SEM images of samples obtained from different calcination temperatures of PAN-AMT composite NFs in air for 2 h: (a) 200°C; (b) 500°C; (c) 600°C .....	149
Figure 5.2 XRD patterns of WO <sub>3</sub> NFs fabricated with three different starting polymers calcination in air at 500°C for 2 h: (a) PVP-WO <sub>3</sub> ; (b) PVA-WO <sub>3</sub> ; (c) PAN-WO <sub>3</sub> .....	150
Figure 5.3 SEM images of WO <sub>3</sub> NFs obtained from three polymers-AMT composite NFs after calcination at 500°C in air for 2h: (a) WO <sub>3</sub> NFs obtained from calcined PVP-AMT as-spun NFs; (b) WO <sub>3</sub> NFs obtained from calcined PVA-AMT as-spun NFs;(c) WO <sub>3</sub> NFs obtained from calcined PAN-AMT as-spun NFs; (d), (e), (f) were the EDS spectra of the samples above, respectively. ....	151
Figure 5.4 SEM images WO <sub>3</sub> -Au composite NFs obtained with calcination from stabilization of three different starting polymer-AMT composite NFs and then deposition (ii) Au NPs with 0.1M concentration of gold aqueous solutions followed with calcination in air at 500°C for 2 h: (a) PVP-AMT; (b) PVA-AMT; (c) PAN-AMT; and (d), (e), (f) are the size distributions of Au particle size.....	152
Figure 5.5 SEM images WO <sub>3</sub> -Au composite NFs obtained with calcination three different starting polymers with AMT composite NFs in N <sub>2</sub> at 500°C for 2 h and then deposition (ii) Au NPs with 0.1M concentration of Au aqueous solutions followed with calcination in air at 500°C for 2 h: (a) PVP-AMT; (b) PVA-AMT; (c) PAN-AMT; and (d), (e), (f) are the size distributions of Au particle size.....	153
Figure 5.6 SEM images of WO <sub>3</sub> -Au composite NFs obtained from calcined PVP-AMT NFs with deposition (ii) Au by different stabilization temperatures followed with calcination in air	

at 500°C for 2h: (a) stabilization at room temperature on the as-spun PVP-AMT NFs; (b) stabilization at 200°C addition on the PVP-AMT pre-treated NFs; (c) stabilization at 500°C to form WO <sub>3</sub> NFs before addition Au.....	154
Figure 5.7 Schematic of three different Au addition routes .....	155
Figure 5.8 SEM images of WO <sub>3</sub> -Au composite NFs obtained from calcined PVA-AMT NFs with three Au addition routes followed with calcination in air at 500°C for 2h: (a) volume inclusion (i) addition Au ions into PVA-AMT ES solution directly before ES; (b) surface deposition (ii) addition Au ions on the surface of PVA-AMT NFs with stabilization after ES; (c) surface deposition (iii) addition Au ions on the surface of WO <sub>3</sub> NFs after calcination....	157
Figure 5.9 SEM images WO <sub>3</sub> -Au composite NFs obtained with calcination from stabilization of PVA-AMT composite NFs and then deposition (ii) Au NPs with three different concentrations of gold aqueous solutions followed with calcination in air at 500°C for 2 h: (a) 0.001M; (b) 0.01M; (c) 0.1M; (d), (e), (f) are the size distributions of Au particle size; and (g), (h), (i) are the size distributions of fiber diameter.....	158
Figure 5.10 XRD patterns of (a) WO <sub>3</sub> NFs and (b) WO <sub>3</sub> -Au composite NFs obtained with calcination from stabilization of PVA-AMT composite NFs and then deposition (ii) Au NPs of 0.1M gold aqueous solutions followed with calcination in air at 500°C for 2 h.....	159
Figure 5.11 (a) TEM images of WO <sub>3</sub> -Au-0.1M composite NFs obtained with calcination from stabilization of PVA-AMT composite NFs and then deposition (ii) Au NPs of 0.1M gold aqueous solutions followed with calcination in air at 500°C for 2 h; (b) High-resolution TEM image of Au NPs embedded WO <sub>3</sub> NFs showing the Au and WO <sub>3</sub> lattices .....	160
Figure 5.12 The variation in responses of WO <sub>3</sub> , WO <sub>3</sub> -Au sensors toward 100 ppm of <i>n</i> -butanol as a function of the operating temperature: (a) WO <sub>3</sub> obtained from different polymers; (b) WO <sub>3</sub> , WO <sub>3</sub> -Au-0.01M and WO <sub>3</sub> -Au-0.1M. ....	163
Figure 5.13 Selectivity of the WO <sub>3</sub> , WO <sub>3</sub> -Au-0.01M and WO <sub>3</sub> -Au-0.1M sensors toward 100 ppm of VOCs at 250 °C.....	164
Figure 5.14 Dynamic response-recovery behaviors of the WO <sub>3</sub> , WO <sub>3</sub> -Au-0.01M and WO <sub>3</sub> -Au-0.1M sensors toward various concentrations of <i>n</i> -butanol at the optimum working temperature (250 °C) .....	168
Figure 5.15 Response vs. concentration curves of the WO <sub>3</sub> , WO <sub>3</sub> -Au-0.01M and WO <sub>3</sub> -Au-0.1M sensors toward <i>n</i> -butanol at 250 °C .....	168
Figure 5.16 (a) The dynamic response-recovery behavior of the WO <sub>3</sub> -Au-0.1M sensor toward 10 ppm of <i>n</i> -butanol at 250 °C; (b) The response and recovery vs. concentration curves of the WO <sub>3</sub> -Au-0.1M sensor toward <i>n</i> -butanol at 250°C. ....	169

Figure 5.17 Response-recovery time vs. *n*-butanol concentration plots of WO<sub>3</sub>, WO<sub>3</sub>-Au-0.01M and WO<sub>3</sub>-Au-0.1M sensors at 250°C ..... 170

Figure 5.18 (a) Response of WO<sub>3</sub>-Au-0.1M sensor to cycling toward *n*-butanol (100 ppm) at 250 °C; (b) Stability evaluation of the WO<sub>3</sub>-Au-0.1M sensors toward 100 ppm of *n*-butanol over a period of 30 days ..... 171

Figure 5.19 Schematic diagram illustrating the formation of WO<sub>3</sub>-Au composite NFs ..... 174

## LIST OF TABLES

Table 1.1 XRD data of different TiO <sub>2</sub> crystalline structures. ....	29
Table 1.2 XRD data of different WO <sub>3</sub> crystalline structures. ....	30
Table 1.3 Information about several noble metals. ....	31
Table 1.4 Sensitivity of different nanostructured materials based on WO <sub>3</sub> . ....	37
Table 2.1 Detailed information of polymer ES solution and ES conditions. ....	70
Table 2.2 Detailed information of polymer–Au ES solution and ES conditions. ....	70
Table 2.3 Details of PAN–Au prepared by second route of surface deposition (ii) ....	72
Table 2.4 Experimental details of TiO <sub>2</sub> NFs by first route of volume inclusion (i). ....	73
Table 2.5 Experimental details of WO <sub>3</sub> NFs by first route of volume inclusion (i). ....	73
Table 2.6 Detailed information of the three different Au addition routes. ....	75
Table 3.1 Stability of different polymer NFs in different solvents with Au ions. ....	101
Table 4.1 Diameters, crystallite size and phase ratio A. of TiO <sub>2</sub> obtained from different calcination temperatures. ....	117
Table 4.2 Au contents, average fiber diameters, Au NPs size, and crystallite size of TiO <sub>2</sub> -Au composite NFs obtained from different Au concentrations. ....	121
Table 4.3 Average diameters, Au NPs size, and crystallite size of TiO <sub>2</sub> -Au composite NFs obtained from different Au introducing routes. ....	125
Table 4.4 Specific surface area, crystallite size and Anatase / Rutile ratio of P25, TiO <sub>2</sub> and TiO <sub>2</sub> -Au with different photocatalytic performance. ....	138
Table 5.1 Diameters and components of WO <sub>3</sub> NFs fabricated from different polymers and atmospheres. ....	147
Table 5.2 Diameters, crystallite size and their specific surface area of WO <sub>3</sub> NFs fabricated with different polymers ....	151
Table 5.3 Measurement results of the mean diameter of fiber and Au NP size of WO <sub>3</sub> -Au composites NFs ....	161
Table 5.4 Selectivity of WO <sub>3</sub> , WO <sub>3</sub> -Au-0.01M and WO <sub>3</sub> -Au-0.1M sensors toward 100 ppm of various VOCs at 250 °C ....	165
Table 5.5 Basic physico-chemical properties of different gases ....	165
Table 5.6 Comparison of sensing performance of various WO <sub>3</sub> based sensors toward 100 ppm of different VOCs. ....	166



## REFERENCES

- [1] R. Jiang, B. Li, C. Fang, and J. Wang, "Metal/semiconductor hybrid nanostructures for plasmon-enhanced applications," *Adv. Mater.*, vol. 26, no. 31, pp. 5274–5309, 2014.
- [2] Band theory of solids.  
at<[http://webs.mn.catholic.edu.au/physics/emery/hsc\\_ideas\\_implementation.htm](http://webs.mn.catholic.edu.au/physics/emery/hsc_ideas_implementation.htm)>
- [3] C. Honsberg, "Doping | PVEducation," pp. 1–2, 2015.  
at <<http://www.pveducation.org/pvcdrom/pn-junction/doping>>
- [4] A. A. Ismail and D. W. Bahnemann, "Photochemical splitting of water for hydrogen production by photocatalysis: a review," *Sol. Energy Mater. Sol. Cells*, vol. 128, pp. 85–101, 2014.
- [5] S. J. Patil, A. V. Patil, C. G. Dighavkar, K. S. Thakare, R. Y. Borase, S. J. Nandre, N. G. Deshpande, and R. R. Ahire, "Semiconductor metal oxide compounds based gas sensors: a literature review," *Front. Mater. Sci.*, vol. 9, no. 1, pp. 14–37, 2015.
- [6] N.-H. Kim, S.-J. Choi, D.-J. Yang, J. Bae, J. Park, and I.-D. Kim, "Highly sensitive and selective hydrogen sulfide and toluene sensors using Pd functionalized WO<sub>3</sub> nanofibers for potential diagnosis of halitosis and lung cancer," *Sensors Actuators B Chem.*, vol. 193, pp. 574–581, Mar. 2014.
- [7] S. M. Woodley and C. R. A. Catlow, "Structure prediction of titania phases: Implementation of Darwinian versus Lamarckian concepts in an Evolutionary Algorithm," *Comput. Mater. Sci.*, vol. 45, no. 1, pp. 84–95, Mar. 2009.
- [8] D. E. Scaife, "Oxide semiconductors in photoelectrochemical conversion of solar energy," *Sol. Energy*, vol. 25, no. 1, pp. 41–54, Jan. 1980.
- [9] R. M. Navarro, F. del Valle, J. A. Villoria de la Mano, M. C. Álvarez-Galván, and J. L. G. Fierro, *Advances in Chemical Engineering - Photocatalytic Technologies*, vol. 36. Elsevier, 2009.
- [10] R. M. Navarro, F. del Valle, J. A. Villoria de la Mano, M. C. Álvarez-Galván, and J. L. G. Fierro, "Photocatalytic water splitting under visible light," vol. 36, no. 09, pp. 111–143, 2009.
- [11] R. M. Navarro, M. C. Sánchez-Sánchez, M. C. Alvarez-Galvan, F. del Valle, and J. L. G. Fierro, "Hydrogen production from renewable sources: biomass and photocatalytic opportunities," *Energy Environ. Sci.*, vol. 2, no. 1, pp. 35–54, Dec. 2009.
- [12] M. Maeda and T. Watanabe, "Visible light photocatalysis of nitrogen-doped titanium oxide films prepared by plasma-enhanced chemical vapor deposition," *J. Electrochem. Soc.*, vol. 153, no. 3, p. C186, Mar. 2006.
- [13] K. Maeda and K. Domen, "Solid solution of GaN and ZnO as a stable photocatalyst for overall water splitting under visible light," *Chem. Mater.*, vol. 22, no. 3, pp. 612–623, Feb. 2010.
- [14] W. Choi, A. Termin, and M. R. Hoffmann, "The role of metal ion dopants in quantum-sized TiO<sub>2</sub>: correlation between photoreactivity and charge carrier recombination dynamics," *J. Phys. Chem.*, vol. 98, no. 51, pp. 13669–13679, Dec. 1994.
- [15] T. Vogt, P. M. Woodward, and B. A. Hunter, "The high-temperature phases of WO<sub>3</sub>," *J. Solid State Chem.*, vol. 144, no. 1, pp. 209–215, Apr. 1999.
- [16] I. Lee, S.-J. Choi, K.-M. Park, S. S. Lee, S. Choi, I.-D. Kim, and C. O. Park, "The stability, sensitivity and response transients of ZnO, SnO<sub>2</sub> and WO<sub>3</sub> sensors under acetone, toluene and H<sub>2</sub>S environments," *Sensors Actuators B Chem.*, vol. 197, pp. 300–307, Jul. 2014.

- [17] A. Maity and S. B. Majumder, "NO<sub>2</sub> sensing and selectivity characteristics of tungsten oxide thin films," *Sensors Actuators B Chem.*, vol. 206, pp. 423–429, Jan. 2015.
- [18] J.-H. Lee, "Gas sensors using hierarchical and hollow oxide nanostructures: overview," *Sensors Actuators B Chem.*, vol. 140, no. 1, pp. 319–336, Jun. 2009.
- [19] X. Bai, H. Ji, P. Gao, Y. Zhang, and X. Sun, "Morphology, phase structure and acetone sensitive properties of copper-doped tungsten oxide sensors," *Sensors Actuators, B Chem.*, vol. 193, pp. 100–106, 2014.
- [20] J. S. Lee, O. S. Kwon, D. H. Shin, and J. Jang, "WO<sub>3</sub> nanonodule-decorated hybrid carbon nanofibers for NO<sub>2</sub> gas sensor application," *J. Mater. Chem. A*, vol. 1, no. 32, p. 9099, Jul. 2013.
- [21] Z. Su, J. Ding, and G. Wei, "Electrospinning: a facile technique for fabricating polymeric nanofibers doped with carbon nanotubes and metallic nanoparticles for sensor applications," *RSC Adv.*, vol. 4, no. 94, pp. 52598–52610, 2014.
- [22] C. G. Silva, R. Juárez, T. Marino, R. Molinari, and H. García, "Influence of excitation wavelength (UV or visible light) on the photocatalytic activity of titania containing gold nanoparticles for the generation of hydrogen or oxygen from water.," *J. Am. Chem. Soc.*, vol. 133, no. 3, pp. 595–602, Jan. 2011.
- [23] S. Guo, S. Dong, and E. Wang, "Polyaniline/Pt hybrid nanofibers: high-efficiency nanoelectrocatalysts for electrochemical devices.," *Small*, vol. 5, no. 16, pp. 1869–76, Aug. 2009.
- [24] C. Wang and D. Astruc, "Nanogold plasmonic photocatalysis for organic synthesis and clean energy conversion.," *Chem. Soc. Rev.*, vol. 43, no. 20, pp. 7188–216, Jan. 2014.
- [25] S. T. Kochuveedu, Y. H. Jang, and D. H. Kim, "A study on the mechanism for the interaction of light with noble metal-metal oxide semiconductor nanostructures for various photophysical applications.," *Chem. Soc. Rev.*, vol. 42, no. 21, pp. 8467–8493, Nov. 2013.
- [26] X. C. Jiang, A. Brioude, and M.P. Pileni, "Gold nanorods: Limitations on their synthesis and optical properties," *Colloids Surfaces A Physicochem. Eng. Asp.*, vol. 277, pp. 201–206, 2006.
- [27] A. Brioude, X. C. Jiang, and M. P. Pileni, "Optical properties of gold nanorods: DDA simulations supported by experiments," *J. Phys. Chem. B*, vol. 109, no. 4, pp. 13138–13142, 2005.
- [28] O. L. Muskens, G. Bachelier, N. Del Fatti, F. Vallée, A. Brioude, X. Jiang, and M.-P. Pileni, "Quantitative absorption spectroscopy of a single gold nanorod," *J. Phys. Chem. C*, vol. 112, no. 24, pp. 8917–8921, 2008.
- [29] K. L. Kelly, E. Coronado, L. L. Zhao, and G. C. Schatz, "The optical properties of metal nanoparticles: the influence of size, shape, and dielectric environment," *J. Phys. Chem. B*, vol. 107, no. 3, pp. 668–677, Jan. 2003.
- [30] N. Tian, Z.-Y. Zhou, S.-G. Sun, Y. Ding, and Z. L. Wang, "Synthesis of tetrahedral platinum nanocrystals with high-index facets and high electro-oxidation activity," *Science*, vol. 316, no. 5825, pp. 732–735, May 2007.
- [31] F. Wang, C. Li, L. D. Sun, H. Wu, T. Ming, J. Wang, J. C. Yu, and C. H. Yan, "Heteroepitaxial growth of high-index-faceted palladium nanoshells and their catalytic performance," *J. Am. Chem. Soc.*, vol. 133, no. 4, pp. 1106–1111, 2011.
- [32] H. Chen, L. Shao, Q. Li, and J. Wang, "Gold nanorods and their plasmonic properties," *Chem. Soc. Rev.*, vol. 42, no. 7, pp. 2679–2724, 2013.
- [33] M. H. Huang, S. Mao, H. Feick, H. Yan, Y. Wu, H. Kind, E. Weber, R. Russo, and P. Yang, "Room-temperature ultraviolet nanowire nanolasers.," *Science*, vol. 292, no. 5523, pp. 1897–1899, Jun. 2001.

- [34] Z.-D. Gao, H.-F. Liu, C.-Y. Li, and Y.-Y. Song, "Biotemplated synthesis of Au nanoparticles-TiO<sub>2</sub> nanotube junctions for enhanced direct electrochemistry of heme proteins.," *Chem. Commun. (Camb)*, vol. 49, no. 8, pp. 774–776, Jan. 2013.
- [35] A. Pearson, H. Zheng, K. Kalantar-Zadeh, S. K. Bhargava, and V. Bansal, "Decoration of TiO<sub>2</sub> nanotubes with metal nanoparticles using polyoxometalate as a UV-switchable reducing agent for enhanced visible and solar light photocatalysis.," *Langmuir*, vol. 28, no. 40, pp. 14470–14475, Oct. 2012.
- [36] Z. W. Seh, S. Liu, M. Low, S.-Y. Zhang, Z. Liu, A. Mlayah, and M.-Y. Han, "Janus Au-TiO<sub>2</sub> photocatalysts with strong localization of plasmonic near-fields for efficient visible-light hydrogen generation.," *Adv. Mater.*, vol. 24, no. 17, pp. 2310–2314, May 2012.
- [37] P. Du, Y. Cao, D. Li, Z. Liu, X. Kong, and Z. Sun, "Synthesis of thermally stable Ag@TiO<sub>2</sub> core-shell nanoprisms and plasmon-enhanced optical properties for a P<sub>3</sub>HT thin film.," *RSC Adv.*, vol. 3, no. 17, p. 6016, Apr. 2013.
- [38] G. Xi, J. Ye, Q. Ma, N. Su, H. Bai, and C. Wang, "In situ growth of metal particles on 3D urchin-like WO<sub>3</sub> nanostructures.," *J. Am. Chem. Soc.*, vol. 134, pp. 6508–6511, April. 2012.
- [39] A. Labidi, E. Gillet, R. Delamare, M. Maaref, and K. Aguir, "Ethanol and ozone sensing characteristics of WO<sub>3</sub> based sensors activated by Au and Pd.," *Sensors Actuators B Chem.*, vol. 120, no. 1, pp. 338–345, Dec. 2006.
- [40] M. Penza, C. Martucci, and G. Cassano, "NO<sub>x</sub> gas sensing characteristics of WO<sub>3</sub> thin films activated by noble metals (Pd, Pt, Au) layers.," *Sensors Actuators B Chem.*, vol. 50, no. 1, pp. 52–59, Jul. 1998.
- [41] Q. Xiang, G. F. Meng, H. B. Zhao, Y. Zhang, H. Li, W. J. Ma, and J. Q. Xu, "Au nanoparticle modified WO<sub>3</sub> nanorods with their enhanced properties for photocatalysis and gas sensing.," *J. Phys. Chem. C*, vol. 114, no. 5, pp. 2049–2055, Feb. 2010.
- [42] S. Vallejos, T. Stoycheva, P. Umek, C. Navio, R. Snyders, C. Bittencourt, E. Llobet, C. Blackman, S. Moniz, and X. Correig, "Au nanoparticle-functionalised WO<sub>3</sub> nanoneedles and their application in high sensitivity gas sensor devices.," *Chem. Commun. (Camb)*, vol. 47, no. 1, pp. 565–7, Jan. 2011.
- [43] L. Chen and S. C. Tsang, "Ag doped WO<sub>3</sub>-based powder sensor for the detection of NO gas in air.," *Sensors Actuators B Chem.*, vol. 89, no. 1–2, pp. 68–75, Mar. 2003.
- [44] D. Chen, L. Yin, L. Ge, B. Fan, R. Zhang, J. Sun, and G. Shao, "Low-temperature and highly selective NO-sensing performance of WO<sub>3</sub> nanoplates decorated with silver nanoparticles.," *Sensors Actuators B Chem.*, vol. 185, pp. 445–455, Aug. 2013.
- [45] T. Samerjai, N. Tamaekong, C. Liewhiran, A. Wisitsoraat, and S. Phanichphant, "CO detection of hydrothermally synthesized Pt-loaded WO<sub>3</sub> films.," *J. Nanosci. Nanotechnol.*, vol. 14, no. 10, pp. 7763–7767, Oct. 2014.
- [46] L. Yin, D. Chen, B. Fan, H. Lu, H. Wang, H. Xu, D. Yang, G. Shao, and R. Zhang, "Enhanced selective response to nitric oxide (NO) of Au-modified tungsten trioxide nanoplates.," *Mater. Chem. Phys.*, vol. 143, no. 1, pp. 461–469, Dec. 2013.
- [47] Z. Huang, Y. Zhang, M. Kotaki, and S. Ramakrishna, "A review on polymer nanofibers by electrospinning and their applications in nanocomposites.," *Compos. Sci. Technol.*, vol. 63, no. 15, pp. 2223–2253, Nov. 2003.
- [48] S. Agarwal, A. Greiner, and J.H. Wendorff, "Functional materials by electrospinning of polymers.," *Prog. Polym. Sci.*, vol. 38, no. 6, pp. 963–991, Jun. 2013.
- [49] X. Lu, C. Wang, and Y. Wei, "One-dimensional composite nanomaterials: synthesis by electrospinning and their applications.," *Small*, vol. 5, no. 21, pp. 2349–2370, 2009.
- [50] Y. Keereeta, T. Thongtem, and S. Thongtem, "Fabrication of ZnWO<sub>4</sub> nanofibers by a high direct voltage electrospinning process.," *J. Alloys Compd.*, vol. 509, no. 23, pp. 6689–6695, 2011.

- [51] D. Li and Y. Xia, "Fabrication of titania nanofibers by electrospinning," *Nano Lett.*, vol. 3, no. 4, pp. 555–560, 2003.
- [52] B. Y. Xia, P. Yang, Y. Sun, Y. Wu, B. Mayers, B. Gates, Y. Yin, F. Kim, and H. Yan, "One-dimensional nanostructures : synthesis , characterization , and applications," *Adv. Mater.*, vol. 15, no. 5, pp. 353–389, 2003.
- [53] C. Zhang, Q. Yang, N. Zhan, L. Sun, H. Wang, Y. Song, and Y. Li, "Silver nanoparticles grown on the surface of PAN nanofiber: Preparation, characterization and catalytic performance," *Colloids Surfaces A Physicochem. Eng. Asp.*, vol. 362, no. 1–3, pp. 58–64, 2010.
- [54] H. Q. Nguyen and B. Deng, "Electrospinning and *in situ* nitrogen doping of TiO<sub>2</sub>/PAN nanofibers with photocatalytic activation in visible lights," *Mater. Lett.*, vol. 82, pp. 102–104, 2012.
- [55] Z. Zhang, Z. Wang, S.-W. Cao, and C. Xue, "Au/Pt nanoparticle-decorated TiO<sub>2</sub> nanofibers with plasmon-enhanced photocatalytic activities for solar-to-fuel conversion," *J. Phys. Chem. C*, vol. 117, no. 49, pp. 25939–25947, 2013.
- [56] T. C. Damato, C. C. S. De Oliveira, R. a. Ando, and P. H. C. Camargo, "A facile approach to TiO<sub>2</sub> colloidal spheres decorated with Au nanoparticles displaying well-defined sizes and uniform dispersion," *Langmuir*, vol. 29, no. 5, pp. 1642–1649, 2013.
- [57] Y. Tang, X.W. Wang, Q.H. Zhang, Y.G. Li, and H.Z. Wang, "Fabrication and characterization of high solid content Co<sub>0.8</sub>Ni<sub>0.2</sub>Fe<sub>2</sub>O<sub>4</sub>/PVP composite nanofibers by direct-dispersed electrospinning," *Synthetic Met.*, vol. 162, no. 3-4, pp. 309-313, Mar. 2012.
- [58] Y. Shen, B. Zhang, X. Cao, D. Wei, J. Ma, L. Jia, S. Gao, B. Cui, and Y. Jin, "Microstructure and enhanced H<sub>2</sub>S sensing properties of Pt-loaded WO<sub>3</sub> thin films," *Sensors Actuators, B Chem.*, vol. 193, pp. 273–279, 2014.
- [59] W.-J. Jin, H. K. Lee, E. H. Jeong, W. H. Park, and J. H. Youk, "Preparation of polymer nanofibers containing silver nanoparticles by using poly(N-vinylpyrrolidone)," *Macromol. Rapid Commun.*, vol. 26, no. 24, pp. 1903–1907, Dec. 2005.
- [60] R. Ostermann, D. Li, Y. Yin, J. T. McCann, and Y. Xia, "V<sub>2</sub>O<sub>5</sub> nanorods on TiO<sub>2</sub> nanofibers: a new class of hierarchical nanostructures enabled by electrospinning and calcination," *Nano Lett.*, vol. 6, no. 6, pp. 1297–302, Jun. 2006.
- [61] Z. Li, H. Huang, T. Shang, F. Yang, W. Zheng, C. Wang, and S. K. Manohar, "Facile synthesis of single-crystal and controllable sized silver nanoparticles on the surfaces of polyacrylonitrile nanofibres," *Nanotechnology*, vol. 17, no. 3, pp. 917–920, Feb. 2006.
- [62] D. Li, J. T. McCann, M. Gratt, and Y. Xia, "Photocatalytic deposition of gold nanoparticles on electrospun nanofibers of titania," *Chem. Phys. Lett.*, vol. 394, no. 4–6, pp. 387–391, Aug. 2004.
- [63] X. Lu, Y. Zhao, C. Wang, and Y. Wei, "Fabrication of CdS nanorods in PVP fiber matrices by electrospinning," *Macromol. Rapid Commun.*, vol. 26, no. 16, pp. 1325–1329, Aug. 2005.
- [64] G. M. Bose, *Recherches Sur La Cause Et Sur La Veritable Théorie De L'Électricité*. Slomac, 1745.
- [65] M. Cloupeau and B. Prunet-Foch, "Electrostatic spraying of liquids in cone-jet mode," *J. Electrostat.*, vol. 22, no. 2, pp. 135–159, Jul. 1989.
- [66] J. F. Cooley, US, 692,631, 1902, "Apparatus for electrically dispersing fluids."
- [67] K. Hagiwara, O. Oji-Machi, K. Ku, Japan,699,615, 1929.
- [68] A. Formhals, US patent 1,975,504, 1934.
- [69] W. Simm, K. Gosling, R. Bonart, B. von Falkai, GB 1346231,1972.

- [70] A. Greiner and J. H. Wendorff, "Electrospinning: a fascinating method for the preparation of ultrathin fibers.," *Angew. Chem. Int. Ed. Engl.*, vol. 46, no. 30, pp. 5670–5703, Jan. 2007.
- [71] D. H. Reneker and I. Chun, "Nanometre diameter fibres of polymer, produced by electrospinning," *Nanotechnology*, vol. 7, no. 3, pp. 216–223, Sep. 2006.
- [72] H. Tong and M. Wang, "Tissue engineering scaffolds formed by pseudo-negative voltage electrospinning." USA, 2011
- [73] O. Hardick, B. Stevens, and D.G. Bracewell, "Nanofibre fabrication in a temperature and humidity controlled environment for improved fibre consistency," *J. Mater. Sci.*, vol. 46, no. 11, pp. 3890-3898, Jun. 2011.
- [74] Q.P. Pham, U. Sharma, and A.G. Mikos, "Electrospinning of polymeric nanofibers for tissue engineering applications: A review," *Tissue Eng.*, vol. 12, no. 5, pp. 1197-1211, May. 2006.
- [75] "Voltage." at<<http://electrospintech.com/voltage.html#VjCnK7cve01>>.
- [76] H. Fong, I. Chun, and D. . Reneker, "Beaded nanofibers formed during electrospinning," *Polymer (Guildf.)*, vol. 40, no. 16, pp. 4585–4592, Jul. 1999.
- [77] I. G. Loscertales, A. Barrero, M. Márquez, R. Spretz, R. Velarde-Ortiz, and G. Larsen, "Electrically forced coaxial nanojets for one-step hollow nanofiber design.," *J. Am. Chem. Soc.*, vol. 126, no. 17, pp. 5376–5377, May 2004.
- [78] M. Kanehata, B. Ding, and S. Shiratori, "Nanoporous ultra-high specific surface inorganic fibres," *Nanotechnology*, vol. 18, no. 31, p. 315602, Aug. 2007.
- [79] Y. Zhou, M. Freitag, J. Hone, C. Staii, A. T. Johnson, N. J. Pinto, and A. G. MacDiarmid, "Fabrication and electrical characterization of polyaniline-based nanofibers with diameter below 30 nm," *Appl. Phys. Lett.*, vol. 83, no. 18, p. 3800, Oct. 2003.
- [80] D. Li, Y. Wang, and Y. Xia, "Electrospinning of polymeric and ceramic nanofibers as uniaxially aligned arrays," *Nano Lett.*, vol. 3, no. 8, pp. 1167–1171, Aug. 2003.
- [81] X. Lu, Q. Zhao, X. Liu, D. Wang, W. Zhang, C. Wang, and Y. Wei, "Preparation and characterization of polypyrrole/tio<sub>2</sub> coaxial nanocables," *Macromol. Rapid Commun.*, vol. 27, no. 6, pp. 430–434, Mar. 2006.
- [82] T.J. Sill, and H.A.V. Recum, "Electro spinning: Applications in drug delivery and tissue engineering," *Biomaterials*, vol. 29, no. 13, pp. 1989-2006, May. 2008.
- [83] W.J. Li, C.T. Laurencin, E.J. Caterson, R.S. Tuan, and F.K. Ko, "Electrospun nanofibrous structure: A novel scaffold for tissue engineering," *J. Biomed. Mater. Res.*, vol. 60, no. 4, pp. 613-621, Jun. 2002.
- [84] A.M. Abdelgawad, S.M. Hudson, and O.J. Rojas, "Antimicrobial wound dressing nanofiber mats from multicomponent (chitosan/silver-NPs/polyvinyl alcohol) systems," *Carbohydr. Polym.*, vol. 100, no. SI, pp. 166-178, Jan. 2014.
- [85] T. A. Schmedake, F. Cunin, J. R. Link, and M. J. Sailor, "Standoff detection of chemicals using porous silicon 'smart dust' particles," *Adv. Mater.*, vol. 14, no. 18, pp. 1270–1272, Sep. 2002.
- [86] K. Yoon, B.S. Hsiao, and B. Chu, "Formation of functional polyethersulfone electrospun membrane for water purification by mixed solvent and oxidation processes," *Polymer*, vol. 50, no. 13, pp. 2893-2899, Jun. 2009.
- [87] Y. Tian, M. Wu, R.G. Liu, Y.X. Li, D.Q. Wang, J.J. Tan, R.C. Wu, and Y. Huang, "Electrospun membrane of cellulose acetate for heavy metal ion adsorption in water treatment," *Carbohydr. Polym.*, vol. 83, no. 2, pp. 743-748, Jan. 2011.
- [88] M. Li, G. Han, and B. Yang, "Fabrication of the catalytic electrodes for methanol oxidation on electrospinning-derived carbon fibrous mats," *Electrochem. commun.*, vol. 10, no. 6, pp. 880–883, Jun. 2008.

- [89] L. Wang, Y. Yu, P.-C. Chen, and C.-H. Chen, "Electrospun carbon–cobalt composite nanofiber as an anode material for lithium ion batteries," *Scr. Mater.*, vol. 58, no. 5, pp. 405–408, Mar. 2008.
- [90] Q. Guo, X. Zhou, X. Li, S. Chen, A. Seema, A. Greiner, and H. Hou, "Supercapacitors based on hybrid carbon nanofibers containing multiwalled carbon nanotubes," *J. Mater. Chem.*, vol. 19, no. 18, p. 2810, Apr. 2009.
- [91] Y.Q. Dai, W.Y. Liu, E. Formo, Y.M. Sun, and Y.N. Xia, "Ceramic nanofibers fabricated by electrospinning and their applications in catalysis, environmental science, and energy technology," *Polym. Advan. Technol.*, vol. 22, no. 2, pp. 326–338, Mar. 2011.
- [92] C.Y. Su, L. Liu, M.Y. Zhang, Y. Zhang, and C.L. Shao, "Fabrication of Ag/TiO<sub>2</sub> nanoheterostructures with visible light photocatalytic function via a solvothermal approach," *Crystengcomm*, vol. 44, no. 11, pp. 3989–3999, 2012.
- [93] H. Liu, J. Kameoka, D. A. Czaplewski, and H. G. Craighead, "Polymeric nanowire chemical sensor," *Nano Lett.*, vol. 4, no. 4, pp. 671–675, Apr. 2004.
- [94] K. Sawicka, P. Gouma, and S. Simon, "Electrospun biocomposite nanofibers for urea biosensing," *Sensors Actuators B Chem.*, vol. 108, no. 1–2, pp. 585–588, Jul. 2005.
- [95] V. Thavasi, G. Singh, and S. Ramakrishna, "Electrospun nanofibers in energy and environmental applications," *Energy Environ. Sci.*, vol. 1, no. 2, pp. 205–221, Jul. 2008.
- [96] Q. Long, M. Cai, J. Li, H. Rong, and L. Jiang, "Improving the electrical catalytic activity of Pt/TiO<sub>2</sub> nanocomposites by a combination of electrospinning and microwave irradiation," *J. Nanoparticle Res.*, vol. 13, no. 4, pp. 1655–1662, Apr. 2010.
- [97] R. Jose, A. Kumar, V. Thavasi, and S. Ramakrishna, "Conversion efficiency versus sensitizer for electrospun TiO<sub>2</sub> nanorod electrodes in dye-sensitized solar cells.," *Nanotechnology*, vol. 19, no. 42, p. 424004, Oct. 2008.
- [98] K. Fujihara, A. Kumar, R. Jose, S. Ramakrishna, and S. Uchida, "Spray deposition of electrospun TiO<sub>2</sub> nanorods for dye-sensitized solar cell," *Nanotechnology*, vol. 18, no. 36, p. 365709, Sep. 2007.
- [99] M. V. Reddy, R. Jose, T. H. Teng, B. V. R. Chowdari, and S. Ramakrishna, "Preparation and electrochemical studies of electrospun TiO<sub>2</sub> nanofibers and molten salt method nanoparticles," *Electrochim. Acta*, vol. 55, no. 9, pp. 3109–3117, Mar. 2010.
- [100] P. Zhu, Y. Wu, M. V. Reddy, A. Sreekumaran Nair, B. V. R. Chowdari, and S. Ramakrishna, "Long term cycling studies of electrospun TiO<sub>2</sub> nanostructures and their composites with MWCNTs for rechargeable Li-ion batteries," *RSC Adv.*, vol. 2, no. 2, pp. 531–537, Dec. 2012.
- [101] V. G. Pol, E. Koren, and A. Zaban, "Fabrication of Continuous Conducting Gold Wires by Electrospinning," *Chem. Mater.*, vol. 20, no. 9, pp. 3055–3062, May 2008.
- [102] M. Stasiak, A. Studer, A. Greiner, and J. H. Wendorff, "Polymer fibers as carriers for homogeneous catalysts.," *Chemistry*, vol. 13, no. 21, pp. 6150–6156, Jan. 2007.
- [103] K. Ebert, G. Bengtson, R. Just, M. Oehring, and D. Fritsch, "Catalytically active poly(amideimide) nanofibre mats with high activity tested in the hydrogenation of methyl-cis-9-octadecenoate," *Appl. Catal. A Gen.*, vol. 346, no. 1–2, pp. 72–78, Aug. 2008.
- [104] E. Formo, E. Lee, D. Campbell, and Y. Xia, "Functionalization of electrospun TiO<sub>2</sub> nanofibers with Pt nanoparticles and nanowires for catalytic applications.," *Nano Lett.*, vol. 8, no. 2, pp. 668–672, Feb. 2008.
- [105] E. A. Obuya, W. Harrigan, D. M. Andala, J. Lippens, T. C. Keane, and W. E. Jones, "Photodeposited Pd nanoparticle catalysts supported on photoactivated TiO<sub>2</sub> nanofibers," *J. Mol. Catal. A Chem.*, vol. 340, no. 1–2, pp. 89–98, Apr. 2011.

- [106] E. Formo, Z. Peng, E. Lee, X. Lu, H. Yang, and Y. Xia, "Direct oxidation of methanol on pt nanostructures supported on electrospun nanofibers of anatase," *J. Phys. Chem. C*, vol. 112, no. 27, pp. 9970–9975, Jul. 2008.
- [107] M. Ni, M.K.H. Leung, D.Y.C. Leung, and K. Sumathy, "A review and recent developments in photocatalytic water-splitting using TiO<sub>2</sub> for hydrogen production," *Renew. Sust. Energ. Rev.*, vol. 11, no. 3, pp. 401–425, Apr. 2007.
- [108] H. Tong, S.X. Ouyang, Y.P. Bi, N. Umezawa, M. Oshikiri, and J.H. Ye, "Nano-photocatalytic materials: possibilities and challenges," *Adv. Mater.*, vol. 24, no. 2, pp. 229–251, Jan. 2012.
- [109] D. R. Kennedy, M. Ritchie, and J. Mackenzie, "The photosorption of oxygen and nitric oxide on titanium dioxide," *Trans. Faraday Soc.*, vol. 54, p. 119, Jan. 1958.
- [110] T. I. Barry and F. S. Stone, "The reactions of oxygen at dark and irradiated zinc oxide surface," *Proc. R. Soc. A Math. Phys. Eng. Sci.*, vol. 255, no. 1280, pp. 124–144, Mar. 1960.
- [111] W. Doerffler, "Heterogeneous photocatalysis I. The influence of oxidizing and reducing gases on the electrical conductivity of dark and illuminated zinc oxide surfaces," *J. Catal.*, vol. 3, no. 2, pp. 156–170, Apr. 1964.
- [112] K. Hashimoto, H. Irie, and A. Fujishima, "TiO<sub>2</sub> photocatalysis : a historical overview and future prospects," *Jpn. J. Appl. Phys.*, vol. 44, no. 12, pp. 8269–8285, 2006.
- [113] A. Fujishima and K. Honda, "Electrochemical photolysis of water at a semiconductor electrode," *Nature*, vol. 238, no. 5358, pp. 37–38, Jul. 1972.
- [114] M. R. Hoffmann, S. T. Martin, W. Choi, and D. W. Bahnemann, "Environmental applications of semiconductor photocatalysis," *Chem. Rev.*, vol. 95, no. 1, pp. 69–96, Jan. 1995.
- [115] R. Wang, K. Hashimoto, A. Fujishima, M. Chikuni, E. Kojima, A. Kitamura, M. Shimohigoshi, and T. Watanabe, "Light-induced amphiphilic surfaces," vol. 388, no. 6641, pp. 431–432, Jul. 1997.
- [116] A. Hagfeldt and M. Graetzel, "Light-Induced Redox Reactions in Nanocrystalline Systems," *Chem. Rev.*, vol. 95, no. 1, pp. 49–68, Jan. 1995.
- [117] M. Dahl, Y. Liu, and Y. Yin, "Composite Titanium Dioxide Nanomaterials," *Chem. Rev.*, vol. 114, no. 19, pp. 9853–9889, Oct. 2014.
- [118] H. Wang, L. Zhang, Z. Chen, J. Hu, S. Li, Z. Wang, J. Liu, and X. Wang, "Semiconductor heterojunction photocatalysts: design, construction, and photocatalytic performances," *Chem. Soc. Rev.*, vol. 43, no. 15, p. 5234, 2014.
- [119] Applications of Photocatalysis.  
at < <http://vdmi.de/englisch/products/applied-photocatalysis.html> >
- [120] M. C. Rao, "Structure and Properties of WO<sub>3</sub> thin films for electrochromic device application," vol. 5, no. 1, pp. 1–8, 2013.
- [121] E. Lassner and W.-D. Schubert, *Tungsten: Properties, Chemistry, Technology of the Element, Alloys, and Chemical Compounds*. Springer Science & Business Media, 2012.
- [122] J. Kukkola, J. Mäklin, N. Halonen, T. Kyllönen, G. Tóth, M. Szabó, A. Shchukarev, J.-P. Mikkola, H. Jantunen, and K. Kordás, "Gas sensors based on anodic tungsten oxide," *Sensors Actuators B Chem.*, vol. 153, no. 2, pp. 293–300, Apr. 2011.
- [123] H. Zhang, Y. Li, G. Duan, G. Liu, and W. Cai, "Tungsten oxide nanostructures based on laser ablation in water and a hydrothermal route," *CrystEngComm*, vol. 16, no. 12, p. 2491, Feb. 2014.
- [124] H. Xia, Y. Wang, F. Kong, S. Wang, B. Zhu, X. Guo, J. Zhang, and S. Wu, "Au-doped WO<sub>3</sub>-based sensor for NO<sub>2</sub> detection at low operating temperature," *Sensors Actuators B Chem.*, vol. 134, no. 1, pp. 133–139, Aug. 2008.

- [125] A. Gurlo, "Nanosensors: towards morphological control of gas sensing activity. SnO<sub>2</sub>, In<sub>2</sub>O<sub>3</sub>, ZnO and WO<sub>3</sub> case studies.," *Nanoscale*, vol. 3, no. 1, pp. 154–165, Jan. 2011.
- [126] M. E. Franke, T. J. Koplín, and U. Simon, "Metal and metal oxide nanoparticles in chemiresistors: does the nanoscale matter?," *2013*, vol. 2, no. 1, pp. 36–50, Jan. 2006.
- [127] I.-D. Kim, A. Rothschild, B. H. Lee, D. Y. Kim, S. M. Jo, and H. L. Tuller, "Ultrasensitive chemiresistors based on electrospun TiO<sub>2</sub> nanofibers.," *Nano Lett.*, vol. 6, no. 9, pp. 2009–2013, Sep. 2006.
- [128] J. Huang and Q. Wan, "Gas sensors based on semiconducting metal oxide one-dimensional nanostructures.," *Sensors (Basel)*, vol. 9, no. 12, pp.9903–9924, Jan. 2009.
- [129] I. D. Kim and A. Rothschild, "Nanostructured metal oxide gas sensors prepared by electrospinning," *Polym. Adv. Technol.*, vol. 22, no. 3, pp. 318–325, 2011.
- [130] M. Tiemann, "Porous metal oxides as gas sensors," *Chem.-Eur. J.*, vol. 13, no. 30, pp. 8376-8388, 2007.
- [131] A. Kolmakov, D. O. Klenov, Y. Lilach, S. Stemmer, and M. Moskovits, "Enhanced gas sensing by individual SnO<sub>2</sub> nanowires and nanobelts functionalized with Pd catalyst particles.," *Nano Lett.*, vol. 5, no. 4, pp. 667–673, Apr. 2005.
- [132] "Solid State Gas Sensors, (Adam Hilger Series on Sensors): P. T. Moseley, B. C. Tofield: 9780852745144: Amazon.com: Books." at <http://www.amazon.com/Solid-State-Sensors-Hilger-Series/dp/0852745141>.
- [133] I. M. Tiginyanu, O. Lupan, V. V. Ursaki, L. Chow, and M. Enachi, *Comprehensive Semiconductor Science and Technology*. Elsevier, 2011.
- [134] Y. Ding, Y. Wang, L. Zhang, H. Zhang, C. M. Li, and Y. Lei, "Preparation of TiO<sub>2</sub>-Pt hybrid nanofibers and their application for sensitive hydrazine detection.," *Nanoscale*, vol. 3, no. 3, pp. 1149–1157, Mar. 2011.
- [135] J. Leng, X. Xu, N. Lv, H. Fan, and T. Zhang, "Synthesis and gas-sensing characteristics of WO<sub>3</sub> nanofibers via electrospinning.," *J. Colloid Interface Sci.*, vol. 356, no. 1, pp. 54–57, Apr. 2011.
- [136] W. Sukbua, J. Muangban, N. Triroj, and P. Jaroenapibal, "Effect of particle sizes on the impedance of electrospun tungsten oxide nanofibers," *Procedia Eng.*, vol. 47, pp. 370–373, 2012.
- [137] J. Leng, X. Xu, N. Lv, H. Fan, and T. Zhang, "Synthesis and gas-sensing characteristics of WO<sub>3</sub> nanofibers via electrospinning," *J. Colloid Interface Sci.*, vol. 356, no. 1, pp. 54–57, Apr. 2011.
- [138] D.V. Bavykin, J.M. Friedrich, and F.C. Walsh, "Protonated titanates and TiO<sub>2</sub> nanostructured materials: Synthesis, properties, and applications," *Adv. Mater.*, vol. 18, no.21, PP.2807-2824, Nov. 2006.
- [139] I.P. Parkin, and R.G. Palgrave, "Self-cleaning coatings," *J. Mater. Chem.*, vol. 15, no. 17, pp. 1689-1695, 2005.
- [140] N. Yamazoe, "Toward innovations of gas sensor technology," *Sensors Actuators B Chem.*, vol. 108, no. 1–2, pp. 2–14, Jul. 2005.
- [141] L. Saadi, C. Lambert-Mauriat, V. Oison, H. Ouali, and R. Hayn, "Mechanism of NO<sub>x</sub> sensing on WO<sub>3</sub> surface: First principle calculations," *Appl. Surf. Sci.*, vol. 293, no. 2, pp. 76–79, 2014.
- [142] T. A. Ho, T. S. Jun, and Y. S. Kim, "Material and NH<sub>3</sub>-sensing properties of polypyrrole-coated tungsten oxide nanofibers," *Sensors Actuators, B Chem.*, vol. 185, pp. 523–529, 2013.
- [143] Y. Li, W. Luo, N. Qin, J. Dong, J. Wei, W. Li, S. Feng, J. Chen, J. Xu, A. A. Elzatahry, M. H. Es-Saheb, Y. Deng, and D. Zhao, "Highly ordered mesoporous tungsten oxides with a large pore size and crystalline framework for H<sub>2</sub>S sensing," *Angew. Chemie Int. Ed.*, vol. 53, no. 34, pp. 9035–9040, 2014.

- [144] S. Luo, G. Fu, H. Chen, Z. Liu, and Q. Hong, "Gas-sensing properties and complex impedance analysis of Ce-added WO<sub>3</sub> nanoparticles to VOC gases," *Solid. State. Electron.*, vol. 51, no. 6, pp. 913–919, 2007.
- [145] G. Xie, J. Yu, X. Chen, and Y. Jiang, "Gas sensing characteristics of WO<sub>3</sub> vacuum deposited thin films," *Sensors Actuators, B Chem.*, vol. 123, no. 2, pp. 909–914, 2007.
- [146] T. Samerjai, N. Tamaekong, C. Liewhiran, A. Wisitsoraat, A. Tuantranont, and S. Phanichphant, "Selectivity towards H<sub>2</sub> gas by flame-made Pt-loaded WO<sub>3</sub> sensing films," *Sensors Actuators, B Chem.*, vol. 157, no. 1, pp. 290–297, 2011.
- [147] M. U. Qadri, A. F. D. Diaz, M. Cittadini, A. Martucci, M. C. Pujol, J. Ferré-Borrull, E. Llobet, M. Aguiló, and F. Díaz, "Effect of Pt nanoparticles on the optical gas sensing properties of WO<sub>3</sub> thin films.," *Sensors (Basel)*, vol. 14, no. 7, pp. 11427–11443, 2014.
- [148] S. Park, H. Kim, C. Jin, S.-W. Choi, S. S. Kim, and C. Lee, "Enhanced CO gas sensing properties of Pt-functionalized WO<sub>3</sub> nanorods," *Thermochim. Acta*, vol. 542, pp. 69–73, 2012.
- [149] S. Piperno, M. Passacantando, S. Santucci, L. Lozzi, and S. La Rosa, "WO<sub>3</sub> nanofibers for gas sensing applications," *J. Appl. Phys.*, vol. 101, no. 12, p. 124504, 2007.
- [150] Y.-S. Shim, H. G. Moon, D. H. Kim, L. Zhang, S.-J. Yoon, Y. S. Yoon, C.-Y. Kang, and H. W. Jang, "Au-decorated WO<sub>3</sub> cross-linked nanodomains for ultrahigh sensitive and selective sensing of NO<sub>2</sub> and C<sub>2</sub>H<sub>5</sub>OH," *RSC Adv.*, vol. 3, no. 2, p. 10452, 2013.
- [151] C. Eid, A. Brioude, V. Salles, J.C. Plenet, R. Asmar, Y. Monteil, R. Khoury, A. Khoury, and P. Miele, "Iron-based 1D nanostructures by electrospinning process," *Nanotechnology*, vol. 21, pp. 125701, 2010.
- [152] V. Salles, S. Bernard, A. Brioude, D. Cornu, and P. Miele, "A new class of boron nitride fibers with tunable properties by combining an electrospinning process and the polymer-derived ceramics route," *Nanoscale*, vol. 2, pp. 215–217, 2010.
- [153] C. Eid, D. Luneau, V. Salles, R. Asmar, Y. Monteil, A. Khoury, and A. Brioude, "Magnetic properties of hematite nanotubes elaborated by electrospinning process," *J. Phys. Chem. C*, vol. 115, pp. 17643–17646, 2011.
- [154] John C. H. Spence, *Experimental high-resolution electron microscopy*, Oxford University Press, 427 p, 1988.
- [155] M. Wu, Q. Wang, K. Li, Y. Wu, and H. Liu, "Optimization of stabilization conditions for electrospun polyacrylonitrile nanofibers," *Polym. Degrad. Stab.*, vol. 97, no. 8, pp. 1511–1519, Aug. 2012.
- [156] Y. Arai, R. J. Akers, and C. R. G. Treasure., *Chemistry of powder production*, 1st English language ed., Chapman & Hall: London, p ix, 281 p, 1996.
- [157] S. J. Gregg and K. S. W. Sing, *Adsorption, surface area, and porosity*, Academic Press: London, Toronto, p xi, 303 p, 1982.
- [158] J. M. Mermet, "Is it still possible, necessary and beneficial to perform research in ICP-atomic emission spectrometry?," *J. Anal. At. Spectrom.*, vol. 20, no. 1, p. 11, Dec. 2005.
- [159] H.-H. Perkampus, *UV-VIS Spectroscopy and Its Applications*. Berlin, Heidelberg: Springer Berlin Heidelberg, p xi, 204 p, 1992.
- [160] M. A. Moharram and M. G. Khafagi, "Thermal behavior of poly(acrylic acid)–poly(vinyl pyrrolidone) and poly(acrylic acid)–metal–poly(vinyl pyrrolidone) complexes," *J. Appl. Polym. Sci.*, vol. 102, no. 4, pp. 4049–4057, Nov. 2006.
- [161] L. Huang, Z.R. Guo, M. Wang, N. GU, "Facile synthesis of gold nanoplates by citrate reduction of AuCl<sub>4</sub><sup>-</sup> at room temperature", *Chinese Chemical Letters*, vol. 17, no. 10, pp. 1405–1408, 2006.
- [162] A. Patterson, "The scherrer formula for X-ray particle size determination," *Phys. Rev.*, vol. 56, no. 10, pp. 978–982, Nov. 1939.

- [163] K. Otto, I. Oja Acik, M. Krunk, K. Tõnsuaadu, and A. Mere, "Thermal decomposition study of  $\text{HAuCl}_4 \cdot 3\text{H}_2\text{O}$  and  $\text{AgNO}_3$  as precursors for plasmonic metal nanoparticles," *J. Therm. Anal. Calorim.*, pp. 1–8, 2014.
- [164] J. Yan, G. Zou, A. Hu, and Y. N. Zhou, "Preparation of PVP coated Cu NPs and the application for low-temperature bonding," *J. Mater. Chem.*, vol. 21, no. 1, pp. 15981–15986, 2011.
- [165] H. Kakida and K. Tashiro, "Mechanism and kinetics of stabilization reactions of polyacrylonitrile and related copolymers III. comparison among the various types of copolymers as viewed from isothermal DSC thermograms and FT-IR spectral changes," *Polym. J.*, vol. 29, no. 7, pp. 557–562, Jul. 1997.
- [166] W. Luo, K. Su, K. Li, G. Liao, N. Hu, and M. Jia, "Substrate effect on the melting temperature of gold nanoparticles," *J. Chem. Phys.*, vol. 136, no. 23, p. 234704, 2012.
- [167] X. Chen and S. S. Mao, "Titanium dioxide nanomaterials: synthesis, properties, modifications, and applications," *Chem. Rev.*, vol. 107, no. 7, pp. 2891–959, Jul. 2007.
- [168] R. Sanjines, H. Tang, H. Berger, F. Gozzo, G. Margaritondo, and F. Levy, "Electronic-structure of anatase  $\text{TiO}_2$  oxide," *J. Appl. Phys.*, vol. 75, no. 6, pp. 2945–2951, Mar. 1994.
- [169] Y. Xiong, I. Washio, J. Chen, H. Cai, Z.-Y. Li, and Y. Xia, "Poly(vinyl pyrrolidone): a dual functional reductant and stabilizer for the facile synthesis of noble metal nanoplates in aqueous solutions," *Langmuir*, vol. 22, no. 20, pp. 8563–8570, Sep. 2006.
- [170] D. A. H. Hanaor and C. C. Sorrell, "Review of the anatase to rutile phase transformation," *J. Mater. Sci.*, vol. 46, no. 4, pp. 855–874, Dec. 2010.
- [171] E. Brillas, "Degradation of the herbicide 2,4-dichlorophenoxyacetic acid by ozonation catalyzed with  $\text{Fe}^{2+}$  and UVA light," *Appl. Catal. B Environ.*, vol. 46, no. 2, pp. 381–391, Nov. 2003.
- [172] Y. Hu, Y. Liu, H. Qian, Z. Li, and J. Chen, "Coating colloidal carbon spheres with CdS nanoparticles: microwave-assisted synthesis and enhanced photocatalytic activity," *Langmuir*, vol. 26, no. 23, pp. 18570–18575, Dec. 2010.
- [173] Y. Hao, X. Shao, B. Li, L. Hu, and T. Wang, "Mesoporous  $\text{TiO}_2$  nanofibers with controllable Au loadings for catalytic reduction of 4-nitrophenol," *Mater. Sci. Semicond. Process.*, vol. 40, pp. 621–630, Dec. 2015.
- [174] B. Ohtani, O. O. Prieto-Mahaney, D. Li, and R. Abe, "What is Degussa (Evonic) P25 crystalline composition analysis, reconstruction from isolated pure particles and photocatalytic activity test," *J. Photochem. Photobiol. A Chem.*, vol. 216, no. 2–3, pp. 179–182, 2010.
- [175] A. Furube, L. Du, K. Hara, R. Katoh, and M. Tachiya, "Ultrafast plasmon-induced electron transfer from gold nanodots into  $\text{TiO}_2$  nanoparticles," *J. Am. Chem. Soc.*, vol. 129, no. 48, pp. 14852–14853, Dec. 2007.
- [176] Q. Xiang, J. Yu, B. Cheng, and H. C. Ong, "Microwave-hydrothermal preparation and visible-light photoactivity of plasmonic photocatalyst Ag- $\text{TiO}_2$  nanocomposite hollow spheres," *Chem. Asian J.*, vol. 5, no. 6, pp. 1466–74, Jun. 2010.
- [177] J. Yu, G. Dai, and B. Huang, "Fabrication and characterization of visible-light-driven plasmonic photocatalyst Ag/AgCl/ $\text{TiO}_2$  nanotube arrays," *J. Phys. Chem. C*, vol. 113, no. 37, pp. 16394–16401, Sep. 2009.
- [178] Q. Xiang, J. Yu, and P. K. Wong, "Quantitative characterization of hydroxyl radicals produced by various photocatalysts," *J. Colloid Interface Sci.*, vol. 357, no. 1, pp. 163–7, May 2011.
- [179] T. A. Ho, T.-S. Jun, and Y. S. Kim, "Material and  $\text{NH}_3$ -sensing properties of polypyrrole-coated tungsten oxide nanofibers," *Sensors Actuators B Chem.*, vol. 185, pp. 523–529, Aug. 2013.

- [180] J. Dummer, M. Storer, M. Swanney, M. McEwan, A. Scott-Thomas, S. Bhandari, S. Chambers, R. Dweik, and M. Epton, "Analysis of biogenic volatile organic compounds in human health and disease," *TrAC Trends Anal. Chem.*, vol. 30, no. 7, pp. 960–967, Jul. 2011.
- [181] H. Wang, Y. Qu, H. Chen, Z. Lin, and K. Dai, "Highly selective n-butanol gas sensor based on mesoporous SnO<sub>2</sub> prepared with hydrothermal treatment," *Sensors Actuators B Chem.*, vol. 201, pp. 153–159, Oct. 2014.
- [182] J. Yue, X. Jiang, and A. Yu, "Molecular dynamics study on metal-deposited iron oxide nanostructures and their gas adsorption behavior," *J. Phys. Chem. C*, vol. 116, no. 14, pp. 8145–8153, Apr. 2012.
- [183] Y. V. Kaneti, Q. M. D. Zakaria, Z. Zhang, C. Chen, J. Yue, M. Liu, X. Jiang, and A. Yu, "Solvothermal synthesis of ZnO-decorated  $\alpha$ -Fe<sub>2</sub>O<sub>3</sub> nanorods with highly enhanced gas-sensing performance toward n-butanol," *J. Mater. Chem. A*, vol. 2, no. 33, p. 13283, Jun. 2014.
- [184] C. Wang, L. Yin, L. Zhang, D. Xiang, and R. Gao, "Metal oxide gas sensors: sensitivity and influencing factors.," *Sensors (Basel)*, vol. 10, no. 3, pp. 2088–106, Jan. 2010.
- [185] Y. V Kaneti, Z. Zhang, J. Yue, Q. M. D. Zakaria, C. Chen, X. Jiang, and A. Yu, "Crystal plane-dependent gas-sensing properties of zinc oxide nanostructures: experimental and theoretical studies.," *Phys. Chem. Chem. Phys.*, vol. 16, no. 23, pp. 11471–11480, Jun. 2014.
- [186] N. BARSAN, D. KOZIEJ, and U. WEIMAR, "Metal oxide-based gas sensor research: How to?," *Sensors Actuators B Chem.*, vol. 121, no. 1, pp. 18–35, Jan. 2007.
- [187] Y. V. Kaneti, J. Yue, X. Jiang, and A. Yu, "Controllable synthesis of ZnO nanoflakes with exposed (10 $\bar{1}$ 0) for enhanced gas sensing performance," *J. Phys. Chem. C*, vol. 117, no. 25, pp. 13153–13162, Jun. 2013.
- [188] X. Yang, V. Salles, Y. V. Kaneti, M. Liu, M. Maillard, C. Journet, X. Jiang, and A. Brioude, "Fabrication of highly sensitive gas sensor based on Au functionalized WO<sub>3</sub> composite nanofibers by electrospinning," *Sensors Actuators B Chem.*, vol. 220, pp. 1112–1119, 2015.
- [189] J. Zhang, X. Liu, M. Xu, X. Guo, S. Wu, S. Zhang, and S. Wang, "Pt clusters supported on WO<sub>3</sub> for ethanol detection," *Sensors Actuators B Chem.*, vol. 147, no. 1, pp. 185–190, May 2010.
- [190] Y. V. Kaneti, J. Moriceau, M. Liu, Y. Yuan, Q. Zakaria, X. Jiang, and A. Yu, "Hydrothermal synthesis of ternary  $\alpha$ -Fe<sub>2</sub>O<sub>3</sub>–ZnO–Au nanocomposites with high gas-sensing performance," *Sensors Actuators B Chem.*, vol. 209, pp. 889–897, Mar. 2015.
- [191] L. Wang, H. Dou, Z. Lou, and T. Zhang, "Encapsulated nanoreactors (Au@SnO<sub>2</sub>): a new sensing material for chemical sensors.," *Nanoscale*, vol. 5, no. 7, pp. 2686–2691, 2013.
- [192] D. A. Egger and E. Zojer, "Anticorrelation between the evolution of molecular dipole moments and induced work function modifications.," *J. Phys. Chem. Lett.*, vol. 4, no. 20, pp. 3521–3526, Oct. 2013.
- [193] C.-Y. Su and H.-C. Lin, "Direct route to tungsten oxide nanorod bundles: microstructures and electro-optical properties," *J. Phys. Chem. C*, vol. 113, no. 10, pp. 4042–4046, Mar. 2009.
- [194] T. He, Y. Ma, Y. Cao, W. Yang, and J. Yao, "Improved photochromism of WO<sub>3</sub> thin films by addition of Au nanoparticles," *Phys. Chem. Chem. Phys.*, vol. 4, no. 9, pp. 1637–1639, Apr. 2002.
- [195] Y. Liu, J. Yu, W. M. Tang, and P. T. Lai, "On the voltage dependence of sensitivity for Schottky-type gas sensor," *Appl. Phys. Lett.*, vol. 105, no. 22, p. 223503, Dec. 2014.



## APPENDICES

### Appendix A: JCPDS Card of gold

#### Name and formula

Reference code:	00-004-0784
Mineral name:	Gold, syn
PDF index name:	Gold
Empirical formula:	Au
Chemical formula:	Au

#### Crystallographic parameters

Crystal system:	Cubic
Space group:	Fm-3m
Space group number:	225

a (Å):	4,0786
b (Å):	4,0786
c (Å):	4,0786
Alpha (°):	90,0000
Beta (°):	90,0000
Gamma (°):	90,0000

Calculated density (g/cm <sup>3</sup> ):	19,30
Measured density (g/cm <sup>3</sup> ):	19,30
Volume of cell (10 <sup>6</sup> pm <sup>3</sup> ):	67,85
Z:	4,00
RIR:	-

#### Subfiles and Quality

Subfiles:	Inorganic Mineral Alloy, metal or intermetallic Common Phase Educational pattern Forensic NBS pattern
Quality:	Star (S)

#### Comments

Color: Yellow metallic

General comments: Opaque mineral optical data on specimen from unspecified locality:  $RR_2Re=71.6$ ,  $Disp.=16$ ,  $VHN_{100}=53-58$ , Color values=.384, .391, 72.7, Ref.: IMA Commission on Ore Microscopy QDF.

Sample source: Sample purified at NBS, Gaithersburg, Maryland, USA and is about 99.997% Au.

Analysis: Spectrographic analysis (%): Si 0.001, Ca 0.001, Ag 0.001(?).

Optical data:  $B=0.366$

Melting point: 1061.6-1063.2

Temperature: Pattern taken at 26 C.

### References

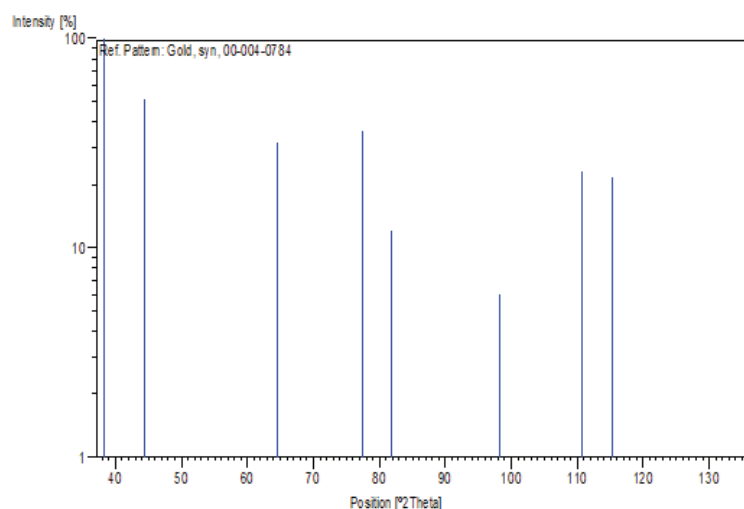
Primary reference: Swanson, Tatge., *Natl. Bur. Stand. (U.S.), Circ. 539, I, 33*, (1953)

Optical data: Winchell., *Elements of Optical Mineralogy*, 17

### Peak list

No.	h	k	l	d [Å]	2Theta [deg]	I [%]
1	1	1	1	2,35500	38,185	100,0
2	2	0	0	2,03900	44,393	52,0
3	2	2	0	1,44200	64,578	32,0
4	3	1	1	1,23000	77,549	36,0
5	2	2	2	1,17740	81,724	12,0
6	4	0	0	1,01960	98,137	6,0
7	3	3	1	0,93580	110,802	23,0
8	4	2	0	0,91200	115,264	22,0
9	4	2	2	0,83250	135,423	23,0

### Stick Pattern



## Appendix B: JCPDS Card of titanium oxide (phase of anatase)

### Name and formula

Reference code:	00-021-1272
Mineral name:	Anatase, syn
PDF index name:	Titanium Oxide
Empirical formula:	O <sub>2</sub> Ti
Chemical formula:	TiO <sub>2</sub>

### Crystallographic parameters

Crystal system:	Tetragonal
Space group:	I41/amd
Space group number:	141
a (Å):	3,7852
b (Å):	3,7852
c (Å):	9,5139
Alpha (°):	90,0000
Beta (°):	90,0000
Gamma (°):	90,0000
Calculated density (g/cm <sup>3</sup> ):	3,89
Volume of cell (10 <sup>6</sup> pm <sup>3</sup> ):	136,31
Z:	4,00
RIR:	3,30

### Subfiles and Quality

Subfiles:	Inorganic
	Mineral
	Alloy, metal or intermetallic
	Corrosion
	Common Phase
	Educational pattern
	Forensic
	NBS pattern

Pigment/Dye  
Quality: Star (S)

### **Comments**

Color: Colorless

General comments: Anatase and another polymorph, brookite (orthorhombic), are converted to rutile (tetragonal) by heating above 700 C.  
Pattern reviewed by Holzer, J., McCarthy, G., North Dakota State Univ, Fargo, North Dakota, USA, *ICDD Grant-in-Aid* (1990). Agrees well with experimental and calculated patterns.

Sample source: Sample obtained from National Lead Co., South Amboy, New Jersey, USA.

Additional pattern: Validated by calculated pattern.  
See ICSD 9852 (PDF 71-1166).

Temperature: Pattern taken at 25 C.

### **References**

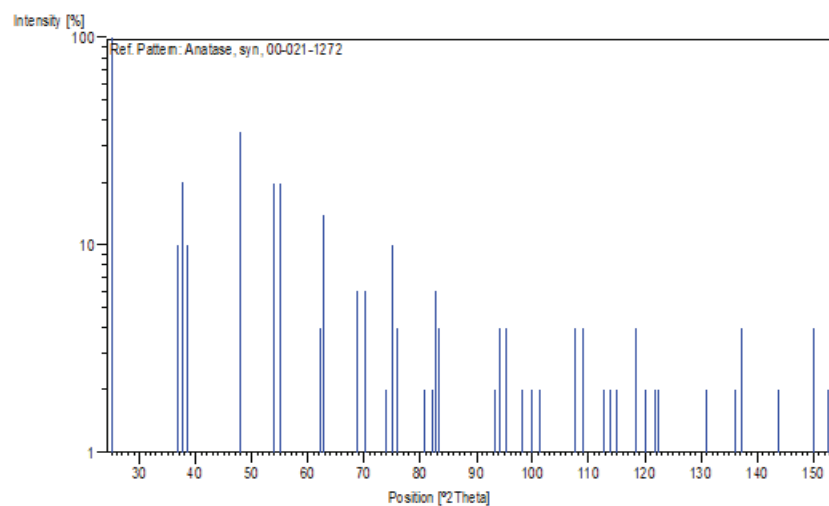
Primary reference: *Natl. Bur. Stand. (U.S.) Monogr. 25, 7, 82, (1969)*

### **Peak list**

No.	h	k	l	d [Å]	2Theta [deg]	I [%]
1	1	0	1	3,52000	25,281	100,0
2	1	0	3	2,43100	36,947	10,0
3	0	0	4	2,37800	37,801	20,0
4	1	1	2	2,33200	38,576	10,0
5	2	0	0	1,89200	48,050	35,0
6	1	0	5	1,69990	53,891	20,0
7	2	1	1	1,66650	55,062	20,0
8	2	1	3	1,49300	62,121	4,0
9	2	0	4	1,48080	62,690	14,0
10	1	1	6	1,36410	68,762	6,0
11	2	2	0	1,33780	70,311	6,0
12	1	0	7	1,27950	74,031	2,0
13	2	1	5	1,26490	75,032	10,0
14	3	0	1	1,25090	76,020	4,0
15	0	0	8	1,18940	80,727	2,0
16	3	0	3	1,17250	82,139	2,0
17	2	2	4	1,16640	82,662	6,0
18	3	1	2	1,16080	83,149	4,0
19	2	1	7	1,06000	93,221	2,0

20	3	0	5	1,05170	94,182	4,0
21	3	2	1	1,04360	95,143	4,0
22	1	0	9	1,01820	98,319	2,0
23	2	0	8	1,00700	99,804	2,0
24	3	2	3	0,99670	101,221	2,0
25	3	1	6	0,95550	107,448	4,0
26	4	0	0	0,94640	108,963	4,0
27	3	0	7	0,92460	112,841	2,0
28	3	2	5	0,91920	113,861	2,0
29	4	1	1	0,91380	114,909	2,0
30	2	1	9	0,89660	118,439	4,0
31	2	2	8	0,88900	120,104	2,0
32	4	1	3	0,88190	121,725	2,0
33	4	0	4	0,87930	122,336	2,0
34	4	2	0	0,84640	131,036	2,0
35	3	2	7	0,83080	135,998	2,0
36	4	1	5	0,82680	137,391	4,0
37	3	0	9	0,81020	143,888	2,0
38	4	2	4	0,79740	150,039	4,0
39	0	0	12	0,79280	152,634	2,0

### Stick Pattern



## Appendix C: JCPDS Card of titanium oxide (phase of rutile)

### Name and formula

Reference code:	00-021-1276
Mineral name:	Rutile, syn
Common name:	titania
PDF index name:	Titanium Oxide
Empirical formula:	O <sub>2</sub> Ti
Chemical formula:	TiO <sub>2</sub>

### Crystallographic parameters

Crystal system:	Tetragonal
Space group:	P42/mnm
Space group number:	136
a (Å):	4, 5933
b (Å):	4, 5933
c (Å):	2, 9592
Alpha (°):	90, 0000
Beta (°):	90, 0000
Gamma (°):	90, 0000
Calculated density (g/cm <sup>3</sup> ):	4, 25
Measured density (g/cm <sup>3</sup> ):	4, 23
Volume of cell (10 <sup>6</sup> pm <sup>3</sup> ):	62, 43
Z:	2, 00
RIR:	3, 40

### Subfiles and Quality

Subfiles:	Inorganic Mineral Alloy, metal or intermetallic Corrosion Common Phase Educational pattern Forensic NBS pattern Pigment/Dye
Quality:	Star (S)

**Comments**

Color:	White
General comments:	No impurity over 0.001%. Two other polymorphs, anatase (tetragonal) and brookite (orthorhombic), converted to rutile on heating above 700 C. Optical data on specimen from <i>Dana's System of Mineralogy, 7th Ed., I 555</i> . Pattern reviewed by Syvinski, W., McCarthy, G., North Dakota State Univ, Fargo, North Dakota, USA, <i>ICDD Grant-in-Aid (1990)</i> . Agrees well with experimental and calculated patterns. Additional weak reflections [indicated by brackets] were observed. Naturally occurring material may be reddish brown.
Sample source:	Sample obtained from National Lead Co., South Amboy, New Jersey, USA.
Optical data:	A=2.9467, B=2.6505, Sign=+
Additional pattern:	Validated by calculated pattern.
Temperature:	Pattern taken at 25 C.

**References**

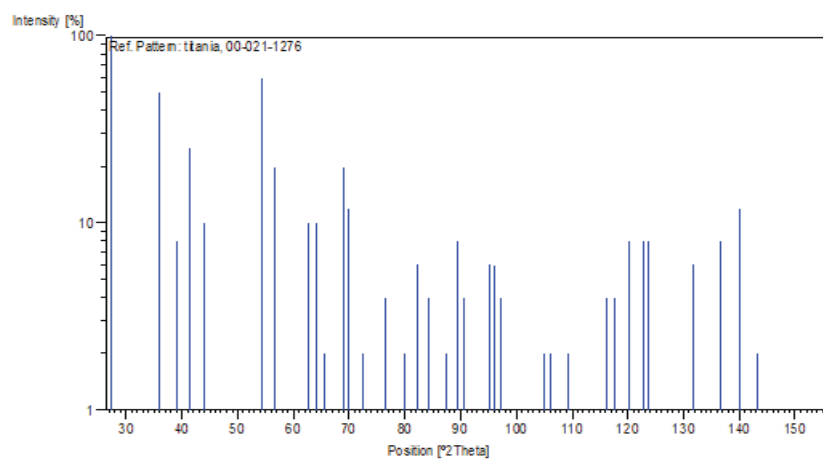
Primary reference:	<i>Natl. Bur. Stand. (U.S.) Monogr. 25, 7, 83, (1969)</i>
Optical data:	<i>Dana's System of Mineralogy, 7th Ed., I, 575</i>

**Peak list**

No.	h	k	l	d [Å]	2Theta [deg]	I [%]
1	1	1	0	3,24700	27,447	100,0
2	1	0	1	2,48700	36,086	50,0
3	2	0	0	2,29700	39,188	8,0
4	1	1	1	2,18800	41,226	25,0
5	2	1	0	2,05400	44,052	10,0
6	2	1	1	1,68740	54,323	60,0
7	2	2	0	1,62370	56,642	20,0
8	0	0	2	1,47970	62,742	10,0
9	3	1	0	1,45280	64,040	10,0
10	2	2	1	1,42430	65,480	2,0
11	3	0	1	1,35980	69,010	20,0
12	1	1	2	1,34650	69,790	12,0
13	3	1	1	1,30410	72,410	2,0
14	3	2	0	1,27390	74,411	1,0
15	2	0	2	1,24410	76,510	4,0
16	2	1	2	1,20060	79,822	2,0
17	3	2	1	1,17020	82,335	6,0
18	4	0	0	1,14830	84,260	4,0

19	4	1	0	1,11430	87,464	2,0
20	2	2	2	1,09360	89,557	8,0
21	3	3	0	1,08270	90,708	4,0
22	4	1	1	1,04250	95,275	6,0
23	3	1	2	1,03640	96,017	6,0
24	4	2	0	1,02710	97,177	4,0
25	3	3	1	1,01670	98,514	1,0
26	4	2	1	0,97030	105,099	2,0
27	1	0	3	0,96440	106,019	2,0
28	1	1	3	0,94380	109,406	2,0
29	4	0	2	0,90720	116,227	4,0
30	5	1	0	0,90090	117,527	4,0
31	2	1	3	0,88920	120,059	8,0
32	4	3	1	0,87740	122,788	8,0
33	3	3	2	0,87380	123,660	8,0
34	4	2	2	0,84370	131,847	6,0
35	3	0	3	0,82920	136,549	8,0
36	5	2	1	0,81960	140,052	12,0
37	4	4	0	0,81200	143,116	2,0
38	5	3	0	0,78770	155,870	2,0

### Stick Pattern



## Appendix D: JCPDS Card of tungsten oxide

### Name and formula

Reference code:	00-032-1395
PDF index name:	Tungsten Oxide
Empirical formula:	O <sub>3</sub> W
Chemical formula:	WO <sub>3</sub>

### Crystallographic parameters

Crystal system:	Anorthic
Space group:	P-1
Space group number:	2
a (Å):	7,3090
b (Å):	7,5220
c (Å):	7,6780
Alpha (°):	88,8100
Beta (°):	90,9200
Gamma (°):	90,9300
Calculated density (g/cm <sup>3</sup> ):	7,30
Measured density (g/cm <sup>3</sup> ):	7,27
Volume of cell (10 <sup>6</sup> pm <sup>3</sup> ):	421,92
Z:	8,00
RIR:	-

### Subfiles and Quality

Subfiles:	Inorganic Alloy, metal or intermetallic Corrosion
Quality:	Star (S)

**Comments**

General comments: Stable from -40 C to 17 C.  
Single-crystal data used.

Additional pattern: See 20-1323.

**References**

Primary reference: Diehl, R. et al., *Acta Crystallogr., Sec. B*, **34**, 1105, (1978)

**Peak list**

No.	h	k	l	d [Å]	2Theta[deg]	I [%]
1	0	0	2	3,84000	23,144	85,0
2	0	2	0	3,76000	23,643	100,0
3	2	0	0	3,65000	24,367	100,0
4	-1	2	0	3,36200	26,490	9,0
5	0	-2	1	3,34600	26,619	13,0
6	-2	0	1	3,31900	26,840	8,0
7	-1	1	2	3,14200	28,383	7,0
8	-1	2	1	3,11500	28,634	13,0
9	1	1	2	3,09300	28,842	18,0
10	-1	-1	2	3,08400	28,928	20,0
11	1	-1	2	3,06940	29,069	8,0
12	0	2	2	2,71220	33,000	20,0
13	-2	0	2	2,66690	33,577	35,0
14	0	-2	2	2,65920	33,677	25,0
15	-2	2	0	2,64100	33,916	25,0
16	2	0	2	2,62680	34,105	35,0
17	2	2	0	2,59810	34,493	25,0
18	-1	2	2	2,56160	35,001	3,0
19	-2	1	2	2,53440	35,389	4,0
20	1	2	2	2,52610	35,509	4,0
21	-2	2	1	2,51520	35,668	7,0
22	1	-2	2	2,49970	35,896	7,0
23	3	-1	1	2,21480	40,705	3,0
24	-2	2	2	2,20190	40,954	17,0
25	2	2	2	2,15580	41,871	30,0

**Stick Pattern**

